UNIVERSITÉ DE STRASBOURG

Université de Strasbourg

École doctorale
Physique, chimie-physique
ED 182
Université de Strasbourg

ÉCOLE DOCTORALE 182

UMR 7504 IPCMS

THÈSE présentée par :

Rémi PASQUIER

soutenue le : **09 février 2024**

pour obtenir le grade de : **Docteur de l'université de Strasbourg**

Discipline/ Spécialité : Physique de la matière condensée

Theory of the electronic structure of spin crossover molecules on metallic surfaces

Théorie de la structure électronique des molécules à transition de spin sur surfaces métalliques

---

THÈSE dirigée par :
  M. Mébarek ALOUANI   Dr., IPCMS, Université de Strasbourg, UMR 7504 CNRS

RAPPORTEURS :
  Mme Roberta POLONI   Dr., SIMaP, Université de Grenoble-Alpes, UMR 5266 CNRS
  M. Sébastien LEBEGUE   Dr., LPCT, Université de Lorraine, UMR 7019 CNRS

EXAMINATEURS :
  M. Jean-François DAYEN   Dr., IPCMS, Université de Strasbourg, UMR 7504 CNRS

Théorie de la structure électronique des molécules à transition de spin sur surfaces métalliques : résumé de thèse

R. Pasquier

Université de Strasbourg, Institut de Physique et de Chimie des Matériaux de Strasbourg,

CNRS-UNISTRA UMR 7504, 67034 Strasbourg, France

La Spintronique est un domaine de la physique qui s'intéresse à l'étude et l'utilisation des degrés de liberté de spin d'un électron en plus de la charge électronique. Il s'agit d'un domaine assez jeune, qui trouve ses origines dans plusieurs travaux effectués au cours des années 80. Un exemple notable est la découverte de la magnétorésistance géante par Fert et Grünberg et 1988, ce qui a mené à plusieurs percées dans le domaine des disques durs et à un prix Nobel en 2007. Ainsi, ce nouveau degré de liberté de spin a entraîné la création d'une grande variété de systèmes électroniques novateurs, parmi lesquels les systèmes hybrides molécule-surface métallique. Ceux-ci ont l'avantage de combiner les propriétés de la surface métallique, telles que leur magnétisme, avec les propriétés moléculaires telles que le phénomène de transition de spin. En effet, dans le champ électrique créé par un ligand de géométrie octaédrique, la quintuple dégénérescence des orbitales d de l'atome métallique complexé, appelé centre octaédrique, est levée en deux groupes d'orbitales de basse énergie (t_{2g}, composée des orbitales hors axes d_{xy}, d_{yz} et d_{zx}) et de haute énergie (e_g, composée des orbitales axiales $d_{x^2-y^2}$ et d_{z^2}). Nous avons ainsi naturellement différents états de spin pour le complexe selon l'appariement desdits spins, et par définition on appelle état de bas spin (LS) celui d'appariement maximal et état de haut spin (HS) celui d'appariement minimal, et ainsi on peut envisager des transitions entre ces différents états : c'est la transition de spin.
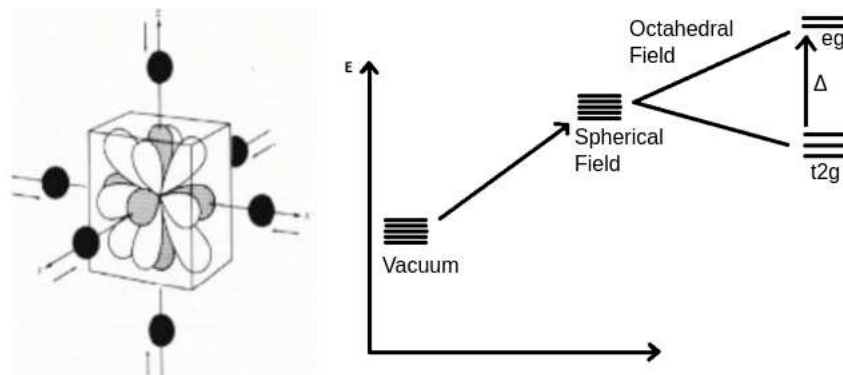

FIGURE 1 – Complexe en symétrie octaédrique avec les orbitales t_{2g} en blanc et e_g en gris, et levée de dégénérescence dans un complexe octaédrique. La figure de gauche provient de [1]

Ce phénomène de transition de spin a été observé pour la première fois dans le cas de la molécule de $Fe(phenanthroline)_2(NCS)_2$ (que l'on désignera par l'abréviation très com-

mune de FePhen désormais) par Baker et Bobonic en 1964 [2], au cours de leur étude de la susceptibilité magnétique de complexes de la forme $Fe(Phen)_2X_2$. Ce système est depuis devenu un exemple de référence pour l'étude de la transition de spin. Le but de cette thèse est ainsi d'étendre les résultats déjà obtenus sur ce système ([3, 4]), notamment adsorbé sur une surface de Cu(100) ([5]), mais également de les appliquer à d'autres systèmes de transition connus dans la littérature. Nous nous attacherons à étudier l'effet relativement inexploré du dopage sur ces systèmes à transition de spin, et nous montrerons comment manipuler l'état de spin grâce à des substitutions des atomes d'hydrogène des ligands. Nous implémenterons également dans le code VASP le calcul de spectres d'absorption à rayons X sur ces systèmes, et étudié l'influence de la surface et de la déformation octaédrique sur le signal. Finalement, nous avons également calculé les images STM au-delà de l'approximation Tersoff-Hamann, et montré et étudié les différences avec cette approche basique. Nous présenterons également quelques résultats préliminaires sur le calcul des phonons et de l'énergie libre dans ces molécules à transition de spin.
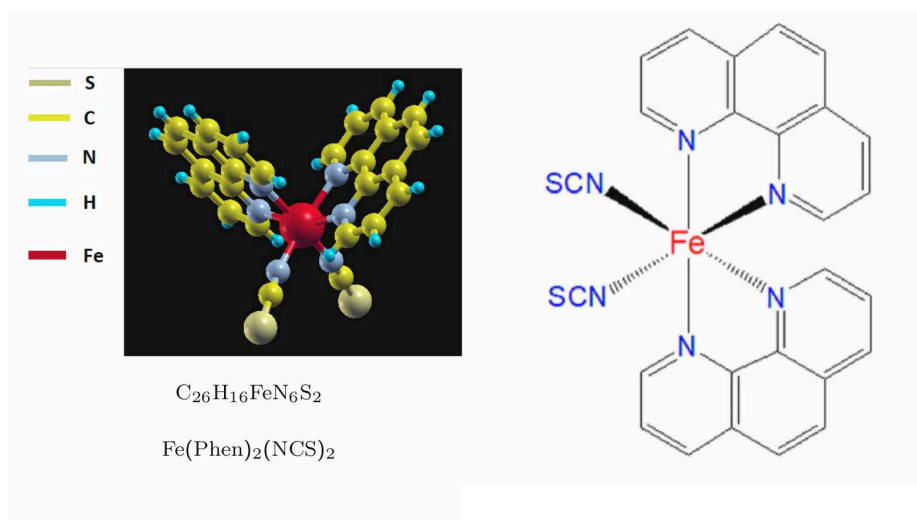

FIGURE 2 – Structure de la molécule de FePhen. La représentation de Cram provient de [6]

Le phénomène de transition de spin est intrinsèquement lié à l'influence du champ électrostatique des ligands sur le centre octaédrique. Ainsi, il paraît légitime de s'intéresser à l'effet d'un changement desdits ligands sur les états magnétiques moléculaires. En particulier, un domaine assez inexploré est celui de l'influence du dopage, par exemple en substituant certains atomes par d'autres dans la composition des ligands. Et c'est ainsi le sujet du pre-

mier article de cette thèse, où nous nous intéressons à l'effet du remplacement des atomes d'hydrogène de la molécule de FePhen par du fluor. On montre ainsi que ladite substitution mène à une profonde transformation de la structure électronique du complexe.
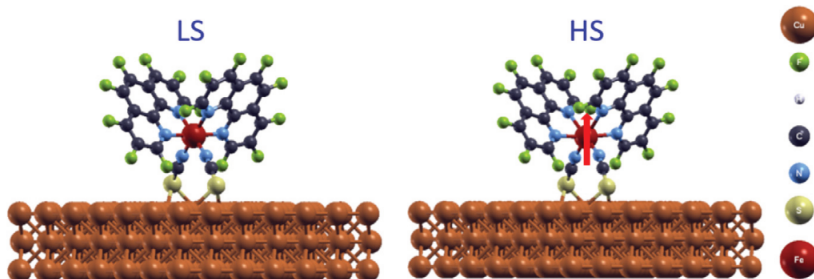

FIGURE 3 – Structure de la molécule de FePhen fluorinée et adsorbée sur une surface de Cu(100) [7]

En premier lieu, nous avons observé que ce dopage entraîne une inversion de l'état de spin de la molécule de FePhen, qui devient alors un complexe HS à basse température que ce soit dans l'état gazeux ou absorbée sur une surface métallique. Une inspection de la géométrie du système montre une distorsion de l'octaèdre de la molécule, associée à une élongation des liaisons Fe-N, ce qui fournit une première explication au phénomène observé car une telle élongation ne peut se traduire que par une réduction du champ électrostatique des ligands au niveau de l'atome central et ainsi du Δ octaédrique, ce qui va naturellement favoriser l'état HS comme vu précédemment.

		LS	HS	ΔE (kJ/mol)
Non-dopée	E_T (eV)	-749.57 (-359.726)	-749.00 (-359.517)	55.3 (20.3)
	μ_{Fe} (μ_{B})	0.00 (0.00)	3.60 (3.72)	
Dopée	E_T (eV)	-887.407 (361.701)	-887.609 (361.977)	-19.6 (-26.8)
	μ_{Fe} (μ_{B})	0.00 (0.00)	3.25 (3.72)	

TABLE I – Énergie totale (E_T) en eV et moment magnétique sur l'atome de fer (μ_{Fe}) en magnétons de Bohr (μ_{B}) pour les états HS et LS des molécules non-dopée et dopée sur une surface de Cu(001), avec les valeurs pour la molécule en phase gazeuse entre parenthèses. La dernière colonne donne la différence entre les valeurs respectives $\Delta E = E_T^{\text{HS}} - E_T^{\text{LS}}$ in kJ/mol [7].
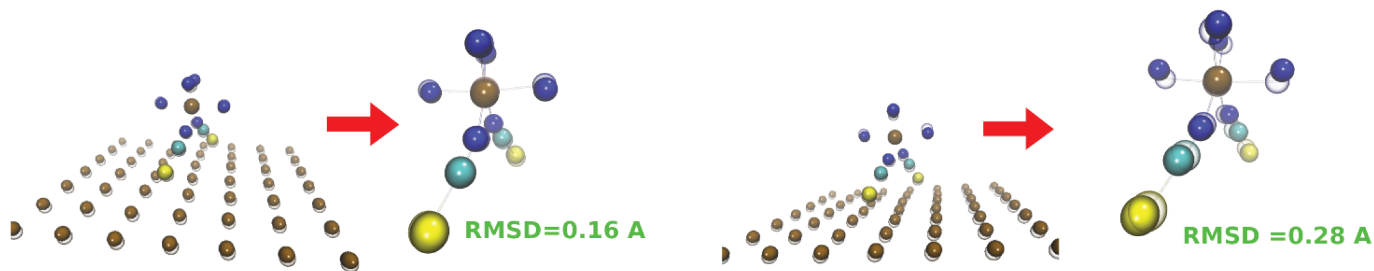
FIGURE 4 – Illustration de la déformation avant et après fluorination de la molecule de Fephen, état LS à gauche et état HS à droite [7]

Une étude plus fine de la structure des densités d'état corrobore ce résultat, en montrant une nette réduction de la séparation entre les pics e_g et t_{2g}, notamment dans l'état HS. L'utilisation couplée de l'analyse de Bader de la répartition et d'un modèle de charge ponctuelle démontre que ces modifications sont issues du ré-arrangement électronique au sein de la molécule, provoqué par la forte électronégativité des atomes de fluor, qui augmente ainsi la charge des ions d'azotes de l'octaèdre central. Ainsi, la répulsion électronique avec le centre octaédrique est accrue, ce qui mène au résultat observé.

Nous procédons ensuite à une étude du spectre phononique dans ces molécules. Nous commençons par un calcul des phonons dans l'approximation harmonique dans la molécule dopée et non dopée. Nous montrons tout d'abord que les fréquences les plus affectées par la transition de spin sont celles associées aux processus dans l'octaèdre central, ce qui correspond aux résultats déjà obtenus [8] et est en accord avec la localisation des élongations de liaisons dans l'octaèdre central au cours de la transition de spin. Nous utilisons ensuite ces fréquences pour calculer l'évolution des principales grandeurs thermodynamiques dans la molécule non-dopée, telles que de la différence d'entropie de vibration, la différence d'enthalpie de vibration et finalement la différence entre l'énergie libre entre les deux états avec la température, qui démontre ainsi une inversion à une température en accord avec les valeurs expérimentales, bien qu'un tel accord soit relativement fortuit au regard des calculs similaires déjà menés dans la littérature. L'utilisation de ces grandeurs thermodynamiques nous permet ensuite de calculer l'évolution de la fraction en états HS avec la température en utilisant la formule de Slichter-Drickamer [9], avec un bon accord avec les résultats expérimentaux.
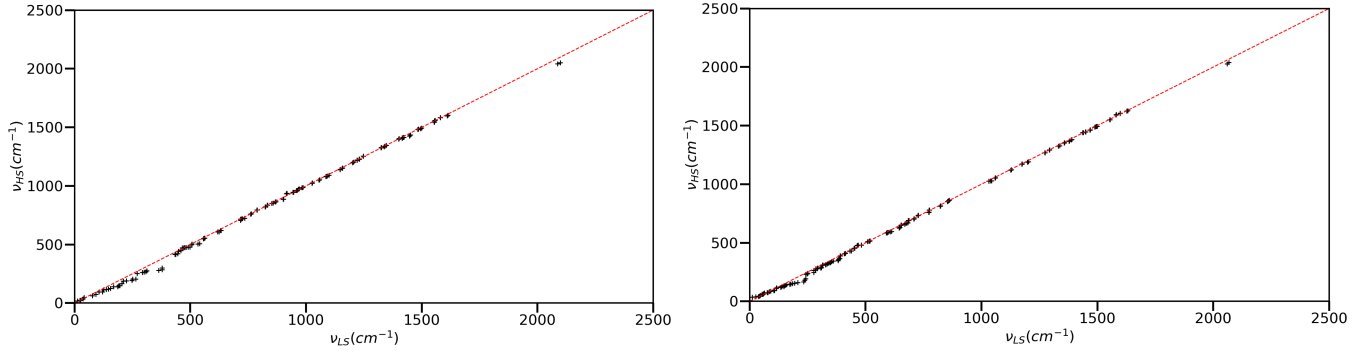
FIGURE 5 – Corrélation HS-LS des fréquences phononiques dans la molécule non-dopée (à gauche) et dopée (à droite)

.

Nous procédons également à la même étude sur la molécule dopée, et nous montrons ainsi que le dopage mène à des modifications sur les fréquences associées aux processus dans l'octaèdre, ce qui correspond au fait que ces liaisons sont les plus affectées après la fluorination de manière très similaire à la transition de spin. Ainsi, le calcul de l'énergie libre démontre que l'état HS est toujours le plus stable à toute température, ce qui confirme que la molécule dopée devrait rester un complexe dans l'état HS expérimentalement ce qui correspond aux attentes théoriques car le phénomène de transition de spin est lié à l'entropie de vibration qui stabilise ainsi l'état HS en allongeant la valeur moyenne des longueurs de liaison.
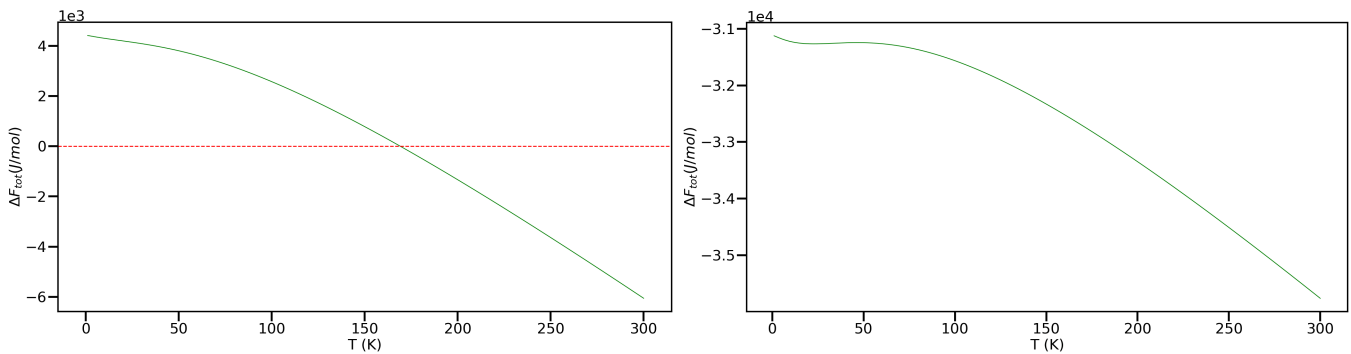

FIGURE 6 – Différence d'énergie libre entre les états HS et LS pour la molécule dopée (à gauche) et non dopée (à droite)

.

Nous montrons ensuite nos résultats de simulation de phonons à partir de la dynamique moléculaire dans la molécule non dopée, qui est une approche commune afin d'obtenir un

spectre au delà de l'approximation harmonique à partir de la transformée de Fourier de la fonction d'autocorrélation des vitesses. Nous calculons ainsi ce spectre à trois température : 100 K, 200 K et 300 K. Nous obtenons ainsi des résultats inconclusifs avec une absence notable des fréquences associées au groupement isothiocyanate, mais qui démontrent néanmoins une transition de spin à une température en accord relatif avec les résultats expérimentaux.
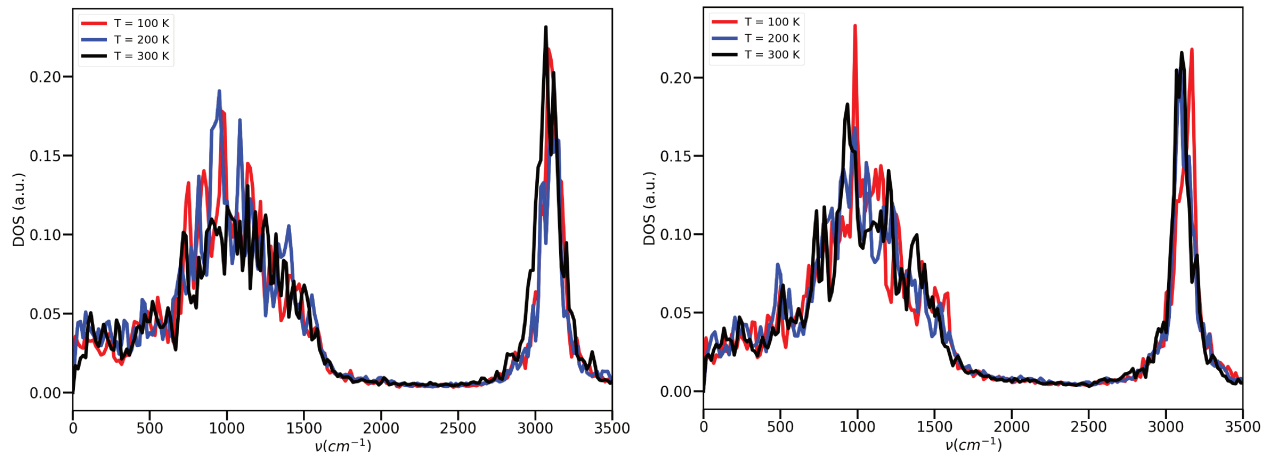

FIGURE 7 – Spectres de phonons en dynamique moléculaire pour la molécule non-dopée dans l'état HS (à gauche) et dans l'état LS (à droite)

.

Le second article de cette thèse porte sur la simulation de spectres d'absorption à rayons X. L'utilisation d'une telle technique expérimentale est commune pour la caractérisation des complexes à transition de spin car les spectres d'absorption sont très sensibles à l'état de spin. En effet, le moment angulaire des photons incidents se couple avec le moment magnétique des atomes du matériau sondé, et ainsi ceci mène à une différence d'absorption selon la polarisation du faisceau incident qui permet de clairement différencier l'état HS de l'état LS. Nous avons utilisé une implémentation personnelle dans le code VASP du calcul de ces spectres dans l'approximation dipolaire, sans effets excitoniques, afin d'obtenir le seuil $L_{2,3}$ de la molécule de FePhen dans les deux états de spin. Les résultats XAS et XMCD obtenus sont en accord qualitatif avec les résultats expérimentaux existants, cependant nos observons des problèmes au niveau des intensités relatives entre les différents pics du signal HS qui montrent l'importance des multiplets et des interactions électron-trou, que nous avons négligés dans cette approche. Cependant, il nous est possible de prendre en compte

ces dernières de manière statique, en créant un trou (ou un demi-trou de Slater) explicitement dans le cortège de coeur et en recalculant les bandes de valence. Mais nous avons montré que ceci entraîne de plus mauvais résultats vis-à-vis des données expérimentales, à cause de l'écrantage du trou par les électrons qui mène à une forte réduction du moment magnétique sur l'atome de fer et ainsi une modification erronée du signal théorique obtenu. En outre, nous avons démontré dans le cadre de notre formalisme la relation entre les spectres d'absorption et les densités d'état partielles des électrons de valence, ce qui nous a permis d'effectuer une analyse des structures sur les spectres d'absorption en termes des structures sur les densités d'états e_g et t_{2g} de l'atome de fer, montrant ainsi de quelles symétries proviennent les différentes contributions des spectres XAS.
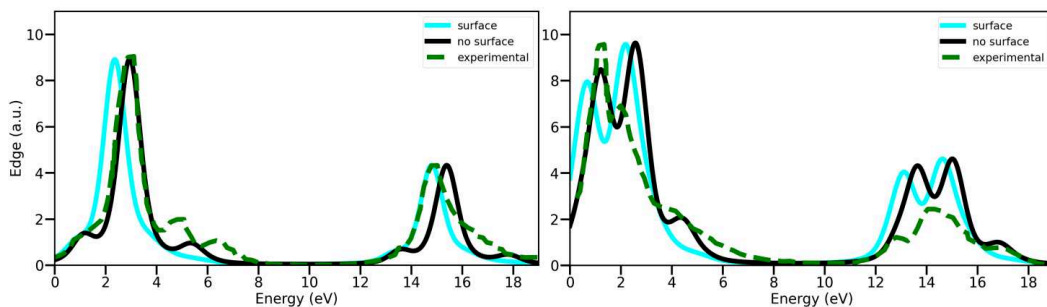

FIGURE 8 – Signaux XAS au seuil $L_{2,3}$ dans l'état LS (à gauche) et HS (à droite) calculés avec et sans surface, comparés aux résultats expérimentaux. [10]

Nous avons également montré que l'angle d'incidence du rayonnement polarisé influe sur le signal XMCD, et peut ainsi être corrélé à la déformation locale de l'octaèdre N_6 autour de l'atome de fer. Finalement, nous avons étudié l'impact de la direction de magnétisation sur le signal XMCD, qui est ainsi reliée à l'anisotropie du moment magnétique sur l'atome de fer. Nous avons estimé la température de blocage de l'aimantation, et montré que les règles de sommes de Thole *etal*. étaient respectées pour plusieurs directions de magnétisation, mais celles-ci nécessitent l'évaluation du moment dipolaire magnétique issue de la déformation de l'octaèdre central dans l'état HS. Toutes ces prédictions nécessitent néanmoins une vérification expérimentale.
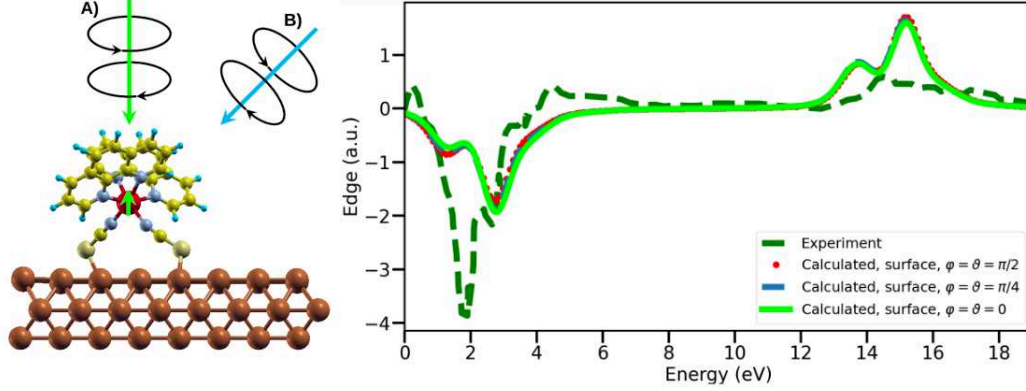
FIGURE 9 – Signaux XMCD au seuil $L_{2,3}$ dans l'état HS sur surface calculés avec différentes orientations d'incidence, comparés aux résultats expérimentaux (uniquement en incidence rasante) et illustration associée [10]

Direction de magnétisation	ΔE (meV)	T_z (μ_B)	m_ℓ (μ_B)		m_s (μ_B)	
			Direct	Intégrale	Direct	Intégrale
(001)	-1.9	-0.101	0.180	0.154	3.635	3.731
(111)	-0.98	-0.092	0.106	0.092	3.637	3.735
(010)	0	-0.092	0.006	0.006	3.635	3.734

TABLE II – Anisotropie magnéto-cristalline ΔE en meV, et calcul du moment magnétique dipolaire (T_z), du moment magnétique (m_s), et du moment angulaire (m_ℓ) en DFT comparés aux valeurs obtenues avec les règles de somme intégrales (en magnéton de Bohr μ_B) pour le site de fer dans la molécule de FePhen avec différentes directions de magnétisation [10]

Finalement, nous présenterons nos résultats concernant la simulation de la microscopie à effet tunnel, qui est un moyen rapide et assez commun pour discriminer entre les états de spin car les différences structurelles sont clairement visibles sur les images obtenues. Ainsi, nous avons calculé les images STM de la molécule de FePhen adsorbée sur une surface en utilisant trois méthodes : la méthode de Tersoff-Hamann, où la pointe est considérée comme un pur état s; la méthode de Chen, où la pointe est décomposée sur toutes les symétries s, p et d; et finalement l'approximation de Bardeen générale, où la pointe est

traitée exactement en *ab-initio*. Nous nous intéressons à deux composés pour la pointe :
une en Fer, soit un composé ferromagnétique, et l'autre en tungstène non-ferromagnétique ;
afin de pouvoir étudier l'influence du magnétisme des états de spin. Nous montrons ainsi
que la formule de Tersoff-Hamann (TH) présente des résultats en accord avec les résultats
expérimentaux et les résultats théoriques précédents [5, 11], reproduisant les lobes issus des
ligands et leur séparation observable sur l'image STM. Nous montrons en outre que les
images dans l'approximation de Chen présentent de grandes similarités avec l'image TH,
mais avec des différences dans la corrugation des lobes qui pourraient être observées avec
des images plus fines que celles obtenues expérimentalement, prises à large distance. Nous
montrons également que les images avec l'approximation de Chen sont en accord avec les
images de pointes idéales avec une symétrie d, en accord avec la structure électronique des
pointes étudiées. Finalement, nous montrons que les images avec la méthode de Bardeen sont
en grand accord avec les images TH, ce qui correspond également aux attentes théoriques
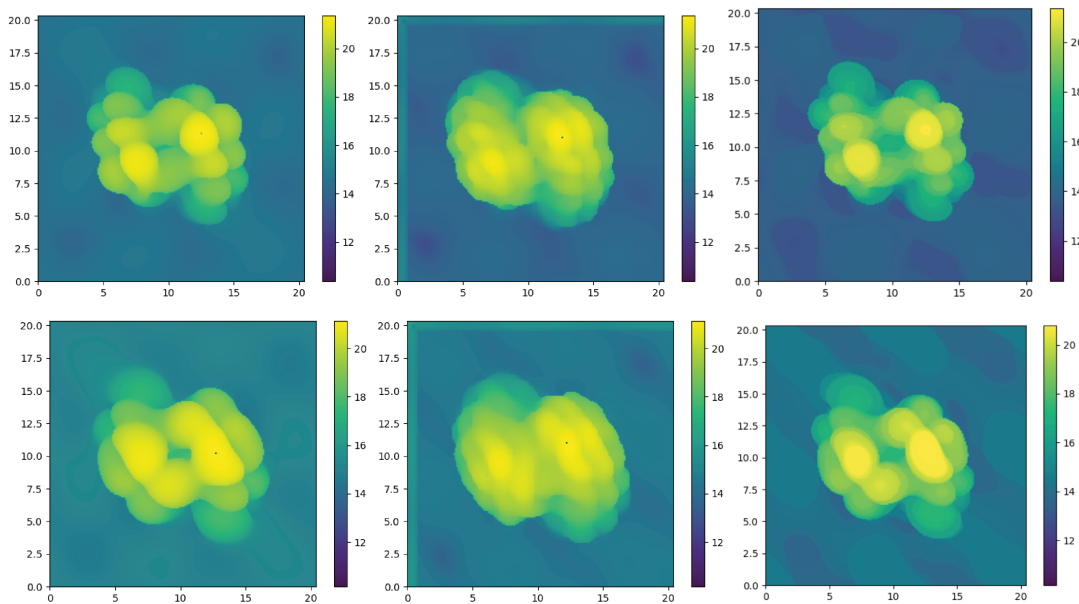car les deux méthodes doivent converger vers la même limite à grande distance.

FIGURE 10 – Images STM de la molécule dans l'état HS (en haut) et dans l'état LS (en
bas), dans l'approximation de Tersoff-Hamann (à gauche), dans celle de Chen (au centre) et
celle de Bardeen (à droite) avec une pointe de Fer.

Pour conclure, nous avons étudié l'influence du dopage sur ces systèmes à transition
de spin, et montré qu'il permet une inversion de l'état de spin, ce qui apparaît fortement

intéressant du point du vue expérimental afin de manipuler la stabilité relative entre les états LS et HS des complexes à transition de spin. Le calcul phononique corrobore la stabilisation de l'état HS vis-à-vis de l'état LS. Nos simulations de spectres XAS et XMCD, en accord relatif, mettent en évidence l'importance des déformations et anisotropies de ces systèmes qui jouent sur le signal résultant et sur leur interprétation, notamment au niveau des règles de sommes de Thole *et al.* avec l'importance du tenseur magnétique dipolaire. Finalement, nous avons étudié la simulation des images STM et montré que les méthodes de Tersoff-Hamann et Bardeen étaient en accord pour la grande séparation entre la pointe et la surface que nous avons utilisée, ce qui est le comportement attendu, tandis que les corrections de la formule de Chen sont relativement restreintes et limitées à de courtes distances.

[1] W. Hempel, *Struktureigenschaftsbeziehungenin Erdalkalisilikat basierenden Leuchtstoffen*, Ph.D. thesis, Universitat Augsburg (2007).

[2] W. A. Baker Jr. and H. M. Bobonich, Magnetic properties of some high-spin complexes of iron(ii), Inorganic Chemistry **3**, 1184 (1964).

[3] S. Gueddida and M. Alouani, Spin crossover in a single fe(phen)$_2$(ncs)$_2$ molecule adsorbed onto metallic substrates : An ab initio calculation, Phys. Rev. B **87**, 144413 (2013).

[4] S. Gueddida and M. Alouani, Calculated impact of ferromagnetic substrate on the spin crossover in a fe$(1, 10-\text{phenanthroline})_2(\text{NCS})_2$ molecule, Phys. Rev. B **93**, 184433 (2016).

[5] T. Miyamachi, M. Gruber, V. Davesne, M. Bowen, S. Boukari, L. Joly, F. Scheurer, G. Rogez, T. K. Yamada, P. Ohresser, E. Beaurepaire, and W. Wulfhekel, Robust spin crossover and memristance across a single molecule, Nature Communications **3**, 938 (2012).

[6] A. Y. Mohamed, M. Lee, K. Kitase, T. Kitazawa, J.-Y. Kim, and D.-Y. Cho, Soft x-ray absorption spectroscopy study of spin crossover fe-compounds : Persistent high spin configurations under soft x-ray irradiation, Crystals **8**, 10.3390/cryst8110433 (2018).

[7] R. Pasquier, K. Rassoul, and M. Alouani, Inverse spin crossover in fluorinated fe(1,10-phenanthroline)2(ncs)2 adsorbed on cu (001) surface, Computational Condensed Matter **32**, e00735 (2022).

[8] T. Bučko, J. Hafner, S. Lebègue, and J. G. Ángyán, Spin crossover transition of fe(phen)2(ncs)2 : periodic dispersion-corrected density-functional study, Phys. Chem. Chem.

Phys. **14**, 5389 (2012).

[9] C. P. Slichter and H. G. Drickamer, Pressure-Induced Electronic Changes in Compounds of Iron, The Journal of Chemical Physics **56**, 2142 (2003), https ://pubs.aip.org/aip/jcp/ARTICLE-pdf/56/5/2142/11048929/2142_1_online.pdf.

[10] R. Pasquier and M. Alouani, Calculated iron $l_{2,3}$ x-ray absorption and xmcd of spin-crossover fe(phen)$_2$(ncs)$_2$ molecule adsorbed on cu(001) surface (2023), arXiv :2309.02078 [cond-mat.mtrl-sci].

[11] S. Gueddida, *Theoretical study of the spin crossover in a single Fe(phen)2(NCS)2 molecule adsorbed onto metallic substrates*, Ph.D. thesis, University of Strasbourg (2014).

Acknowledgements

First and foremost, I would like to acknowledge Roberta Poloni, Sébastien Lebègue and Jean-François Dayen, for agreeing to sit on my jury and taking the time to carefully and thoroughfully reading my manuscript, which was evident from the deep and complex discussion on the day of the defense. Hence, I would like to thank Dr. Poloni and Dr. Lebègue for respectively coming from Grenoble and Nancy for this very purpose, as reviewers of my thesis. I would also like to thank Dr. Dayen as examiner of my thesis, but also for having been part alongside Dr. Lebègue of my thesis monitoring committee which has provided a very fruitful oversight during my PhD. Obviously, I would like to commend my supervisor, Mébarek Alouani, for his invaluable support and help throughout these PhD years, as navigating through the murky intricacies and mysteries of the 40 years old VASP code would have been an impassable journey without him.

On a broader scale, as this PhD was carried within the Département de Magnétisme des Objets Nanostructurés (DMONS) of the Institut de Physique et de Chimie des Matériaux de Strasbourg (IPCMS), and I would like to thank the head of the DMONS, Yves Henry, and the head of the IPCMS, Pierre Rabu, for allowing me to pursue my doctorate. My work being numerical physics, I also owe many thanks to the IT services of the IPCMS, but also of the CCUS, of the TGCC, of the CINES and of the IDRIS, for their essential technical support through my kajillion hours of CPU use. I would also like to thank the administrative services of the IPCMS for their quick answers and solutions to my issues, especially Christine Bonnin, head of the HR department of the IPCMS, and Véronique Wernher, secretary of the DMONS. Finally, I would like to thank the ITI QMat for their help through these years, during my Master degree and during my PhD. Having been a member since its very inception, they have provided me with inestimable assistance, especially from a financial aspect, to carry me through my studies. Hence, I would like to personally salute Aleena Gradt, Project manager of QMat, and Matthieu Bailleul, director of the executive committee of QMat, for their help. On a more personal level, I would like to thank all the people I've shared my office with, especially Khaled Rassoul as some of his early results proved essential to my work, and Hilaire Mba and Audrey Djeudi for all the interesting scientific work we carried together on topics beyond the realm of this thesis. More generally, I would also like to thank all the scientists I've met during all the colloquia, schools, workshops and meetings I've done during my PhD for the very valuable discussion.

Table des matières

Liste des figures

Liste des tableaux

Introduction

0.1 Some historical milestones

The topic of spin-transition or spin crossover (SCO) physics was initiated by the seminal work of Cambi and co-workers during the 30s, who studied, among other things, Fe(III) compounds of the form $Fe(R_2NCS_2)_3$, underlining the anomalous behaviour of their magnetic susceptibility with respect to the temperature ([1, 2, 3]) and showing for the first time a temperature driven transition between two spin states. These studies also emphasized the strong sensitivity of the spin state to the nature of the (R) ligands, and in some cases intermediate values of the magnetization were observed. Foundational work done at the same time by Pauling and co-workers on the properties of the ligand-metal bond ([4]) led them to the idea of incorrectly describing these results in terms of an intermediate spin state, although Pauling did in fact foresee the possibility of a equilibrium in a general bistable system based on the nature of the bonding ([5]).

After a period of relative dormancy dictated by the requirements of the Second World War, the subject of SCO had a rebirth starting from the end of the 50s, spearheaded by a number of novel breakthroughs, including the famous work of Orgel ([6, 7]), who used ligand field theory (LFT) to correctly describe the previous results as stemming from an equilibrium between two spin configurations: a low spin one and a high spin one. This, among other works, led to the recognition of LFT as a very valuable tool in understading the properties of SCO compounds, which coincided with a genuine explosion of the research activity on the spin transition topic from the beginning of the 60s. Remarkable examples include the study of the magnetic states of various Iron(II) and Cobalt(II) compounds by Busch *et al.*, which led to the discovery of cobalt(II) spin crossover systems ([8]). At roughly the same time, we can also note the discovery of the spin transition behaviour in Fe(II) SCO molecules following the extensive work of Baker and Bobonich in 1964 ([9]), then Madeja and König in 1967 ([10]), on systems of the form $[Fe(Phen)_2X_2]$, including the now widely studied $Fe(phenanthroline)_2(NCS)_2$ parent system on which we shall focus more thoroughly in another part. The first studies on the pressure effects were also carried during the same period, by various groups including for example Martin and Ewald [11], who tried to extend the work of Cambi on Fe(III) systems. These systems

have received a fair amount of attention, and the first use of Mössbauer spectroscopy to study the SCO phenomenon was indeed demonstrated on Iron(III) dithiocarbamites [12] during the same era before being used by Madeja and König in their seminal studies on Fe(II) compounds [10]. Another study of particular interest on these Fe(III) systems was the work of Hendrickson *et al.* during the 80s, showing that the characteristics of the spin-transition phenomenon in the powdered crystalline phases depends on the granularity of the crystallites, underlining the strong contribution of long-order interactions on the SCO in multimeric systems [13].

Therefore, the period starting from the 80s was mainly characterized by a massive increase in interest on multimeric and polynuclear SCO compounds as the result of Henrickson *et al.*, among others, emphasized the importance of studying covalent bondings between SCO molecules and supramolecular long-range interactions to understand the difference with the purely monomeric results that were obtained during the previous decades. Without going in excessive depth as it is not the subject of this thesis, we can note that important results include the first forays into dinuclear Fe(II) and Co(II) compounds by the groups of Kahn and Zarembowitch [14, 15], the study of trinuclear Fe(III) with Htrz bridges by Reedjik, Haasnoot *et al.* [16, 17] that showed that only the central ion undergoes the spin transition whereas the edge remains in the HS state with a weak exchange interaction, while Brooker *et al.* [18] showed a simultaneous crossover in a dinuclear Co(II) complex with a strong exchange. We can also note the discovery at roughly the same era of a tetranuclear 2x2 square Fe(II) compound with a variety of observed spin transitions by the groups of Lehn and Ruben [19].

To conclude, the topic of spin-crossover materials is a buzzing research field, most notably because of the numerous nanotechnological promises entailed by the mastery of the transition between the spin states that show clear commercial potentialities for e.g. novel memory, display or storage devices. For example, as emphasized by Létard *et al.* [20], systems with a significant amount of hysteresis exhibit a memory effect, where their behaviour depends on their past history, that could be leveraged to design memristive components, as demonstrated for example by Miyamachi *et al.* in 2012 [21]. Besides, the spin-crossover mechanism also plays an important role in certain natural processes, for example within haemoglobin where the structural changes between spin states allow for a very efficient transport of oxygen and therefore influenced the evolution of species [22, 23]. As such, the continuous strife for better theoretical results on the topic is a worthwhile enterprise.

0.2   The principles of spin-transition

In vacuum, the electrons of an atomic system are organised in degenerate levels that can be indexed by their angular quantum number l. To understand the SCO in transition metal compounds, we are interested in the d-subshell that has a fivefold degeneracy, containing the

so-called d_{xy}, d_{yz}, d_{zx} (along the diagonal directions) and the $d_{x^2-y^2}$ and d_{z^2} orbitals (along the axes). In the electronic field created by a ligand of octahedral geometry, this fivefold degeneracy of the d-orbitals is lifted as some of these orbitals are aligned with the axes (and therefore, the ligands) and others are out of the axes. This leads to the splitting of the d-subshell in two degenerate states of lower energy (t_{2g}, composed of 3 orbitals) and higher energy (e_g, 2 orbitals) separated by the energy splitting Δ. We therefore have different spin-states for the complex, depending on whether the spins remain paired (low spin state) or stand in the higher energy states (high spin state) for all transition metals with a configuration between d^4 and d^7. The choice between these two possibilities is naturally depending on the difference between the energy splitting Δ and the pairing energy P, with $\Delta << P$ favouring a high spin (HS) state and $\Delta >> P$ a low spin (LS) state. In the particular case where Δ and P become relatively close, an artificial transition between the two states induced by an external stimulus becomes possible: this is called a spin transition or a spin crossover. Naturally, this spin transition is correlated to length differences between the HS and LS state. Indeed, the strength of the Ligand Field, and therefore the energy splitting, obviously depends on the distance between the coordination centre and the chelating ligands, with a HS state being correlated to longer distances in order to reduce Δ whereas the LS state is correlated to shorter distances to increase this splitting. Note that this crossover phenomenon almost only exists within the complexes of first-row, 3d transition metals [24] but note that there are extremely rare examples of 4d SCO complexes [25]. However, to the extent of the author's knowledge, no 5d thermal spin crossover complexes have been observed.

The thermodynamical properties of the spin crossover phenomenon were studied by Sorai *et al.*, who showed that the SCO is a entropy-driven process [26, 27], and as such relies on both electronic and vibrational contributions to the energetic balance, especially in the solid state which is linked to the so-called cooperativity of the system [28] that describes how local changes in the individual molecules are correlated to global changes at the solid scale. As a consequence, the HS state is the most stable state at higher temperatures, but note however that the LS to HS transition during heating can be highly non trivial.

A very convenient and useful way to monitor a spin-transition within a solid sample is to measure and plot the HS fraction γ_{HS}, or equivalently the magnetization, in the sample with respect to the temperature. One can then distinguish several types of spin transition based on the general shape of the plot within broadly five categories [24]:

— The first case corresponds to systems with low cooperativity, so that the solid basically acts as a set of independent SCO molecules in a lattice. Therefore, the fraction γ_{HS} naturally follows a Boltzmann distribution with respect to the temperature. This is typical of a spin-crossover behaviour in solution, where the cooperativity is non-existent [29].

— The second case corresponds to systems with stronger cooperativity, so that a single molecule switching triggers a cascade transition across the solid which is therefore des-

cribed by a noticeable increase of the HS fraction at the so-called transition temperature, which can be anywhere from somewhat gradual to extremely abrupt [30] depending on the cooperativity of the system.

— The third case corresponds to systems with a particularly strong cooperativity, so that the spin transition leads to noticeable structural changes within the solid. This causes an hysteresis to appear on the plot [31], linked to the stabilization of the spin states by the necessity of the system to undergo a crystallographic phase transition during the switch from a spin state to the other .

— The fourth case corresponds to systems with a multistep transition, and is quite uncommon. It is often linked to physical peculiarities within the system such as multinuclear complexes or multiple possible lattice sites for the SCO molecules leading to different transitions between the inequivalent sites, and cases with 8 steps in the transition have been reported in very complex systems [32].

— The final case corresponds to system with an incomplete HS to LS transition at low temperatures, and it is often related to some kind of lattice related hindrance effects where the geometry of the system constrains the spin state at some lattice points. In some cases, the population may also be kinetically trapped in the HS state as the structural transition can be a slow process [33]. Note that the trapping of an LS population at high temperature can also happen in some SCO compounds but it is rarer as the thermal and vibrationnal effects should in principle act against any kinetic or structural barrier.

Note that in rare cases, the structural phase changes linked to the spin-crossover might lead to an anomalous entropically disfavorable reverse spin-crossover phenomenon with a partial HS to LS conversion with heating on a small temperature range, although it is always the HS state that will be favoured at the higher temperatures as the vibrationnal degrees of freedom get populated [34]. This importance of the lattice contribution on the transition has actually initiated a drive to study these complexes in solution, especially within the context of ligand engineering, so as to remove all solid-state effects on the SCO [29].

The entropic nature of the SCO also implies that the spin-transition phenomenon can be driven by a variety of external perturbations beyond temperature. First of all, a very important discovery was the influence of an external radiation on the spin-crossover phenomenon. The so-called LIESST (Light Induced Excited Spin State Trapping) effect is based on the idea of irradiating a LS solid-state sample at low temperature, which triggers a conversion to a metastable HS state that decays back to the LS state with heating above a temperature known as the LIESST critical temperature or T(LIESST) [35]. As such, the system remains trapped in the HS state if the temperature is low enough, with extreme lifetimes in some cases (up to several days) [28]. A particularly interesting aspect of this is that it is also possible to reversely turn the excited state back to the ground state by irradiating the sample with a longer wavelength, an effect known as the reverse-LIESST [36, 37] with very obvious applications for memory and

storage devices. The use of these external radiations along with temperature manipulation can also have an influence on the hysteretical structure of the spin transition phenomenon, with the discovery of the LITH (Light Induced Thermal Hysteresis) [38] where a LIESST sample under constant irradiation shows an hysteretical cycle under a simultaneous thermal loop. We can also note the "mirror" effect, with the LIOH (Light Induced Optical Hysteresis) [39] where the temperature is kept constant but the irradiation is cycled. A related effect is the LiPTH (Light Perturbed Thermal Hysteresis) [40] where a SCO sample undergoing a thermal hysteresis shows a shift of the transition cycle under an external irradiation, with its "mirror" effect LiPOH (Light Perturbed Optical Hysteresis) [40]. Finally, the use of photo-sensitive ligands can lead to a spin crossover linked to the geometrical changes of the ligands under irradiation, which is the so-called LD-LISC phenomenon (Ligand Driven Light Induced Spin Crossover) which was mostly observed within solution [41]. Interestingly, a very similar effect to the LIESST can be triggered by using soft x-rays leading to the SOXIESST effect (Soft X-ray Induced Excited Spin State Trapping) [42] or hard x-rays with HAXIESST [43] and nuclear decay leading to the NIESST effect (Nuclear decay Induced Excited Spin State Trapping) [28].

The influence of pressure has already been mentioned earlier. As the pressure reduces the bond length between the coordination centre and the ligands, it usually stabilizes the LS state. Equivalently, the enthalpy of a system depends on the pressure p with a term pV, so that the HS state should be energetically disfavorable as it is the system with the higher volume V [44]. Most notably, this can trigger a transition in a normally stable HS system: examples of paramount importance are Ferropericlase $(Mg, Fe)O$ [45] and Perovskite $(Mg, Fe)SiO_3$ [46], two HS minerals which undergo a transition to an LS state under the massive pressure conditions of the Earth mantle with important changes on various physical properties such as the density, elasticity or viscosity, leading to noticeable consequences on the associated geophysical processes. The opposite effect of stabilizing the HS state has also been observed in some cases, as pressure can trigger structural phase changes that may favor a high spin state [47].

Naturally, the application of a magnetic field should also have an impact on the spin transition, and indeed it stabilizes the HS state with a shift in the transition temperature that can be computed and verified experimentally [48, 49]. Using the susceptibility χ of the spin states, one can show using the magnetic moment $\mu_m = \chi B$ that the enthalpy is shifted by a value $\Delta E_m = -1/2\chi B^2$ because of the Zeeman effect. The HS state is paramagnetic, so that $\chi_{HS} > 0$ whereas the LS state is either diamagnetic or very weakly paramagnetic with $|\chi_{LS}| << \chi_{HS}$ so that its contribution can be neglected. Therefore, a magnetic field should favor the HS state and disfavor the LS state. The case of an electric field was also studied and it was shown that it is possible to selectively stabilize either the HS or LS state depending on the polarity of the electric current [50, 21].

Finally, chemical manipulation is rarer but also exists, being mostly observed in solution.

Hence, it is possible to induce a spin state switching by solvating a SCO compound [51], by modifying the ligands with an extremely famous example being the aforementioned case of hemoglobin which undergoes a spin state change under the coordination of oxygen [4]), or in very rare cases by a coordination change on the metal center itself [52].

0.3 Fe(II) systems

Fe(II) systems are d^6 complexes, which therefore have a $(^6t_{2g}\,^0e_g)$ population in the LS state of spin S=0 and a $(^4t_{2g}\,^2e_g)$ population in the HS state of spin S=2. As we have said earlier, the SCO in Fe(II) compounds was first observed in the case of the $Fe(phenanthroline)_2(NCS)_2$ (usually abbreviated as FePhen) molecule by Baker and Bobonich in 1964 ([9]), who studied the magnetic susceptibilties of several high-spin Fe(II) complexes of the general form $[Fe(Phen)_2X_2]$. They showed that, for the isothiocyanate ligand (NCS), the magnetic moment is sharply decreasing with the temperature. This was later explained in 1967 by König and Madeja ([10]), who demonstrated the transition between low spin and high spin states thanks to thermal excitation. They measured the magnetic susceptibility, showing a decrease of the magnetic moment with a critical temperature around $T_c \approx$ 175 K. Using Mössbauer spectroscopy, they showed that the compound was in a $^5T_2$ high-spin state at high temperature and a $^1A_1$ low-spin state at lower temperatures, and therefore undergoes a thermal induced spin transition between these two states. These extensive studies led to a strong focus on Fe(II) compounds during the early years of the field, being used as prototypical systems to assess the influence of a wide variety of parameters on the SCO phenomenon [24]. The FePhen molecule is the prototypical example of the $[Fe(diimine)_2(X)_2]$ class of complexes, and more generally of the $Fe(II)N_6$ family which encompasses the majority of the most studied SCO compounds because of the spectacular resilience of the spin crossover phenomenon to extensive modifications of the molecule, leading to a pretty thorough knowledge of the general effects of ligands on the relative energetics of the spin states. For example, an entire field of research was built around general substitution and replacement of the ligands, showing a wide range of effects depending on the nature of the transformation done on the molecule, with a very common idea being the replacement of the isothiocyanate ligands by selenocyanate ligands $[NCSe^-]$. These are characterized by a stronger field as compared to the pristine isothiocyanate which leads to a stabilization of the LS state, with the selenated FePhen molecule showing a spin transition temperature of $T_c \approx$ 235 K. [53].

There is a massive ongoing effort to study SCO compounds on metallic surfaces. Indeed, harnessing the bistability of the spin crossover molecules requires a functionalization based on their adsorption on surfaces in order to create building blocks for novel spintronics devices, and the knowledge of the characteristics of the interaction between a given SCO molecule and a given surface, both from a theoretical and experimental point of vue, appears as a

natural requirement to achieve this task. This is a very young field, owing to the difficulties encountered during the deposition of SCO compounds on surfaces as most of them aren't sublimable without decomposition which therefore prevents the use of vacuum evaporation. Hence, other methods such as wet-coating approaches are required, which have several disadvantages such as less control over the coating thickness or more impurities [54]. The first results of SCO molecules on surfaces were hence obtained in 1988 by Barraud *et al.* [55, 56] using Langmuir-Blodgett films of FePhen aliphatic derivatives on CaF_2 slides that exhibited spin crossover but with marked impurities related effects as expected. More recently, Alam *et al.* have grafted SCO molecules on a highly ordered pyrolytic graphite (HOPG) [57]. They showed that the resulting STM images show a noticeable contrast between the HS and LS states, with a significant difference of conductance heralding their functionalizability as memory storage components. This anticipated results obtained with vacuum evaporated systems that were developed at roughly the same time, most notably FePhen [58, 21].

As such, the field has known rapid progress during the 2010s, with several successive successes in the sublimation of increasingly complex and varied spin crossover systems ([59, 60, 61]. For more details about the surface growing of SCO systems, see [62] linked to a string of discoveries such as the promotion of SCO behaviour thanks to the surface polarization [63], in relation to the development of an intense field of work organised around the idea of manipulating the cooperativity of SCO molecules on surfaces by either tuning the ligand [64] or the substrate [65], with varying success. Naturally, the coupling of SCO molecules with magnetically active surfaces, especially ferromagnetical surfaces, has been extensively studied. A strong coupling between the ferromagnets and the SCO molecules has been demonstrated [66], leading to the possibility of manipulating the resulting spinterface states by an external stimuli with obvious functional promises [67] for novel spintronics applications, although this also entails the possibility of permanently locking the spin state because of the very same interactions [54] so that a fair amount of fine tuning is required. As such, given the importance of this field, it is of no surprise that several reviews on the topic have already been released, to which we forward the reader for more information. As such, for a general outlook on the topic, see [54]. For the characterization of SCO compounds on surfaces, that we did not tackle yet but which will be one of the main topics of this thesis, see [68].

0.4   The FePhen molecule

The FePhen molecule being one of the, if not the most studied system in the entire field, we will dedicate the following section to the description of its properties.

0.4.1 Structural properties

The FePhen molecule is an octahedral SCO complex, with a central Iron coordination centre encapsulated within an octahedral cage of nitrogen atoms, from two 1,10-phenanthroline ($C_{12}H_8N_2$) and two isothiocyanate (NCS) ligands. Its structure under various conditions has been extensively studied, with solid state structural parameters having been determined at room pressure at 298 K, so in a mostly HS state, and 130 K in a mostly LS state [69]. The difference of chemical properties between these two ligands leads to a fairly deformed octahedral geometry, with the $Fe - NCS$ bonds being shorter than the $Fe - Phen$ bonds, with an average length of 1.95 Å for the former and 2.05 Å in the LS state. It crystallizes in a Pbcn space group in both spin states, and this structure remains stable even at high pressure with some small changes in the lattice parameter [70, 71]. Hence, most of the changes associated with the spin transition phenomenon are located at the molecular level. The most striking difference are the elongations within the octahedral cage, with an increase of 0.2 Å for the $Fe - Phen$ bonds and 0.1 Å for the $Fe - NCS$ bonds during the LS to HS thermal transition, the difference being related to the fact that the Phen groups are better π-acceptors than NCS, and thus this leads to a stronger π-backbonding effect on the former than the latter [72]. An increase in the bonding angles can also be observed, from $91.6°$ in the LS state to $92.9°$ in the HS state.

0.4.2 Transition properties

The Fephen molecule undergoes a steep transition at a critical temperature of $T_c =175$ K, with a very small hysteresis of 1 K. As we have emphasized earliert, it is one of the most extensively studied transition in literature, being still used as a benchmark for any new experimental or theoretical development in the field.
Obviously, there is a massive literature about the thermal transition that was studied in all possible phases, including the single molecule [21], in powder [58], in thin film [69] or in the solid state [69]. The results show that the molecule undergoes a complete transition in the powder state, jumping from a magnetization of 0.5 μ_B at 130 K to 5.2 μ_B at 298 K with a steep transition. In the solid state, the high temperature limit at 298 K is the same with a magnetization of 5.2 μ_B, but the transition is much more gradual at 175 K with a noticeable amount of molecules trapped in the HS state at 130 K where a remanent magnetization of 2.2 μ_B was measured. This can be linked to several phenomena, from defects in the solid-state to geometrical interactions quenching the transition as we have emphasized earlier. The transition in thin films is similar to the solid-state one, although with less quenching at low temperature with a remanent magnetization around 1 μ_B at 100 K.

The effects of pressure were also well analysed, hailing from Drickamer *et al.* pioneering

studies on the matter [73], who showed that it stabilizes the LS state as expected. This was extended by Ksenofontov *et al.* [74], who studied the evolution of the transition between 10^5 Pa and 1.3 GPa. They showed that pressure suppresses the hysteresis and leads to a more gradual transition, with an increase of the critical temperature that is naturally equivalent to a stabilization of the LS state. However, one can show that the susceptibility of this transition temperature to the pressure, $\partial T_c / \partial P = \Delta V / \Delta S$ decreases as the pressure increases [74]. This, along with the proportion of trapped HS states remaining constant at low temperatures, strongly suggests the existence of some steric effects at play preventing a total conversion of the HS population into the LS state. Note that the softening of the transition indicates a loss of cooperativity as the pressure increases, that is naturally correlated to the loss of HS population. Boussekssou *et al.* also studied the effect of pressure pulses on the transition [75], and showed that the pressure pulse leads to a reversible decrease of the HS fraction in the ascending branch of the hysteresis and an irreversible decrease of the HS fraction in the descending branch, as one could have expected. Interestingly, this is the exact opposite of magnetic pulses, as we will see in the next paragraph.

Indeed, the effect of a magnetic field has also been studied, starting from the work of Gütlich *at al.* [48]. They have measured the transition properties under a field of 1 T and 5.5 T, and showed that the transition temperature decreases as the strength of the magnetic field increases, with excellent qualitative accordance with the theoretical result. This was extended by Boussekssou *et al.* [49], who studied the influence of a pulsed magnetic field and showed that it induces a reversible increase of the HS fraction in the descending branch and an irreversible increase of the HS fraction in the ascending branch, which is the exact opposite of the pressure pulse effect. Indeed, the enthalpy contains a pV term for the pressure, while the magnetic contribution is $-1/2\chi B^2$ so it is clear that these two perturbations should have an opposite effect [75, 49]. An interesting fact is that one can clearly observe a longer response time to the magnetic pulse in the ascending branch (90 ms) as compared to the descending branch (50 ms), which was to be expected as relaxing from the ascending branch requires going to the descending branch (hence the irreversibility) whereas relaxing from the descending branch does not involve a branch switch, and vice-versa for the pressure pulse.

Similarly, the effects of irradiation within FePhen have been extensively documented. The LIESST phenomenon within FePhen was discovered by Decurtins *et al.* [35, 76, 77], who measured a T(LIESST) of 55 K. In the same work, the transition path during the LIESST is also intuited: the irradiation leads to a pumping from the $^1A_1$ low spin state to a set of several ^1T and ^1MLCT (Metal-to-Ligand Charge Transfer) excited states. These are highly unstable states, which should rapidly undergo a relaxation to the $^1A_1$ state. However, the existence of spin-orbit can lead to an alternative spin-forbidden decay path through ^3T states and then ultimately to the $^5T_2$ state which has no relaxation channel to the $^1A_1$, hence the stability of the LIESST HS state. This was further analysed by Heber and Casson [78], Lee *et al.* [79] and later

by Kato *et al.* [80], who used a variety of techniques to conclusively show the optical pumping of the LS ground states in the excited states without any light-induced thermal transfer effects. The SOXIESST effect was discovered within FePhen by Collison *et al.* [81], and then was studied by Davesne *et al.* [82] who used it to flesh out the details on this at that time still pretty unexplored effect. They showed that the phenomenon had broad similarities with the LIESST effect both on the excitation path and the dynamics of the process, along with demonstrating the combined use of the LIESST and SOXIESST effects for a precise controlability of the excitation. HAXIESST was dicovered in this system by Vankó *et al.* [83], who also emphasized the similarities with the LIESST phenomenon, where the metastable HS state and the reverse HS to LS relaxation dynamics are the same than for LIESST. However, the energy of the hard x-rays is way too high to excite the MLCT states, and as such the excitation process follows another path through secondary electrons leading to different excitation dynamics.

0.5 Theoretical approaches to spin-transition systems

The genuine popularity and potential of spin crossover molecules has naturally led to a strong drive for accurate theoretical methods to understand and predict the properties of SCO molecules. First, we have the purely theoretical models which started as soon as Cambi's original results with the work of Pauling *et al.* [5, 4], that anticipated the idea of an equilibrium between spin states to describe these results. Besides, in more recent years, there has been a considerable use of *ab-initio* methods such as DFT or HF methods to study the spin-transition from first principles, which revealed the fact that properly reproducing the energetics of the spin states is a challenging task [84].

0.5.1 Theoretical models

Various theoretical models have been developed over the years to explain the spin-crossover phenomenon following the early work of Pauling. As we have emphasized earlier, any such model has to take into account the fact that the transition is entropy-driven, and therefore it should include the vibrationnal contribution to the free energy balance between the spin states, along with the cooperativity of the system to properly describe non-Boltzmann and hysteretic transitions. The most famous and widely used example is the Slichter and Drickamer model [85], which gives a pretty good insight about the SCO in the solid-state and we will therefore give more details about it. In the very commonly used form, it gives the HS fraction γ_{HS} with respect to temperature:

$$\ln \left[(1 - \gamma_{HS}) / \gamma_{HS} \right] = (\Delta H_{HS \leftrightarrow LS} + \Gamma (1 - 2\gamma_{HS})) / RT - \Delta S_{HS \leftrightarrow LS} / R \ , \tag{1}$$

where $\Delta H_{HS\leftrightarrow LS}$ is the transition enthalpy, $\Delta S_{HS\leftrightarrow LS}$ is the transition entropy, and by virtue of the definition of the free energy we have that the critical temperature is given by $T_c = \Delta H_{HS\leftrightarrow LS}/\Delta S_{HS\leftrightarrow LS}$. Γ is the interaction parameter between the HS states and LS states, which is closely related to the so-called degree of cooperativity $C = \Gamma/2RT_c$, and it can be considered positive for our intents (the case of a negative Γ is also considered in the original paper). R is the ideal gas constant and T is the temperature. The close links with Guggenheim's approach for regular solutions [86] and to the Bragg-Williams model for the thermal effects on atoms in alloys [87] have been extensively discussed [85, 88, 89].

The parameters that we have introduced have a temperature and pressure dependence. The pressure being an external parameter usually kept constant during $\gamma_{HS}(T)$ measurements, its related effects can be taken into account by carrying calculations or experiments at different pressure values. This is a requirement for a proper understanding of exotic pressure effects in certain systems such as hematin [85]. The temperature dependence of the entropy and enthalpy differences is commonly neglected as one is often mostly interested in a short region around the transition over which these parameters can be considered to be constant. The case of the cooperativity parameter Γ is much more complex, as it was introduced phenomenogically in the original paper. Therefore, its variations with respect to the temperature and the pressure are not well known (see [90]), and as such it is often kept constant.

As noted by the original authors, this is a transcendental equation and one can solve it graphically as detailed in the paper, but as a short summary we have:

— One can clearly see that when $\Gamma = 0$, the equation always admits one single solution only which translates to a single possible branch for the fraction. This is the first type of SCO molecule in the classification we presented earlier in this thesis, with a more-or-less Boltzmann shape without any hysteresis.

— When Γ does not vanish, there can be several solutions for the fraction depending on the temperature. As shown in the original paper, a closer look at the free energy shows that not all these solutions have the same stability and as such this can be used to explain the discontinuous behaviour and the hysteresis observed for the second and third cases of the classification, as the system will jump from one minima to the other as the temperature varies around the critical point. One can derive a critical value of the cooperativity $\Gamma_c = 2RT_c$ above which the system will exhibit an hysteretical behaviour.

As such, this model can be used to explain the influence of cooperativity on the shape of the transition that we mentioned, and is often used as a fit on experimental HS fraction/magnetization curves to extract enthalpy/entropy and cooperativity values near the transition temperature. This model, which stems from an inherently mean-field treatment of the free energy (see [89]), has been greatly extended beyond this approximation in recent times. The domain structure, which has been thus far neglected by virtue of this mean field nature, was first studied by Sorai *et al.* [27], before receiving a more thorough treatment

by Purcell and Edwards [91] who have extended the cooperativity by taking into account supplementary interactions between the HS states themselves and the LS state themselves. Other models of interest include the so-called elastic model of Spiering *et al.* [92], where the SCO molecules in a metal diluted system are described as impurities within an idealised anharmonic and elastic crystal leading to pretty good qualitative results even for most of the anomalous transitions. We can also note Kambara's approach [93], who coupled the ligand field theory of the individual molecule to symmetric deformations of the crystal, leading to a good description of pressure effects and cooperative interactions on the spin transition [94]. There has been a drive to understand the domain structure of hysteretic systems using the relay hysteron theory of Preisach [95] and the closely related Everett theorems [96], with however pretty mixed results depending on the complex studied. The use of effective Ising-like lattice models along with Monte Carlo simulation methods yielded pretty accurate results for the simulation of metal dilution, effects of pressure or metadynamical studies of the transiton path [97, 98, 99, 100, 101].

0.5.2   *Ab-initio* approaches

As we have emphasized, simulating spin crossover molecules with DFT methods is a complex task. While accurate geometries are nowadays accessible with most DFT methods, the relative energetics of the HS and LS states are notoriously hard to reproduce as these states are by definition separated by a small energy difference [102].

Swart *et al.* [103] have examined the performance of different DFT functionals for predicting the relative spin state (low, intermediate, or high) energies of seven iron complexes for which experimentally determined ground states are known. They found that the employed exchange and correlation functionals can be divided into two groups, one that particularly disfavors high spin states, i.e., standard functionals such as LDA, BLYP, and PBE, and the other where this is much less the case as for hybrid and improved GGAs and most of the meta-GGAs. They found that the energy difference between these two groups can be as much as 20 kcal/mol, showing that the choice of the DFT functional to compute the spin state of Fe(II) and Fe(III) complexes should be examined carefully [104]. The same conclusions were reached by Ganzenmüller *et al.* [105].

The work of Pierloot *et al.* [106] goes in the same direction, as they showed that BP86 and other GGAs tend to over stabilize the LS states with respect to the HS states, whereas the adiabatic difference with the hybrid functionals is heavily influenced by the extent of admixture of exact exchange, i.e., each TM complex is described by different exact-exchange parameters. As for the CASPT2 calculations, one can observe a slight overstabilization of the HS state in some cases, although it is possible to obtain accurate results using extensive basis sets based on an adequate CASSCF reference wave function making it computationally prohibitive, even

using high performance computers. In more relatively recent work, they show that the origin of the over stabilization of the HS with respect to the LS states by CASPT2 can be attributed to an inappropriate description of the (3s-3p) correlation [107].

Sanvito and coworkers [108] have also found that DFT functionals are unable to produce an accurate HS-LS energy difference for several ions complexes and attribute this failure to the DFT reduced exchange, as 50% of Hartree-Fock (HF) exchange in hybrid functionals produced accurate energy differences in their case. However, this conclusion was contradicted by Kulik and coworkers [109] who showed that the partial charge decreases on iron with a delocalization to the ligands as the HF exchange is increased. They therefore concluded the HS-LS energy difference in TM complexes can not be accurately obtained with a single percentage of HF exchange.

Cirera and Paesani [110, 111] studied ligand driven light-induced spin changes (LD-LISC) in many cis/trans isomers of iron complexes, showing that in their case only calculations based on the TPSSh functional provide accurate SCO temperatures.

Wilbraham *et al.* [112] studied the spin-state orderings in nine Fe(II) and Fe(III) complexes with ligands of varying strength using multiconfiguration pair-density functional theory (MC-PDFT), which is much less computationally expensive than the complete active space second order perturbation theory (CASPT2). However, while this method reproduced qualitatively the results of CASPT2, it was found to strongly depend on the active space size.

On the other hand, Vela and coworkers [113] have used PBE functionals including the Hubbard U and D3 van der Waals correction to benchmark nine Fe(II) and Fe(III) complexes against reference experimental values and showed that the values of U are different for each reported iron complex. However, all values of U were small in comparison to the self-consistent values obtained by Poloni *et al.* [114]. This is also compatible with the early work of Lebègue and coworkers[115], who used low values of U to produce the HS-LS energy difference of the $\mathrm{Fe(phen)}$ and $\mathrm{Fe(btr)}$ compounds.

To conclude, a huge variety of exchange and correlation schemes have been used to study the HS-LS energy differences, and they show the difficulty of a given method in getting systematically accurate results over a wide range of SCO compounds. Only methods that have been benchmarked to reference experimental data, by adjusting for example either the HF exchange mixture [106, 108, 109] or the Hubbard U parameter [113, 115, 116, 117], have consistently produced accurate HS-LS energies, with an obvious transferability issue.

0.5.3   Theoretical Results on FePhen

As we said earlier, Lebegue *et al.* have pioneered the studies of the FePhen molecule within a periodic DFT code using VASP with a LDA+U approach [115]. They have studied the energetics of the various experimental HS and LS geometries at low and high temperature by varying the value of the Hubbard parameter U, showing that a value of U = 2.5 eV and J = 0.95 eV leads to a very good agreement with experimental results in their case, with the DOS splitting and population concurring with the theoretical expectation. However, they emphasized the lack of predictability of the LDA+U method as they also showed that one could selectively stabilize one state or the other by varying the value of U. In a second paper, they carried another calculation both in the molecular and the solid state, using LDA+U along with DFT-D2 Van der Waals corrections which play a significant role in the crystalline phase. Using a phonon calculation within the harmonic approximation, they carried a precise study of the transition enthalpy and entropy within both phases, underlining the great influence of cooperative effects on the SCO in the solid state with a computed transition barrier in accordance with experimental results [118].

This study was greatly extended by Gueddida *et al.*, who also used GGA+U+DFT-D2 within VASP to carry an extensive study of the FePhen molecule on paramagnetic or ferromagnetic metallic surfaces [116]. They demonstrated the very strong adsorption of the molecule on the substrate, stabilizing both the HS state and the LS state on the surface as observed experimentally with a strong barrier through a metastable $S = 1$ unlike the free molecule with a sudden $S = 2$ to $S = 1$ switch. They also showed that passivating the surface with a nitrogen layer greatly weakens the bonding between the molecule and the surface, allowing for an easier transition between the spin states as observed experimentally. Interestingly, the use of a Cobalt surface has the same effect, but also induces a spin polarization of the LS state and a RKKY type ferromagnetic coupling between the surface and the iron centre through the NCS groups [117]. Interestingly, DOS and Bader calculations seem to show that beyond this particular polarization effect for ferromagnetic surfaces, the amount of charge transfer and influence of the surface on the ligand field is quite reduced, which underlines the fact that the DFT calculations alone are not sufficient to explain the experimentally observed Kondo effect as the results do not show a peak at the Fermi energy in the DOS. STM calculations have also been carried in the Tersoff-Hamann approximation, with decent agreement with experimental results [119]. In more recent times, Zhang [120] has shown, using the LDA+U method with a DZP basis set, that the use of non-metallic substrates has a non-trivial effect, and can either stabilize the HS state or the LS state depending on the chemical environment and the defects in the surface, with the example of a graphene surface switching the Fe(Phen) molecule to a HS state. As they indicate, this is linked to electronic structure changes and charges transfer during the adsorption process along with strong changes in the molecular phonon spectrum. The case of metallic surfaces was studied more in depth by Sanchez-de-Armas *et al.* [121], who

computed the energetics of FePhen adsorbed on Au(111), Cu(111) and Ag(111) surfaces within VASP. They showed a pretty good correlation between the strength of the interaction between the molecule and the surface (as obtained from quantities such as the adsorption energy or the molecule-surface distance), and the energetical stabilization of the LS state with respect to the HS state with copper having the strongest bonding and gold the weakest, corroborating earlier results by Gueddida [119].

Chapitre 1

Theory

1.1   Introduction

For a given atomic system of N particles $\Psi(X_1, ..., X_N)$, with the X_i being a general coordinate of the position r_i and the spin σ_i, the wavefunction follows the Schrödinger equation:

$$H\Psi = E\Psi, \tag{1.1}$$

wher H is the Hamiltonian of the system.

To study the physical properties of the system, it is therefore necessary to solve this equation. However, this problem has only been analytically solved for N=2 ; hence, since condensed matter systems are usually constituted of a much larger amount of particles (up to the Avogadro number $N \approx 10^{23}$), an analytical solution of the problem is not possible for most systems of interest. Besides, directly tackling this issue computationally is not reasonable for larger systems with a huge number of degrees of freedom. Then, we need sensible approximations in order to be able to solve the equation numerically.

A major first approach is the Born-Oppenheimer approximation [122], which consists in splitting the nuclear and electronic degrees of freedom (DOF). It is then possible to purely compute the electronic DOF while considering the nuclear DOF as frozen, then update the nuclear DOF using for example the Hellmann-Feynman theorem [123].
Nonetheless, this approximation alone is usually not sufficient to make this problem computationally tractable and we still need more efficient methods, as the electronic equation still is a prohibitive computation for larger systems.

Such a method can be found thanks to the powerful tool of density functional theory (DFT). Originating from work done by Hohenberg and Kohn [124] as an extension to

Thomas-Fermi theory [125], it consists in an elegant and exact rewriting of the Schrödinger equation in terms of the electronic density of the system. This leads to recasting the issue into a variational problem of this density, which is much simpler numerically to solve, although some approximations still need to be done.

1.2 The Hohenberg-Kohn theorems

The density functional theory is based on the two theorems of Hohenberg and Kohn [124]. For the previous quantum system $\Psi(X_1, ..., X_n)$, we have the following:

First Hohenberg-Kohn theorem: The energy of the system can be written exactly as a functional of the electronic density in the following way:

$$E[n] = T[n] + E_{ext}[n] + E_H[n] + E_{xc}[n],$$

(1.2)

where:

— T is the kinetic energy functional.

— E_{ext} is the scalar external potential functional applied on the electronic system, coming from the frozen nuclei potential (and from eventual other external sources), which can be recasted as:

$$E_{ext} = \int V_{ext}(\mathbf{r})n(\mathbf{r})\mathrm{d}\mathbf{r}.$$

(1.3)

— E_H is the Hartree functional, which can be written in the form:

$$E_H = \frac{1}{2} \int \int \frac{n(\mathbf{r})n(\mathbf{r}')}{|\mathbf{r} - \mathbf{r}'|}\mathrm{d}\mathbf{r}\mathrm{d}\mathbf{r}'.$$

(1.4)

— E_{xc} is the exchange correlation functional, coming from the geometric exchange potential and the electronic correlation.

Second Hohenberg-Kohn theorem: The exact ground state density n_0 of the system is the one that minimizes this functional:

$$\left.\frac{\delta E[n(\mathbf{r})]}{\delta n(\mathbf{r})}\right|_{n \to n_0} = 0.$$

(1.5)

While the problem has now been recasted in an apparently much simpler form, there is still a major issue : we have no analytical form for the kinetic energy functional and the exchange-correlation functional. There are several approaches to solve the problem of the kinetic energy, the most popular - and the one we use - is the Kohn-Sham ansatz.

1.3   The Kohn-Sham Ansatz

The Kohn-Sham ansatz posits the existence of a fictious non-interacting electron system that yields the exact same density as the real interacting system [126]. More precisely, we can split the previous kinetic energy functional as:

$$T[n] = T_s[n] + T_{int}[n] = -\sum_i \int \Phi_i^*(\mathbf{r}) \frac{\Delta}{2} \Phi_i(\mathbf{r}) \mathrm{d}^3\mathrm{r} + T_{int}[n], \tag{1.6}$$

where the Φ are called the Kohn-Sham orbitals corresponding to this fictious non-interacting system, and we have by definition that $n(\mathbf{r}) = \sum_i^N |\Phi_i(\mathbf{r})|^2$. The T_{int} is the interaction contribution to the kinetic energy, which we will use to rescale the exchange-correlation $E_{xc} \rightarrow E_{xc}' = E_{xc} + T_{int}$. This allows us to rewrite the energy functional as:

$$E[n] = T_s[n] + E_{ext}[n] + E_H[n] + E_{xc}'[n], \tag{1.7}$$

and then, using the variational theorem on the Kohn-Sham orbitals with a fixed total number of particles:

$$\frac{\delta}{\delta\Phi_i^*(\mathbf{r})} \left(E[n] - \sum_i \epsilon_i \int \Phi_i^*(\mathbf{r}) \Phi_i(\mathbf{r}) \mathrm{d}\mathbf{r} \right) = 0, \tag{1.8}$$

which yields the so-called **Kohn-Sham equations**, usually written in the form:

$$\left(-\frac{\Delta}{2} + V_{eff}(\mathbf{r}) \right) \Phi_i(\mathbf{r}) = \epsilon_i \Phi_i(\mathbf{r}). \tag{1.9}$$

They take a form similar to the Schrödinger equation of a system in the effective potential V_{eff}, which can be written as:

$$V_{eff} = V_{ext} + \frac{\delta E_{xc}'[n]}{\delta n(\mathbf{r})} + \int \frac{n(\mathbf{r}')}{|\mathbf{r} - \mathbf{r}'|} \mathrm{d}\mathbf{r}'. \tag{1.10}$$

The variational problem can then be solved self-consistently computationally, by initially taking an ansatz for the density and then solving the corresponding Kohn-Sham equations to get a new density, and looping this procedure until convergence.

However, in order to achieve this, we still need to find a form for the exchange-correlation functional. This has been one of the most outstanding issues in the field of density functional theory, and an analytical expression for this functional is still not known (although closed expressions are known in terms of density matrices [127, 128]) Here, approximations have to

be made.

1.4 Local approximations to the exchange-correlation functional

As explained before, the exact form of the exchange-correlation density functional can't be casted in a analytical closed expression. The local density approximation proposes to write this functional as a local function of the density, that is, a functional of the density at a given point in space:

$$E_{xc}^{LDA}([n]) = \int \epsilon_{xc}[n(\mathbf{r})]n(\mathbf{r})\mathbf{dr}, \tag{1.11}$$

where $\epsilon_{xc}[n]$ is a local functional of the density at the point $\mathbf{r}$. One of the most popular and successful forms for this functional is the jellium functional, where the $\epsilon_{xc}[n]$ is taken to be the functional of an homogeneous electron gas (also called a jellium). This functional is then usually split in two parts $\epsilon_{xc}[n] = \epsilon_x[n] + \epsilon_c[n]$, where $\epsilon_x[n]$ is the Dirac exchange functional, whose exact analytical form was first derived by Dirac as an extension to Thomas-Fermi theory [129]:

$$E_x[n] = -\frac{3}{4}\left(\frac{3}{\pi}\right)^{1/3}\int n(\mathbf{r})^{4/3}\mathbf{dr}. \tag{1.12}$$

The second part is the correlation functional, which has no exact analytical form although several mathematical forms have been proposed for it, for example based on accurate quantum Monte-Carlo simulations of the jellium [130].

The extension to a non-trivial electronic spin polarization has been extensively studied and is quite straightforward for the exchange part using the so-called scaling relations [131], but the correlation part requires more finesse and is often built by interpolating in some way between the paramagnetic and ferromagnetic limits. This yields the local spin density approximation (LSDA) [131]:

$$E_{xc}^{LSDA}([n^\uparrow, n^\downarrow]) = \int \epsilon_{xc}[n^\uparrow, n^\downarrow]n(\mathbf{r})\mathbf{dr} = \int \epsilon_{xc}[n^\uparrow, n^\downarrow]\left(n^\uparrow(\mathbf{r}) + n^\downarrow(\mathbf{r})\right)\mathbf{dr}. \tag{1.13}$$

Henceforth, it should be understood that this spin generalization can be done for all the following results. However, for brevity and clarity reasons, it will not be shown explicitely.

A natural extension of L(S)DA arises by taking into account higher derivative orders of

the density in the exchange-correlation functional:

$$E_{xc}^{meta-GGA}([n]) = \int \epsilon_{xc}[n(\mathbf{r}), \nabla n(\mathbf{r}), \Delta n(\mathbf{r}), ...]n(\mathbf{r})\mathbf{dr}. \qquad (1.14)$$

The expansion is almost always cut at the second order which leads to the so-called *meta-generalized gradient approximations* (meta-GGA) to the exchange-correlation functional [132], although we should note that higher order derivatives have been explored within the context of machine-learning approaches to DFT [133, 134]. The popular generalized gradient approximation (GGA) is obtained by truncating even further the functional at the first derivative order in the density. It should be emphasized that these are still local functionals of the density, only depending on the value of the density at some point and its derivatives, although they are often referred to as semi-local (or even confusingly as non-local) functionals. Truly non-local functionals of the density have also been studied [135], but are much less commonly used.

In the GGA approximation, the exchange-correlation functional is not as easy to obtain as in LDA. Indeed, merely doing a naive gradient expansion of the density in the exchange-correlation integral yields inaccurate results because such functionals do not respect integral constraints of the exact exchange-correlation functionals unlike LDA [135]. Rather, one needs to carefully modify these naive expansions in order to properly reproduce said rules, leading to the most notable examples of GGA such as the Perdew-Wang 91 (PW91) functional, and the closely related Perdew-Becke-Ernzerhof (PBE) functional, that we will use for our calculations [136, 137].

However, note that there is no guarantee that such gradient-based expansions will necessarily yield better results than a pure LDA. Indeed, because of the necessity to artificially correct the naive gradient expansion in order to respect the integral sum rules, whereas these are exactly respected by LDA, it is entirely conceivable than GGA may lead to worse results for some systems. For example, GGA is required to get a ferromagnetic ground state for bulk iron, as LDA yields a wrong paramagnetic ground state [138, 139], but one can show that the magnetic stabilization energy is also grossly overestimated with GGA in other magnetic systems [140]. Still, GGA is known to yield superior results with respect to experimental references in many cases [135, 141]

1.5 Solving the Kohn-Sham equations : The Projector Augmented Wave Method

1.5.1 Introducing the general eigenvalue problem

In order to solve the Kohn-Sham equations, a natural method is to expand the system wavefunction over a complete basis of functions Φ in order to turn the issue into a generalized eigenvalue problem:

$$|\Psi\rangle = \sum_{i}^{\infty} c_i |\Phi_i\rangle,$$ (1.15)

which leads to the following form for the (Kohn-Sham) Schrödinger equation, after projection over a given state Φ_j:

$$\sum_{i}^{\infty} c_i \langle\Phi_j| H |\Phi_i\rangle = E \sum_{i}^{\infty} c_i \langle\Phi_j|\Phi_i\rangle.$$ (1.16)

Introducing the S overlap matrix $S_{ij} = \langle\Phi_i|\Phi_j\rangle$ and the coefficient vector $\vec{c}$, this can be rewritten as:

$$H\vec{c} = ES\vec{c},$$ (1.17)

which leads directly to the generalized eigenvalue problem:

$$\det(H - ES) = 0.$$ (1.18)

Solving the Kohn-Sham equations then requires solving this generalized eigenvalue problem and getting the corresponding generalized eigenvectors. Computationally, we need to restrict the basis set to a finite size as it would be impossible to use an infinite basis numerically, and to find the smallest such finite basis to complete this task, as this generalized eigenvalue problem has a significant complexity in the basis set size N, roughly $O(N^3)$. In fact, for larger systems, most notably those with a surface like ours, this equation is not solved. Rather, the strategy is to directly minimize the Energy functional as the complexity scaling in N is less steep for this operation. This is the spirit of the so-called Orbital-Free DFT methods (OF-DFT) [142], that are less popular than orbital Kohn-Sham DFT methods because of accuracy issues, although there has been great progress over the recent years to correct these [143].

Finding an adequate reduced basis to solve the Kohn-Sham equation is a fairly complex task. Indeed, the coulombian potential is divergent near the nuclei. Therefore, all electronic states have non-negligible values close to this pole, especially core states. As such,

since valence states have to be orthogonal to the core states, valence wavefunctions tend to have strong oscillations near the nuclei; and are hence hard to compute, requiring a large set of plane waves to be described satisfactorily.

There are several approaches to this issue. One of them is to use pseudopotentials [144], where the combined nuclear and core electronic potential is described by a smooth effective tabulated potential up until a certain radius, where they match the all electron potentials. The Kohn-Sham equations can then be solved for the valence states in this potential. This method has the advantage of supressing the divergent potential behaviour, and also to greatly reduce the number of wave functions to be computed as only the valence states have to be calculated. However, an obvious flaw of this method is that information of the system is lost close to nuclei. Still, this approach proved to be highly successful and is one the most commonly used nowadays [145].

Another way is to use the so-called augmented plane-waves (APW) [146]. The idea is based on the fact that there seems to be two regions of drastically different behaviour for the valence wavefunctions: a quasi-flat potential region far from the nucleus, and a quasi-atomic potential close to the nuclei. As such, close to the nuclei, the valence wavefunction should look like spherical atomic wavefunction; whereas smooth plane waves have to be expected far from the nuclei. The augmentation strategy then consists in combining these two observations: the wavefunctions will be described by atomic partial waves inside a certain augmentation spherical region around each nuclei, whereas smoother wave functions will be used in the interstitial flat potential regions. Both sets of wavefunctions are then differentiably matched at the augmentation spheres boundaries.

There exists in fact a more general scheme, which includes the advantages of both pseudopotential and APW methods. It is called the projector augmented wave (PAW) method, introduced by Blöchl [147].

1.5.2   The PAW method

As said earlier, the all electron single particle wavefunction is characterized by a highly oscillatory behaviour near the nucleus, and is therefore numerically hard to compute. To solve this complex issue, the PAW method [147] proposes the following scheme.

We consider a linear transformation T between the all electron Kohn-Sham wavefunction $|\Psi_n\rangle$ (where n is an index of the band and of the k-point) and a fictious, smooth wavefunction $|\tilde{\Psi}_n\rangle$ such as:

$$|\Psi_n\rangle = T |\tilde{\Psi}_n\rangle. \tag{1.19}$$

From until now, all values associated to the pseudo auxilliary Hilbert Space of these fictious wavefunctions will be denoted using a tilde.

Given that the wavefunction is already smooth beyond a certain distance from the nuclei, we can restrict the transformation inside the various augmentation spheres Ω_R for nuclei centered at R:

$$T = 1 + \sum_R T_R. \tag{1.20}$$

This allows us to define a complete set of pseudo smooth partial waves, associated to the real partial waves in each augmentation sphere by the correpsonding transformation:

$$|\Phi_\Lambda\rangle = (1 + T_R)|\tilde{\Phi}_\Lambda\rangle. \tag{1.21}$$

It should be emphasized that Λ is a general index of the position R, of the angular momentum and of the spin. Besides, the all electron and pseudo partial waves naturally match outside of the augmentation spheres.

Inside the augmentation region, the pseudo wavefunction can then be written as a linear combination of these pseudo partial waves:

$$|\tilde{\Psi}_n\rangle = \sum_\Lambda c_\Lambda^n |\tilde{\Phi}_\Lambda\rangle. \tag{1.22}$$

By the linearity of the T opeartor, we then trivially have that the all electron wavefunction can be written as:

$$|\Psi_n\rangle = \sum_\Lambda c_\Lambda^n |\Phi_\Lambda\rangle, \tag{1.23}$$

which allows us to write that:

$$|\Psi_n\rangle = |\tilde{\Psi}_n\rangle + \sum_\Lambda c_\Lambda^n (|\Phi_\Lambda\rangle - |\tilde{\Phi}_\Lambda\rangle). \tag{1.24}$$

The coefficient c_Λ also have to be linear functionals of the pseudo wavefunction, as T is a linear transformation. This allows us to define projector functions $|\tilde{p}_\Lambda\rangle$ such that:

$$c_\Lambda^n = \langle \tilde{p}_\Lambda | \tilde{\Psi}_n \rangle. \tag{1.25}$$

This naturally leads to the closure relation $\sum_\Lambda |\tilde{\Phi}_\Lambda\rangle \langle \tilde{p}_\Lambda| = 1$ inside the augmentation spheres, which leads to the orthogonality condition:

$$\langle \tilde{p}_\Lambda | \tilde{\Phi}_{\Lambda'} \rangle = \delta_{\Lambda\Lambda'}. \tag{1.26}$$

As this is only valid within the augmentation regions, this leads to no restrictions on the projector functions beyond Ω_R. Usually, projectors are taken to be localized within the augmentation region, although it's entirely possible for them to be extended beyond.

This leads to the following form for the transformation T:

$$T = 1 + \sum_\Lambda (|\Phi_\Lambda\rangle - |\tilde{\Phi}_\Lambda\rangle) \langle \tilde{p}_\Lambda|, \tag{1.27}$$

which allows us to express the transformation T in terms of the all electron and pseudo partial waves, as well as the projector functions.

1.5.3 Operators in the PAW formalism

We defined a linear transformation between the all electron Hilbert space and the pseudo Hilbert space that allows one to associate a pseudo wavefunction to each all electron wavefunction. As such, these pseudo wavefunctions are the new variational parameters, and we therefore need a way to extract observables from operators acting on the PS Hilbert space. As such, we need to find the expression of these operators in the PS Hilbert space, and their expectation values.

To achieve this, we first note that:

$$\langle \Psi_n | A | \Psi_n \rangle = \langle \tilde{\Psi}_n | T^\dagger A T | \tilde{\Psi}_n \rangle, \tag{1.28}$$

which allows us to define the transformed operator $\tilde{A} = T^\dagger A T$. Assuming the operator A to

be semilocal and expanding the T transformation, we obtain the following form:

$$\tilde{A} = A + A^l - \tilde{A}^l \tag{1.29}$$

$$A^l = \sum_{\Lambda,\Lambda'} |\tilde{p}_\Lambda\rangle \langle\Phi_\Lambda| A |\Phi_{\Lambda'}\rangle \langle\tilde{p}_{\Lambda'}| \tag{1.30}$$

$$\tilde{A}^l = \sum_{\Lambda,\Lambda'} |\tilde{p}_\Lambda\rangle \langle\tilde{\Phi}_\Lambda| A |\tilde{\Phi}_{\Lambda'}\rangle \langle\tilde{p}_{\Lambda'}|. \tag{1.31}$$

Note that A^l and $\tilde{A}^l$ are ill-defined if the partial waves are unbound. As such, both AE and PS partial waves need to cancel each other beyond the augmentation region.

Finally, evaluating the expectation value leads to the following general form:

$$\langle A \rangle = \langle\tilde{A}\rangle + \langle A^l\rangle - \langle\tilde{A}^l\rangle$$

$$\langle\tilde{A}\rangle = \sum_n f_n \langle\tilde{\Psi}_n| A |\tilde{\Psi}_n\rangle \tag{1.32}$$

$$\langle A^l\rangle = \sum_{n,\Lambda,\Lambda'} f_n \langle\tilde{\Psi}_n|\tilde{p}_\Lambda\rangle \langle\Phi_\Lambda| A |\Phi_{\Lambda'}\rangle \langle\tilde{p}_{\Lambda'}|\tilde{\Psi}_n\rangle \tag{1.33}$$

$$\langle\tilde{A}^l\rangle = \sum_{n,\Lambda,\Lambda'} f_n \langle\tilde{\Psi}_n|\tilde{p}_\Lambda\rangle \langle\tilde{\Phi}_\Lambda| A |\tilde{\Phi}_{\Lambda'}\rangle \langle\tilde{p}_{\Lambda'}|\tilde{\Psi}_n\rangle, \tag{1.34}$$

where f_n is the occupation of the n state.

It should be understood that this form is valid for a general semilocal operator, most notably the monoelectronic density $n(\mathbf{r})$ which will be written as:

$$n(\mathbf{r}) = \tilde{n}(\mathbf{r}) + n^l(\mathbf{r}) - \tilde{n}^l(\mathbf{r}), \tag{1.35}$$

with the right hand side being defined as before.

This can also be done for the energy functional E, which be generally written as:

$$E = \sum_n f_n \langle\Psi_n| - \frac{1}{2}\nabla^2 |\Psi_n\rangle + \frac{1}{2}\int \mathbf{dr}\int \mathbf{dr}'\frac{(n+n^Z)(n+n^Z)}{|\mathbf{r}-\mathbf{r}'|} + \int \mathbf{dr}n\epsilon_{xc}(n), \tag{1.36}$$

with n^Z the nuclear density. The dependance on $\mathbf{r}$ and $\mathbf{r}'$ for the densities is implicit.

This can be written under the transformation scheme as:

$$E = \tilde{E} + E^l - \tilde{E}^l \tag{1.37}$$

$$\tilde{E} = -\sum_n f_n \langle \tilde{\Psi}_n | \frac{\nabla^2}{2} | \tilde{\Psi}_n \rangle + \frac{1}{2} \int d\mathbf{r} \int d\mathbf{r}' \frac{(\tilde{n} + n_c)(\tilde{n} + n_c)}{|\mathbf{r} - \mathbf{r}'|} + \int d\mathbf{r} \tilde{n} \epsilon_{xc}(\tilde{n}) \tag{1.38}$$

$$+ \int d\mathbf{r} \tilde{n} v_t$$

$$E^l = -\sum_{n,\Lambda,\Lambda'} f_n \langle \tilde{\Psi}_n | \tilde{p}_\Lambda \rangle \langle \Phi_\Lambda | \frac{\nabla^2}{2} | \Phi_{\Lambda'} \rangle \langle \tilde{p}_{\Lambda'} | \tilde{\Psi}_n \rangle + \frac{1}{2} \int d\mathbf{r} \int d\mathbf{r}' \frac{(n^l + n^Z)(n^l + n^Z)}{|\mathbf{r} - \mathbf{r}'|} \tag{1.39}$$

$$+ \int d\mathbf{r} n^l \epsilon_{xc}(n^l)$$

$$\tilde{E}^l = -\sum_{n,\Lambda,\Lambda'} f_n \langle \tilde{\Psi}_n | \tilde{p}_\Lambda \rangle \langle \tilde{\Phi}_\Lambda | \frac{\nabla^2}{2} | \tilde{\Phi}_{\Lambda'} \rangle \langle \tilde{p}_{\Lambda'} | \tilde{\Psi}_n \rangle + \frac{1}{2} \int d\mathbf{r} \int d\mathbf{r}' \frac{(\tilde{n}^l + n_c)(\tilde{n}^l + n_c)}{|\mathbf{r} - \mathbf{r}'|} \tag{1.40}$$

$$+ \int d\mathbf{r} \tilde{n}^l \epsilon_{xc}(\tilde{n}^l) + \int dr \tilde{n}^l v_t,$$

where v_t is a localized potential in the augmentation region that can be arbitrarily chosen in order to correct the partial wave expansion truncation error and to dampen the near singularities of the coulombian potential. As $\tilde{n}$ and $\tilde{n}^l$ coincide exactly in the augmentation regions, its contribution to the total energy vanishes exactly. Besides, n_c is the so-called compensation density: to understand its contribution, one should first remember that the Hartree energy can be written as:

$$E_H = \frac{1}{2} \int d\mathbf{r} \int d\mathbf{r}' \frac{n_{tot}(\mathbf{r}) n_{tot}(\mathbf{r}')}{|\mathbf{r} - \mathbf{r}'|}, \tag{1.41}$$

with $n_{tot}(\mathbf{r}) = n(\mathbf{r}) + n^Z(\mathbf{r})$. As such, by using the transformation formula of the density, we notice the fact that the density within the augmentation region interacts with the interstitial density, which prevents us from naively splitting the Hartree energy in the usual three contributions. To solve this, we use a classic trick: the compensation density n_c is introduced in order to supress the localized potential contribution outside the augmentation region and allow us to conveniently split the energy in the three previous contributions.

1.6 Strongly Correlated systems: the LDA+U method

1.6.1 The issue of strong correlations

In certain materials, the Coulomb repulsion between electrons exceeds their kinetic energy and therefore constrains them to remain localized in quasi-atomic orbitals. Such materials could even appear to be conductors according to conventional band theory, which

underestimates electron-electron interaction, but are in fact insulating: they are then called Mott insulators [148]. Such strongly-correlated materials are naturally very complex to describe with DFT as the exact form of the energy-correlation functional is not known. In fact, most of the commonly-used LDA and GGA exchange-correlation functional fail at describing this insulating behaviour as they have a tendency to underlocalize electrons, and therefore misrepresent the characteristic orbital polarization of the insulator [149, 130].

Strongly-correlated materials are usually described thanks to models such as the Hubbard model [150]. In a real-space second quantized formalism, the model can be written as for the simplest one-band case:

$$H_{Hub} = -t \sum_{<i,j>,\sigma} \left(c_{i,\sigma}^{\dagger} c_{j,\sigma} + h.c. \right) + U \sum_i n_{i,\uparrow} n_{i,\downarrow}, \tag{1.42}$$

where $< i, j >$ should be understood as a sum over nearest neighbours. The hopping between adjacent sites is controlled by the amplitude t, whereas the on-site Coulomb repulsion is described by the parameter U. It appears naturally that for the limit case where $U >> t$, the on-site term dominates the hopping term and therefore forces the electrons to remain localized: this is characteristic of a Mott insulator state (which is in fact the eigenstate of the Hamiltonian for t vanishing).

The LDA+U approach [151] is then based on the idea of splitting the electrons in two parts: the strongly-correlated electronic states, usually located within the d or f shells, will be described using a correction based on this U dominated Hubbard model, whereas the other states will be described using the usual DFT formalism. It should be understood that while this method is usually called LDA+U, it is really a correction valid for a generic approximate DFT method, not just LDA.

1.6.2   the LDA+U formalism

We can therefore write the energy functional as:

$$E^{LDA+U}[n, n_i] = E^{LDA}[n] - E_{dc}^{LDA}[n_i] + E^{cor}[n_i], \tag{1.43}$$

where n_i are the density terms for the strongly localized orbitals (the d orbitals for Fe). The $E^{cor}[n_i]$ is the Hubbard correction: since this is an additive correction to take into account the electronic Coulomb interaction, it is necessary to remove the part of this interaction that is described within the LDA formalism itself, hence the double counting term $E_{dc}^{LDA}[n_i]$. In the

original formulation, the functional could be written as [152, 153, 154]:

$$E^{LDA+U}[n, n_i] = E^{LDA}[n] + \frac{U}{2} \sum_{i \neq j} n_i n_j - \frac{U}{2} n_d(n_d - 1), \qquad (1.44)$$

with $n_d = \sum_i n_i$.

For spin-polarised calculation, it is necessary to take into account the exchange interaction between electrons of the same spin. By introducing the exchange energy J, we can show that the correction takes the form:

$$E^{LDA+U} = E^{LSDA} + \frac{U - J}{2} \sum_{m,\sigma} (n_{m\sigma} - n_{m\sigma}^2). \qquad (1.45)$$

A problem that immediately arises from this form is that the $n_{m\sigma}$ occupation terms are not rotationally invariant and any rotation of the localized basis set used to define them will lead to a natural modification of the orbitals which will become a linear combination of the pre-rotation orbitals. To solve this issue, a more general formulation [155] based on the density matrix ρ can be introduced as the trace is a rotational invariant. We can now write the correction as:

$$E^{LDA+U} = E^{LSDA} + \frac{U - J}{2} \left[\sum_{m,\sigma} \rho_{mm}^\sigma - \sum_{m,m',\sigma} (\rho_{mm'}^\sigma \rho_{m'm}^\sigma) \right]. \qquad (1.46)$$

Finally, we need to emphasize that the non-sphericity of the interactions has thus far been neglected. It is possible to take it into account in an even more general scheme [156]:

$$E^{LDA+U} = E^{LSDA} + E^{Hub} - E_{dc}^{LSDA} \qquad (1.47)$$

$$E^{Hub} = \frac{1}{2} \sum_{\{m\},\{\sigma\}} n_{m_1 m_3}^\sigma \left[\langle m_1, m_2 | V_{e-e} | m_3, m_4 \rangle - \delta_{\sigma\sigma'} \langle m_1, m_2 | V_{e-e} | m_4, m_3 \rangle \right] n_{m_2 m_4}^{\sigma'}$$

$$\qquad (1.48)$$

$$E_{dc}^{LSDA} = \frac{U}{2} n_d(n_d - 1) - \frac{J}{2} \sum_\sigma (n_d^\sigma(n_d^\sigma - 1)), \qquad (1.49)$$

where the m states are the localized orbital basis set.

Using atomic states as this set, the electron-electron potential V_{e-e} can be expanded in terms of Slater integrals F^k:

$$\langle m_1, m_2 | V_{e-e} | m_3, m_4 \rangle = \sum_k a_k(m_1, m_3, m_2, m_4) F^k. \qquad (1.50)$$

The a_k coefficient can be expressed as a product of Clebsch-Gordan coefficients. For the d orbitals, only the F^0, F^2 and F^4 integrals are relevant, as higher order a_k terms in the expansion vanish. In practice, these integrals are not used themselves as the Coulomb interaction is screened in solids, and they are treated as parameters specified in terms of U and J.

1.7 The Van der Waals interaction in DFT: a short presentation of the DFT-D2 method

Van der Waals forces are originating from long range electronic correlations, that can evidently not be described accurately by DFT as the exchange-correlation functional has no exact form. Given their importance for various physical system, for example in the case of molecular adsorption on surfaces, this has led to a huge amount of research to find a suitable implementation of Van der Waals interactions in the DFT formalism. While there are several solutions to this problem [157], a very pragmatic and empirical but popular approach for this is given by the DFT-D method of Grimme, later extended into the DFT-D2 method [158, 159].

The idea is that the dispersion-corrected total energy can be written as:

$$E_{DFT-D} = E_{DFT} + E_D, \tag{1.51}$$

where E_{DFT} is the energy obtained from the Kohn-Sham DFT calculation, and E_D is the empirical dispersion correction, which will be written as:

$$E_D = -S_6 \sum_{i=1}^{N_a-1} \sum_{j=i+1}^{N_a} \frac{C_6^{ij}}{R_{ij}^6} f_d(R_{ij}), \tag{1.52}$$

where S_6 is a global scaling factor that depends only on the density functional used. C_6^{ij} is the dispersion parameter for the pair of atoms ij and N_a is the number of atoms. The f_d function is a damping function to prevent from having a diverging value for a small inter-atomic distance, and can be written as:

$$f_d(R_{ij}) = \frac{1}{1 + \exp(-d(R_{ij}/R_{0ij} - 1))}, \tag{1.53}$$

where $R_{0ij} = R_{0ii} + R_{0jj}$ is the sum of the atomic Van der Waals Radii of the atomic pair ij. The parameter d is usually fixed at $d = 20.0$.

All the C_6^{ii} and R_{0ii} parameters are tabulated for chemical elements [160], with the interatomic dispersion parameter being computed as the geometric mean:

$$C_6^{ij} = \sqrt{C_6^{ii} C_6^{jj}}. \tag{1.54}$$

It is possible to take into account higher dispersion orders through C_8 or C_{10} coefficient, but this can be counterproductive as they will interact with the damping function and can lead to worse results. These coefficients therefore require a modification of the damping logic (i.e. see the DFT-D3 method [161]).

Chapitre 2

Energetical aspects of the Spin-crossover phenomenon

2.1   Introduction

As we have emphasized earlier in the introduction, bistable spin crossover systems have significant potential as building blocks for highly innovative spintronics devices. As such, achieving this promise necessarily entails the mastery of the energetics of these SCO systems, both from a theoretical and experimental point of view, in order to be able to properly address and manipulate both spin states. As such, the point of the following section is to introduce several novel results on the energetics of spin-crossover molecules on metallic surfaces. More precisely, we will focus on the FePhen system adsorbed on a Cu(001) surface, because of the extensive literature on its electronic properties both in the gas phase and on the surface [119]. We will start by recomputing several quantities such as the adiabatic energy difference and the transition barrier in our case, and we will then introduce at the same time our new results about the ligand doping effects on the energetics of the spin crossover mechanism as a novel approach to manipulate the spin states in a SCO system. Finally, we will also show some results about the calculation of phonons within these systems, first in the harmonic approximation to demonstrate the computation of thermodynamical quantities in order to study the stability and the evolution of the spin states with respect to temperature. We will then focus on our tentative foray into calculations beyond the harmonic approximation using molecular dynamics.

2.2   Computational details

All calculations were carried using the projected augmented wave (PAW) method [162] as implemented in VASP (Vienna Ab initio Simulation Package) [163]. The exchange-correlation

contribution was evaluated within the generalized gradient approximation (GGA) [137]. Van der Waals interactions between the molecule and the substrate are taken into account using Grimme's DFT-D2 approximation [159]. The localized d states of iron were described with the rotationally invariant DFT+U method of Dudarev and coworkers [164]. The values of the Hubbard parameter U and exchange parameter J were set respectively to 3.0 eV and 0.9 eV to properly reproduce the iron spin moment and the expected energy difference between the two spin states of Fe(II) in our case [116, 117], as this is the most consistent and convenient approach to obtain accurate adiabatic energy differences without relying on highly precise but prohibitvely costly methods such as CASSCF or Full CI as we have emphasized earlier in the introduction. For lack of anything better, these values will moreover be kept constant for all systems studied throughout this part as all self-consistent approaches to recompute these parameters yield unrealistically large overcorrections to the energetics of the FePhen molecule [113, 165, 166, 167].

The substrate was simulated using three layers of copper grown along the (001) direction, with each plane containing 36 (6x6) atoms of copper, for a total of 159 atoms in the supercell to fully describe the H(F)-Fephen/Cu(001) system. The dimensions of this periodic cell were $(17.8 \times 17.8 \times 33.6 \text{ Å})$ for both the gas phase and the molecule adsorbed on the copper substrate. The total energy is converged to 10^{-5} eV and the plane waves cut-off energy is set at 500 eV. The atoms are allowed to move until the forces are below 10^{-3} eV/Å in each direction of the cell axes. The calculation of the Fermi level is carried with a Gaussian integration method [168] using a width of 0.1 eV. This electronic entropy is removed when calculating the total energy. Due to the large size of the supercell, we restricted our k-point mesh to the Γ point.

2.3   Some results on FePhen

We will start by recomputing some already available theoretical results on the FePhen molecule for consistency purposes, as we have no guarantee that the newer implementations of VASP will yield the same results as the earlier implementations especially with the immense sensitivity of the spin state energetics to the method used. Some important structural properties are given in the table 2.1

	HS (free)	HS@Cu(001)	LS (free)	LS@Cu(001)
Fe-NCS (Å)	2.00	2.03	1.92	1.90
Fe-N(Phen) (Å)	2.23	2.19	1.98	1.98
Fe-N (Å)	2.15	2.14	1.96	1.95
C-N(NCS) (Å)	1.20	1.18	1.19	1.18
C-N(Phen) (Å)	1.35	1.35	1.35	1.35
C-C (Å)	1.41	1.41	1.41	1.41
C-H (Å)	1.09	1.09	1.09	1.09
C-S (Å)	1.61	1.65	1.61	1.65
S-Cu (Å)	N/A	2.06	N/A	2.12
SCN-Fe-NCS (°)	102.4	96.3	91.6	91.3
Fe-N-C(NCS) (°)	140.8	168.1	161.4	169.7
N-C-S (°)	177.5	176.8	178.8	174.4
ζ (Å)	0.620	0.420	0.145	0.222
Δ	$2.645 \cdot 10^{-3}$	$1.300 \cdot 10^{-3}$	$1.727 \cdot 10^{-4}$	$2.309 \cdot 10^{-4}$
Σ (°)	89.9	78.7	34.2	35.3
Θ (°)	255.5	246.8	103.2	108.8

TABLE 2.1 – Average values for various bond lengths, angles and deformation parameters within the free FePhen molecule and adsorbed on the surface, both in the HS and LS state.

In the previous table, the deformation parameters are most commonly defined as:

$$\zeta = \frac{1}{6} \sum_{i=1}^{6} \left| d_i - \bar{d} \right| \tag{2.1}$$

$$\Delta = \frac{1}{6} \sum_{i=1}^{6} \left| \frac{d_i - \bar{d}}{\bar{d}} \right|^2 \tag{2.2}$$

$$\Sigma = \frac{1}{12} \sum_{i=1}^{12} \left| \Phi_i - 90 \right| \tag{2.3}$$

$$\Theta = \frac{1}{24} \sum_{i=1}^{24} \left| \theta_i - 60 \right| \quad , \tag{2.4}$$

where the d_i are the 6 Fe $-$ N bonds in the molecule and $\bar{d}$ the average length (also reported in the table), the Φ_i are the *cis* N $-$ Fe $-$ N angles in the molecule and the Θ_i are the angles between twisting triangular planes. These parameters were computed thanks to the `OctaDist` code [169].

The structural results are also similar to what was obtained previously both experimentally [71] and theoretically [115, 116, 119], with the augmentation of the octahedral bond lengths in the HS state with respect to the LS state, along with a widening of the bond angle between the isothiocyanate groups and a closure of the Phen bond angle, leading to a strong deformation of the octahedral geometry in the HS state wrt the LS state. One can also note a stretching of the NCS groups for the molecule adsorbed on the surface when compared to the free molecule,

a normal result as the molecule is quite strongly bound to the copper surface. One point of major difference, however, lies in the fact that one can note that the bonding angle between the isothiocyanate ligand SCN-Fe-SCN is way higher in the HS state than what was found in litterature, with a value of 102.4° to be compared with the previously available experimental value of 95.1°, a result that is in accordance with other theoretical calculations [121]. Heuristically, it is well known that the intermolecular interactions between the neighbouring molecules play a significant role in the crystalline properties of SCO molecules and therefore one could then argue that this angle is kept constrained by said interactions as the experimental values were obtained within the crystal by XRD methods. The results yield an adiabatic energy difference of 0.21 eV for the molecule without a surface, and 0.57 eV for the molecule with a surface which is in accordance with the previously available results, showing the fairly strong adsorption of the molecule on the surface [119].

2.4 Doping

We will now focus on showing the effects of fluorination on the FePhen molecule, by carrying a total substitution of the hydrogen atoms within the FePhen molecule by fluorine atoms. For simplicity, we will label H-Fephen the unfluorinated molecule, and F-Fephen the fluorinated molecule. Note that such a full fluorination of organic molecules was already realised experimentally, for example on molecular materials such as Polythiophenes, Polyphenylenes or organometallic complexes [170]. In addition, the partial fluorination of phthalocyanines has already been carried, with zinc phthalocyanines (ZnPc) being fluorinated at 25%, 50% and 100% [171]. Fully fluorinated cobalt phthalocyanines were also used to show spin polarized interface states [172]. As such, partial doping exhibit potentialities for the fine-tuning of the adiabatic energy difference in order to achieve an energetically efficient SCO switching.
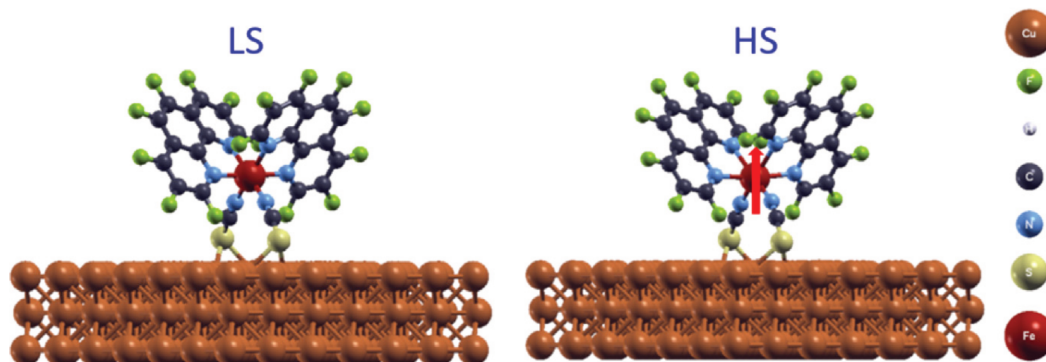
FIGURE 2.1 – Structure of the doped molecule on the surface after relaxation. Reproduced from [173]

After relaxation, we observe no striking modifications of the overall geometry of the complex which remains quasi-octahedral after doping as one can see on figure 2.1 and in the struc-

tural table 2.3, which means that the overall structural properties of the compound have not been significantly affected by the fluorine substitution. However, a closer inspection shows that the Fe-N bonds of the phenanthroline cage around the iron coordination centre have been stretched, especially in the HS state with an increase of the average value of 0.07 Å for the free molecule and 0.05 Å for the adsorbed molecule in the HS state, and 0.02 Å for the free molecule and 0.05 Å for the adsorbed molecule in the LS state. This stretching can also be seen from the fact that all the deformation parameters that we have previously introduced have a bigger value after doping. As the strength of the crystal field splitting is directly related to the ligand potential, and as such to the interatomic distance between the ligand and the central atom, one can already expect some changes in the electronic structure. In table 2.2, we give the energetic and magnetic states for both the pristine and fluorinated states. As one can clearly see, we observe a clear inversion of the spin state ordering after doping, with a positive adiabatic energy difference for the undoped molecule and a negative one after fluorination, with or without the surface. The adsorption-related structural properties are not greatly changed, with a surface-to-molecule distance of 1.97 Å in the LS state and 1.95 Å in the HS state, which are slighty reduced values compared to the data available for the undoped molecule.

		LS	HS	ΔE (kJ/mol)
Unfluorinated	E_T (eV)	-749.57 (-359.726)	-749.00 (-359.517)	55.3 (20.3)
	μ_{Fe} (μ_{B})	0.00 (0.00)	3.60 (3.72)	
Fluorinated	E_T (eV)	-887.407 (361.701)	-887.609 (361.977)	-19.6 (-26.8)
	μ_{Fe} (μ_{B})	0.00 (0.00)	3.25 (3.72)	

TABLE 2.2 – Total energy (E_T) in eV and iron magnetic moment (μ_{Fe}) in Bohr magneton (μ_{B}) for the high spin (HS) and low spin (LS) states of the unfluorinated and fluorinated Fephen molecule adsorbed on the Cu(001) substrate (the values for the free molecule are between parenthesis). The last column shows the total energy difference $\Delta E = E_T^{\mathrm{HS}} - E_T^{\mathrm{LS}}$ in kJ/mol. Reproduced from [173].

The root median square displacements (RMSD) of the overlap between the states before and after doping show a deformation of the octahedral cage around the coordination centre, which appears to be more important in the HS state than in the LS state, as seen in figure 2.2. However, it also appears that the doped LS state on the surface is quite strongly stretched compared to the free molecule as one can see on the table 2.3, with a ζ parameter growing from 0.158 Å in the free molecule to 0.374 Å in the molecule on the surface (and a similar behaviour for Δ), whereas the increase was much more restricted for the undoped case going from 0.145 Å to 0.222 Å. Interestingly, the opposite behaviour can be observed for the case of the HS state. Moreover, the angular deformations are also reduced in the same time, with the Σ parameter going down from 75.8 to 49.1 (and idem for Θ) within the LS state, and a similar behaviour in the HS state. Interestingly, doping the molecule and restricting the atomic movement yields a lowering of the adiabatic energy difference but no inversion, showing that

the atomic relaxation plays an important part in the inversion of the energetic ordering of the states. As such, the strong electronegativity of fluorine drives a subtle but noticeable atomic and electronic rearrangement of the molecule that yields a hitherto unobserved spin state inversion in the low spin FePhen molecule. To rationalize this, we will proceed with a Bader analysis of the electron distribution.

FIGURE 2.2 – Superposition on the iron atom of the octahedral and (NCS) groups of the relaxed H-Fephen and F-Fephen molecules on the substrate in the two magnetic state (LS-left, HS-right), in color for the F-Fephen, and transparent for the H-Fephen. Reproduced from [173].

	HS (free)	HS@Cu(001)	LS (free)	LS@Cu(001)
Fe-NCS (Å)	1.99	2.03	1.94	1.89
Fe-N(Phen) (Å)	2.30	2.24	2.00	2.03
Fe-N (Å)	2.20	2.17	1.98	1.98
C-N(NCS) (Å)	1.20	1.18	1.19	1.18
C-N(Phen) (Å)	1.33	1.34	1.35	1.35
C-C (Å)	1.41	1.41	1.41	1.41
C-F (Å)	1.34	1.34	1.34	1.34
C-S (Å)	1.60	1.66	1.61	1.67
S-Cu (Å)	N/A	1.95	N/A	1.97
SCN-Fe-NCS (°)	118.0	103.2	92.0	95.1
Fe-N-C(NCS) (°)	158.2	168.1	143.4	170.0
N-C-S (°)	178.4	177.8	179.3	175.1
ζ (Å)	0.837	0.585	0.158	0.374
Δ	$4.542 \cdot 10^{-3}$	$2.304 \cdot 10^{-3}$	$2.123 \cdot 10^{-4}$	$1.119 \cdot 10^{-3}$
Σ (°)	146.4	88.2	75.8	49.1
Θ (°)	405.3	298.5	189.7	147.8

TABLE 2.3 – Average values for various bond lengths, angles and deformation parameters within the free doped FePhen molecule and adsorbed on the surface, both in the HS and LS state.

2.5   Bader analysis

The subject of the atomic distribution in a molecule is a delicate matter. Indeed, as the electrons are shared in bonds within the molecular structure, one can not in theory uniquely

define atomic boundaries - and therefore atoms - within a molecule. This conceptual difficulty was noted by Bader [174, 175], who therefore introduced Bader analysis in order to deal with this issue. The idea is to find the spatial minima of the electronic density, and then to compute the perpendicular intersecting surfaces of these points: the so-called zero-flux surfaces (because they are the surfaces through which the derivative of the density, the electronic flux, vanishes). This defines a decomposition of the supercell into elementary volumes, called Bader volumes, that can be considered as the molecular equivalent for atoms, allowing one to carry a systematic and rigorous analysis of the electronic repartition within the molecular system. Carrying this procedure, we will focus on the electronic distribution in a select subset of the atoms in the FePhen molecule before and after fluorination because of the relative symmetry between both Phen groups. We can then compute the number of valence electrons of the molecule, and thus obtain the electronic transfers linked to the doping process as shown in figure 2.3.

As one can see on the figure, there is a significant electron transfer happening on the carbon atoms bonded with fluorine, as the strong electronegativity of said atom leads to an electronic depopulation of the carbon centres. In turn, this leads to the increase of the charge on the Nitrogen atoms as these anions are attracted to the more strongly positively charged carbon cation. Therefore, the effective charge on the Nitrogen atom increases, which can be seen on the Bader analysis, and the ligand electrostatic field thus becomes stronger. This increases the repulsion with the coordination centre, leading to the observed bond length elongation. As such, the balance between the pairwise repulsion and the ligand screening swings towards the former, which stabilizes the HS state wrt the LS state. Interestingly, it appears that the doping increases the charge on the Iron coordination centre, which can rationalized as the longer bond lengths should lead to a weakening of said bonds, and as such an electronic repopulating of the metal atom. To have a more qualitative understanding of the effects of this doping on the coordination centre itself, especially on the octahedral splitting, we will now focus on the iron-projected density of states.

2.6 Density of states

We have now computed the projected density of states on the iron centre, shown in figure 2.4, resolved in t_{2g} and e_g subshells. The ligand-field strength is naturally defined as the difference of energy between these two levels, however the imperfect octahedral symmetry lifts the degeneracy within the subshells themselves so we will take the difference between the highest peaks of t_{2g} and e_g characters. Note that using the centre of mass of the subshell densities is also possible in theory, but the significant amount of hybridization in the spectrum leads to a uneven spread of the distribution compared to the purely octahedral case and therefore to spurious values for the calculation of the centre of mass, so we will not use it.
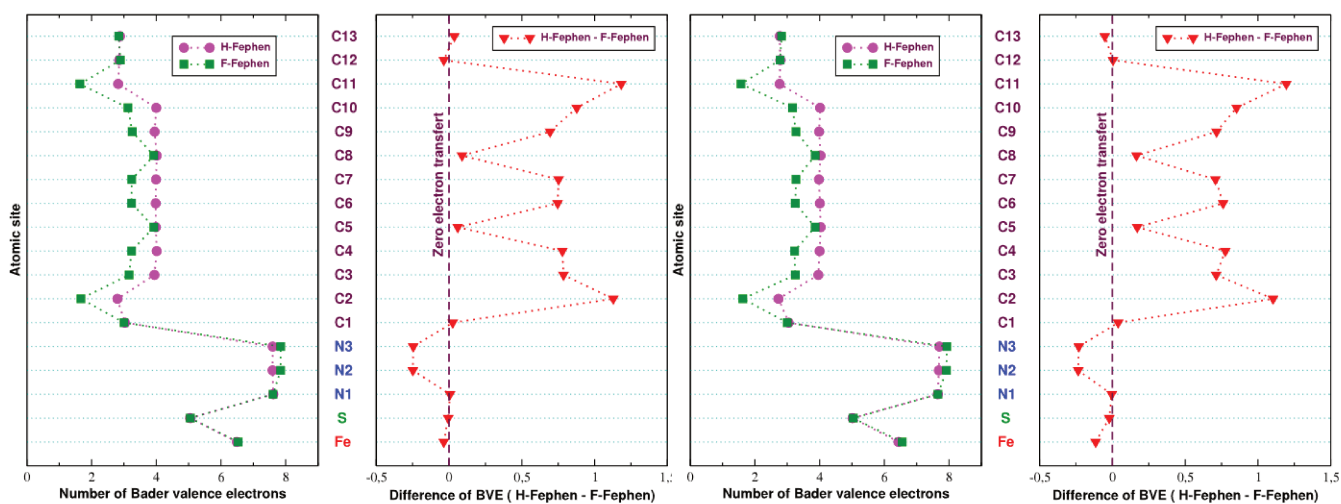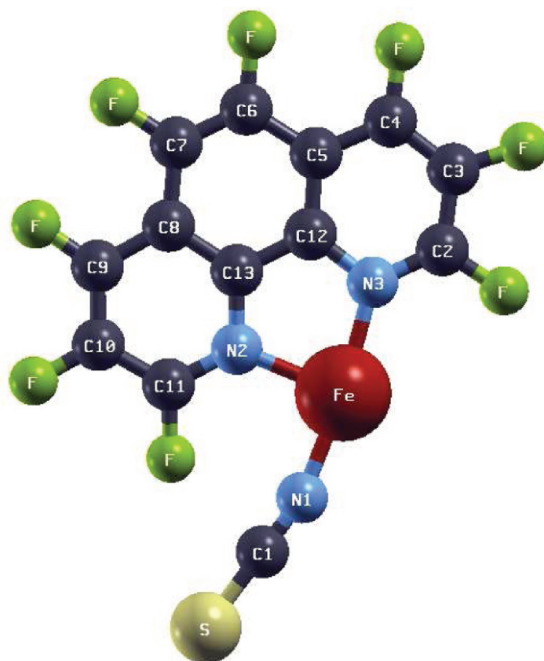
Figure 2.3 – From left to right: (1) LS Valence Bader electrons (VBE) per atom for H-Fephen (pink dots), F-Fephen (green squares), (2) LS VBE difference between H-Fephen and F-Fephen (red triangles) for each site in the LS state, (3) and (4) are respectively same as for (1) and (2) but for HS state. The labels of atoms are as shown on the top picture of the moiety of the molecule. Reproduced from [173].
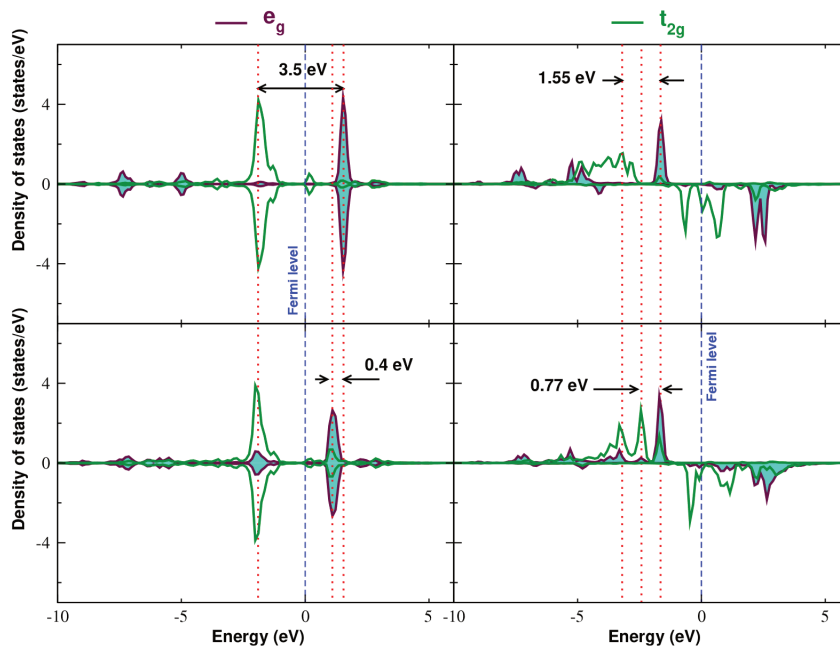
FIGURE 2.4 – LS (left), HS (right) iron d-DOS for the Fe(Phen)$_2$(NCS)$_2$ molecule on Cu(001) surface, H-Fephen (top) and F-Fephen(bottom). The e_g states are shown in brown and filled green and t_{2g} states in green. The red vertical dotted lines show the alignments of states and the reduction of the ligand field. The Fermi energy level is set at zero. Reproduced from [173].

As we can see on the results and as expected, the fluorination leads to a reduction of the ligand field from 3.5 eV to 3.1 eV in the LS state, and 1.55 eV to 0.77 eV in the HS state, linked to shifts of the t_{2g} and e_g towards the d-subshell barycentre. Naturally, this reduction of the octahedral Δ value will stabilize the HS state. As such, it appears that the doping has very perceptible effects on the splitting of the iron spectrum. To demonstrate this, we will use a ligand-field theoretical approach: it consists in computing the effects of the electrostatic potential of the ligands, essentially at the first neighbour level only, on the atomic orbitals of the coordination centre, which was already used with great success to explain the SCO just as we emphasized in the introduction [176]. We neglect all hybridization effects and use point-charge like ligand charges. As such, we assume a +2 charge on the central Iron atom, as we are dealing with a FeII ion, and a spread -2 charge on the neighbouring nitrogen atoms to maintain electronic neutrality. As the t_{2g} and e_g subshells are not rotationally stable, i.e. get intermixed under a rotation, we need to align both DFT and Ligand-field octahedra along the same reference axis in order to have a meaningful comparison of their respective populations. This reference axis is taken to be the z direction of the global supercell, and as such both the DFT DOS and LFT calculations have to be rotated toward this axis. This was done and implemented in both cases and an early version of the VASP code was described in [177]; our newer implementation makes extensive use of the Kabsch algorithm [178] for both the DFT and LFT calculations. Of course, we need to add spin-resolved effects: the simplest way to do so is to

add a Stoner exchange interaction [179] to the model:

$$H^{\sigma,I} = V + \frac{I}{2}(1 - 2\sigma) \; , \tag{2.5}$$

where V is the Ligand-Field potential, I the Stoner parameter and σ is the spin. DFT calculations yielded a value of $I = 3$ eV, whereas the potential is given by the sum of the point-charge like Nitrogen Ligand contributions:

$$\begin{aligned}
V(\mathbf{r}) &= \sum_{i=1}^{6} \frac{q_i}{|\mathbf{r} - \mathbf{R_i}|} \\
&= 4\pi \sum_{i=1}^{6} q_i \sum_{l=0}^{\infty} \sum_{m=-l}^{l} \frac{(-1)^m}{2l+1} Y_m^l(\mathbf{r}) Y_{-m}^l(\mathbf{R_i}) \frac{r_<^l}{r_>^{l+1}} \; ,
\end{aligned} \tag{2.6}$$

where the second line is nothing but the usual Laplace expansion of the Coulomb potential, with the usual $r_>$ and $r_<$ notations for the maximum and minimum between r and R_i. The q_i are the effective product charges of the coordination centre and the ligands, and the $\mathbf{R_i}$ are the vectors linking them obtained from the relaxed DFT structure. This Hamiltonian can be diagonalised in the d-shell (see appendix A), yielding the results of figure 2.5.
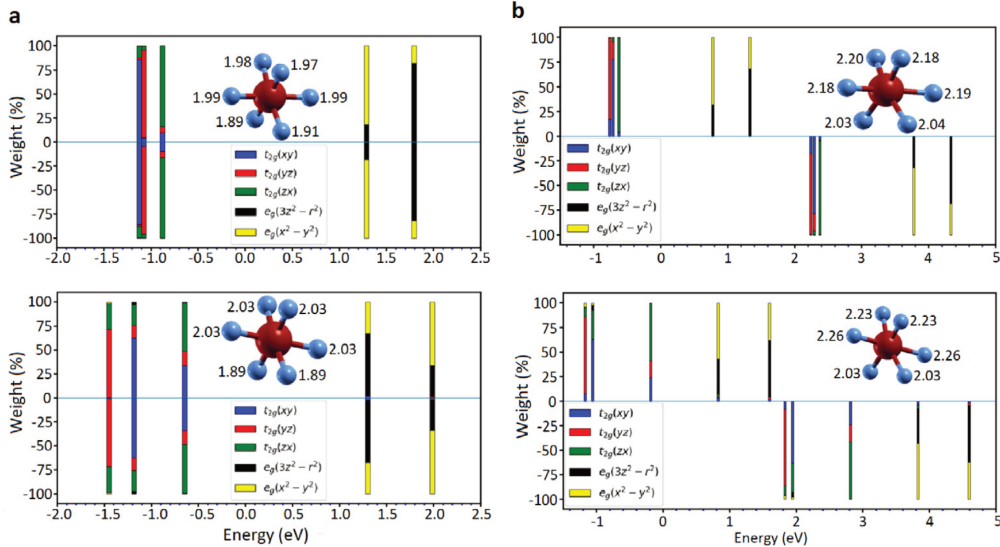
FIGURE 2.5 – Ligand-field splittings using the point-charge model for both the LS (a) and HS (b) state and for the unfluorinated (top plots) and the fluorinated (bottom plots) Fephen. The distorted octahedron obtained from ab initio calculation are shown in the insets (the bond lengths are in Å). The color code shows the different symmetries of the eigenvectors. Reproduced from [173].

As one can clearly see, the model correctly predicts that the ligand field splitting is smaller in the HS state wrt to the LS state, and that it is further weakened by fluorination, although the results are not quantitatively accurate. Besides, the model also correctly predicts the degeneracy lift of the e_g and t_{2g} subshells, but as expected the apparent intermixing of the e_g

and t_{2g} on the DFT calculation is not reproduced as these are linked to additional neglected phenomena such as hybridization.

2.7 Electronic barrier

The aim of this part is to describe the transition barrier between both spin states before and after fluorination. As the Fephen molecule undergoes a thermal SCO at $T_c = 175$ K, a very natural way of doing so would be to carry a molecular dynamics (MD) calculation at a sufficiently high temperature above T_c, and let the system evolve naturally towards the HS state while monitoring the energy (or the other way around at low temperature). However, the existence of local minima on the energy surface greatly restricts the usefulness of such a method as the system could in theory remain trapped in these, and therefore fail to explore the totality of the energy barrier, although the method was used with success in some crystalline systems [180].

A possible solution to fix this issue is to use the so-called Laio-Parrinello metadynamics [181], where a repulsive (usually Gaussian) potential is added to the energy surface at each step of the MD so that the system can escape these local minima. However, there is still an issue: as the magnetization in our system is a discrete, non differentiable quantity of the Cartesian positions, it cannot be a collective variable of the system. As such, there is in principle no way to add a magnetic bias within the metadynamics procedure in order to force a spin flip, and as such the convergence of the SCO barrier is rather slow as the system samples and fills many non-ground spin states during the process.

We will therefore proceed in a different manner: we start by interpolating a set of images between the HS and LS coordinates. We will now use two different methods to sample the barrier: the first one is the well known Nudged Elastic Band (NEB) method [182], which has been extensively used to study transition paths. It consists in first interpolating many possible transition points, often called images, from the initial to the final states and relaxing them with constraints originating from fictitious spring forces between neighboring images, in order to maintain a constant distance between them along the reaction path. The calculations converge when the MEP is found, but this method is difficult to converge and is computationally prohibitive for systems with many atoms per unit cell, we have also used what we called the constrained minimization method (CMM). We fixed the NCS-Fe-NCS angle of each image and relaxed them, therefore approximating the path as the one resulting from these interpolated systems, This method should in principle be a rough approximation to the NEB, as the NEB method is an iterative method ideally converging towards the MEP whereas our method consists in interpolating an approximate path along some chosen order parameter of the transition without any further iteration, while being aware of the fact that there is no gua-

rantee that this is the actual path followed during the transition. Besides, in this way, the CMM method can also be seen as a static approximation to the slow growth method in molecular dynamics [183], which is theoretically known to never yield the exact transition path along the chosen coordinate unless the process is infinitesemal or averaged over an infinite amount of realizations (this is the celebrated Jarzynski inequality [184]). As such, we emphasize that we do not expect the method to yield an accurate transition path, we are only looking for a reasonable estimation of the transition path and barrier for the (meta)stability of the spin states. The computation is done using the NEB method as implemented within VASP.

This is indeed what we can observe in the results shown in figure 2.6, as the NEB method produces a barrier that is quite bigger in the undoped system, and somewhat higher in the doped system, than the CMM. As the NEB method is theoretically optimal, this is certainly a sign of incomplete convergence. However, one can note both system seem to converge towards the same path near the LS state, indicating that the CMM method is quite accurate when one needs to sample the path far from the barrier and that therefore we have a quite optimal result at these points. As such, it appears that the system does indeed follow a progressive opening of the NCS-Fe-NCS angle near the LS state on the transition path. Note that, as expected, the barrier is clearly smaller in the doped molecule (≈ 0.5 eV for the CMM) than in the undoped molecule (≈ 0.65 eV for the CMM), facilitating the reversible transition between the two spin states. Interestingly, interpolation between the two barriers show that a partial fluorination of 50% should yield a degeneracy between the HS and the LS states, assuming that the barrier evolves linearly with the doping, leading to the possibility of tunneling between the two states.
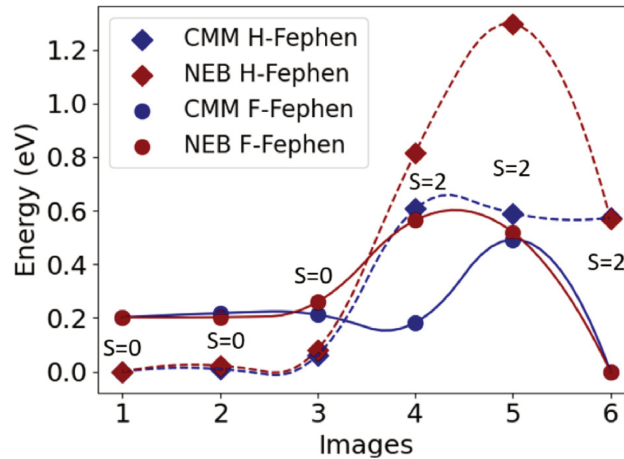
FIGURE 2.6 – HS-LS minimal energy path and transition barrier for the unfluorinated (left) and the fluorinated (right) Fephen molecule adsorbed on Cu(001) surface. The constrained minimization method (see text) are in dark green and the NEB method in dark red. The spin state S of each image is also shown. The continuous curves are quadratic interpolations used as guides to the eye. Reproduced from [173].

Thus, the calculation shows that the high spin state is lower than the low spin state in the fluorinated molecule, meaning that we can keep the molecule in the high spin state even

at low temperatures (we will study the thermodynamical stability of the states in the next part). Hence, a thermal SCO will not be possible, unlike for the pristine molecule. However, the switching should be possible by another external excitation. For example, a reversible STM electrical switching of the fluorinated molecule is in principle possible. The electric field should drive the HS state to the LS state and vice versa at a fixed temperature, like performed experimentally by Miyamachi *et al.*[185, 21] on the undoped molecule. As we saw earlier, irradiation and especially LIESST is also a possibility, but in this case it will be a anomalous HS to LS LIESST that has very interestingly already been observed for SCO molecules on metallic surfaces [186]. However, it is not clear what will be the rate of switching of the fluorinated molecule, and there is *a priori* no way to decide on a lower or higher rate than for the pristine molecule obtained by STM [21] as the excitation pathway is completely different from the usual LIESST phenomenon as it involves an indirect switching thanks to the effects of photo-electrons heralding from the interaction of the substrate with the irradiation light [186]. Hence, the existence of LIESST within the bulk phase of the doped molecule is not a certainty. However, pressure should in this case be a very efficient way to trigger the transition as it naturally stabilizes the LS phase.

2.8   Phonons

The next section will be dedicated to the calculation of intramolecular phonons in the spin crossover molecules as these play a role of paramount importance in the spin transition phenomenon. We will start with a short reminder on the theoretical and numerical aspects of the matter.

2.8.1   Theoretical aspects

Assume a molecular system with N_a atoms of coordinates x_i^α, with $i \leq N_a$ the atomic index and $\alpha = 1, 2, 3$ the Cartesian coordinates, perturbed around the equilibrium of energy E_0 with displacements δ_i^α. One can then Taylor expand the energy of the system:

$$E = E_0 + \sum_{k \geq 1, \{\alpha_k\}, \{i_k\}} \frac{1}{k!} \Phi_{i_1,\dots,i_k}^{\alpha_1,\dots,\alpha_k} \delta_{i_1}^{\alpha_1} \dots \delta_{i_k}^{\alpha_k}, \tag{2.7}$$

where the $\{\alpha_k\}$, $\{i_k\}$ stand for the set of all α_p and i_p up to $p = k$. The $\Phi_{i_1,\dots,i_k}^{\alpha_1,\dots,\alpha_k}$ are the so-called interatomic force constants of order k (IFC_k). It should be noted that since we are working near the equilibrium, the order 1 IFC_1 are vanishing as they correspond to the forces acting over the atom at the equilibrium. The force acting on atom i along direction α can then be

derived by differentiating with respect to these coordinates:

$$F_i^\alpha = - \sum_{k \geq 2} \frac{1}{(k-1)!} \Phi_{i_1,\dots,i_k}^{\alpha_1,\dots,\alpha_k} \delta_{i_1}^{\alpha_1} \dots \delta_{i_k}^{\alpha_k}. \tag{2.8}$$

Several important physical quantities can be derived from the set of the IFC, including the so-called dynamical matrix from the IFC_2:

$$D_{i,j}^{\alpha,\beta} = \frac{\Phi_{i,j}^{\alpha,\beta}}{\sqrt{M_i M_j}}, \tag{2.9}$$

where M_i is the mass of atom i. Note that in general, the dynamical matrix is defined as the Fourier transform of the IFC_2, but we will restrict ourselves to the gamma point in our calculations given the size of our systems. Diagonalizing this matrix yields the phonon spectrum (using Einstein's summation convention):

$$D_{i,j}^{\alpha,\beta} X_{\alpha,n}^i = (\omega_n)^2 X_{\beta,n}^j. \tag{2.10}$$

The $X_{\alpha,n}^i$ are the so-called phonon modes associated to the phonon frequencies ω_n. Note that the IFC_2 are real symmetric (and therefore hermitian) by the symmetry of second derivatives, and therefore so is the dynamical matrix. As such, the spectrum is real and the eigenvectors are orthonormal. Note that the eigenvalues can be negative even though they are defined to be the squares of the phonon frequencies, which are then purely imaginary. The phonon plane wave dispersion, evolving as $\exp(i\omega_n t)$, therefore becomes hyperbolic and as such the associated elongation direction is unstable: we then have a possible phase transition, and the associated modes are usually referred to as soft modes. The computation of phonon modes therefore is a quite useful tool in the study of phase stability and transition states.

From this spectrum, one can extract important thermodynamical quantities such as:

— trivially, the phonon density of states (νDOS):

$$\rho(\omega) = \sum_n \delta(\omega - \omega_n). \tag{2.11}$$

— the vibrational enthalpy H_ν at temperature T, which in the very common harmonic approximation is:

$$H_\nu = \hbar \sum_n \omega_n \left(\frac{1}{2} + f_{BE}(\hbar\omega_n, T) \right) = ZPE + \hbar \sum_n \omega_n f_{BE}(\hbar\omega_n, T), \tag{2.12}$$

where f_{BE} is the Bose-Einstein distribution and ZPE is the so-called zero-point vibrational energy.

— the vibrational free energy F_ν (also in the harmonic approximation):

$$F_\nu = ZPE + k_B T \sum_n log \left(1 - \exp \left(\frac{-\hbar \omega_n}{k_B T} \right) \right). \tag{2.13}$$

— the vibrational entropy $S_\nu = (H_\nu - F_\nu)/T$.

From these quantities, one can compute the Gibbs free energy G of the system:

$$G = E_0 + PV + F_\nu - TS_r = H_{el} + F_\nu - TS_r, \tag{2.14}$$

where E_0 is the previously defined equilibrium energy, P and V are the pressure and volume of the system, H_{el} the electronic enthalpy defined as the sum of the two previous terms, and S_r are the non-vibrational contributions to the entropy. They are composed of the magnetic entropy defined as $S_{mag} = R \log(2S + 1)$, with R the ideal gas constant and S the total spin of the system, and the rotational entropy. We neglect the translational entropy, along with the rotational and translational enthalpy because these are identical in both spin states so that they do not contribute to the free energy balance, along with all thermal effects on E_0 as these are vanishingly small compared to the previously introduced contributions.

By definition, the transition between the HS and LS states at the transition temperature T_c is linked to the vanishing of the Gibbs free energy difference between the states:

$$
\begin{aligned}
& G_{HS}(T_c) = G_{LS}(T_c) \\
\Longleftrightarrow \; & [E_0 + PV + F_\nu]_{HS}(T_c) - T_c S_{r,HS} = [E_0 + PV + F_\nu]_{LS}(T_c) - T_c S_{r,LS} \\
\Longleftrightarrow \; & T_c = \frac{[E_{0,HS} + (PV)_{HS} + F_{\nu,HS} - E_{0,LS} + (PV)_{LS} + F_{\nu,LS}](T_c)}{S_{r,HS} - S_{r,LS}},
\end{aligned}
\tag{2.15}
$$

where the notation $[A](T_c)$ indicates that all the terms A between the brackets depend on temperature and should therefore be evaluated at the temperature of transition T_c. Then, equation (2.15) yields a theoretical way to compute the transition temperature by solving for the value of T_c. This is pretty complex in practice as it requires knowing both the electronic enthalpy and the vibrational free energy at all temperatures, which is linked to several issues. First, the electronic enthalpy is indirectly a function of temperature through the thermal dilatation effects on the volume of the unit cell, and therefore on the internal energy E_0 and the PV term. As such, an accurate knowledge of the evolution of the volume with temperature is required, using for example Parrinello-Rahman or Wentzcovitch dynamics [187, 188] if one is to compute the free energy in a crystalline SCO system.

For isolated molecules in a supercell, one can safely neglect both these thermal dilatation effects and the PV difference between the HS and LS states, leading to the following equation:

$$T_c = \frac{\Delta E_{0,HS-LS} + \Delta F_{\nu,HS-LS}(T_c)}{S_{r,HS} - S_{r,LS}}, \tag{2.16}$$

where the ΔE term is the adiabatic energy difference, which is independent of the temperature and can therefore be evaluated once at 0K with a typical DFT calculation.

Second, the phonon eigenvalues depend both on the volume of the unit cell and on temperature, i.e. $\omega_n = \omega_n(V, T)$. As such, an accurate determination of the vibrational free energy should involve the computation of the spectrum at all temperatures. In practice, several approximations can be made to simplify the problem:

— in the harmonic approximation (HA) [189], the dependence of ω on temperature is completely neglected and the only temperature effects come from the Bose-Einstein statistics. This is formally exact when the IFC_k are all neglected except for the second order, and one can easily see that the system is then formally equivalent to a set of $3N_a$ independent harmonic oscillators. The spectrum is then evaluated at some reference volume V_0 (usually the $T = 0$ K volume in DFT) and then kept constant for all calculations: $\omega(V, T) = \omega_{HA}(V_0)$. This is a surprisingly effective approximation, and it allows for an easy analytic evaluation of important quantities such as the previously introduced vibrational free energy. However, it obviously can't reproduce thermal dilatation effects, which therefore require a more refined approach.

— in the isothermal quasi-harmonic approximation (QHA) [190], the thermal dependence of the phonon eigenvalues is entirely contained in the volume variations: $\omega(V, T) = \omega_{QHA}(V(T))$. Informally, this can be seen as an "harmonic approximation for each volume", and all the formulas derived in the harmonic approximation remain valid as the only correction required is to formally substitute the invariant spectrum with the QHA eigenvalues: $\forall F, F(\{\omega_{HA}(V_0)\}) \rightarrow F(\{\omega_{QHA}(V(T))\})$. In particular, this means that anharmonic effects are not properly taken into account within this approximation and the IFC_k expansion is still technically truncated at the second order, but with an effective set of volume-dependent $IFC_2^{eff}(V(T))$. However, this is still a very successful approximation for most usual phonon derived quantities, but it naturally can't account for isochoric thermal effects.

— the proper treatment of isochoric effects requires explicitly taking into account anharmonic terms [191, 192], usually up to the third or fourth order in practice. This leads to the formal need to modify all the statiscally-derived physical quantities such as the free energy, although in practice the harmonic expressions are commonly kept as the corrections are minimal. These higher order parameters can be of crucial importance for some calculations, as they can be shown to be directly related to important quantities such as the Grüneisen parameters, the thermal expansion coefficient or the stress tensor (note that these could also be computed from the QHA, but the results will be less accurate).

In practice, the methods to carry an actual calculation of IFC_k from an ab initio approach are manifold. For example, for DFT, the two major such approaches at the harmonic level are the finite difference method ([193, 194]) and the density functional perturbation theory

(DFPT) method ([195, 196]). The finite difference method relies on obtaining the IFC_k by moving atoms and computing the related change of energy with DFT calculations. The IFC_k can then be computed from these changes as the k-order derivatives of the energy with respect to displacements. This is obviously a very brute force method and it requires a huge number of calculations, up to $(3N_a)^p$ at order p, although there are several theorems and symmetries that allow to significantly reduce this number (but the computational cost is still huge). However, several results have shown that it leads to very satisfactory results, even when extended for strong anharmonic results ([197, 198]), and as such is still very commonly used. DFPT, on the other hand, relies on the use of the perturbative expansion of DFT (the so-called Sternheimer's equation [199]) to compute the perturbed wavefunctions and energies with respect to the ionic displacements, and then deduce the IFC_k in a similar way than with the finite difference method. DFPT is naturally less computationally heavy than finite differences (especially with the existence of the famed 2n+1 theorem), but its perturbative nature leads to issues for strong anharmonicities at higher orders ([200, 201]). Therefore, a significant number of theoretical methods have been developed in the last twenty years in order to explicitly tackle the particular issue of these strongly anharmonical systems without having to rely on costly finite difference methods (see reference [202] for the most notable examples.)

A very common way to compute the spectrum at some temperature T is to carry an AIMD calculation, and then compute the autocorrelation function of the atomic velocities (VACF) calculated during the AIMD simulation:

$$g_v(\tau) = \int v(t)v(t+\tau)\mathrm{d}t \ .\tag{2.17}$$

One can show [203] that the phonon density of states is the Fourier transform of the normalized VACF:

$$\rho(\omega) = \int e^{i\omega t}\frac{g_v(t)}{g_v(0)}\mathrm{d}t.\tag{2.18}$$

In practice, this naturally requires a sufficiently long sampling time in order to properly evaluate both the convolution function and the resulting density of states. Note that a very similar result can be derived from the position autocorrelation function. [204]

2.8.2 Results

A short reminder on the harmonic approximation

We will start by giving the results for the harmonic approximation. The calculation was done within the VASP code, using the finite differences method with a two points centered stencil. To obtain accurate forces values, the energy was converged to $10^{-6}eV$. As such, given the strongly increased computationnal costs associated with the more stringent convergence criterion, we could not compute the spectrum for the molecule adsorbed on the surface and

we will restrict ourselves to the free molecule. We will begin with the results for the pristine FePhen molecule, starting with the correlation between the HS and LS states as seen in figure 2.7.

FIGURE 2.7 – Correlation between the phonon frequencies in the LS and HS states, for the undoped molecule without a surface.

As one can see, our results are in complete accordance with the already available results of Lebegue *et al.* [118]. One can clearly observe the characteristical frequency changes between the LS and HS molecules, with a softening of the N-C-S stretching modes around 2100 cm^{-1} of roughly 45 cm^{-1} and of the Fe-Ligand stretching around 100-400 cm^{-1} of 60 cm^{-1} on average. This was to be expected as these bond are stretched during the LS to HS transition, which naturally softens the oscillation frequency.

The thermodynamical calculations within the harmonic approximation at the experimental critical temperature of T_c yield a vibrational entropy difference between the HS and LS states of ΔS_{vib} = 29.0 J/mol/K and a vibrational entropy difference of ΔH_{vib} = -7.3 kJ/mol, in relative accordance with the previously obtained results. Note that the total entropy includes the magnetic entropy $\Delta S_{mag} = R \log(5)$ = 13.4 J/mol/K, along with the rotationnal entropy of ΔS_{rot} = 0.6 J/mol/K, which leads to a total value of ΔS = 43.0 J/mol/K. The total enthalpy includes an electronic contribution of $\Delta H_{el} = 14.5$ kJ/mol, therefore amounting to ΔH = 7.2 kJ/mol, which is surprisingly close to the experimental value of 9 kJ/mol. Interestingly, evaluating the transition temperature using equation 2.16 yields a value of T_c = 167 K, in remarkable accordance with the experimental value although this is completely fortuitous as the extensive litterature on the topic shows that this value is extremely sensitive to numerical errors and approximations, especially since soft modes have the strongest impact on the entropy and these are often noticeably anharmonic and as such can't be systematically evaluated with a decent accuracy [205].

The thermal variation of the vibrational entropy, vibrational enthalpy and total free energy

differences are given in figures 2.8 and 2.9.
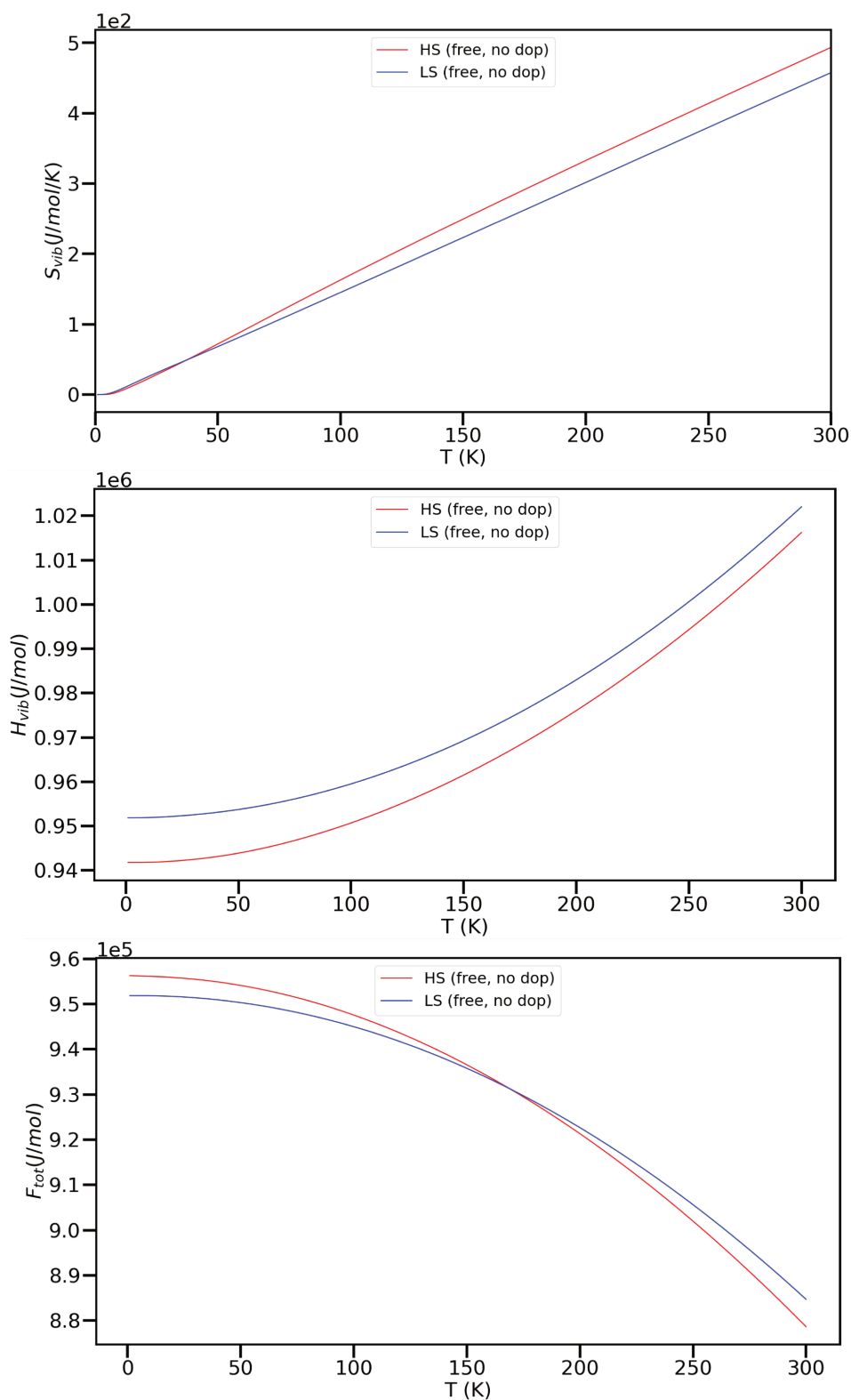
FIGURE 2.8 – Thermal evolution of the vibrational entropy S_{vib}, vibrational enthalpy H_{vib} and total free energy $F_{tot} = H_{vib} - TS_{vib} + F_{el} + F_r$ for the undoped molecule without the surface in both spin states. Note that F_{tot} is arbitrarily shifted by the value of F_{el} in the LS state, it being a constant, so that $F_{tot} = F_{vib}$ in the LS state.

FIGURE 2.9 – Difference between the values for the HS and LS states of the vibrational entropy ΔS_{vib}, vibrational enthalpy ΔH_{vib} and total free energy ΔF_{tot} for figure 2.8

Therefore, as one can see, the vibrations stabilize the HS state with respect to the LS state, with a stronger vibrationnal entropy (except at very low temperatures) and a smaller vibrationnal enthalpy in the HS state. This therefore drives the free energy of the HS state down as compared to the LS state, which eventually leads to the sign switching of the free energy difference at the critical temperature and therefore to the spin transition phenomenon. Based on these quantities, one can then use the Slichter-Drickamer model to compute the HS fraction, the result being given in figure 2.10. One can clearly see how the cooperativity modifies the

general shape of the spin transition phenomenon, as it becomes more and more abrupt with the appearance of an hysteresis above the critical value of the cooperativity. Using the literature value of Γ = 3.0 kJ/mol [206, 207], we have also computed the theoretical evolution of the HS fraction and compared it to available experimental results [208] in figure 2.11, showing a good agreement.
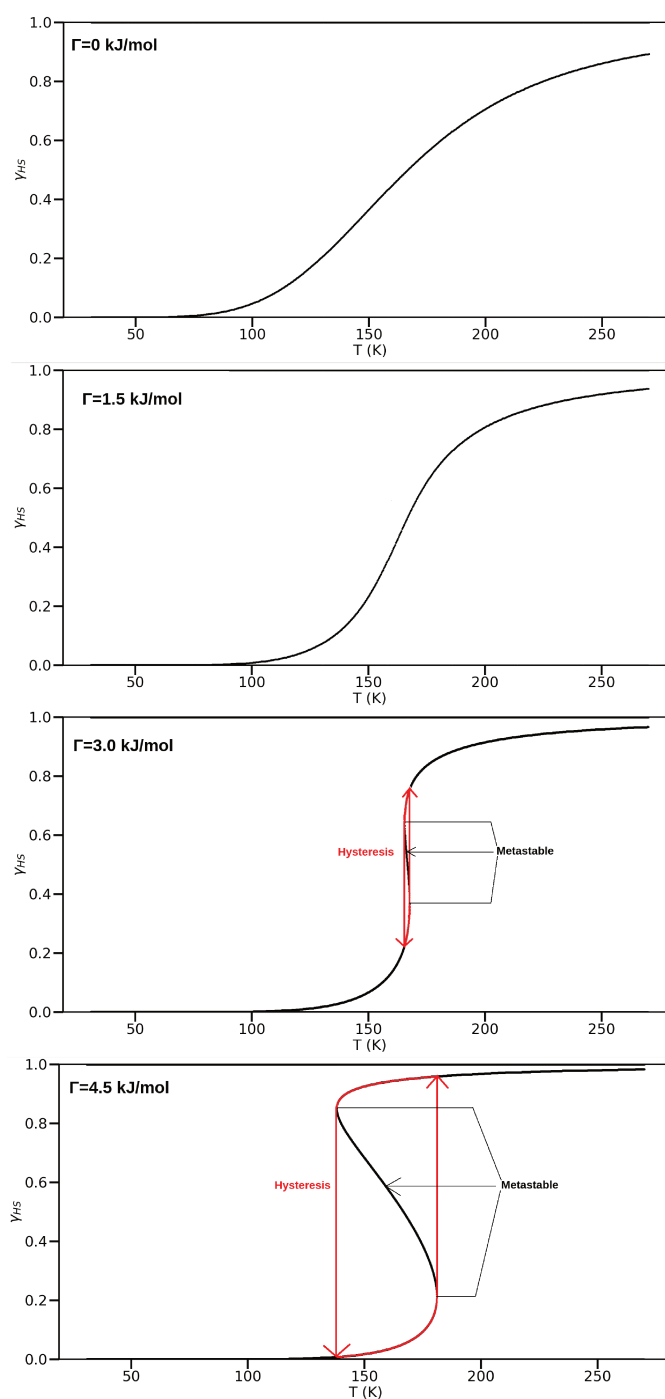
FIGURE 2.10 – Calculated thermal evolution of the HS fraction γ_{HS} for several values of the cooperativity parameter. The critical cooperativity is Γ_c = 2.8 kJ/mol using our computed value of T_c = 167 K for the critical temperature.
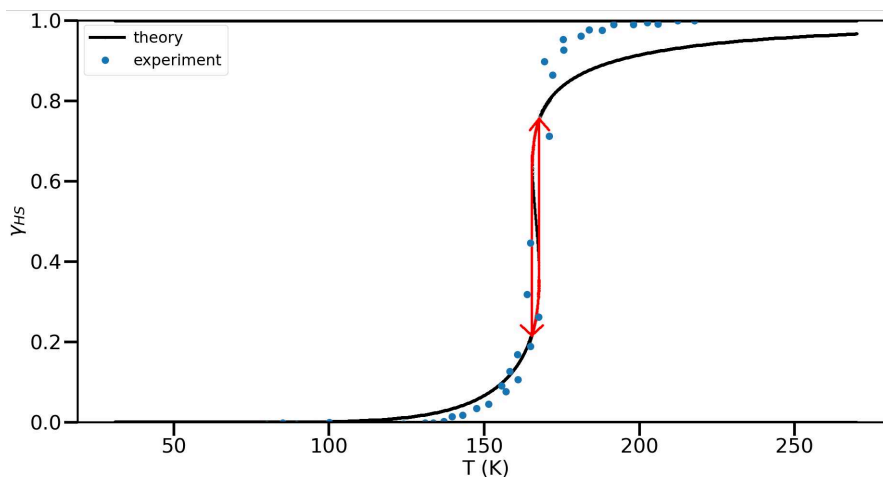
Figure 2.11 – Calculated thermal evolution of the HS fraction γ_{HS} for the literature value of the cooperativity parameter Γ_c = 3.0 kJ/mol [206, 207], compared with the experimental results [208] disregarding the $\approx$ 20 % remnant of HS states at low temperatures and shifting the experimental transition at the computed value of 167 K.

We will now proceed with a comparison to the doped FePhen molecule. As before, we first give the results of the correlation between the HS and LS states, along with a direct comparison to the previous case on the figure 2.12.
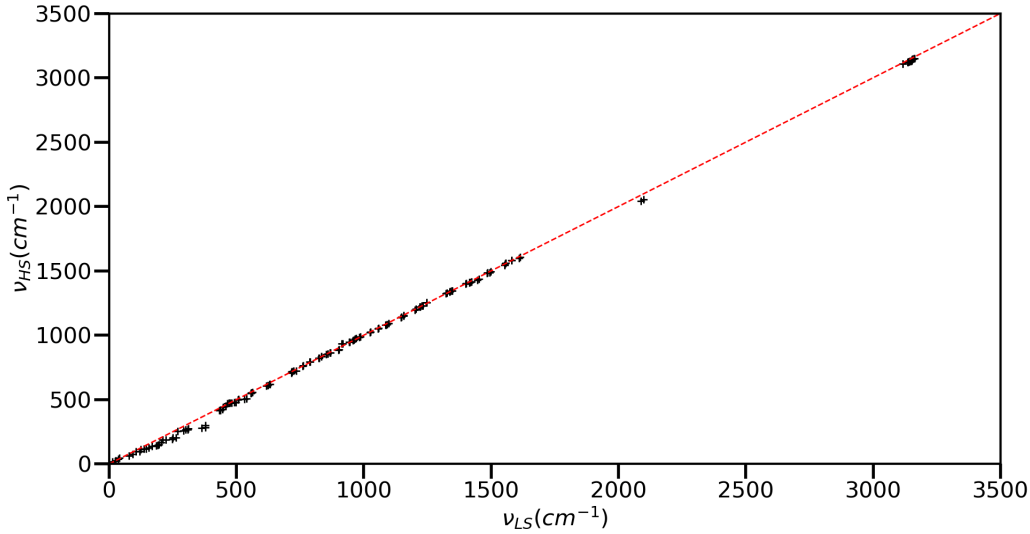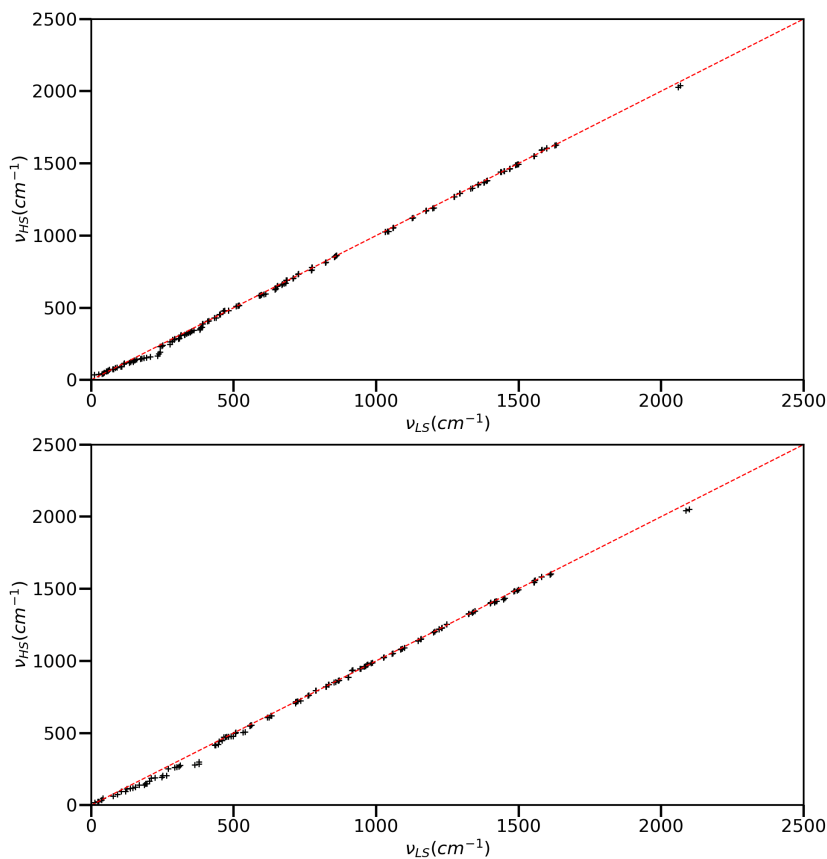

Figure 2.12 – Correlation between the phonon frequencies in the LS and HS states on the top for the doped molecule without a surface, along with the correlation for the undoped molecule restricted over the relevant range on the bottom

Now, there are several regions of interest. First of all, the calculation shows an absence of the 3000-3100 cm^{-1} frequency region on the plot that corresponds to the C-H bond stretching in an aromatic cycle, which is naturally missing in the doped molecule. As such, we decided to restrict figure 2.12 to frequencies below 2500 cm^{-1}. The N-C-S stretching frequencies around 2100 cm^{-1} are visibly not affected by the doping procedure. The first major difference comes in the region around 1300-1500 cm^{-1}, where we note more modes for the doped molecule than for the undoped molecule. These frequencies correspond to C-F stretching modes, with the higher frequencies being associated with in-phase processes. We also note the disappearance of modes in the 1000 cm^{-1} region after doping, and these are associated with bending in C-H bonds. These are replaced with the appearance of C-F in-phase bending frequencies around 800 cm^{-1}, and regular bending frequencies in the 300 cm^{-1} [209, 210]. Once again, the modes that are the most affected by the spin crossover are the N-C-S and Fe-N stretching, although visibly less than for the undoped molecule with a shift of 30 cm^{-1} for the N-C-S modes and 40 cm^{-1} for the Fe-Ligand modes on average, the frequencies being already quenched by the inherent stretching of the bond linked to the doping. At the undoped critical temperature of 175 K, the doped molecule shows a vibrational entropy difference of ΔS_{vib} = 7.1 J/mol/K and a vibrational enthalpy difference of ΔH_{vib} = -4.7 kJ/mol. Adding the other contributions yields a total entropy difference of ΔS_{tot} = 20.5 J/mol/K and a total enthalpy difference of ΔH_{tot} = -29.2 kJ/mol. Just as before, we will also plot the evolution of these thermodynamical quantities in the figures 2.13 and 2.14

In these figures, we can see that the free energy difference never crosses the zero value and is in fact always decreasing, and as such the HS state always remains the more stable phase at all temperatures as one could have expected since thermal effects should favorize the HS as we have emphasized earlier. In these conditions, solving the Slichter-Drickamer calculation yields a trivial $\gamma_{HS} = 1$ line so we will not reproduce the results here. Interestingly, however, one can note that the vibrational entropy is stronger in the LS state than in the HS state on a wider range than for the undoped molecule, up to roughly 120 K; indicating that it stabilizes the low spin state which may appear a bit counterintuitive, although at higher temperatures the HS state ends up being the more stabilized. Besides, the massive difference in enthalpy between these states and the magnetic entropy prevent any switching of the spin state, in accordance with the idea that the SCO is an entropy-driven phenomenon.
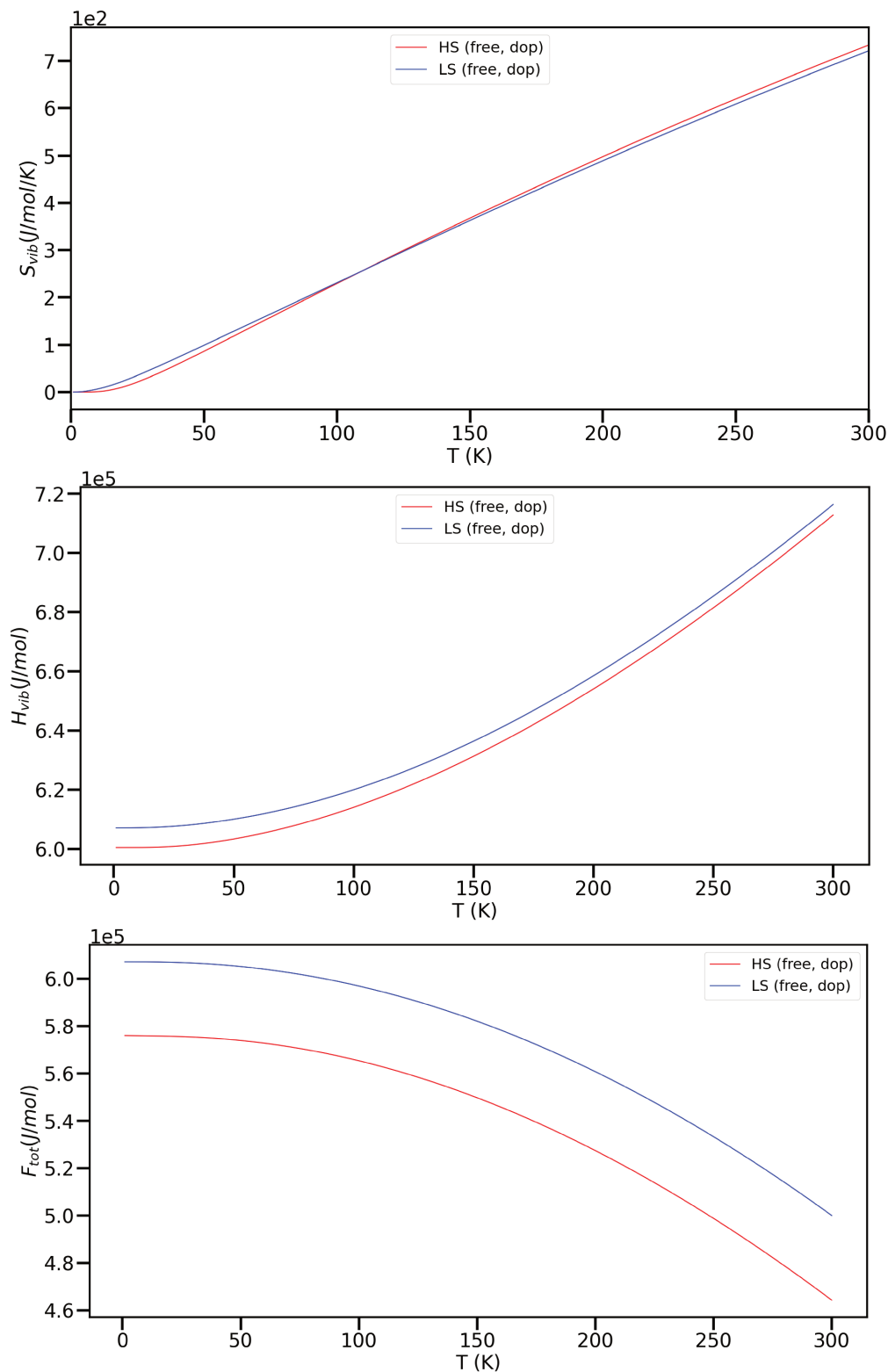
FIGURE 2.13 – Thermal evolution of the vibrational entropy S_{vib}, vibrational enthalpy H_{vib} and total free energy $F_{tot} = H_{vib} - TS_{vib} + F_{el} + F_r$ for the doped molecule without the surface in both spin states.
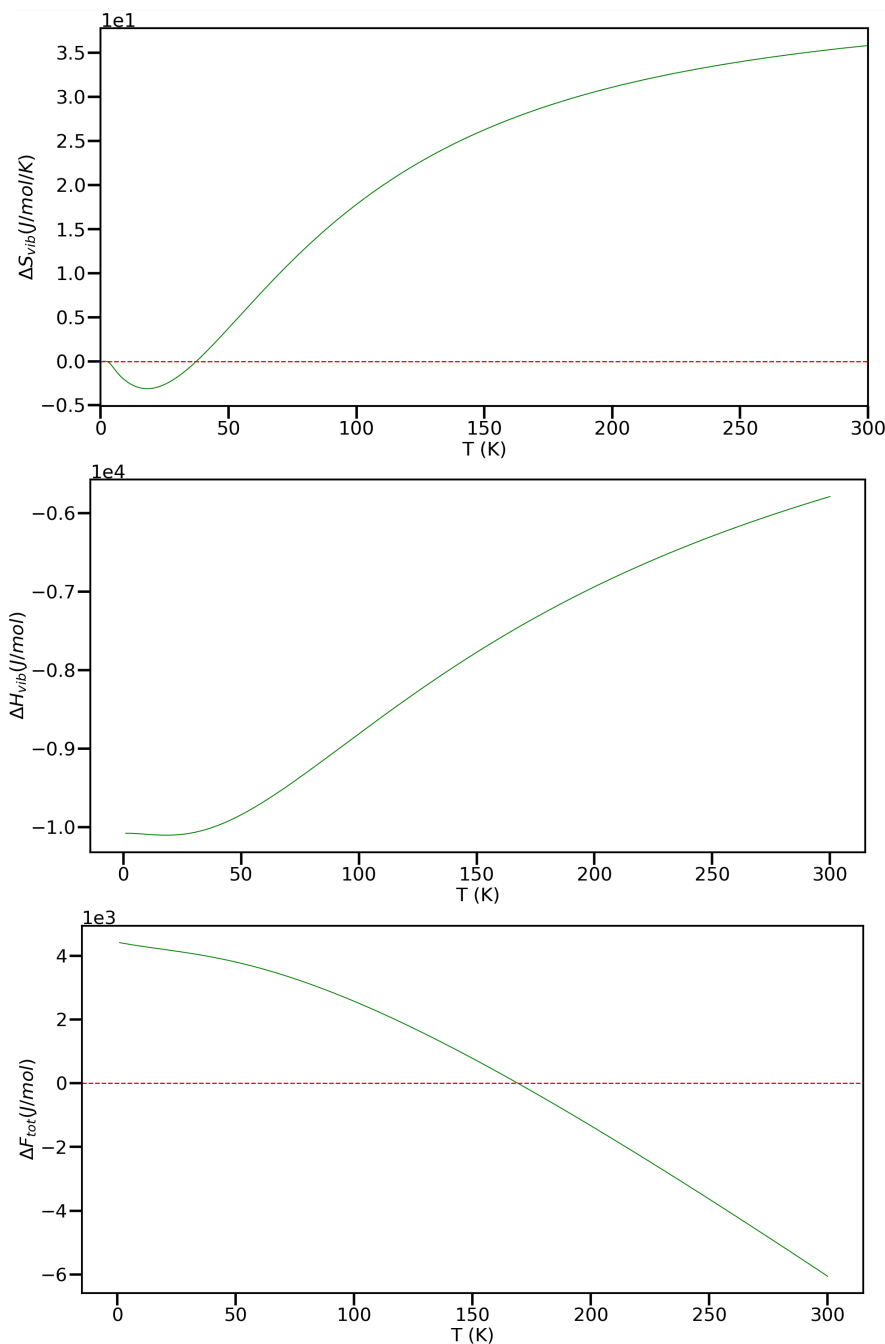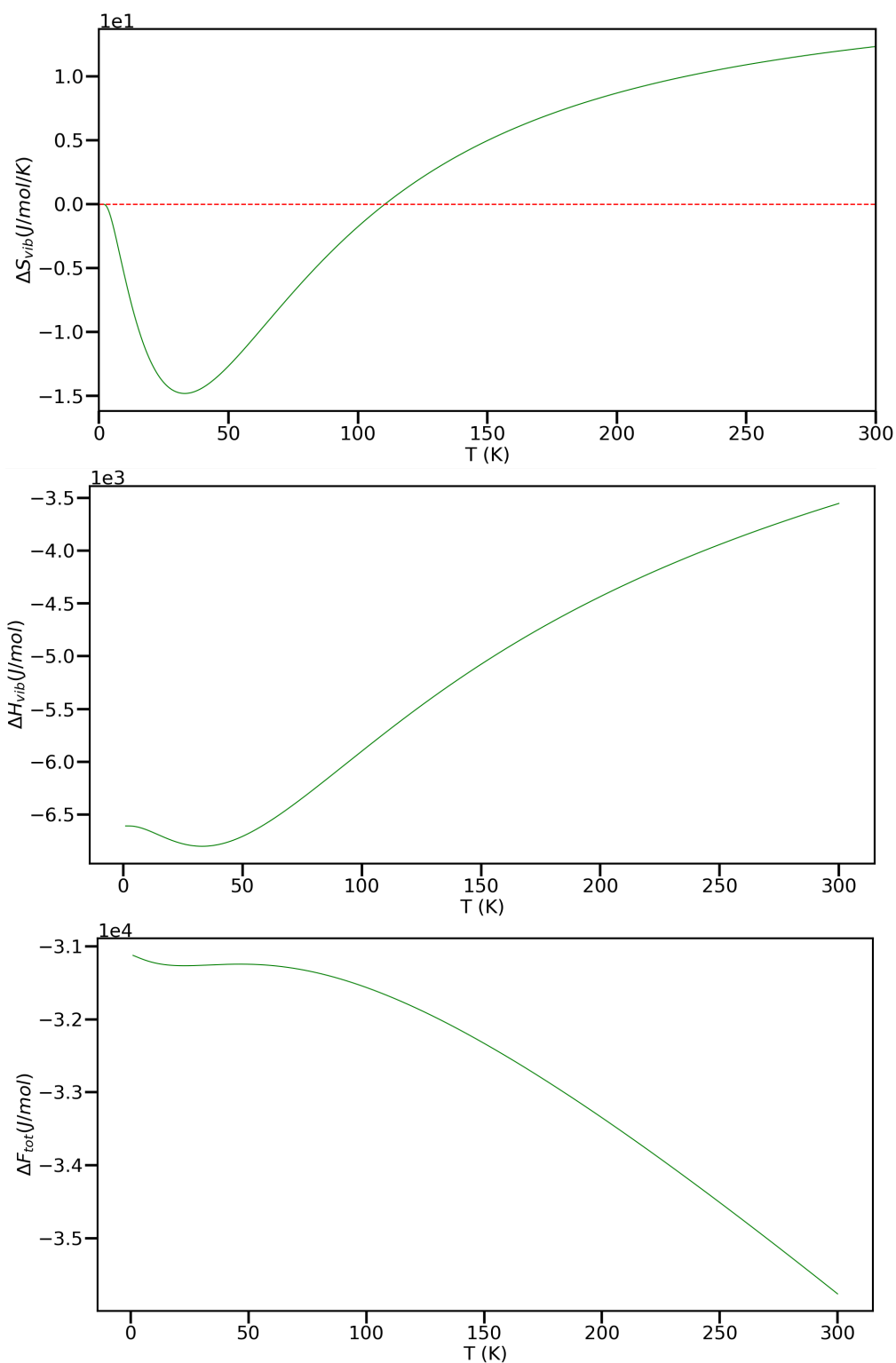
FIGURE 2.14 – Difference between the values for the HS and LS states of the vibrational entropy ΔS_{vib}, vibrational enthalpy ΔH_{vib} and total free energy ΔF_{tot} for figure 2.13 .

Going beyond the harmonic approximation

As we have emphasized earlier, the harmonic approximation is sufficiently accurate for many purposes but fails at properly reproducing temperature related effects, especially near strongly unharmonic points such as a phase transition. As such, the use of post-harmonic approximations for phonon frequencies could provide fruitful results about the physics of the spin-crossover phenomenon, especially given the fact that to the extent of our knowledge such calculations have never been carried for intramolecular phonon modes. In this part, we are going to give some results about the simulation of phonons beyond the harmonic approximation, using molecular dynamics simulations of the free FePhen system at several temperatures. This is done without the substrate as the associated increase in numerical cost proved to be prohibitive because of the large amount of simulation points required to compute the Fourier transform with a sufficient accuracy, even in the case where the surface atoms are constrained not to move. The MD calculations are done using an Andersen thermostat [211] with a time step of 0.1 fs along with a collisional probability of $0.02\,\mathrm{fs}^{-1}$, for a total simulation time of 1 ps. The first 1000 steps are not taken into account for the calculation of the Fourier transform to allow for a sufficient thermalization of the system because of the inherent probabilistic nature of the thermostat. Still, convergence was hard to achieve as we faced several memory related issues that prevented us from carrying the calculation for the doped molecule, and as such the following part will be restricted to the undoped molecule. Note that we have monitored the magnetization during the MD to guarantee that both systems remain in their respective spin states.

We will start with the densities of state. We have computed the densities of state at 100 K, 200 K and 300 K; which we are reproducing in figure 2.15, which shows the temperature evolution of the spectrum within the HS ans LS states. As one can see, the densities correctly reproduce most of the spectrum, with a clearly apparent fingerprint region below $1500\mathrm{cm}^{-1}$ and a very intense C-H stretching peak at $3100\mathrm{cm}^{-1}$. However, we note the very noticeable exception of the N-C-S stretching frequencies around $2100\mathrm{cm}^{-1}$ that is barely apparent, whereas it is usually a very strong signal in experimental spectra [212]. This is quite inconvenient as these are some of the driving frequencies behind the spin-crossover phenomenon, and we could not explain such a discrepancy with respect to the expected result, although these frequencies contribute much less to the total energy balance than the clearly apparent Fe-Ligand stretching modes around $100 - 400\ \mathrm{cm}^{-1}$. Besides, we do not observe any striking evolution of the frequencies with respect to temperature.

Naturally, one can integrate over these densities of states to compute the evolution of thermodynamical quantites such as the free energy with temperature, which leads to the values in table 2.4:
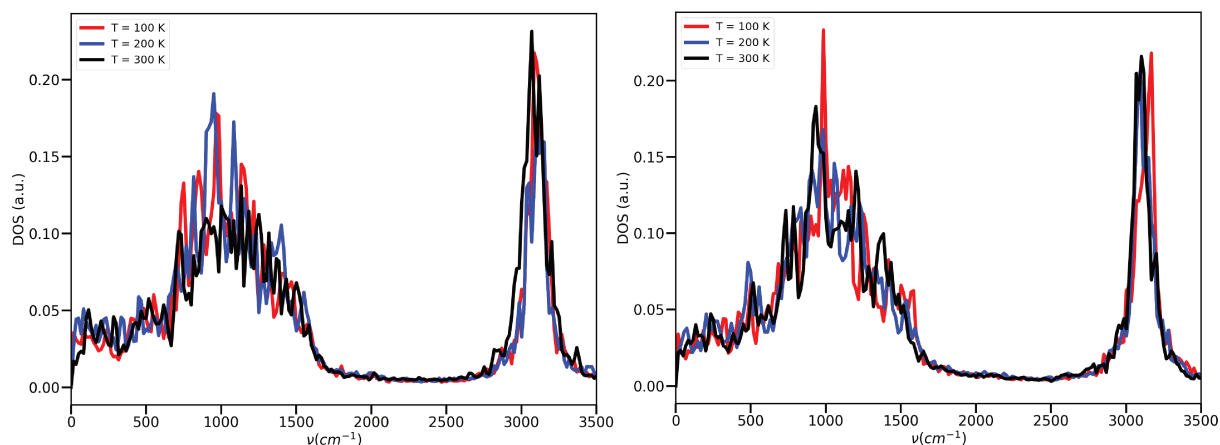
FIGURE 2.15 – Comparison of the phonon densities of states in the FePhen molecule at 100 K, 200 K and 300 K in the HS (left) and the LS state (right)

	HS			LS			Δ		
	100 K	200 K	300 K	100 K	200 K	300 K	100 K	200 K	300 K
S_{vib} (J/mol/K)	50.1	133.3	181.2	41.9	111.5	184.3	8.2	21.8	-3.1
H_{vib} (kJ/mol)	1422.6	1368.5	1550.9	1416.6	1399.1	1443.3	6.0	-30.6	107.6
F_{vib} (kJ/mol)	1417.6	1341.8	1496.5	1412.4	1376.8	1388.0	5.2	-35.0	-108.5
F_{tot} (kJ/mol)	1430.7	1353.5	1506.9	1412.4	1376.8	1388.0	18.3	-23.3	118.9
$S_{vib,HA}$ (J/mol/K)	163.1	332.7	493.5	145.3	301.6	457.7	17.8	31.1	35.8
$H_{vib,HA}$ (kJ/mol)	950.7	976.1	1016.2	959.5	983.0	1022.0	-8.8	-6.9	-5.8
$F_{vib,HA}$ (kJ/mol)	934.4	909.6	868.2	945.0	922.7	884.7	-10.6	-13.1	-16.5
$F_{tot,HA}$ (kJ/mol)	947.5	921.2	878.5	945.0	922.7	884.7	2.5	-1.5	-6.2

TABLE 2.4 – Evolution of various thermodynamical quantities with respect to the temperature in the undoped FePhen molecule, along with their corresponding value in the harmonic approximation. As before, the total free energy values are shifted by the value of the electronic free energy in the LS state.

We can note that there is a massive discrepancy between the values obtained within the harmonic approximation, and the values obtained from the Fourier transform of the VACF. Most notably, the vibrational entropy is severely underestimated with the VACF as compared to the harmonic calculation by a factor $\approx 2 - 4$ depending on the temperature. Besides, the vibrational enthalpy is overestimated by a factor ≈ 1.5. This leads to a severely overestimated energy difference between the HS and LS states, although we do observe a crossover at an interpolated temperature of 144 K, which is still in decent agreement with our previous results all things considered. However, it seems that the HS state at 300 K is massively destabilized, so that another spurious inversion of the HS and LS stability is observed between the HS and LS state. This could be ascribed to insufficient sampling time for the VACF although one should note that the Andersen thermostat leads to a spurious decorrelation of the velocities because

of its stochastic nature [213], and as such the VACF collapses much faster with time than in reality so that the sampling time should in principle not be the main culprit. Therefore, other numerical phenomena might also be at play, which could also explain the quasi-total extinction of the N-C-S stretching frequency on the spectrum, and hence this issue is still being investigated.

2.9 Conclusion

In this first part, we have studied some energetical aspects of the spin-crossover phenomenon. More precisely, we first showed that the substitution of hydrogen by fluorine in the spin crossover Fephen molecule induces a profound transformation of its electronic structure, leading to the inversion of the magnetic state for the free and adsorbed molecule on a Cu(001) surface. This was correlated to a noticeable modification of the bond lengths and angles between the ligands and the central iron atom, though the overall geometry remains unaffected. Through the use of Bader analysis, we showed that a significant amount of electronic redistribution takes place after doping, leading to a modification of the electronic charge on the nitrogen octahedral cage which stretches the ligand-metal bond. This can be seen in the density of states, with a strong reduction of the $e_g - t_{2g}$ ligand-field energy splitting, especially in the HS state. One can also note a reduction of the transition barrier between the HS and LS states after doping, although our results are still pretty crude (especially the NEB method which is extremely hard to converge). We have also carried an harmonic calculation of the phonon spectrum within these molecules using a (two-points centered) finite-difference method. We have therefore showed that the main frequency difference betwen the HS and LS states lie in the N-C-S and Fe-Ligand stretching modes for both the undoped and doped molecule, as one could have expected given the fact that these bonds are the most affected by the spin-crossover phenomenon, in accordance with earlier calculations [118]. Using these values, we carried a free-energy study exhibiting a transition in the undoped molecule at a surprisingly accurate temperature of 167 K as compared to the experimental value of 175 K, although this in entirely fortuitous given the fact that previous calculations using very similar methods have led to highly inaccurate values of the transition temperature as the main driving force behind these errors is the value of the vibrational entropy which is very strongly dependent on low frequency modes, that are hard to compute properly as they tend to be strongly anharmonic. The doped molecule, on the other hand, does not exhibit any spin transition as the HS state always remains more stable than the LS state. These frequencies have also been used in a computation of the evolution of the HS fraction with respect to the temparture in the undoped molecule using the Slichter-Drickamer model, in decent agreement with experimental results. Our preliminary results on post-harmonic simulations based on molecular dynamics are sadly highly inconclusive and are at this time still being further developed, although we do observe

a free energy crossing at a temperature of 144 K in relative accordance with the experimental result.

Chapitre 3

Simulation of X-ray Absorption Spectroscopy in Spin-crossover systems

Note: The following Thesis Chapter, along with appendices B and C, are directly adapted from a paper that was published within Physical Review B. As per official guidelines of the American Physical Society, the bibliographical citation can be found in [214]. Statement: Copyright © 2024 by American Physical Society. All rights reserved.

3.1 Introduction

X-ray absorption spectroscopy (XAS) and x-ray magnetic circular dichroism (XMCD) are two of the most commonly used techniques to study spin crossover molecules. Indeed, they are based on the coupling between the angular momentum of an incident photon beam and the magnetic momentum of the Iron electrons within the HS and LS states, which therefore show distinctive spectra owing to their repective magnetic properties [215, 216, 79, 217, 21]. Naturally, these spectra have been measured and widely used for the FePhen molecule, for example by Miyamachi *et al.* during their studies of the Fephen system both in the gas phase and adsorbed on a Cu(100) surface. Fundamentally, the HS to LS transition in Fe(II) complexes is associated to the spin transition $(t_{2g})^{3\uparrow}(e_g)^{2\uparrow}(t_{2g})^{1\downarrow} \rightarrow (t_{2g})^{3\uparrow}(t_{2g})^{3\downarrow}(e_g)^0$ (see Ref. [173]), and it is therefore interesting to compute the LS and HS XAS $L_{2,3}$ edges from first principles and compare them directly to experimental results to validate this spin transition. To this end, we calculated the x-ray absorption spectra and XMCD of the Fephen molecule both on the gas phase and adsorbed on a Cu(100) surface in the electric dipole approximation and compared our findings to the aforementioned experimental results [21].

After a short theoretical introduction, we will first show that the distortion within the Iron octahedron leads to a dependence of the XMCD spectra on the direction of the incident circularly polarized x-ray beam. In addition, we have also computed the XMCD for different

magnetization directions in order to exhibit the anisotropy of the orbital magnetic moment. We will also show that the calculation without static core hole effects is in better agreement with experiment. We then give an interpretation of the HS and LS XAS and XMCD in terms of the $e_g - t_{2g}$ split density of states. Finally, we demonstrate how to utilize the XMCD sum rules to compute the spin and orbital magnetic moments, as well as the importance of the magnetic dipole moment for the determination of the spin magnetic moment. The derivation and implementation of the magnetic dipole moment in the VASP package, as well as the approximation of the XAS by weighted partial density of states of the conduction electrons are provided in the appendices. The calculation was carried using exactly the same parameters as for the previous chapter on energetics for consistency. As such, we refer the reader to said part for the details of the DFT methods used. Note that the computation of the spectrum did require an increase in the number of bands calculated as compared to a normal calculation to properly reproduce the conduction states, but this did not affect the previously established results in any way.

3.2   Theory: X-ray absorption and XMCD

One can define the x-ray absorption cross-section with polarization μ in a general way using Fermi's golden rule [218]:

$$\sigma^\mu(\omega) = \frac{4\pi\alpha\hbar}{m_e^2\omega} \sum_{if} |\langle f|p_\mu|i\rangle|^2 \, \delta(\hbar\omega - \epsilon_f + \epsilon_i). \tag{3.1}$$

Here, α is the fine-structure constant, m_e is the electron mass, i and f stand respectively for the core states and the conduction states, and their energies ϵ_i and ϵ_f). Here $p_\mu = -i\hbar\nabla_\mu$ is the projection of the momentum operator on the $\{\mu = -1, 0, 1\}$ polarization direction. These directions, along with the corresponding cross-section, are defined as:

$$\sigma^{\mu=\pm} : p_{\mu=\pm} = \frac{\mp 1}{\sqrt{2}} (p_x \pm ip_y) \tag{3.2}$$

$$\sigma^{\mu=0} : p_{\mu=0} = p_z.$$

There are several ways to calculate the x-ray absorption cross-section, ranging from the analytical evaluation of transition matrix elements [219] to core-hole [220] or ligand field DFT methods [221]. In this study, our approach is based on the PAW method within the DFT calculations to compute these matrix elements, and it was already used to compute the K and $L_{2,3}$ edges in iron to achieve quantitative agreement with experimental data [222]. Here, we extend our method by including the plane wave contribution and enabling computation of the XMCD spectra for any direction of the magnetization and any direction of the incident circularly polarized x-ray. We have also determined the XAS in terms of the partial density

of states of the probed atom. This will be used later to analyze the different features in the XAS in terms of the parent e_g and t_{2g} density of states of the ideal octahedron. Note that in this formalism, its straightforward to include the effect of a static core hole or to use the Slater transition rule[223, 224] where only one half core state is included. However, the static core hole usually only improves the K-edge spectrum, but it seldom leads to improved $L_{2,3}$ edges compared to calculations with the initial state[225]. Indeed, we will show below that the initial state calculation agrees better with experiment than calculations using a static full core hole or Slater's half hole.

Within PAW [147], the core states are considered frozen and kept unchanged in the pseudo-potential files, and they are usually fully relativistic $|J, M\rangle$, i.e., solutions to the Dirac equation [226]. This means that we need to work in a $|JMLS\rangle$ coupled basis set:

$$|i\rangle = |J, M\rangle = \sum_{m',s} \langle \ell', m', 1/2, s|J, M\rangle |\ell', m', 1/2, s\rangle = \sum_{m',s} C^{J,M}_{\ell',m',1/2,s} |\ell', m', 1/2, s\rangle, \quad (3.3)$$

where ℓ, m and s the usual angular momentum and spin quantum numbers, the $C^{J,M}_{\ell',m',1/2,s}$ are the usual Clebsch-Gordan coefficients and $\ell' = 1$ for the $L_{2,3}$ edges. It should be noted that we disregard the contribution of the minor part of the Dirac bispinor when computing the matrix elements because the conduction states are scalar relativistic and the small component contribution is negligible. The conduction states are the computed Kohn-Sham orbitals $|n, \mathbf{k}, s\rangle$, which can be written in the PAW method as:

$$|f\rangle = |n, \mathbf{k}, s\rangle = |\widetilde{n, \mathbf{k}, s}\rangle + \sum_{p,\ell,m} \widetilde{P}^{n,\mathbf{k},s}_{p,\ell,m}(|p, \ell, m, s\rangle - |\widetilde{p, \ell, m}, s\rangle), \quad (3.4)$$

where n is the band index, $\mathbf{k}$ the wavevector and s the spin index and $\widetilde{P}^{n,\mathbf{k},s}_{p,\ell,m}$ is the projection value of the pseudo Kohn-Sham wave functions on the PAW projector functions (for more details see Ref. [147]). Here p is used for multiple projector functions to improve the atomic basis set. Usually p is limited to one or two projector functions per angular momentum ℓ.

It should be noted that our implementation can include only the static core-hole effects using a supercell geometry, unlike other PAW implementations, such as the Taillefumier *et al.* method [227] where a continued fraction formulation was used to compute the K-edge x-ray absorption near-edge structures in presence of a core hole. However, our calculations do not include multiplet structures and dynamical core-hole screening. Although this appears to be a drastic approximation, we will show that our implementation is sufficient to obtain qualitative agreement with experiment. The $|\widetilde{n, \mathbf{k}, s}\rangle$ are the so-called pseudo wave functions associated with the pseudo-partial waves $|\widetilde{p, \ell, m}, s\rangle$, whereas the $|p, \ell, m, s\rangle$ are the all electron partial waves. The pseudo and plane wave contributions will be shown to be negligible as the $3d$

electrons of iron are strongly localized within the augmentation region, and these corrections are hence extremely small up to several dozens of eV above the Fermi level. They are therefore only relevant for EXAFS, which is not the subject of this work. This naturally leads us to limit the calculation to the relevant photo-electron energy range when not including the plane wave contribution. These partial waves are indexed by p the projector index, and ℓ, m and s the usual angular momentum and spin quantum numbers, with $P_{p,\ell,m}^{n,\mathbf{k},s}$ the associated projection value of the Kohn-Sham pseudo wave functions:

$$P_{p,\ell,m}^{n,\mathbf{k},s} = \langle g_{p,\ell,m,s} | \widetilde{n,\mathbf{k},s} \rangle, \tag{3.5}$$

where $g_{p,\ell,m,s}$ are the usual PAW projector functions. Note that VASP uses cubic harmonics $\mathcal{Y}_\ell^m$ whereas the formula is computed for spherical harmonics Y_ℓ^m. We should then transform the projections back into the spherical basis when doing the actual computation by using the usual unitary transformation U from cubic to spherical harmonics. We can show that it amounts in writing the projections as $P_p^{n,\mathbf{k},s} = U^{-1} * \widetilde{P}_p^{n,\mathbf{k},s}$, where $\widetilde{P}_p^{n,\mathbf{k},s}$ represents the vector of the cubic projections, as given by Eq. 3.4, that are computed by VASP.

Using these formulas together with the golden rule, we can find:

$$\sigma^\mu(\omega) = \frac{4\pi\alpha\hbar}{m_e^2\omega} \sum_{M,n,\mathbf{k},s} \left| \sum_{p,\ell,m,m'} C_{\ell',m',1/2,s}^{J,M} \langle p,\ell,m|p_\mu|\ell',m'\rangle P_{p,\ell,m}^{*n,\mathbf{k},s} \right|^2 \delta(\hbar\omega - \epsilon_{n\mathbf{k}s} + \epsilon_{JM}), \tag{3.6}$$

where we have used the fact that the spin is conserved by the momentum operator. The $\epsilon_{n\mathbf{k}s}$ and ϵ_{JM} are respectively the Kohn-Sham eigenvalues and the relativistic core energies. Note that VASP does not compute the spin-orbit splitting between the $(J-1/2)$ and $(J+1/2)$ core states, and we have therefore taken this splitting from the result of a relativistic all electron atomic program calculation[228]. This also implies that the spectra $\sigma^\mu(\omega)$ are J dependent, although this will be kept implicit in our notations.

Using Wigner-Eckart's theorem [229, 230], one can then show that:

$$\langle p,\ell,m|p_\mu|\ell',m'\rangle = \frac{C_{\ell',m',1,\mu}^{\ell,m}}{C_{\ell',0,1,0}^{\ell,0}} \langle p,\ell,0|p_0|\ell',0\rangle. \tag{3.7}$$

We therefore recover the so-called dipolar selection rules: $\ell = \ell' \pm 1$ and $m = \mu + m'$. Using angular momentum algebra [230], we have the following closed formula that will be used to compute the reduced matrix element for each projector p:

$$\begin{aligned}
\langle p,\ell,0\,|\nabla_0|\,\ell',0\rangle =& \delta_{\ell,\ell'+1} \frac{\ell}{\sqrt{(2\ell-1)(2\ell+1)}} \left[(\phi_{p,\ell}\,|\partial_r|\,\phi_{\ell'}^c) - (\ell-1)\left(\phi_{p,\ell}\,|r^{-1}|\,\phi_{\ell'}^c\right) \right] \\
&+ \delta_{\ell,\ell'-1} \frac{\ell+1}{\sqrt{(2\ell+1)(2\ell+3)}} \left[(\phi_{p,\ell}\,|\partial_r|\,\phi_{\ell'}^c) + (\ell+2)\left(\phi_{p,\ell}\,|r^{-1}|\,\phi_{\ell'}^c\right) \right],
\end{aligned} \tag{3.8}$$

where we introduced the radial functions associated with the core ϕ^c or the conduction states ϕ, along with the radial integration $(\phi_{p,\ell} \,|r^\alpha|\, \phi_{\ell'}^c) = \int dr \phi_{p,\ell}(r) r^{\alpha+2} \phi_{\ell'}^c(r)$. Note that for most weakly relativistic systems such that $\alpha^2 Z^2 << 1$ (including iron, where $\alpha^2 Z^2 \approx 0.03$), the fine structure corrections to the radial eigenfunctions are very small [231] and consequently one can safely use non-relativistic radial wave functions for the core states. However, VASP allows us to compute the relativistic radial wave functions by solving Dirac's equation, so we will use them.

To conclude, in the momentum representation, the following expression for the absorption spectrum can be shown:

$$\sigma^\mu(\omega) = \frac{4\pi\alpha\hbar^3}{m_e^2\omega} \sum_{M,n,k,s} \left| \sum_{p,\ell,m,m'} C_{\ell',m',1/2,s}^{J,M} \frac{C_{\ell',m',1,\mu}^{\ell,m}}{C_{\ell',0,1,0}^{\ell,0}} \langle p,\ell,0 \,|\nabla_0|\, \ell',0 \rangle P_{p,\ell,m}^{*n,\mathbf{k},s} \right|^2 \delta\left(\hbar\omega - \epsilon_{n\mathbf{k}s} + \epsilon_{JM}\right).$$

(3.9)

The polarization is defined as in equation (3.2), and the XAS and XMCD corresponding respectively to the $\sigma_{XAS} = \frac{1}{3}(\sigma^0 + \sigma^- + \sigma^+)$ and $\sigma_{XMCD} = \sigma^- - \sigma^+$ spectra are computed using Eq. 3.9. The matrix elements $\langle p,\ell,0 \,|\nabla_0|\, \ell',0 \rangle$ are computed using equation (3.8), with the radial integrations being cut at the augmentation radius for consistency. However, given the low symmetry of the molecule under study, it is important to note that the dependence of the XMCD signal on the direction of the incident circularly polarized light is a signature of the distortion of the iron octahedron. Here we use a global coordinates system (O, x, y, z), and assume that the direction of incident light is given by the two spherical angles (ϑ, φ). We can therefore write the cross-section σ_{XMCD} for any incident light direction specified by ϑ, φ as shown in Fig. 3.1. The figure shows also that the spin quantization direction is fixed along a given direction, as it would be done experimentally with a magnetic field. Here we take the (001) direction as a reference. It will be shown later that this direction corresponds to the lowest total energy when the spin-orbit coupling is included. We need therefore to rotate the matrix elements from the local frame of reference (O, x', y', z'), where the z' direction is along the incident light, to the global frame. This transformation is provided by the direction cosine rotation matrix:

$$R(u,v,w) = R_{z'}(\varphi) \cdot R_{y'}(\vartheta) = \begin{pmatrix} \frac{uw}{\sqrt{1-w^2}} & -\frac{v}{\sqrt{1-w^2}} & u \\ \frac{vw}{\sqrt{1-w^2}} & \frac{u}{\sqrt{1-w^2}} & v \\ -\sqrt{1-w^2} & 0 & w \end{pmatrix},$$

(3.10)

where the direction cosines are defined as $u = x/r$, $v = y/r$, and $w = z/r$, where $r = \sqrt{x^2 + y^2 + z^2}$. We can show that the the XMCD signal for any direction (ϑ, φ) is given by

$$\sigma_{XMCD}(\omega) = u\sigma^{yz}(\omega) + v\sigma^{zx}(\omega) + w\sigma^{xy}(\omega),$$

(3.11)

and where $\sigma^{\mu\nu}$ is given by

$$\sigma^{\mu\nu}(\omega) = \frac{4\pi\alpha\hbar}{m_e^2\omega} \sum_{if} \Im\left(\langle f|p_\mu|i\rangle\langle i|p_\nu|f\rangle\right) \delta(\hbar\omega - \epsilon_f + \epsilon_i). \tag{3.12}$$

Here $\Im$ is the imaginary part, and $\mu, \nu = x, y,$ or z. For an ideal octahedron, the lateral components σ^{yz} and σ^{zx} are vanishing so that we have $\sigma_{XMCD}(\omega) = w\sigma^{xy}(\omega) = \cos(\vartheta)\sigma^{xy}(\omega)$, which is a well known result [232].
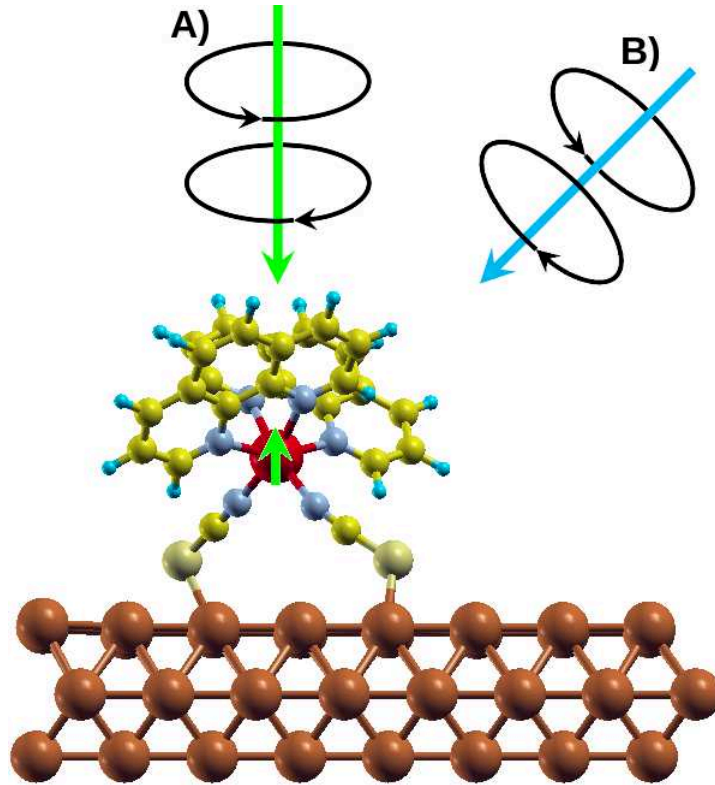
FIGURE 3.1 – Fephen molecule on top of the Cu(001) surface. The direction of the incident circularly polarized light is along the z-direction (A) and along $\vartheta = \varphi = \pi/4$ (B). The spin magnetic moment direction is set along the z-direction, perpendicular to the Cu(001) surface, when the spin-orbit coupling is included.

We will now proceed with a derivation of the plane wave contribution to the spectrum. Going back to equation 3.6, the total plane wave contribution can be split into two parts: the pseudo partial wave contribution $|\widetilde{p, \ell, m}\rangle$ and the actual plane wave part $|\widetilde{n, \mathbf{k}, s}\rangle$, so the Golden Rule could be written as:

$$\begin{aligned}
\sigma^\mu(\omega) = \frac{4\pi\alpha\hbar}{m_e^2\omega} \sum_{M,n,\mathbf{k},s} \Bigg| &\sum_{p,\ell,m,m'} C_{\ell',m',1/2,s}^{J,M}(\langle p,\ell,m| - \langle\widetilde{p,\ell,m}|)p_\mu|\ell',m'\rangle P_{p,\ell,m}^{*n,\mathbf{k},s} \\
&+ \sum_{m'} C_{\ell',m',1/2,s}^{J,M}\langle\widetilde{n,\mathbf{k},s}|p_\mu|\ell',m'\rangle \Bigg|^2 \delta(\hbar\omega - \epsilon_{n\mathbf{k}s} + \epsilon_{JM}).
\end{aligned} \tag{3.13}$$

Obviously, the calculation of the pseudo partial wave contribution is identical to that of the previously calculated partial wave part. On the other hand, the plane wave contribution is more involved. One starts by the plane wave expansion:

$$\langle r|\widetilde{n, \mathbf{k}, s}\rangle = \frac{1}{\sqrt{\Omega}} \sum_{\mathbf{G}} c_{\mathbf{G}}^{n,\mathbf{k},s} \langle r|\mathbf{k} + \mathbf{G}\rangle = \frac{1}{\sqrt{\Omega}} \sum_{\mathbf{G}} c_{\mathbf{G}}^{n,\mathbf{k},s} e^{i(\mathbf{k}+\mathbf{G})(\mathbf{r'}+\tau_\alpha)}. \tag{3.14}$$

where $\mathbf{r} = \mathbf{r'} + \tau_\alpha$ is the global electron position, split into the nucleus position τ_α and the local position (with respect to the nucleus) $\mathbf{r'}$. Note that the $|\mathbf{k} + \mathbf{G}\rangle$ are the eigenfunctions of the momentum operator p_μ: $p_\mu|\mathbf{k} + \mathbf{G}\rangle = (k_\mu + G_\mu)|\mathbf{k} + \mathbf{G}\rangle$. The plane wave expansion is normalized by the system volume Ω. In this local frame, one can then carry a partial wave expansion of the plane wave:

$$e^{i(\mathbf{k}+\mathbf{G})\cdot\mathbf{r'}} = 4\pi \sum_{\ell,m} i^\ell j_\ell(|(\mathbf{k} + \mathbf{G})| |\mathbf{r'}|) Y_\ell^{m\,*}(\widehat{\mathbf{k} + \mathbf{G}}) Y_\ell^m(\widehat{\mathbf{r'}}), \tag{3.15}$$

where the j_ℓ are the usual spherical Bessel functions. Therefore, we can write the following:

$$\langle \widetilde{n, \mathbf{k}, s}|p_\mu|\ell', m'\rangle = \frac{4\pi}{\sqrt{\Omega}} \sum_{\mathbf{G},\ell,m} i^{-\ell} (c_{\mathbf{G}}^{n,\mathbf{k},s}(k_\mu + G_\mu))^\star Y_\ell^m(\widehat{\mathbf{k} + \mathbf{G}}) e^{-i(\mathbf{k}+\mathbf{G})\cdot\tau_\alpha} \tag{3.16}$$

$$\int \mathrm{d}r\, r^2 j_\ell(|(\mathbf{k} + \mathbf{G})|\, r) \phi_{\ell'}(r) \int \mathrm{d}\widehat{\mathbf{r}}\, Y_{\ell'}^{m'}(\widehat{\mathbf{r}}) Y_\ell^{m\,*}(\widehat{\mathbf{r}}).$$

Then, using the orthogonality of the spherical harmonics, we get that:

$$\langle \widetilde{n, \mathbf{k}, s}|p_\mu|\ell', m'\rangle = \frac{4\pi}{\sqrt{\Omega}} \sum_{\mathbf{G}} i^{-\ell'} (c_{\mathbf{G}}^{n,\mathbf{k},s}(k_\mu + G_\mu))^\star Y_{\ell'}^{m'}(\widehat{\mathbf{k} + \mathbf{G}}) e^{-i(\mathbf{k}+\mathbf{G})\cdot\tau_\alpha} \tag{3.17}$$

$$\int \mathrm{d}r\, r^2 j_{\ell'}(|(\mathbf{k} + \mathbf{G})|\, r) \phi_{\ell'}(r).$$

This contribution can then be added to the absorption cross section using formula (3.13). As shown in Fig. 3.2, the effects of this contribution to the $L_{2,3}$ XAS and XMCD are extremely small, being roughly two to three orders of magnitude smaller than the corresponding signal so that one cannot see any difference between the corrected and uncorrected signals. This was to be expected as we are only interested in a limited energy range above the Fermi energy for the $L_{2,3}$ edges, that are primarily associated with the $3d$ part of the eigenfunctions well localized within the augmentation region so that the pseudo partial wave and plane wave contributions should vanish almost exactly as we see here. As such, we can very safely disregard any plane wave contribution for this calculation and only take the partial wave into account.
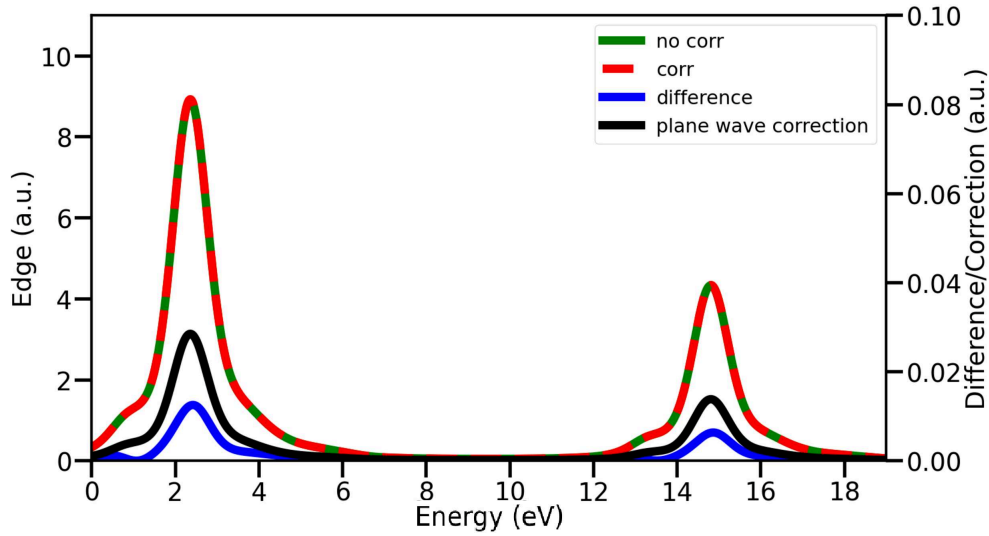
FIGURE 3.2 – Comparison between the all electron partial wave (green) and the full PAW wave function (red) calculated iron L$_{2,3}$ XAS spectra for the LS state. The negligible difference (blue) of the spectra as well as the plane wave contribution to the XAS (black) are shown on the right scale.

To utilize the so called XMCD sum rules[233, 234, 235] to compute the spin and orbital moments, we need to compute the number of electrons in the valence states n_e as we are truncating the plane wave component of the wave function, and we are therefore restricting ourselves to the augmentation region contribution to the density of states, which will not integrate to the theoretical values of $n_e = 6$ below the Fermi energy or $n_e = 10$ over the entire energy range. In practice, carrying the integration of the density of states over this restricted range yields less accurate values for the sum rules than the theoretical value of $n_h = 4$, that we will therefore use. We will also show in the results that we need to evaluate the magnetic dipole contribution $\langle T_z \rangle$ to obtain accurate values of the spin and orbital magnetic moments. The $\langle T_z \rangle$ contribution will be directly evaluated in DFT. First of all, the magnetic dipole tensor can be defined as:

$$\hat{\mathbf{T}} = \hat{\mathbf{S}} - 3\hat{\mathbf{r}}(\hat{\mathbf{r}} \cdot \hat{\mathbf{S}})/|r|^2, \tag{3.18}$$

where $\hat{\mathbf{S}}$ is the vector spin operator, and $\hat{\mathbf{r}}$ is the position operator. With a spin quantization axis along z, the magnetic dipole operator can then be written:

$$\hat{\mathbf{T}} = \hat{S}_z - 3\hat{\mathbf{r}}(\hat{r}_z \hat{S}_z)/|r|^2. \tag{3.19}$$

As we said earlier, one can show that the sum rules normally include a $\langle \hat{T}_z \rangle$ contribution in the valence shell of angular momentum ℓ. We will now explicitly compute the value of this tensor using DFT in order to estimate this quantity. We start by writing the $\hat{T}_z$ tensor as:

$$\hat{T}_z = \hat{S}_z(1 - 3\hat{r}_z^2/|r|^2) = \hat{S}_z(1 - 4\pi(\hat{Y}_1^0)^2), \tag{3.20}$$

where Y_1^0 is the spherical tensor operator associated to the spherical harmonic Y_1^0. Then, its mean value in some shell of electrons with angular momentum ℓ can be evaluated in the PAW method as:

$$\langle \hat{T}_z \rangle = \sum_{n,\mathbf{k},s} f_{n,\mathbf{k},s} \langle n, \mathbf{k}, s | \hat{T}_z | n, \mathbf{k}, s \rangle \tag{3.21}$$

$$= \sum_{n,\mathbf{k},s} f_{n,\mathbf{k},s} \sum_{\substack{p,m \\ p',m'}} P_{p',\ell,m'}^{*n,\mathbf{k},s} P_{p,\ell,m}^{n,\mathbf{k},s} \langle p', \ell, m', s | \hat{T}_z | p, \ell, m, s \rangle,$$

where we once again disregard the plane wave contribution as we are only interested in the augmentation region in this calculation, and we introduced the Fermi occupations $f_{n,\mathbf{k},s}$ so that the sum naturally only runs over the occupied states. Using its definition, the matrix elements of $\hat{T}_z$ in the partial wave basis can be written as:

$$\langle p', \ell, m', s | \hat{T}_z | p, \ell, m, s \rangle = \langle p', \ell, m', s | \hat{S}_z (1 - 3\hat{r}_z^2 / |r|^2) | p, \ell, m, s \rangle \tag{3.22}$$

$$= \langle p', \ell, m', s | \hat{S}_z (1 - 4\pi (\hat{Y}_1^0)^2) | p, \ell, m, s \rangle$$

$$= m_s (\langle p', \ell, m, s | p, \ell, m, s \rangle \delta_{m,m'} - 4\pi \langle p', \ell, m', s | (\hat{Y}_1^0)^2 | p, \ell, m, s \rangle),$$

where m_s is the magnetic moment. Using the definition of the spherical harmonics [230], one can show that:

$$(\hat{Y}_1^0)^2 = \sqrt{\frac{1}{4\pi}} \hat{Y}_0^0 + \sqrt{\frac{1}{5\pi}} \hat{Y}_2^0. \tag{3.23}$$

This leads to the following:

$$\langle p', \ell, m', s | \hat{T}_z | p, \ell, m, s \rangle = -4\sqrt{\frac{\pi}{5}} m_s \langle p', \ell, m', s | (\hat{Y}_2^0) | p, \ell, m, s \rangle. \tag{3.24}$$

The matrix element involves an integral over three spherical harmonics Y_2^0, Y_l^m and $Y_l^{m'}$. This is known in the literature as a Gaunt coefficient [230], and can be shown to be equal to:

$$\langle p', \ell, m', s | (\hat{Y}_2^0) | p, \ell, m, s \rangle = \sqrt{\frac{5}{4\pi}} C_{2,0,\ell,m}^{\ell,m'} C_{2,0,\ell,0}^{\ell,0} (p', \ell | p, \ell) \ , \tag{3.25}$$

where the $(p', \ell | p, \ell)$ are the radial integration as defined in Eq. 3.8. By angular selection rules, we directly have that $m' = m$. Therefore, we obtain that:

$$\langle \hat{T}_z \rangle = -2 \sum_{n,\mathbf{k},s} f_{n,\mathbf{k},s} \sum_{\substack{p,m \\ p'}} P_{p',\ell,m}^{*n,\mathbf{k},s} P_{p,\ell,m}^{n,\mathbf{k},s} m_s C_{2,0,\ell,m}^{\ell,m} C_{2,0,\ell,0}^{\ell,0} (p', \ell | p, \ell), \tag{3.26}$$

which we implemented directly in VASP.

3.3 Results and discussion

To illustrate the effect of various atoms of the molecule on the electronic structure of the iron atom, and therefore on its high spin state XAS absorption and XMCD, we depict in Fig. 3.3 the magnetization isosurface at $\pm 0.025 \mu_B$ per unit cell for the undistorted (top left) and distorted (top right) (as in the molecule on the copper surface) FeN_6 cluster together with that of the molecule in the gas phase (bottom left) and that on the substrate (bottom right). Due to the direct hybridization of the p orbitals of nitrogen with those of the iron site, the magnetic moments of all the N atoms are oriented opposite to that of the iron site. This does not apply to the case of the free FeN_6 octahedron. This is because the nitrogen atoms are chemically bonded to the carbon atoms of the phenanthroline. Table 3.1 shows the iron number of electrons and magnetic moment in FeN_6 cluster and in the molecule. It is clear from the table that the distortions have only a slight impact on the electronic distribution of the iron atom, but as shown later, the XMCD is considerably modified. As a result, new σ^{xz} and σ^{zy} signals appear. This is also true for the free molecule as compared to the molecule on the Cu(001) substrate, as the Fe$-$N bond lengths of the free molecule deviate differently from the average bond length than for the adsorbed molecule. We found that the relative root mean-square deviation percentage for the free molecule is 5.1% whereas it is 3.6% for the adsorbed molecule.

System	n_s	n_p	n_d	m_s (μ_B)	m_p (μ_B)	m_d (μ_B)
Ideal FeN_6	0.370	0.422	5.838	0.039	-0.029	3.237
Distorted FeN_6	0.386	0.460	5.877	0.030	-0.004	2.996
Fe in Fephen	0.327	0.451	5.982	0.017	0.026	3.696
Fe in Fephen/Cu(001)	0.304	0.407	6.007	0.017	0.022	3.635

TABLE 3.1 – Iron site number of electrons and spin magnetic moments in units of μ_B per s, p and d orbitals for ideal and distorted FeN_6 cluster together with the Fephen molecule in the gas phase and the one adsorbed on Cu(001) surface.

The XAS and XMCD $L_{2,3}$ spectra were computed for the Fephen molecule up to 6.5 eV above the Fermi energy. The L_2 and L_3 edges are split by the relativistic $p_{1/2} - p_{3/2}$ spin-orbit energy, which we found to be 12.45 eV using an atomic all-electron relativistic program [228]. The program also produced a $p_{3/2}$ energy shift of 0.66 eV towards higher energy for the spin-polarized state compared to the non spin-polarized one. The $L_{2,3}$ edges are broadened by a Gaussian function of full-width of 0.25 eV and a Lorentzian function of 0.5 eV, leading to a Voigt profile with a broadening ≈ 0.6 eV, in agreement with experimental results [236]. To find out how important the effect of the static core hole on the XAS is, we have performed the calculation including a static core hole in the core $2p$ states, and also half hole according to the Slater transition rule. We have compared in Fig. 3.4 the calculation of XAS and XMCD

(a) Undistorted FeN$_6$

(b) Distorted FeN$_6$

(c) Fephen molecule

(d) Fephen on Cu(001)
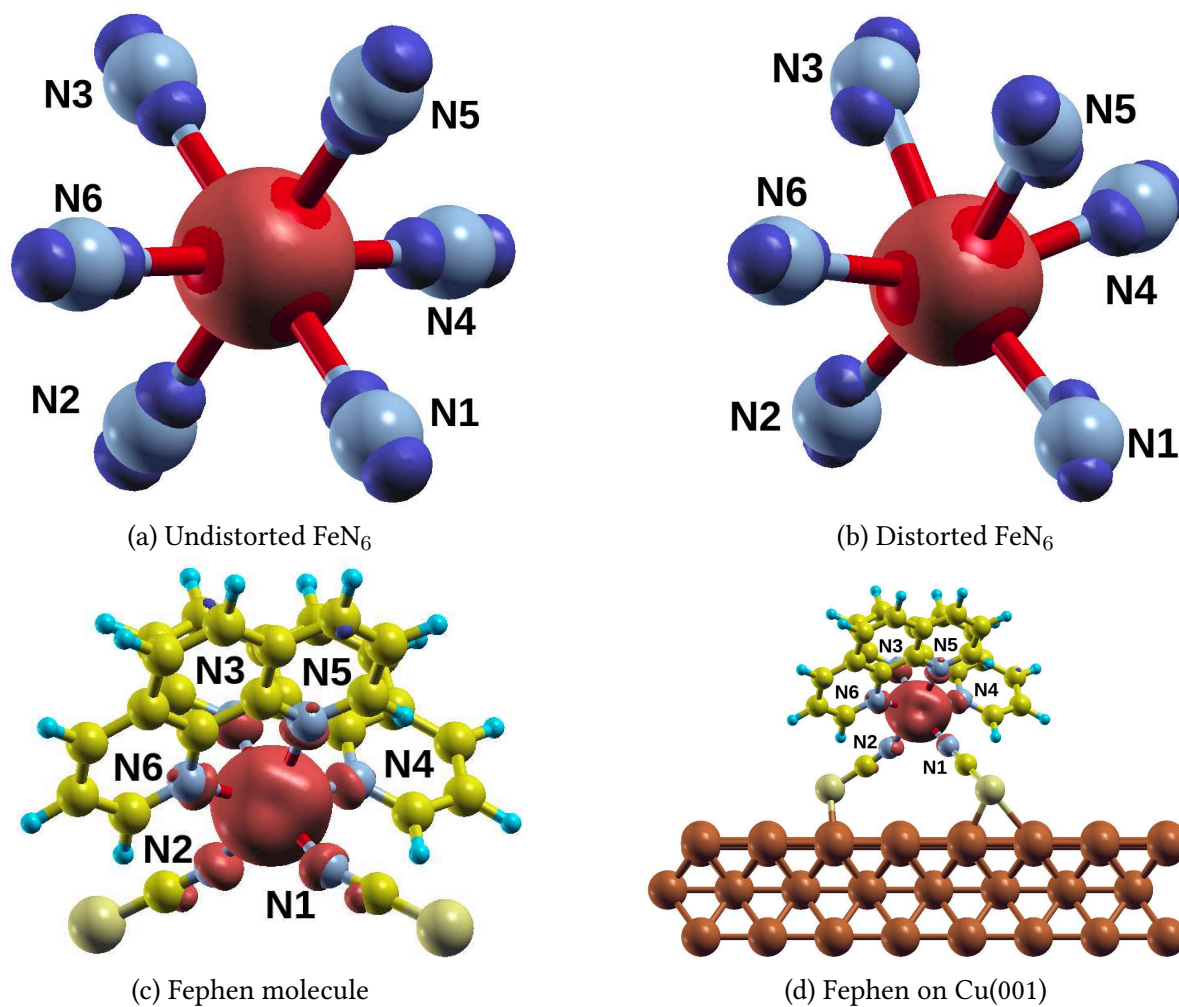
FIGURE 3.3 – Comparison of the high-spin isosurface of the magnetization density of undistorted (a) and distorted (b) FeN$_6$ cluster with that of the Fephen in (c) gas phase and (d) adsorbed on the Cu(001) surface. The red color represents the positive magnetization (majority spin up), and blue the negative magnetization (minority spin down). For all cases, the isosurface is taken to be $\pm 0.025 \mu_B$ per unit cell.

using the so called initial state, where no core hole is included, with the calculation using a full core hole and that using a Slater half hole. We observe that the structures in the LS XAS are shifted linearly towards low energies by 2 eV for the full core hole and 1 eV for the half hole. This shift correspond to the screening of the core hole by the additional photo-electron that remains on the iron site. The linear reduction of the peak intensity also corresponds to the overall reduction in the number of unoccupied states in the $3d$ density of states of iron. The situation is similar for the HS XAS, but less pronounced than for the LS case, and we observe a clear reduction of the peak intensities. The reduction of the peak intensity of the first structure is clearly in disagreement with experiment as it will be shown in Fig. 3.5. The calculated spin magnetic moment is also drastically reduced from 3.696 μ_B without core hole to 3.06 μ_B with a half core hole and 2.452 μ_B for a full selfconsistent core hole. This shows the limitation of XAS calculations using a static core hole. Unfortunately, calculations beyond a static core hole, such as using the Bethe-Salpeter equation to compute the electron-hole interaction, are not feasible for such a large system because of the prohibitive computer cost[237, 238] and have been used only for materials with small number of atoms per unit cell.
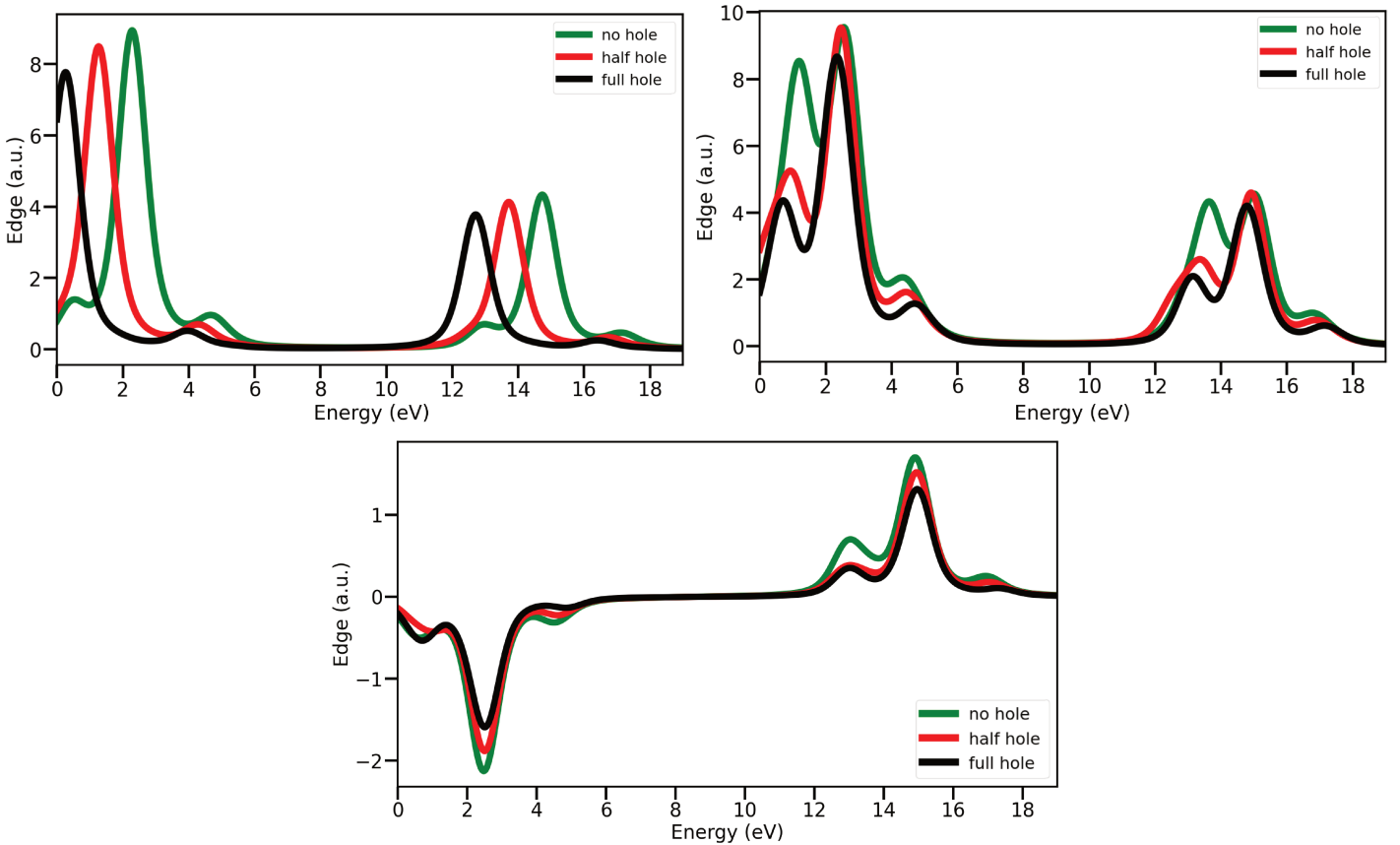
FIGURE 3.4 – $L_{2,3}$ XAS for the Fephen molecule without core-hole (green), with the Slater transition rule half hole (red) and the full hole (black), both for the LS (top left) and HS (top right) and the corresponding HS XMCD spectra (bottom).

Since calculations including a static core hole deviate more from the experimental XAS spectra of Miyamachi *et al.* [21], we have shown in Fig. 3.5 the calculated x-ray XAS and XMCD using the initial state and compared our results to this experimental spectra. We have adjusted the energy reference by shifting the theoretical LS spectrum relative to the HS one by our computed value of 0.66 eV. We have then plotted the experimental LS spectrum for the gas phase by adjusting the well-defined L_3 peak as a reference point, the HS spectrum being then automatically obtained and compared to the experimental one. We can see that the calculation reproduces the $L_{2,3}$ edges in the LS state, but as expected the multiplets, which are not taken into account in the calculation, are not reproduced. It is interesting to note that the spectrum for the molecule on the surface is similar to that of the gas phase, apart from the structure at about 5 eV which is strongly reduced. The two spectra for the gas phase and for the adsorbed molecule are shifted by the difference of their respective Fermi levels. In the case of the HS state, we note a less accurate agreement between the theoretical and experimental results as the experimental peaks are slightly shifted and have different intensities for the L_2 and L_3 edges. These differences might be dependent on the dynamics of the core-hole[239], although we still have a qualitative agreement.

For the XMCD, we have made calculations for three alignments of the magnetic moment. The first for the moment along the (001) easy axis, and the second and the third for the moment along the (111) and (010) directions. Note that the magnetic moment direction has a negligible effect on the total XAS. These XMCD results for various magnetization directions will be used later to determine the orbital magnetic moment anisotropy by means of the XMCD sum rules. As it can be seen from Fig. 3.5 the agreement with the experimental data is only qualitative. This is expected, as the XMCD simulation is notoriously complex. It relies on the difference between two relatively close spectra for left and right circular polarizations, and it is therefore extremely sensitive to numerical errors and approximations. Indeed, one can easily observe that the XMCD spectrum vanishes exactly if spin-orbit coupling is not taken into account as both spin channels will then couple identically with the photon helicity, and therefore both left and right polarizations give the same results. As such, the value of the orbital moment is strongly dependent on the accuracy of the spin-orbit treatment, which, therefore, constitutes an important source of error as it is numerically very difficult to compute accurately for such a large molecule.
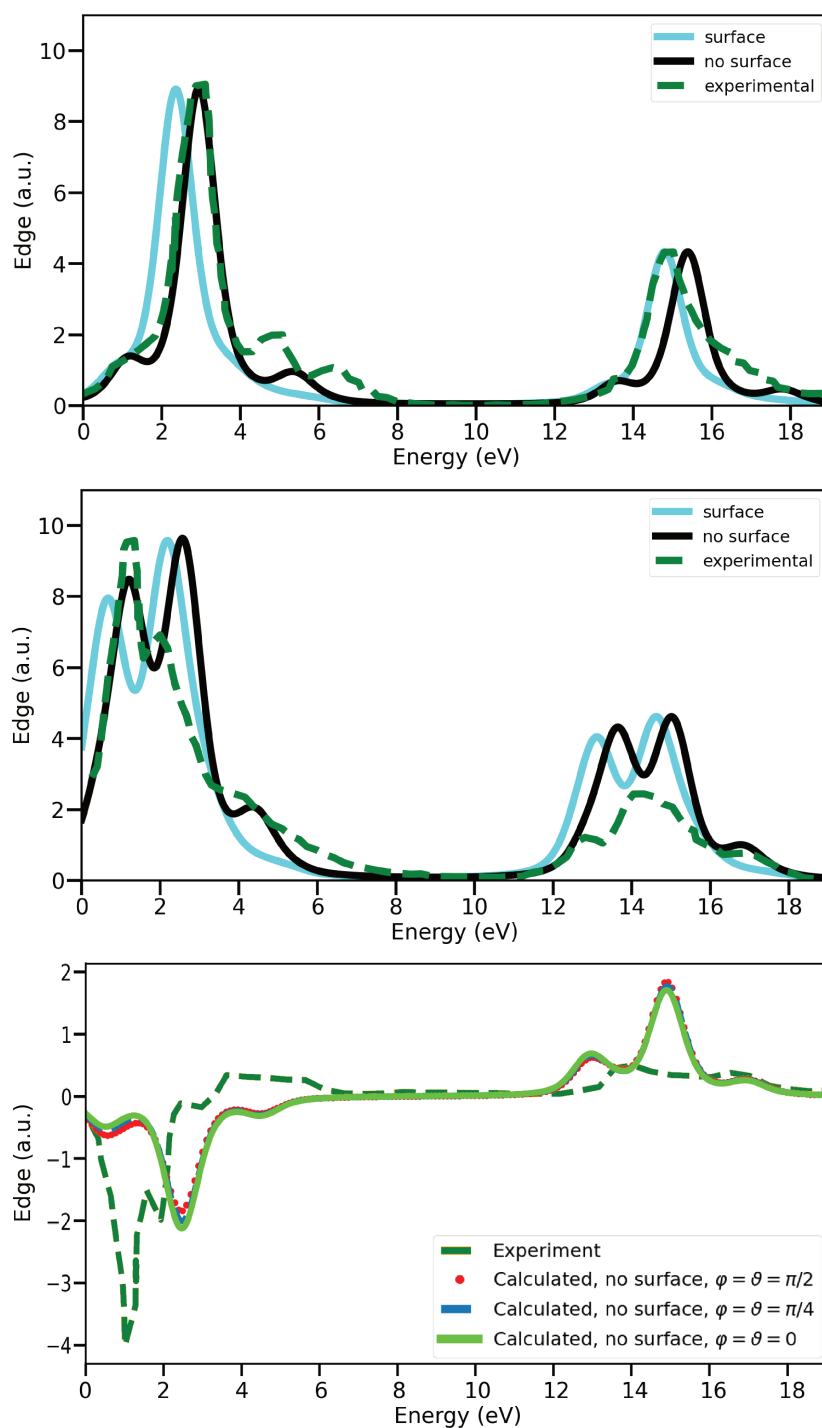
FIGURE 3.5 – L$_{2,3}$ XAS for the Fephen molecule in the LS state (top), HS state (second) and HS XMCD for the free molecule (third) compared with the experimental results of Ref. [21] for the gas phase. The XMCD is calculated for the magnetic moment aligned along the (001) direction (green), the (111) (dot-dashed blue) and (010) (dashed red).

So far we have only compared our calculation to the experimental results of the Fephen molecule on the gas phase. However, Miyamachi *et al.*[21] have also measured the XAS of the Fephen molecule adsorbed on the Cu(001) surface and found that the L$_{2,3}$ XAS corresponds to a mixture of 46% of HS and 54% of LS signals. The LS and HS mixture is found by fitting

the XAS of the two layers of Fephen molecules adsorbed on Cu(001) using the gas phase XAS spectra of the LS and HS. It is surprising to notice that the XAS for gas phase provided a good fit to the XAS of the molecule adsorbed on the Cu(001) surface. To shed some light on the experimental data we have also made a fit of the experimental XAS by combining our LS and HS XAS of the molecule adsorbed on the surface. We have proceeded as an experiment by combining $r\sigma^{LS}(\omega + \Delta) + (1 - r)\sigma^{HS}(\omega + \Delta)$, where $\Delta = 0.7$ eV is the energy difference between the corresponding peak positions of the LS XAS of the gas phase and that of the molecule adsorbed on the Cu(001) surface, and r is the amount of LS proportion.

As shown in Fig. 3.6 the amount r of the LS was found to be 37% for the best agreement with experiment whereas experimentalists found 54%. We have also shown in the figure the the spectrum corresponding to the experimental LS amount of 54% which was not very different from the optimal r amount of 37%. As stated above the agreement of the experimental XAS spectra of the gas phase molecule with the one where the molecule is adsorbed on the surface is surprising. As shown by our calculation, the Fermi level of the molecule adsorbed on the surface is shifted by 1.2 eV towards higher energy with respect to the gas phase. It is therefore unlikely that the XAS experimental peak positions of the free molecule and the one adsorbed on the surface are not shifted with respect to one another, but it is possible that a significant part of the molecules is not adsorbed on the surface since the FePhen layer had a 2 ML thickness. This claim could be experimentally checked and explored, e.g. by trying to measure the spectra on a thinner surface.
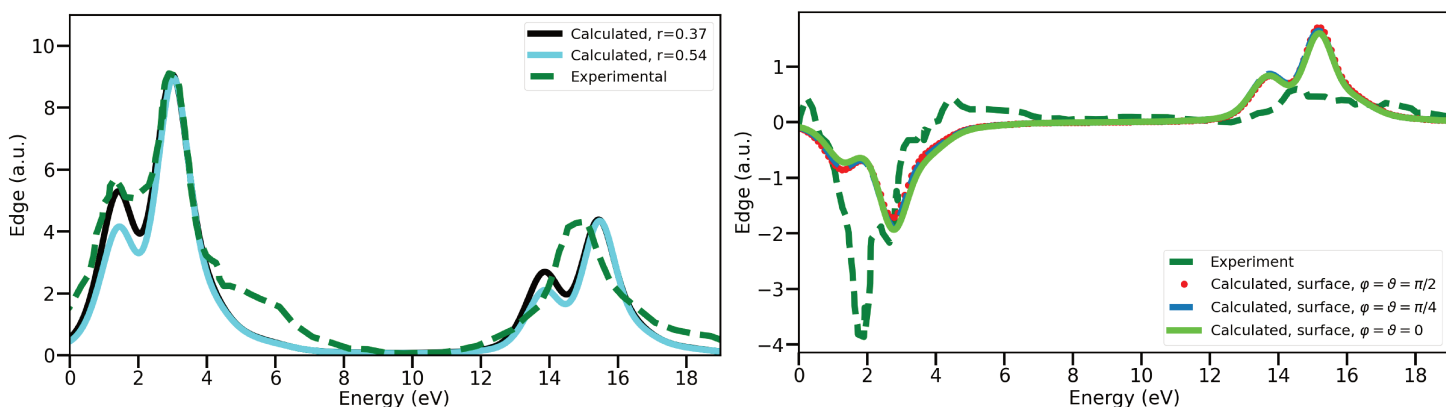
FIGURE 3.6 – On the left, linear combination of LS (37% black, 54% blue) and HS (63% black, 46% blue) $L_{2,3}$ XAS for the Fephen molecule on Cu(001) compared with the experimental results of Ref. [21]. The figure on the right shows the XMCD at the $L_{2,3}$ of iron for the molecule adsorbed on Cu(001) compared to the experimental results of [21]. The XMCD is calculated for the magnetic moment aligned along the (001) direction (green), the (111) (dot-dashed blue) and (010) (dashed red).

As explained in the calculation method, we have found that the dependance of the XMCD on the direction of the incident light can be used to provide the deformation of the iron octahedron, whereas the dependance on the magnetization direction produces the anisotropy of

the orbital magnetic moment. To support our idea, we have depicted in Fig. 3.7 the $\sigma^{\mu\nu}$ components as given by Eq. 3.12 for the $L_{2,3}$ iron atom in the molecule on Cu(001) and for the iron atom in the distorted and undistorted FeN$_6$ octahedra. For the undistorted tetrahedron, the σ^{yz} and σ^{zx} are exactly zero due to symmetry and the code also produces zero, whereas these two components of the σ tensor do not vanish for the distorted octahedron, as shown in Fig. 3.7 (bottom). It is clear that if we set the direction of the circularly polarized light along (010) or (100) direction, while keeping the magnetization along the (001) direction, we will observe only σ^{yz} or σ^{zx} as shown by Eq. 3.12. It is therefore interesting to emphasize that this kind of experiment will directly give the effect of the octahedron distortion on the XMCD signal. One can set a database of XMCD spectra for a direction where the the XMCD should be zero for a perfect octahedron and machine learning can be used to predict the octahedron distortion of SCO molecules adsorbed on metallic surfaces. These theoretical predictions are interesting and need future experimental confirmation, as most available results yet deal with the crystalline phase which is clearly isotropic.
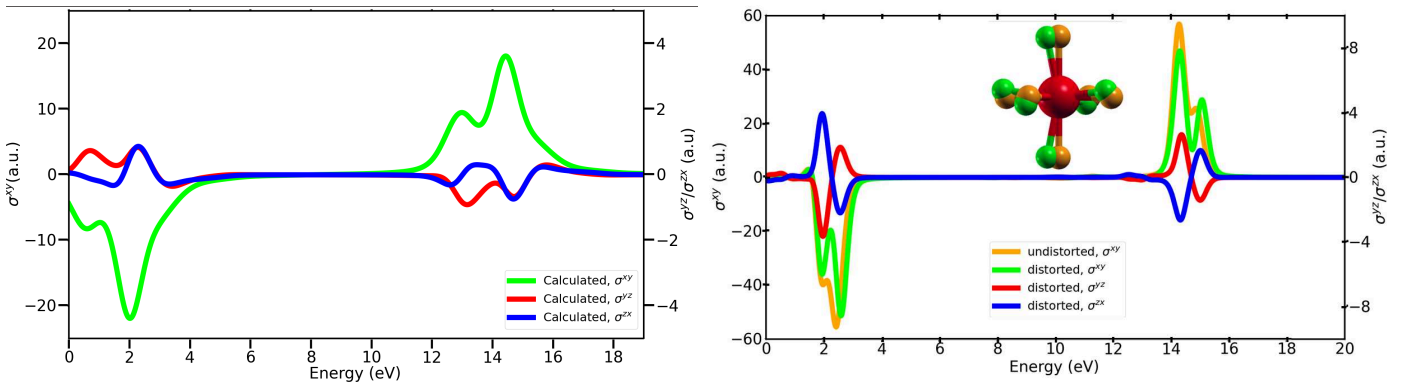
FIGURE 3.7 – Calculated $\sigma^{\mu\nu}$ (see Eq. 3.12) for the HS Fephen molecule (left) when the magnetic moment is aligned along the (001) axis and for perfect and deformed FeN$_6$ octahedron (right). σ^{yz} and σ^{zx} are strictly zero by symmetry for the undistorted octahedron (not shown). The scale of σ^{yz} and σ^{zx} is on the right. The inset shows the the deformation of the octahedron (Nitrogen atoms in green) as in the molecule case compared to the non deformed one (Nitrogen in orange).

To understand the structures in the XAS, we have compared them in Fig. 3.8 with the spin-polarized e_g and t_{2g} symmetry representations of the iron site density of states. As expected from the d^6 electronic configuration of the ground state, the density of states shows that the primary states contributing to the LS XAS signal are from the unoccupied parent e_g states. As for the HS XAS, the main contribution are from the minority spin parent t_{2g} and e_g states. This is due to the splitting of the e_g and t_{2g} states caused by the strong crystal-field effect and in part to the splitting of the states due to the distorted iron octahedron. [173] This interpretation is compatible with the structural and electronic structure transition from the HS to LS which involves the spin transition $(t_{2g})^{3\uparrow}(e_g)^{2\uparrow}(t_{2g})^{1\downarrow} \rightarrow (t_{2g})^{3\uparrow}(t_{2g})^{3\downarrow}(e_g)^0$ as shown in Ref. [173].

The figure also shows that the states contributing to the HS XMCD spectrum are naturally the same as those for the HS XAS.
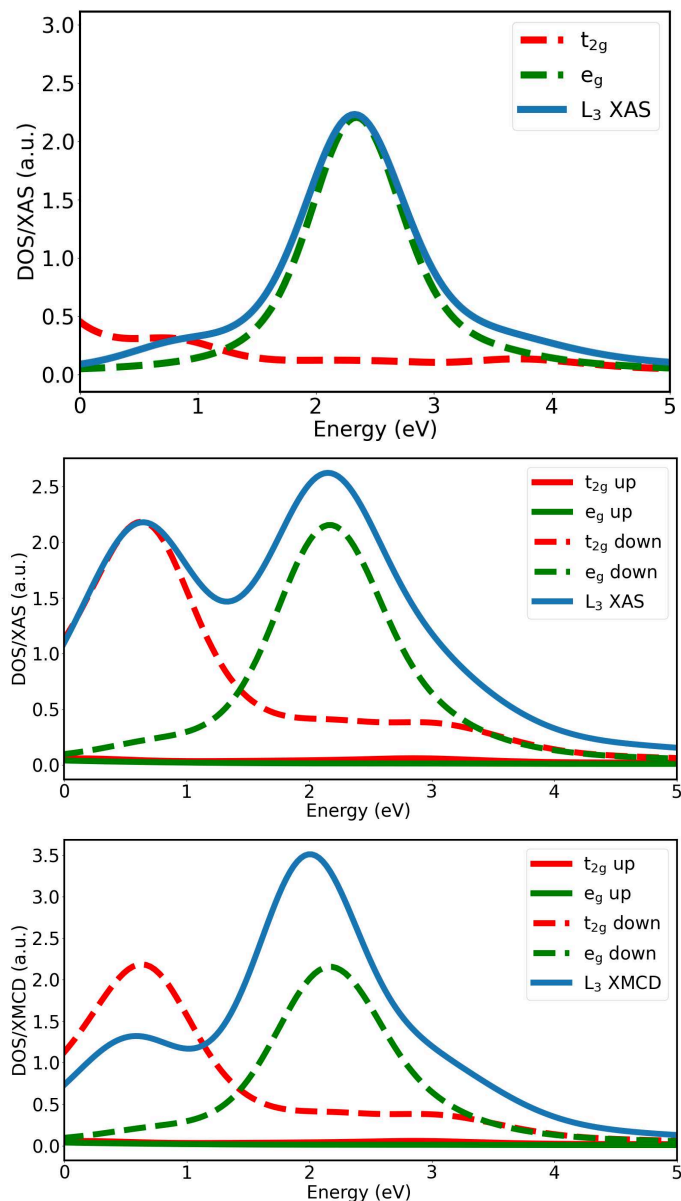
FIGURE 3.8 – The iron site spin polarized e_g and t_{2g} symmetry decomposed unoccupied density of states compared to the calculated XAS L_3 spectrum for both LS (top) and HS (middle) and to HS XMCD (bottom).

It is evident that the sum rules should be vanishing in the LS state and the numerical calculation concurs with this analytical result. However, this is not the case in the HS state, for which we get the results shown in Table 3.2. These results are obtained from the XMCD spectra presented in Fig. 3.5 when the polarization is along the (001), (111) and (010) directions. We did not evaluate the sum rules for the experimental spectrum because we encountered normalization issues, which lead to nonphysical values (e.g. m_ℓ has a computed value of several μ_B). The table also shows that the magneto-crystalline energy ΔE is lowest when the

magnetic moment is oriented along the (001) direction and the hard axis is aligned with the (010) direction. This energy ΔE is equivalent to a blocking temperature of 22 K, which is very low considering the super-paramagnetic aspect of the molecular crystal.

Magnetization direction	ΔE (meV)	T_z (μ_B)	m_ℓ (μ_B)		m_s (μ_B)	
			Direct	Sum rule	Direct	Sum rule
(001)	-1.9	-0.101	0.180	0.154	3.635	3.731
(111)	-0.98	-0.092	0.106	0.092	3.637	3.735
(010)	0	-0.092	0.006	0.006	3.635	3.734

TABLE 3.2 – Magneto-crystalline anisotropy energy ΔE in meV, direct calculation of magnetic dipole (T_z), spin moment (m_s), and orbital moment (m_ℓ) compared to those obtained using the XMCD sum rules (in units of Bohr magneton μ_B) for the iron site of the SCO Fephen in the HS state for various directions of the iron magnetic moment. The hard axis total energy is -1045.48985 eV.

We can make several interesting observations:

— The magnetic dipole tensor is non-vanishing, and its value is non-negligible as it makes up for roughly 10% of the magnetic moment contribution. One could have expected this, as it was shown that this operator takes a finite value for ideal Fe^{+2} octahedral complexes in the HS state when spin-orbit coupling is taken into account [240]. However, as we show in the appendices, relativistic corrections are not the dominant contribution to the value of this tensor in our case as they are almost negligible. Instead, it appears that the likely origin of this behavior is imperfect octahedral geometry of the high spin complexes which significantly lifts the degeneracy of the t_{2g} and e_g states, and as such removes the symmetries that nullify the value of T_z.

— The orbital momentum sum rule yields a slightly underestimated value of $0.154\mu_B$ compared to the directly calculated value of $0.180\mu_B$ when the magnetization is oriented along the easy axis (001). As the accuracy of this value depends directly on the integral of the XMCD signal, such an agreement is quite surprising as one would expect a worse accordance especially given the relatively poor agreement between the theoretical and experimental spectra that demonstrated the limitation of the model. We have also to note that the sum rules are an approximate theoretical results and as such the range of their validity has been debated [239, 241], although they ought to be decently respected for Fe^{2+} compounds, according to Schwitalla and Ebert [239]. It should also be emphasized that the integrated spectra over the relevant energy range, used for the sum rules, are in general less sensitive to the details of their structures and shapes. [241]

— The spin-moment sum rule appears to yield a quite accurate value of $3.731\mu_B$ compared to direct calculated value of $3.635\mu_B$. We can appreciate here the importance of the

magnetic dipole correction, as without it the sum rule would only yield a moment of $3.377\mu_B$, which is still within an acceptable range from the expected value. It appears, therefore, that this spin sum rule is less sensitive to inaccuracies in the XMCD spectrum than the orbital moment sum rule. This is not surprising, as the orbital moment is much smaller compared to the spin magnetic moment and is consequently much more prone to errors.

3.4 Conclusion

Our implementation of the XAS and XMCD spectra within VASP was used to compute the $L_{2,3}$ edges for both the low-spin and high-spin iron site within a SCO Fephen molecule in the gas phase and adsorbed on a copper surface. We found that the plane wave contribution to the x-ray matrix elements within the electric dipole approximation are fully compensated by the pseudo-partial contribution to the PAW wave function within the XAS energy range.

The calculated XAS and XMCD results are in qualitative agreement with the available experimental results, although with relative intensity issues in the HS state that underscore the importance of multiplet and dynamics of the core-hole effects for a comprehensive understanding of the spectrum. We noticed that the simple static core hole of Slater transition rule half hole did not improve the agreement with experiment. The calculation using the initial state produced the best agreement with experiment and the overall features in both the HS and LS spectra are understood in terms of the parent e_g and t_{2g} representations of the iron $3d$ DOS. We have also found that the dependence of the XMCD signal on the direction of incident x-ray circularly polarized light can be used to directly measure the deformation in the iron octahedron. As discussed above, one could attempt to establish a database for the σ^{yz} and σ^{zx} XMCD directions, which are zeros for a perfect octahedron, and use machine learning to determine directly the octahedron distortion of the SCO molecules.

We have also shown that the XMCD for different magnetization directions is related to the anisotropy of the iron orbital magnetic moment. As a result, the sum rules yields the correct orbital and spin magnetic moments as compared to direct calculations for different orientations of the spin magnetic moment, as long as one takes into account the contribution of the magnetic dipole moment originating from the geometrical deformation of the iron site octahedron in the HS state. These theoretical predictions await future experimental confirmation.

Chapitre 4

STM beyond the Tersoff-Hamann approximation

4.1 Introduction

The Scanning Tunnel Microscopy (STM) images of FePhen adsorbed on a molecule have been measured ([21]), showing two distinctive lobes for the Phen groups pointing towards the STM tip. The images show an apparent difference between LS and HS images as the increase of the bond length and bonding angles leads to a clear separation between the lobes in the HS state when compared to the LS state, along with an increase of the corrugation height. The interesting part lies in the measure of the conductance in the HS state in contrast with the LS state, which shows a clear conductance peak in the HS state at zero bias whereas the LS state is relatively insensitive to the bias applied. This Kondo resonance is a classic signature of the HS spin state in SCO molecules on metallic surfaces [242], it is however extremely sensitive to various parameters such as the nature of the surface or the Ligands, owing to and typically showing the strong influence of these parameters on important aspects of the Kondo physics within these systems such as the spin state (the Kondo impurity) or the bath of conduction electrons from the surface. The simulation of STM images within the Tersoff-Hamann approximation, with a pure s-wave tip, on the FePhen molecule has already been carried ([119]), showing results that concur with experimental results with however predictable accuracy shortfalls stemming from the very strong approximation done. It could therefore be interesting to see what differences are observed with more general levels of approximation, which will be the goal of this part. We will start by introducing the various commonly studied layers of approximation associated to the (one-particle) calculation of STM, being the Bardeen formula [243], the Chen approximation [244] and finally the Tersoff-Hamman approximation [245, 246], before using them to compute the theoretical STM images with comparison to previously available theoretical and experimental results.

4.2 Theoretical aspects

4.2.1 A General introduction : Bardeen's formula

One of the most popular approaches to simulate STM images is the Bardeen transfer formalism, which consists in a very convenient one-particle elastic approximation to the tunneling current, neglecting all direct interaction between the tip and the surface. We will now proceed with a demonstration of this formula, closely following the derivation in the ref ([247])

Assume a system composed of a tip, a surface and a separation vacuum. If the tip and the surfaces are supposed to be sufficiently separated, their respective wavefunctions can be assumed to follow a free system Schrödinger's equation:

$$i\hbar\partial_t\Psi_{S/T} = \left(-\frac{\hbar^2}{2m}\nabla^2 + V_{S/T}\right)\Psi_{S/T},$$
(4.1)

where $\Psi_{S/T}$ is the surface (respectively tip) wavefunction and $V_{S/T}$ the associated potential. These wavefunctions are associated with the stationnary states $\Psi_{S/T;n}$, satisfying the time-independent Schrödinger equation:

$$\left(-\frac{\hbar^2}{2m}\nabla^2 + V_{S/T}\right)\Psi_{S/T;n} = E_{S/T;n}\Psi_{S/T;n},$$
(4.2)

where we introduced the eigenenergies $E_{S/T;n}$ so that $\Psi_{S/T} = \Psi_{S/T;n}\exp(-iE_{S/T;n}t/\hbar)$. Now, assume that we bring both systems closer: naturally, the new wavefunction of the coupled system then follows the Schrödinger equation of the total potential, which is the sum of the surface and tip potentials:

$$i\hbar\partial_t\Psi = \left(-\frac{\hbar^2}{2m}\nabla^2 + V_S + V_T\right)\Psi.$$
(4.3)

We will now use perturbation theory to solve the equation, therefore implicitly assuming a slow and adiabatic transformation from the non-interacting to the interacting case, which is the case experimentally as the tip movement (in s) is much slower than the average electronic relaxation time (in fs). Assuming that the system is initially in some given state $\Psi_{S;n}$, expanding the coupled wavefunction over the surface and tip eigenfunctions yields:

$$\Psi = a_n(t)\Psi_{S;n}\exp(-iE_{S;n}t/\hbar) + \sum_{m=1}^{\infty} c_m(t)\Psi_{T;m}\exp(-iE_{T;m}t/\hbar),$$
(4.4)

where we have $a_n(t \to -\infty) = 1$ and $c_m(t \to -\infty) = 0$ by definition. We will now assume that the sets of free tip and surface wavefunctions are mutually orthogonal, so that $\int \mathrm{d}^3r\,\Psi_{S;n}^*\Psi_{T;m} \approx 0$. We can then apply Schrödinger's equation on this definition of Ψ and

project it on some given state $\Psi_{T;p}$, which yields:

$$i\hbar\partial_t c_p(t) = \langle\Psi_{T;p}|V_T|\Psi_{S;n}\rangle \exp\left(-i\frac{(E_{S;n} - E_{T;p})}{\hbar}t\right), \tag{4.5}$$

where we neglected the time variation of $a_n(t) \approx 1$ because of the adiabatic approximation, and all second order perturbative terms. As all quantities on the right side are time-independent except for the explicit time in the exponential, one can integrate this and get:

$$c_p(t) = \lim_{\eta\to 0} \frac{\langle\Psi_{T;p}|V_T|\Psi_{S;n}\rangle}{(E_{S;n} - E_{T;p} + i\eta)} \exp\left(-i\frac{(E_{S;n} - E_{T;p} + i\eta)}{\hbar}t\right). \tag{4.6}$$

We introduced a regularization parameter η to take into account the case where $E_{S;n} = E_{T;p}$, which is the elastic transport condition.

Using the definition of the wavefunction (4.4), one can clearly see that $|c_p|^2$ is the transition probability from the initial state $\Psi_{S;n}$ to this given state $\Psi_{T;p}$, which therefore writes:

$$|c_p|^2 = \lim_{\eta\to 0} \frac{|\langle\Psi_{T;p}|V_T|\Psi_{S;n}\rangle|^2}{(E_{S;n} - E_{T;p})^2 + \eta^2} \exp\left(\frac{2\eta t}{\hbar}\right), \tag{4.7}$$

one can then take the derivative with respect to time in order to get the transition rate:

$$\Gamma_{s,p}(t) = \lim_{\eta\to 0} \frac{2\eta}{\hbar} \frac{|\langle\Psi_{T;p}|V_T|\Psi_{S;n}\rangle|^2}{(E_{S;n} - E_{T;p})^2 + \eta^2} \exp\left(\frac{2\eta t}{\hbar}\right). \tag{4.8}$$

We can now take the limit as it is properly defined (in the distributional sense) and we get the Fermi Golden Rule of this problem:

$$\Gamma_{s,p}(t) = \frac{2\pi}{\hbar}\delta(E_{S;n} - E_{T;p})\,|\langle\Psi_{T;p}|V_T|\Psi_{S;n}\rangle|^2. \tag{4.9}$$

We now need to evaluate the transition matrix element. we first write:

$$\langle\Psi_{T;p}|V_T|\Psi_{S;n}\rangle = \int \mathrm{d}^3r\,\Psi_{T;p}^* V_T \Psi_{S;n} = \int_{z\in\Omega_T} \mathrm{d}^3r\,\Psi_{S;n}\left(\frac{\hbar^2}{2m}\nabla^2 + E_{T;p}\right)\Psi_{T;p}^*, \tag{4.10}$$

where we define Ω_T as the volume of space where the tip potential V_T does not vanish, disjoint from the similarly defined volume Ω_S for the surface as we assumed at the beginning of this derivation. The second equality is nothing but Schrödinger's equation applied to the tip wavefunction $\Psi_{T;p}^*$.

Now, using the elastic tunneling condition $E_{T;p} = E_{S;n}$, we have:

$$\langle \Psi_{T;p}|V_T|\Psi_{S;n}\rangle = \int \mathrm{d}^3 r \Psi_{T;p}^* V_T \Psi_{S;n} = \int_{z \in \Omega_T} \mathrm{d}^3 r \Psi_{S;n} \left(\frac{\hbar^2}{2m} \nabla^2 + E_{S;n} \right) \Psi_{T;p}^*$$

$$= \int_{z \in \Omega_T} \mathrm{d}^3 r \Psi_{S;n} \frac{\hbar^2}{2m} \nabla^2 \Psi_{T;p}^* + \int_{z \in \Omega_T} \mathrm{d}^3 r E_{S;n} \Psi_{S;n} \Psi_{T;p}^*$$

$$= \int_{z \in \Omega_T} \mathrm{d}^3 r \Psi_{S;n} \frac{\hbar^2}{2m} \nabla^2 \Psi_{T;p}^* + \int_{z \in \Omega_T} \mathrm{d}^3 r \left(-\frac{\hbar^2}{2m} \nabla^2 + V_S \right) \Psi_{S;n} \Psi_{T;p}^*$$

$$= \frac{\hbar^2}{2m} \int_{z \in \Omega_T} \mathrm{d}^3 r \left(\Psi_{S;n} \nabla^2 \Psi_{T;p}^* - \Psi_{T;p}^* \nabla^2 \Psi_{S;n} \right), \tag{4.11}$$

where we applied Schrödinger's equation to the surface wavefunction $\Psi_{S;p}$ for the third equality, and V_S is supposed to vanish within Ω_T as we say earlier so that we get the final line. Now, it can be easily seen that:

$$\Psi_{S;n} \nabla^2 \Psi_{T;p}^* - \Psi_{T;p}^* \nabla^2 \Psi_{S;n} = \nabla \left(\Psi_{S;n} \nabla \Psi_{T;p}^* - \Psi_{T;p}^* \nabla \Psi_{S;n} \right). \tag{4.12}$$

This yields the following result:

$$\langle \Psi_{T;p}|V_T|\Psi_{S;n}\rangle = \frac{\hbar^2}{2m} \int_{z \in \Omega_T} \mathrm{d}^3 r \nabla \left(\Psi_{S;n} \nabla \Psi_{T;p}^* - \Psi_{T;p}^* \nabla \Psi_{S;n} \right) \tag{4.13}$$

$$= \frac{\hbar^2}{2m} \int_{z \in \partial\Omega_T} \mathrm{d}\mathbf{S} \left(\Psi_{S;n} \nabla \Psi_{T;p}^* - \Psi_{T;p}^* \nabla \Psi_{S;n} \right), \tag{4.14}$$

where we applied Stokes' theorem to get the final result, which is known as Bardeen's transfer matrix formula. The integral should therefore be calculated on any surface on the boundary $\partial\Omega_T$ enclosing the infinite volume Ω_T, and is usually taken to be a plane at half distance between the tip and the surface.

We therefore have the transition probability between two states of the tip and the surface. To get the full probability, we need to sum over all possible pairs of such states. As such, we get the total current formula, also known as Bardeen's formula:

$$I = \frac{2\pi e}{\hbar} \sum_{n;p} \left[f(E_{S;n} - E_S^F) - f(E_{T;p} - E_T^F) \right] |M_{pn}|^2 \delta(E_{S;n} - E_{T;p} - eV), \tag{4.15}$$

where we introduced the Fermi energies of the surface E_S^F and the tip E_T^F, and the tip potential V. The matrix element M_{pn} is the one defined earlier, so $M_{pn} = \langle \Psi_{T;p}|V_T|\Psi_{S;n}\rangle$. We have also introduced the Fermi-Dirac distribution $f(E)$.

Assuming a quasi-continuous spectrum, one can take the continuous limit of the integral, which yields:

$$I = \frac{2\pi e}{\hbar} \int \mathrm{d}E \left[f(E - E_S^F) - f(E - eV - E_T^F) \right] |M(E, E - eV)|^2$$

$$\times \rho_S(E) \rho_T(E - eV), \tag{4.16}$$

where the matrix element $M(E, E - eV)$ is the continuous equivalent of the matrix transition element M_{pn}, and ρ_S and ρ_T are respectively the surface and tip density of states, which can be defined as $\rho_{S/T}(E) = \sum_n \delta(E - E_{S/T;n})$.

As most STM measurement are done near zero Kelvin to avoid all thermal effects on the sample, we can take the low temperature limit where the Fermi functions can be replaced by Heaviside step functions and as such the current can be shown to become:

$$I = \frac{2\pi e^2 V}{\hbar} \left| M(E_S^F, E_T^F) \right|^2 \rho_S(E_S^F) \rho_T(E_T^F), \tag{4.17}$$

which is strongly reminiscent of a local form of the Julliere model of conductance ([248]), with the added matrix transfer element that will depend on the relative location of the tip as compared to the surface.

4.2.2 Chen's approximation

The so-called Chen approximation [244] consists in expanding the tip wavefunction over the set of spherical harmonics:

$$\Psi_{T;p} \approx \sum_\beta c_{T;p,\beta} \Phi_\beta, \tag{4.18}$$

where the Φ are the basis functions of the expansion, that can be factorized as $\Phi_\beta = \Phi_{lm} = R_{lm} Y_{lm}$, where R is a the radial wavefunction and Y a spherical harmonic.

We will first consider the case of a single wavefunction tip $\Psi_{T;p} = c_{T;p,lm} R_{lm} Y_{lm}$. Since we assumed the separation between the tip and the surface to be sufficiently large, their respective wavefunctions follow the free particle Schrödinger equation near the separation surface:

$$\left(\nabla^2 - \kappa_p^2 \right) \Psi(r) = 0. \tag{4.19}$$

We introduced the vacuum decay constant $\kappa_p = \sqrt{2m E_{T;p}}$. One can then apply this equation to this case for the tip and get that the radial wavefunctions R_{lm} are in fact modified spherical Bessel functions of the second kind $R_{lm} = k_l(\kappa_p |\mathbf{r} - \mathbf{r_0}|)$, where $\mathbf{r_0}$ is the position of the tip apex atom. These functions have the following recurrence properties:

$$(2l + 1)k_l(z) = z k_{l-1}(z) - z k_{l+1}(z) \tag{4.20}$$

$$z \frac{d}{dz} k_l(z) = z k_{l+1}(z) + l k_l(z), \tag{4.21}$$

for any $z > 0$. Now, the associated Green function follows the equation:

$$\left(\nabla^2 - \kappa_p^2 \right) G(\mathbf{r} - \mathbf{r_0}) = -\delta(\mathbf{r} - \mathbf{r_0}), \tag{4.22}$$

which admits a spherical wave as solution:

$$G(\mathbf{r} - \mathbf{r_0}) = \frac{\exp\left(-\kappa_p \left|\mathbf{r} - \mathbf{r_0}\right|\right)}{4\pi \left|\mathbf{r} - \mathbf{r_0}\right|} = \frac{\kappa_p}{4\pi} k_0(\kappa_p \left|\mathbf{r} - \mathbf{r_0}\right|). \tag{4.23}$$

Using the Bessel recurrence relation of equation (4.20), one can show that there exists a set of derivative operators $\partial_{p,lm}$ acting on the Green function to yield the Basis functions $\Phi_{lm} = 4\pi/\kappa_p \, \partial_{p,lm} G$. These operators are known in this context as Chen's differentiation operators, and they can written up to the d shell as:

Y_{lm}	s	p_x	p_y	p_z	d_{xy}	d_{yz}	$d_{x^2-y^2}$	d_{zx}	d_{z^2}
$\partial_{p,lm}$	1	$\kappa_p^{-1}\partial_x$	$\kappa_p^{-1}\partial_y$	$\kappa_p^{-1}\partial_z$	$\kappa_p^{-2}\partial_x\partial_y$	$\kappa_p^{-2}\partial_y\partial_z$	$\kappa_p^{-2}\left(\partial_x^2 - \partial_y^2\right)$	$\kappa_p^{-2}\partial_z\partial_x$	$3\kappa_p^{-2}\partial_z^2 - 1$

TABLE 4.1 – List of adimensional Chen operators up to the l=2 case

Using the Bardeen transfer matrix formula (4.13), one can show that for a purely s tip $\Psi_{T;p} = C k_0(\kappa_p \left|\mathbf{r} - \mathbf{r_0}\right|)$, where C is some normalization constant, we have:

$$\begin{aligned}
M_{pn} &= \frac{\hbar^2}{2m} \int_{z\in\Omega_T} \mathrm{d}^3 r \left(\Psi_{S;n}\nabla^2\Psi_{T;p}^* - \Psi_{T;p}^*\nabla^2\Psi_{S;n}\right) \\
&= \frac{\hbar^2 C}{2m} \int_{z\in\Omega_T} \mathrm{d}^3 r \left(\Psi_{S;n}\nabla^2 k_0(\kappa_p \left|\mathbf{r} - \mathbf{r_0}\right|) - k_0(\kappa_p \left|\mathbf{r} - \mathbf{r_0}\right|)\nabla^2\Psi_{S;n}\right) \\
&= \frac{2\pi\hbar^2 C}{\kappa_p m} \int_{z\in\Omega_T} \mathrm{d}^3 r \left(\Psi_{S;n}\nabla^2 G(\mathbf{r} - \mathbf{r_0}) - G(\mathbf{r} - \mathbf{r_0})\nabla^2\Psi_{S;n}\right) \\
&= -\frac{2\pi\hbar^2 C}{\kappa_p m} \int_{z\in\Omega_T} \mathrm{d}^3 r\,\Psi_{S;n}\delta(\mathbf{r} - \mathbf{r_0}) \\
&= -\frac{2\pi\hbar^2 C}{\kappa_p m}\Psi_{S;n}(\mathbf{r_0}), \tag{4.24}
\end{aligned}$$

where equations (4.22) and (4.19) yield the fourth line. Note that the sample wavefunction has the same decay constant as the tip because we are studying elastic tunneling, which conserves the energy. This is the well known Tersoff-Hamann transfer matrix formula, that will be studied in depth in the next subsection, but we can already see that the matrix element is proportional to the sample wavefunction at the tip position.

As a straightforward and very important consequence of this, we can compute the derivative $\partial_{p,lm}^0 \Psi_{S;n}(\mathbf{r_0})$, where ∂^0 should be understood as a derivative along the tip coordinates $\mathbf{r_0} = (x_0, y_0, z_0)$:

$$\begin{aligned}
-\frac{2\pi\hbar^2 C}{\kappa_p m}\partial_{p,lm}^0\Psi_{S;n}(\mathbf{r_0}) &= \frac{2\pi\hbar^2 C}{\kappa_p m} \int_{z\in\Omega_T} \mathrm{d}^3 r \left(\Psi_{S;n}\nabla^2\partial_{p,lm}^0 G(\mathbf{r} - \mathbf{r_0}) - \partial_{p,lm}^0 G(\mathbf{r} - \mathbf{r_0})\nabla^2\Psi_{S;n}\right) \\
&= \frac{\hbar^2 C}{2m} \int_{z\in\Omega_T} \mathrm{d}^3 r \left(\Psi_{S;n}\nabla^2\Phi_{lm}(\mathbf{r} - \mathbf{r_0}) - \Phi_{lm}(\mathbf{r} - \mathbf{r_0})\nabla^2\Psi_{S;n}\right) \\
&= M_{lm,n}, \tag{4.25}
\end{aligned}$$

so that the derivatives of the sample wavefunction yield the matrix elements $M_{lm,n}$ with a pure lm tip, a result that is known as Chen's derivative rule. A more involved derivation can be used to show that the result still holds in the general case considered in equation (4.18), which leads to the so-called Chen's summation rule:

$$\Psi_{T;p} \approx \sum_{lm} c_{T;p,lm} k_l Y_{lm} \iff M_{pn} = -\frac{2\pi\hbar^2}{\kappa_p m} \sum_{lm} c_{T;p,lm} \partial^0_{p,lm} \Psi_{S;n}(\mathbf{r_0}), \qquad (4.26)$$

so that the Matrix transition element can be written in the general case as a linear combination of the lm derivatives of the sample wavefunction, with the same coefficients as for the wave expansion itself.

We will now focus on two particular aspects of this formula: the decay length and the expansion coefficients.

The decay length

In the previous section, we have introduced the characteristic decay length κ_p. As the tip is not an ideal atom, this decay length needs to be evaluated carefully as the wavefunctions are not rigorously exponentially decaying. One needs to introduce the following integral quantities:

$$\Sigma_x = \frac{1}{\Delta_z} \int z \mathrm{d}z = \frac{z_{max}^2 - z_{min}^2}{2\Delta_z} \qquad (4.27)$$

$$\Sigma_{x^2} = \frac{1}{\Delta_z} \int z^2 \mathrm{d}z = \frac{z_{max}^3 - z_{min}^3}{3\Delta_z} \qquad (4.28)$$

$$\Sigma_y = \frac{1}{\Delta_z} \int \log(\Psi_{T;p}) \mathrm{d}z \qquad (4.29)$$

$$\Sigma_{y^2} = \frac{1}{\Delta_z} \int \log(\Psi_{T;p})^2 \mathrm{d}z \qquad (4.30)$$

$$\Sigma_{xy} = \frac{1}{\Delta_z} \int z \log(\Psi_{T;p}) \mathrm{d}z, \qquad (4.31)$$

where the integrals are evaluated over the range $[z_{min}, z_{max}]$, and Δ_z is the step of integration. Note that $[z_{min}, z_{max}]$ is a subset of the total range of the wavefunctions as the exponential behaviour is only true asymptotically, and such evaluating an effective decay with this method will lead to spurious results if the range of the z-values comes too close to the tip. In practice, the cutoff z_{max} is taken to be half the height of the vacuum region between the tip and the surface, so that $\Delta_z =: 2(z_{max} - z_{min})/N$, with N the total number of points in the grid. Now, assuming a perfectly exponential wavefunction $\Psi_{T;p} = A_{T;p}(x, y) \exp(-\kappa_p z)$, the following

results can be shown:

$$\frac{\Sigma_{xy} - \Delta_z \Sigma_x \Sigma_y}{\Sigma_{x^2} - \Delta_z \Sigma_x^2} = -\kappa_p \tag{4.32}$$

$$\frac{\Sigma_y \Sigma_{x^2} - \Sigma_x \Sigma_{xy}}{\Sigma_{x^2} - \Delta_z \Sigma_x^2} = \frac{\log(A_{T;p}(x,y))}{\Delta_z} \tag{4.33}$$

$$\left| \frac{\Sigma_{xy} - \Delta_z \Sigma_x \Sigma_y}{\sqrt{\left(\Sigma_{x^2} - \Delta_z \Sigma_x^2\right)\left(\Sigma_{y^2} - \Delta_z \Sigma_y^2\right)}} \right| = 1. \tag{4.34}$$

Therefore, one can evaluate the effective exponential parameters for an arbitrary tip using these formulas. In practice, only the first formula of equation (4.32) is needed to get the effective decay, the third formula is then used to gauge the quality of the approximation as it can be shown to be strictly inferior to its ideal value of 1 when the tip is not perfectly exponential (a direct consequence of the Cauchy-Schwarz inequality). The second formula can be used to compute an effective amplitude, allowing one to perform an analytical continuation of the exponential approximation of the tip wavefunctions above the cutoff z_{max} although we will not be interested in that aspect here.

The projection coefficients

The expansion of the tip wavefunction in terms of hydrogenoid wavefunctions requires the evaluation of the coefficients $c_{T;p,lm}$.

Obviously, carrying the projection of the wavefunction yielded by some DFT code over a localized basis will yield these coefficients, although one needs to be careful as these basis sets are not complete over the entire space and as such the projection will not be norm-preserving. Another way of evaluating these coefficients stems from the approximate orthogonality of the hydrogen wave function within the augmentation sphere Ω_A:

$$\int_{\Omega_A} |\Psi_{T;p}|^2 \, \mathrm{d}^3 r = \sum_{lm,l'm'} c_{T;p,lm} c^*_{T;p,l'm'} \int_{\Omega_A} \Phi^*_{l'm'} \Phi_{lm} \mathrm{d}^3 r \approx \sum_{lm} |c_{T;p,lm}|^2, \tag{4.35}$$

and as such the tip density of states can be written as:

$$\rho_T(E) = \sum_p \left(\int_{\Omega_A} |\Psi_{T;p}|^2 \, \mathrm{d}^3 r \right) \delta(E - E_{T;p}) = \sum_p \left(\sum_{lm} |c_{T;p,lm}|^2 \, \delta(E - E_{T;p}) \right)$$

$$\leftrightarrow \rho_T(E) = \sum_p \rho_{T;p} \delta(E - E_{T;p}), \tag{4.36}$$

where the $\rho_{T;p}$ are the tip partial occupations, projected over the p band of the tip. As such, one could define the projections as $c_{T;p,lm} = \sqrt{\rho_{T;p}}$ and therefore weight the different Chen channels with the partial occupations. The main advantage of this method is that the partial

occupations are a very usual output from any DFT code as they are used to define the very commonly used partial densities of states, whereas the projections coefficients themselves usually require more involvement as we emphasized earlier.

The last method is to consider idealized lm tips. In that case, one can take any mixture of states such that $\sum_{\beta} |c_{T;p,lm}|^2 = 1$, and the tip decay is usually fixed at unity: $\kappa_p = 1$ Å^{-1}.

4.2.3 The Tersoff-Hamann approximation

As we emphasized earlier, the particular case of the pure ideal s tip Chen approximation leads to the very well known Tersoff-Hamann approximation. In this case, we have in the discrete case:

$$|M_{pn}|^2 = \left| \frac{2\pi\hbar^2 C}{\kappa_p m} \Psi_{S;n}(\mathbf{r_0}) \right|^2$$

$$\rightarrow I = \frac{8\pi^3\hbar^3 C^2 e}{m^2} \sum_n \left[f(E_{S;n} - E_S^F) - f(E_{T;p} - E_T^F) \right] |\Psi_{S;n}(\mathbf{r_0})|^2 \, \delta(E_{S;n} - E_{T;p} - eV)$$

$$\rightarrow I = \frac{8\pi^3\hbar^3 C^2 e}{m^2} \sum_n \left[f(E_{S;n} - E_S^F) - f(E_{T;p} - E_T^F) \right] \rho_S(\mathbf{r_0}, E_{S;n})\delta(E_{S;n} - E_{T;p} - eV),$$

$$(4.37)$$

and in the continuous case:

$$I = \frac{8\pi^3\hbar^3 C^2 e}{m^2} \int dE \left[f(E - E_S^F) - f(E - eV - E_T^F) \right] |\Psi_{S;n}(\mathbf{r_0})|^2 \rho_S(E - E_S^F)\rho_T(E - eV - E_T^F)$$

$$= \frac{8\pi^3\hbar^3 C^2 e}{m^2} \rho_T(E_T^F) \int_0^{eV} dE \rho_L^S(\mathbf{r}, E + E_S^F),$$

where we introduced the local density of states (LDOS) of the surface $\rho_L^S(\mathbf{r}, E) = \sum_{\mu} |\Psi_{\mu}(\mathbf{r})|^2 \delta(E - E_{\mu})$. This is the so-called Tersoff-Hamann formula, which shows that the tunneling current is a map of the local density of states of the surface, which allows a fast estimation of the STM images as the LDOS can be very easily evaluated within any DFT code starting from the Kohn-Sham states. Doing a low voltage, low temperature expansion of this previous formula yields:

$$I \approx \pi eV \rho^T(E_F)\rho_L^S(\mathbf{r}, E_F) \tag{4.38}$$

$$G \approx \pi e \rho^T(E_F)\rho_L^S(\mathbf{r}, E_F), \tag{4.39}$$

The last line defines the local Tersoff-Hamann conductance at low temperatures, a formula that is formally identical to the local Julliere model. As such, this is the formula commonly used to compute STM images at the Tersoff-Hamann approximation within DFT, as they are in this case nothing but contour maps of the local density of states (up to a normalization factor which is inaccessible anyway as we have emphasized earlier).

4.3   Methods

The calculation is done through a personal Python implementation of the previous methods, that takes however extensive inspiration from the seminal bSKAN code of Hofer *et al.* ([249, 250]) that is the standard for the simulation of STM images within and beyond the Tersoff-Hamann approximation. As such, exactly like bSKAN does, the code uses as an input wavefunctions from VASP that are Fourier transformed along x and y, using the STM module implemented within VASP itself. This leads to several numerical simplifications, and most notably, the Bardeen transfer matrix integration becomes analytical which massively reduces the numerical cost of the Bardeen method (for more details, see [250]). Our implementation makes an extensive use of the `opt_einsum` module of Python ([251]), that allows for very efficient parallelised and vectorized calculations of tensor contractions for an extremely fast evaluation of the current using the massive Fourier matrices that arise as a result of the calculation of the transfer matrix elements within the Fourier basis (several hundreds of GB of RAM are required for a Bardeen transfer matrix calculation). The Fourier transformation is carried over a 16 Å range with steps of 0.1 Å, so over 160 points, starting from a distance of 7 Å above the top of the molecule down to the metallic surface ; and a distance from 2 Å to 18 Å above the apex for the tips, so that the apex of the tip and the top of the sample are separated by 9 Å. Note that the HS state is shifted 0.2 Å higher than the LS state in the supercell. For consistency, the molecule is converged using exactly the same parameters as for the other chapters so we refer once again the reader to the first part for the details of the DFT calculation.

As we are interested in a magnetically non-trivial system, we have considered two tip materials : tungsten (non-ferromagnetic) and iron (ferromagnetic). We have tried to consider several geometries, as the shape of the tip is known to play a major role on the resulting image [252] : a large commensurate system sharing its lateral dimensions with the molecular supercell, so $20.4{\times}20.4$ Å^2. This system is built from a 5x5x3 slab of metal topped with a metal pyramid, which is therefore not a periodic system within the supercell although this is perfectly acceptable as the Bardeen formula only requires the wavefunction at the tip apex and these vanish way before the edges of the surface so that the calculation is strongly agnostic to such finite size effects. We have also tried to use the smaller supercell geometry that is used by Mandi *et al.* in their own pioneering study on post Tersoff-Hamann methods of calculation [252]. However, we had memory related numerical issues with the latter as the required k-point sampling to obtain meaningful results led to excessive computationnal costs for the image simulation. As such, we will only use the commensurate tips for this paper, which have the advantage of leading to diagonal Bardeen matrix elements in the Fourier basis [250] and as such to significantly reduced computational costs for the complete Bardeen method along with being in accordance to the theoretical result for an integration over an infinite separation surface.

The tips are all converged using VASP, in the GGA approximation using the PBE functionnal using the same cutoff as the molecule so 500 eV. As the geometry of the tips that we are using is non-standard, in the sense that it does not correspond to a known stable system, ionic relaxation of the tips leads to deformations especially around the apex, which is going to greatly impact the final image obtained as it is strongly sensitive to the apex wavefunctions and hence to its geometry. Therefore, for consistency and reproducibility purposes, we do not allow the ionic positions of the tip to relax although we do recognise that this is not ideal. As we have a purely metallic tip, we are not using LDA+U in this case, nor are we using DFT-D2 Van der Waals corrections as these play no role in such a system.
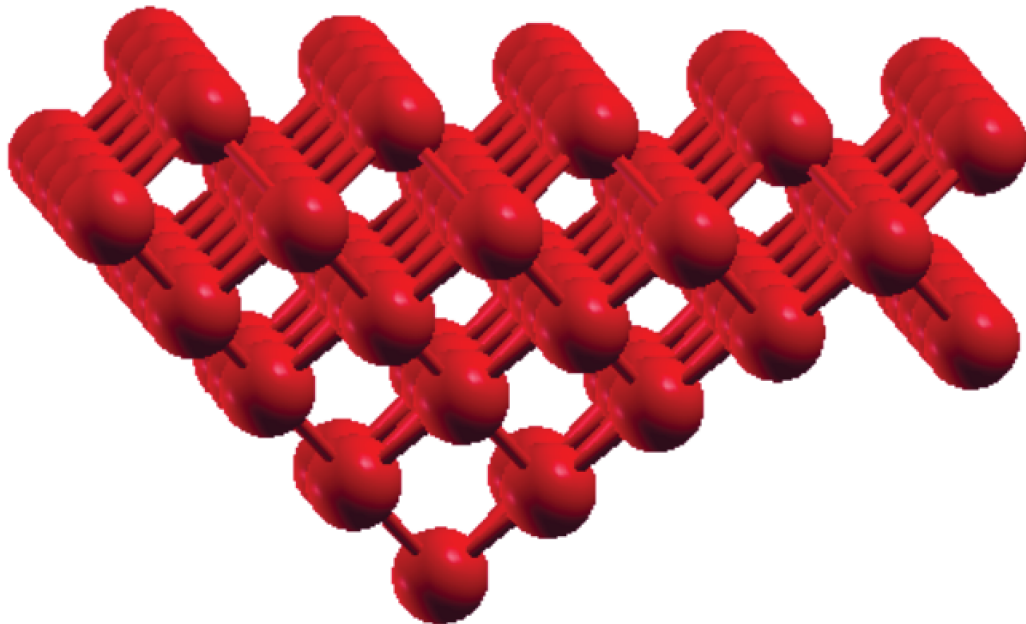
FIGURE 4.1 – Geometry of the theoretical STM tip

4.4 Experimental Results

The experimental STM images have been measured by Miyamachi *et al.* [21]. They show a clear difference between the HS and LS state, with a striking separation of the lobes of 1.1 nm in the former as compared to 0.8 nm in the latter. A corrugation difference of 30 pm between the HS and LS state has also been measured. Note that these images were taken at a large distance from the sample so as to be able to see clusters of such molecules on the surface, and as such the fine details of the images cannot be observed from the results.
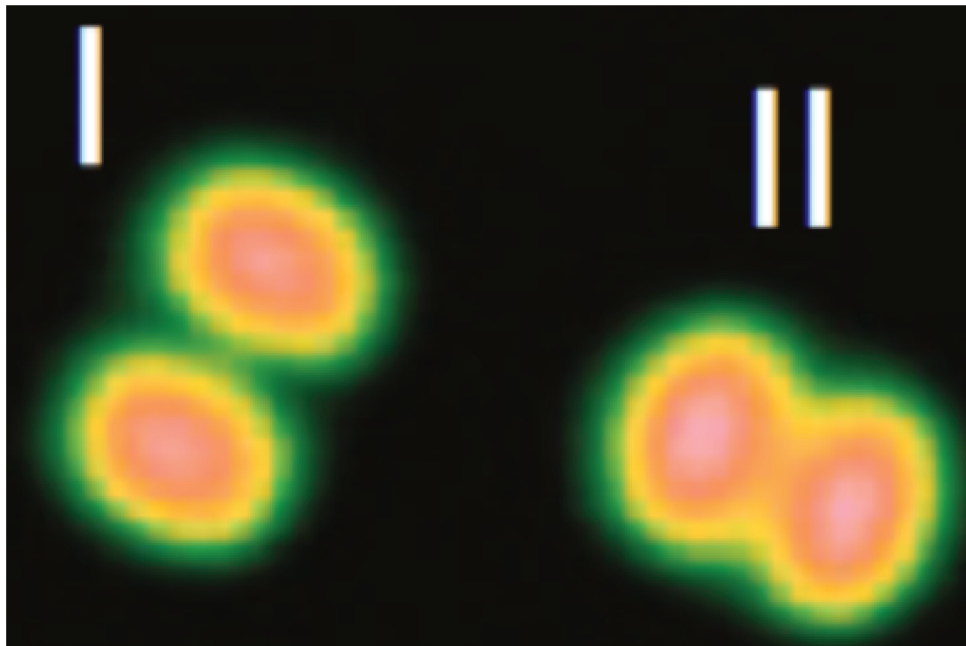
FIGURE 4.2 – Experimental constant current comparison of the STM images for the HS state (I) on the left and the LS state on the right (II). Reproduced from [21]

As such, we will now proceed with the theoretical computation of these images. We need to obtain both constant current and height images as the former will be obtained by using the maximal current value measured on the latter taken at a certain distance, however the latter cannot be rigorously normalized as we have already emphasized and is rarely studied experimentally as stabilizing the tip at a constant current value is much easier, and as such we will mainly focus on the constant current images and we will not study the constant height images unless stated otherwise. Besides, the qualitative information that can be extracted from either one of these images is the same.

4.5   Tersoff-Hamann approximation

As a first result, we will recompute within our code the Tersoff-Hamann images in the HS and LS states on the surface. To proceed, we took the maximal value of the "current" at 2 Å above the topmost point of the system and we used it to scan the image in the constant current mode, which corresponds to the usual experimental procedure for STM images. However, remember that there is no way to numerically compute the actual value of the current because of normalization issues so the absolute value of the computed current has no physical meaning whatsoever. We chose a very short distance from the top of the molecule for comparison purposes, as the d-tip images are decaying extremely fast as we will see in the next part, keeping in mind that we have to stay sufficiently far from the system to stay in the conditions of the Bardeen formula. We integrate up to 100 meV below the Fermi energy.

FIGURE 4.3 – Comparison of the Tersoff-Hamann (s tip) constant current STM images for the HS state on the left and the LS state on the right, along with their corresponding constant height image on the bottom. All lengths are in Å, the current value for the constant height image is in arbitrary units. Note that as we said earlier, there is a shift in height between the HS and LS molecules by 0.2Å, so that the axes on the constant current images are the same for both spin states up to said shift. Please note that the black dot on the picture is an unfortunate byproduct of the code but it does not affect the calculations in any way.

The images are in accordance with the previously established results [119, 173], with the two lobes of the FePhen molecule clearly visible both on the height and current images, showing a greater separation in the HS state in contrast with the LS state. As one can easily see, the current images are clearly much more detailed than the height images, so that only focusing on the first appears as a justified choice. The lobes of maximal height on the constant current images are separated by 5.3 Å on the HS image and by 4.6 Å on the LS image, although the difference is clearly not as striking as on the experimental results. Using the constant height images, one can see that the value of the current is higher in the HS state (2.3×10^{-8} a.u.) than in the LS state (7.2×10^{-9} a.u.) at a similar distance from the sample. Nonetheless, there are still noticeable differences between the experimental and theoretical images owing both the experimental conditions that we have already mentioned but also to the theoretical method

itself as the Tersoff-Hamann formula leads to excessively detailed pictures because of the perfect s tip. As such, we will now go beyond this approximation by using the Chen derivative rule for s,p and d tips.

4.6   Chen approximation

We will now extend our previous results by computing the images within the Chen approximation [244]. We will start with pure p and d tips, and then compute the images for the more realistic tips that we have introduced earlier.

4.6.1   Pure tips

We will now give the images for all the pure s, p and d tips. The p tip is defined as the weighted tip contructed from the three p states $\Psi_T = \frac{1}{\sqrt{3}}\left(p_x + p_y + p_z\right)$ and the d tip from the five d states $\Psi_T = \frac{1}{\sqrt{5}}\left(d_{xy} + d_{yz} + d_{xz} + d_{x^2-y^2} + d_{z^2}\right)$. The images were taken using the same parameters than for the Tersoff-Hamann images.
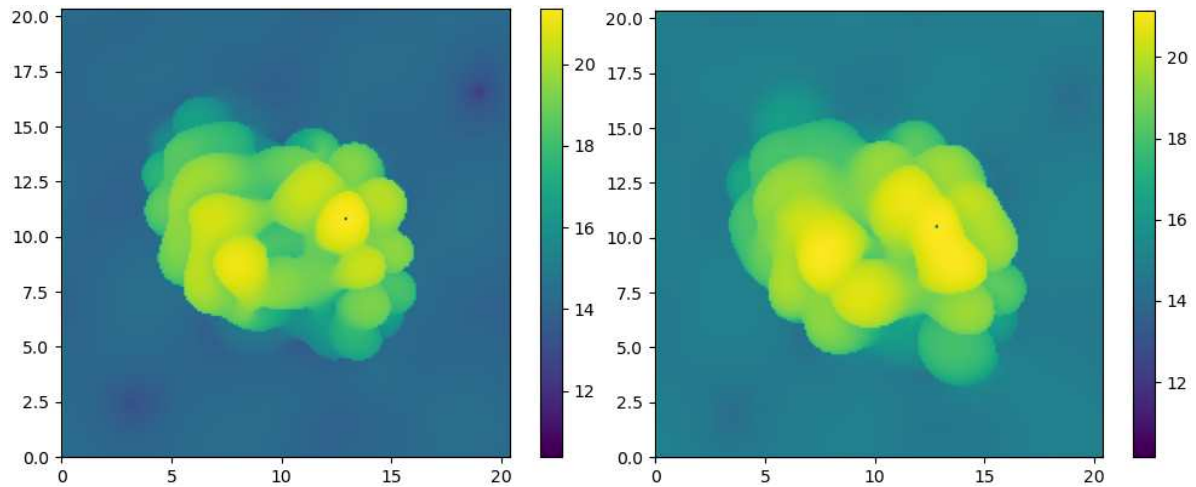
FIGURE 4.4 – Comparison of the p tip constant current STM images for the HS state on the left and the LS state on the right, All quantities are in Å.

As on can see, the s tip and p tip images show very strong similarities at first glance, with similar appearance and organization of the corrugation lobes in the HS and LS states. A very convenient way to quantify this is to compute the correlation factor between these images [253, 254]. Doing so, we get a value of 0.966 between the HS images and 0.974 between the LS images for both tips, which is appreciably close to 1 and therefore shows their similarity. Note however that this value is skewed towards 1 by the background which cannot be entirely neglected during this calculation. The separation between the lobes of maximal height is of

5.3 Å in the HS state and 4.6 Å in the LS state. These results are indeed very similar to what was obtained with the s tip, and as such the ideal balanced p tip is quite similar to the ideal s tip.
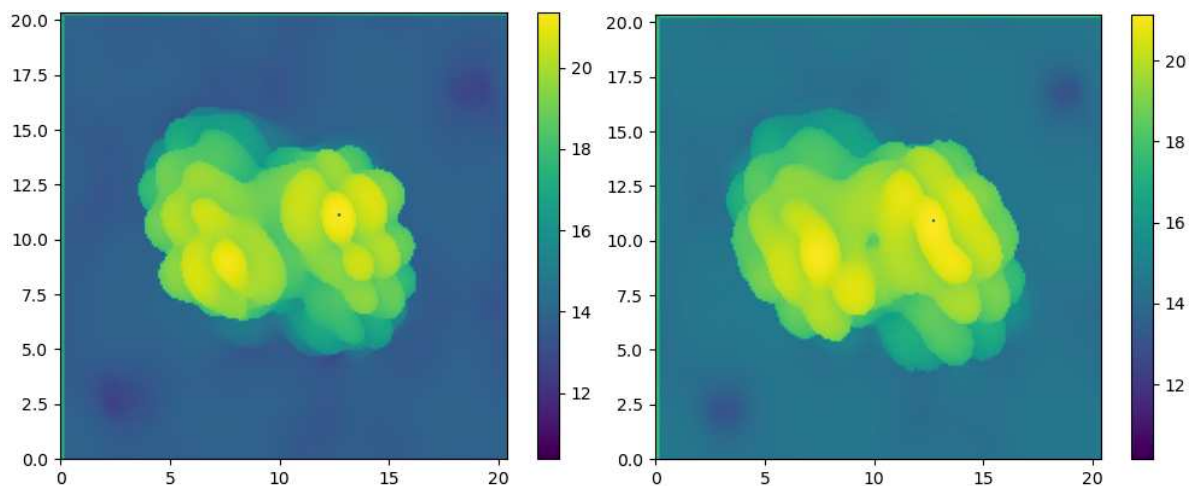
FIGURE 4.5 – Comparison of the d tip constant current STM images for the HS state on the left and the LS state on the right. All quantities are in Å.

In this case, the STM images are still similar to the previous results but one can start to clearly note the difference with the previous cases, with the corrugation lobes being smaller than for the previous tips. In fact, this appears to be a general trend, as the p tip corrugation lobes were also smaller than for the s tip (see 4.6). The correlation matrix yields a factor of 0.930 in the HS state and 0.954 in the LS state, which is indeed smaller than for the p tip indicating less agreement with the s tip, although this is still indicative of a strong overlap between the images. Besides, the correlation between the p tip and the d tip yields a value of 0.941 in the HS state and 0.958 in the LS state, showing that the d tip is slightly closer to the p tip than to the s tip but not by a truly significant margin. The separation between the lobes, especially in the HS state, is however the most clearly visible here and is quite reminescent of the experimental result, with a value of 5.6 Å in the HS state and 5.3 Åin the LS state which are larger values than for the previous tips.
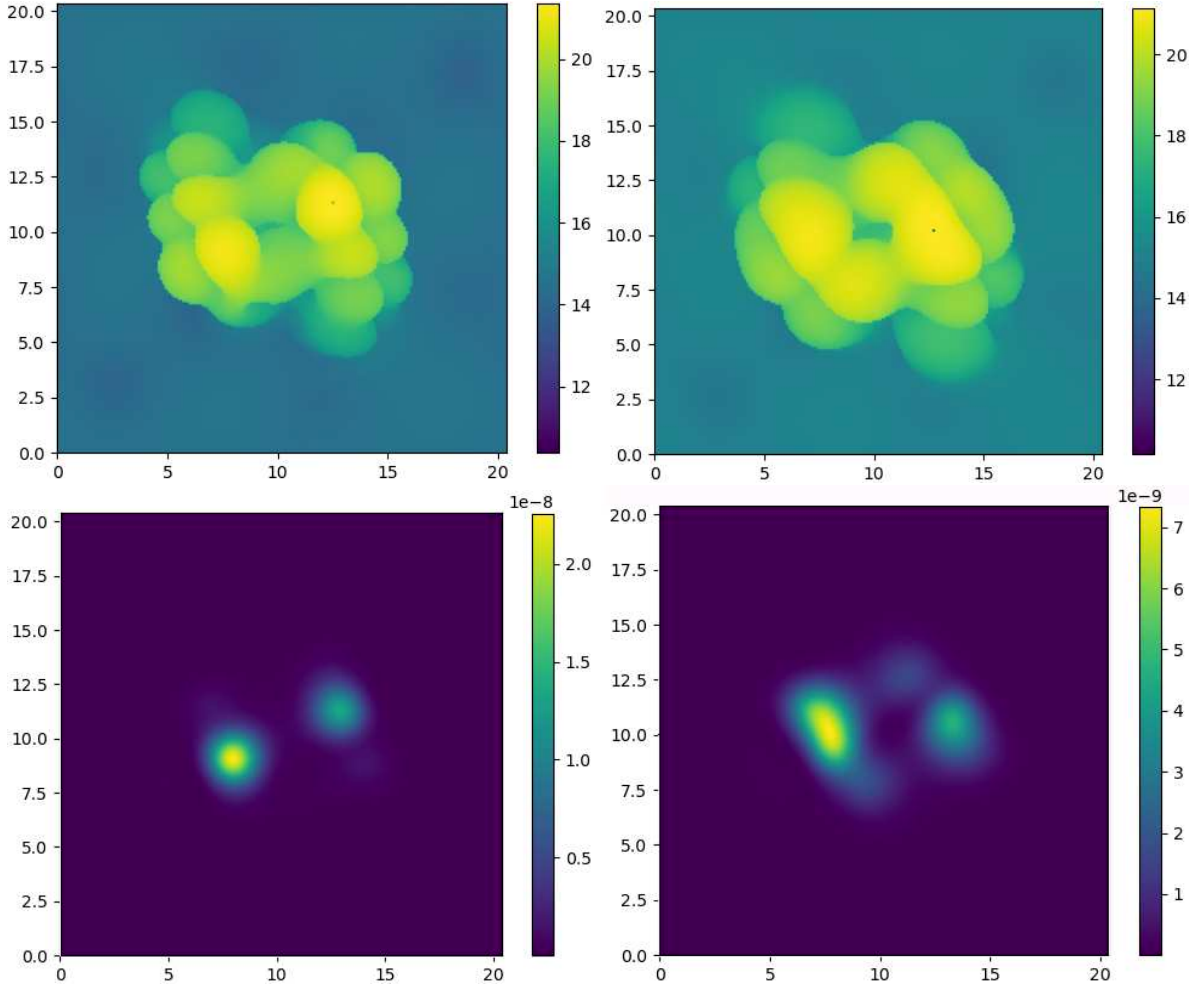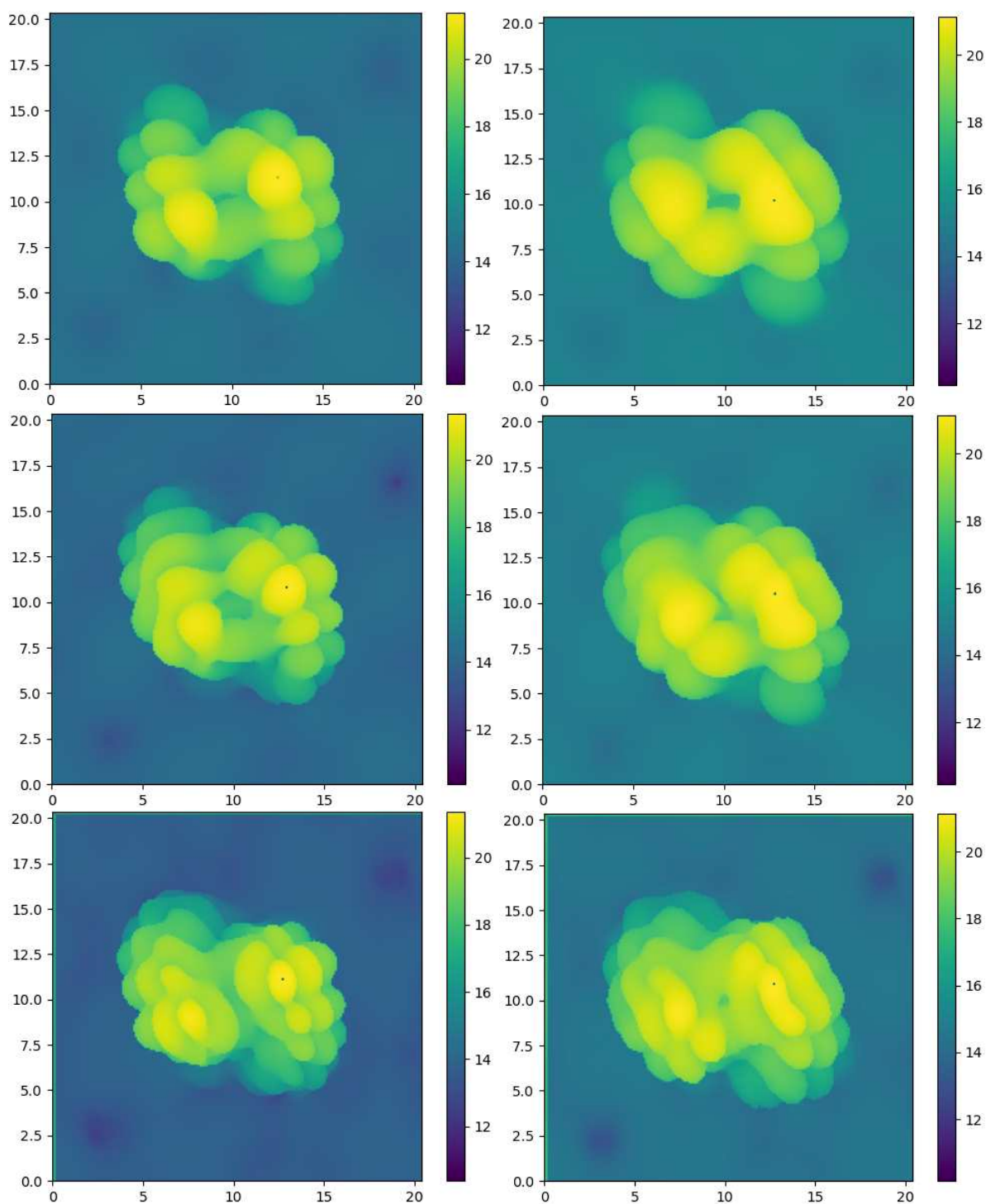
FIGURE 4.6 – Comparison of the s,p and d tip constant current STM images for the HS state on the left and the LS state on the right.

As a sidenote, the correlation between the HS and LS images themselves yield a value of 0.941 for the s tip, 0.929 for the p tip and 0.916 for the d tip, showing that the images from both spin states still show a fair amount of similarity. Beyond obvious background contribution, this was to be expected as the difference in geometry between both systems is not massive and as such there is a fair overlap with most of the molecule beyond the topmost points of the

main lobes. As such, the value of the correlation is skewed towards 1 because of these points, points stemming from an idealised tip and that are clearly visible on the theoretical images but not on the experimental images which shows a clear difference between both spin states. Hence, going beyond the idea of a perfect tip towards a more realistic mixture of states such as the one used within the total Chen derivative formula is a natural step as it could yield results in better accordance with the litterature by taking into account the actual electronic structure of the tip.

4.6.2 Realistic tips

We will now proceed with calculations of the STM images using Chen's formula. However, because of numerical issues, we could not compute these images on a grid as dense as for the previous cases, and as such all images within this part were computed on a coarser grid than before and then interpolated back to the larger grid. We realize that this is not ideal as it will lead to blurrier images, so that the comparison with the previous images is going to be imperfect, although the loss in quality will remain limited as we will see.

Projection coefficients

Unlike the previous cases, the use of realistic tips within the Chen approximation leads to several changes from the previous idealized cases. Indeed, we now have to explicitly take into account the electronic structure of the tip. At the Chen approximation level, we do need to reconstitute the tip wavefunctions to compute the decay length for all eigenstates, which is done by using the formula previously introduced and taking the maximal value of the resulting decay parameter over the xy grid as this will naturally correspond to the vertical direction under an ideal tip. However, we do not require any more information from these wavefunctions themselves as we do not need to carry a numerical integration of the Bardeen transfer matrix elements. Hence, only the projections coefficients and the eigenvalues truly need to be stored and used as is. As such, we will begin with a quick comparison of the two main ways to compute these coefficients, which are to take the direct projection coefficients from the DFT code, which is the theoretically exact method, or the square root of the tip partial occupations which is an approximation over the previous case as we will neglect the relative phases between. Very conveniently, VASP returns both sets of data in the same file so we can readily evaluate both approaches without any supplementary calculation. Note that energy conservation between the tip and surface eigenvalues is assured by the use of a Gaussian smearing of the tunneling matrix elements, with a width of 0.01 eV:
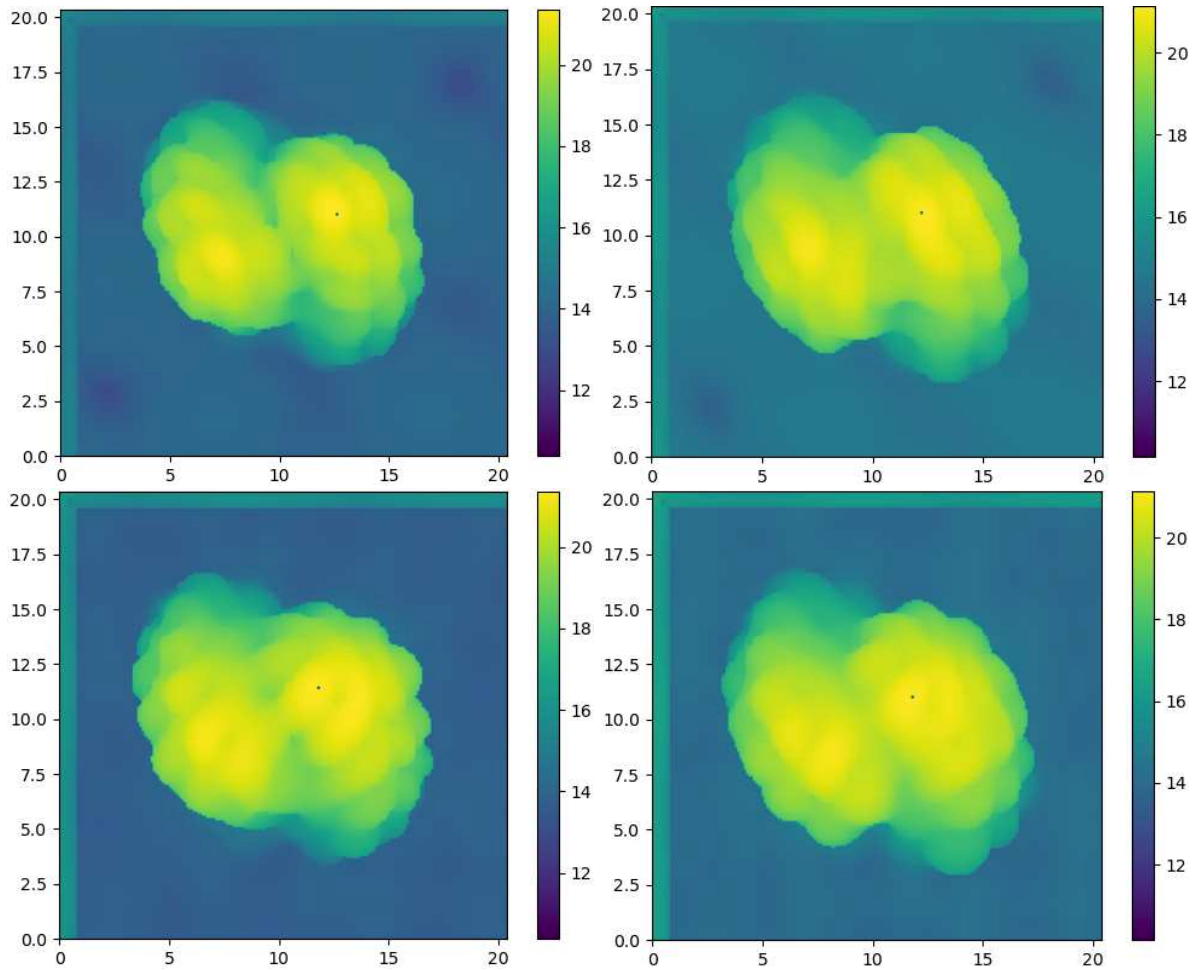
FIGURE 4.7 – Comparison of the Chen rule constant current STM images for an iron tip in the HS state on the left and in the LS state on the right, with complex projection coefficients on the top and population projection coefficients on the bottom. Note that the green band at the edges of the images is a purely numerical effect

As one can easily see, there are indeed a few differences between both methods, as it seems that the population projection coefficients slightly overestimates the overlap between both lobes as compared to the complex coefficients. We can compute correlation factors of 0.958 in the HS state and 0.973 in the LS state, which are somewhat high values compared to what we saw earlier but one should remember that the images required an interpolation, which blurs the fine details so that the correlation gets skewed towards 1. Still, one can easily see that both images do show a clear amount of similarity. As both approaches can be evaluated at the same time in our case, since VASP yields both sets of coefficents within the same file, we will be only interested in the complex coefficients as they don't incur any approximation in the projection of the wavefunction over the atomic orbitals beyond the use of an augmentation cutoff for the radial integration. As we have noted earlier, this does imply that the projection coefficients are not normalised, and therefore they need to be renormalized before their use in Chen's formula.

Iron and Tungsten tips

We will now proceed with a comparison between the images obtained with an iron tip and those obtained with a tungsten tip:

FIGURE 4.8 – Comparison of the Chen rule STM images for the HS state on the left and the LS state on the right, with an iron tip on the top and a tungsten tip on the bottom.

Both tips show a great similarity, with the major difference being that the overlap between the lobes appears to be bigger with the iron tip than with the tungsten tip although the separation remains the same. This leads to a correlation factor of 0.947 in the HS state and 0.967 in the LS state. Besides, both images show a great similarity with the pure iron d tip image, so that we have correlation values with the d tip of 0.952 for the Fe tip and 0.967 for the W tip in the HS state, and 0.976 for the Fe tip and 0.967 for the W tip in the LS state. As both Iron and Tungsten have d states near the Fermi energy, such a result is not surprising as the tips should be mostly with a d character which is exactly what we see on these images, but it is interesting to see that the ferromagnetic character of the iron tip does not really affect the images as compared to a magnetically trivial tungsten tip.

4.7   Bardeen approximation

In order to compute images within the Bardeen approximation, we need to be careful as the necessity to carry an actual integration of the overlap between the tip and surface wavefunctions in order to compute the Bardeen matrix elements entails a fair amount of subtleties depending on the nature of the tip and/or the sample. In our case, a very important issue lies in the fact that we are studying a molecule on a surface, which is a system with a very salient topography compared to the usual slabs, and this will have an impact on the definition of the separation surface for the integration. Most notably, one should be mindful about the integration plane as it should in theory be in the vacuum region separating the tip and the surface, and is usually taken at half distance between these two, but the exact location within this region does not matter as the value of the transition current does not vary much (see for example [255]). As such, we used a large separation distance of 9 Å so that the plane is located 2 Å above the molecule and 7 Å below the tip to guarantee a sufficient distance from the apex.
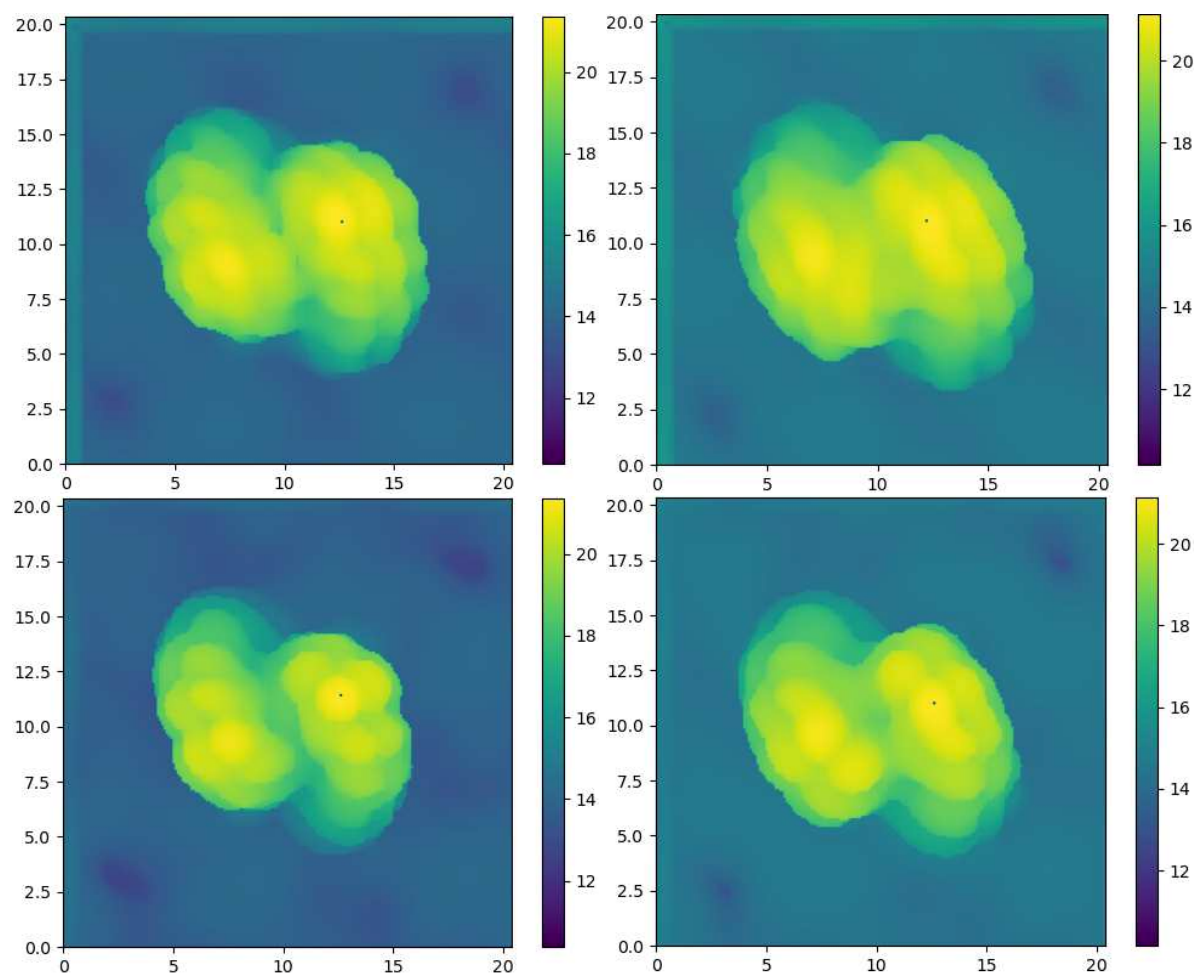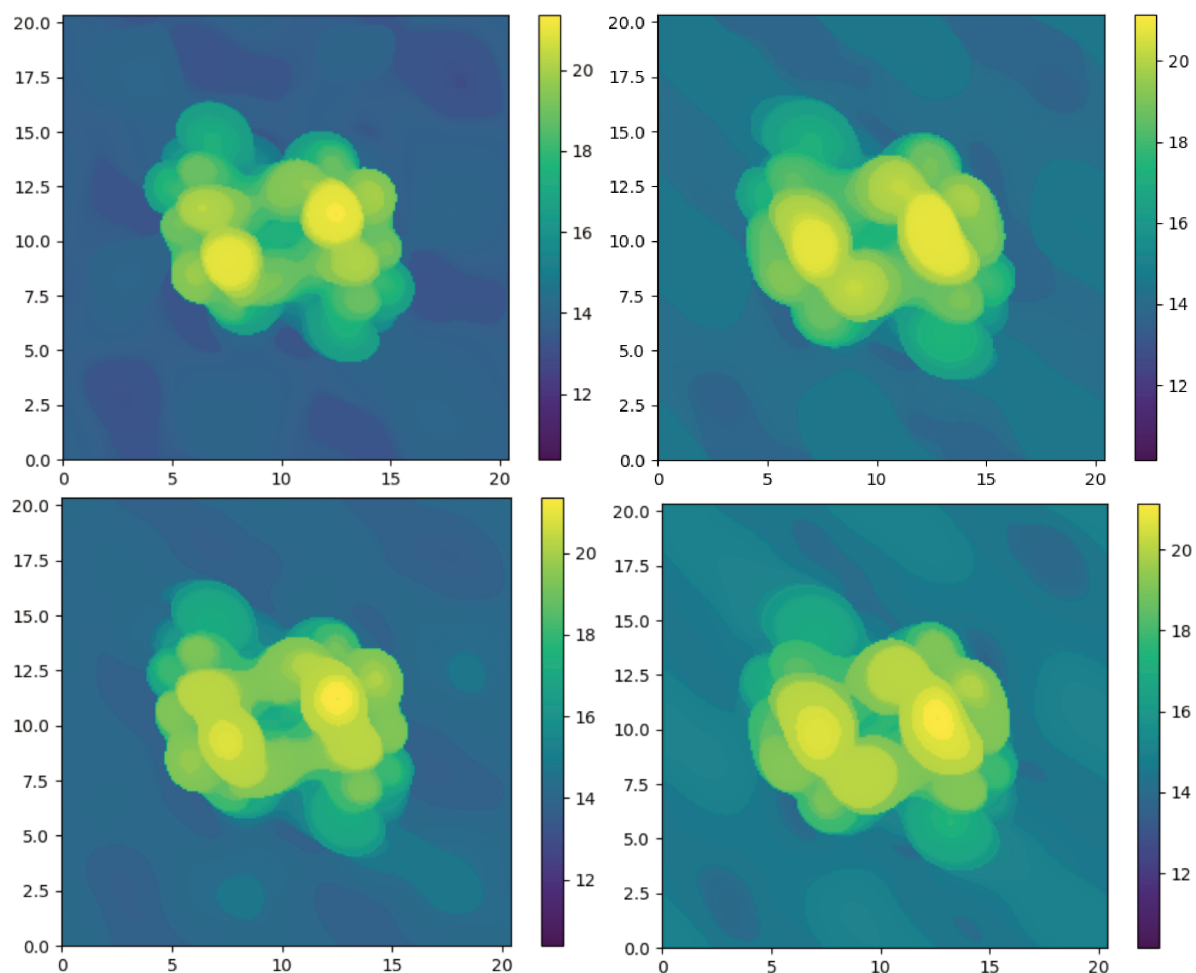

FIGURE 4.9 – Comparison of the Bardeen rule STM images for the HS state on the left and the LS state on the right, with an iron tip on the top and a tungsten tip on the bottom.

As one can easily see from the images, the Bardeen images are in great agreement with the Tersoff-Hamann s tip images and the experimental results, with a correlation in the HS state of 0.950 between the Fe tip and the s tip, and 0.935 between the W tip and the s tip. The tip themselves show slight discrepancies, with a correlation of 0.894 between the Fe tip and the W tip, as one can see that the lobes are more localized with the Fe tip that is closer to the s tip image as compared to the W tip where they are more diffuse. In the LS state, the correlation between the Fe tip and the s tip is 0.946, whereas it has a value of 0.972 between the W tip and the s tip and 0.985 between the two tips themselves. As such, both tips show a great similarity in this case, although it is the W tip that is closer to the Tersoff Hamman result with more diffuse lobes, however not by a significant amount. Hence, just as in the Chen case, the electronic structure difference does not play a large role in the images, which are in strong agreement with the Tersoff Hamann images. This result can easily be understood by the fact that we took a large separation length between the tip and the surface, so that we are approaching the large distance limit of the Bardeen approximation which is identical to the Tersoff-Hamann formula [255], whereas the Chen formula leads to corrections that certainly are only meaningful at shorter distances in our case and vanish very fast just as we said earlier. Hence, to properly demonstrate this behaviour, one could redo these calculations with smaller separation distances and see if the results are converging towards the Chen images, although time constraints prevented us from doing so within this thesis and this is still a work in progress.

4.8   Conclusion

In this part, we have studied the simulation of STM images beyond the Tersoff-Hamann approximation. We have developed a personal implementation of the calculation of STM images within the Bardeen transfer matrix approach that is interfaced with the VASP code, based on the influential bSKAN code [249] which is the most used code for this purpose. We first started by recomputing the images within the Tersoff-Hamann approximation, showing that our results broadly agrees with the previously available experimental and theoretical litterature as our images clearly show the strength of the Tersoff-Hamann approximation in reproducing the general features of the STM images, with a visible set of two lobes being separated by a larger distance in the HS state compared to the LS state, although the excessive detail and corrugation leads to noticeable diffrences with the experimental results. As such, we computed the images within the Chen approximation, starting with pure p and d tips, and showed that these images have great similarities with the s tip, although one can clearly see corrugation differences on the images that may impact the eventual experimental images depending on the nature of the tip. The exact Chen approximation with a ferromagnetic (iron) and non-magnetic tip (tungsten) yield results in great similarity with those of a d tip, in accordance

with their electronic structure, whereas the Bardeen approximation shows a great accordance with the Tersoff-Hamann case as one could have expected from the large separation that we have used between the tip and the surface. Howerver, we note a lack of apparent difference between these two tips, indicating that the use of a ferromagnetic tip should not in principle bring much diffrence on the STM images over the non-ferromagnetic one in our case, although this is awaiting experimental confirmation.

Conclusion and Perspectives

In this Thesis, we have used ab-initio methods, mainly density functionnal theory within the VASP code, to extend the theoretical physics of spin crossover molecules on metallic surfaces.

In a first part, we have studied the fluorine doping of a Fephen molecule in a free phase or adsorbed on a Cu(001) substrate. Starting from a study of the energetics of the spin states, we have observed that this doping leads to an inversion of the spin state which then stays in the high spin state at low temperature, whether the molecule is in the gas phase or absorbed on the metal surface. Looking at the geometry of the system, we show that while the overall geometry of the complex is not affected by the doping, we observe a clear elongation of the Ligand-metal bonds which leads to a stronger deformation of the central octahedron of the complex. Such elongations can only weaken the Fe-N bond, and therefore decrease the electrostatic field of the ligands at the level of the central atom. As such, this should lead to a reduction of the octahedral Δ and therefore stabilize the HS state with respect to the LS state as we saw earlier. This is demonstrated by computing the densities of state, which show a clear reduction in the separation between the e_g and t_{2g} peaks, and therefore of the octahedral Δ, which is more noticeable in the HS state. The combined use of the Bader analysis of the charge distribution and a point charge model demonstrates that the doping leads to a wide electronic rearrangement within the molecule radiating from the C-F bonds in the Phen Ligand and caused by the high electronegativity of the fluorine atoms, which ultimately increases the charge of the nitrogen ions in the central octahedron. Thus, the electronic repulsion with the octahedral centre is increased, leading to a stretching of the bonds and hence to the observed result. We have also used the Nudged Elastic Band (NEB) to compute the transition path and show that the transition barrier is reduced in the doped molecule, so that the reversible transition from the HS state to the LS state should be easier in principle.

As such, our doping procedure potentially opens a new way to manipulate the spin crossover phenomenon in molecules on metallic surfaces, and most notably to fine tune the balance between the HS and LS states by partially fluorinating the system in order to reduce the amount of energy required to trigger the SCO to create efficient spintronical devices, although this is still awaiting for an experimental realization and confirmation as the energetics of

spin crossover systems is a fairly complex matter to simulate properly. To go further, we were interested in studying other doping compounds, beginning with the other halogen atoms beyond Fluorine. Early results seem to indicate a competition between the decreasing electronegativity of the successive halogens which restabilizes the LS state, and the increasing steric hindrance induced by the size of the doping atoms which stabilizes the HS state by causing widespread stretching across the molecule. However, we are still awaiting for experimental data about the realizability of said systems before truly proceeding any further. We have also computed the phonon spectrum within the harmonic approximation in the undoped and doped system, using a finite difference method, and we showed that in both cases the spin crossover phenomenon is mainly linked to frequencies associated with the N-C-S and Fe-N bonds. We do observe a softening of these modes in the doped molecule, which together with the reversal of the spin states leads to the stabilization of the HS state against the LS state at all temperatures. This was to be expected as entropy will in most cases stabilize the former over the latter as we have shown earlier, so that the molecule always remains in the HS state. The calculation of of the phonon spectrum in the undoped molecule, on the other hand, clearly shows an inversion of the spin state at a transition temperature of 167 K, appreciably close to the experimental result, as the stronger vibrationnal enthalpy in the HS state than in the LS state drives the transition from one state to the other. The use of the Slichter-Drickamer model along with the thermodynamic quantities derived from the previous calculation allowed us to compute the evolution of the HS fraction with Temperature, with decent agreement to the available experimental results. However, our calculation of the phonon spectrum beyond the harmonic approximation is still highly inconclusive, and as such, we would like to go further in that direction. First of all, we were interested in other methods to compute the phonon spectrum beyond the harmonic approximation. Most notably, we also tried to use the so-called TDEP method ([202]), which relies in a linear fit of AIMD extracted displacements and forces in order to extract the phonon spectrum. However, the convergence of the linear regression parameters to the phonon spectrum proved to be extremely slow with our large molecule, even when using regularization techniques, so that we could only obtain highly inaccurate spectra. We also tried to use the so-called SCAILD method ([256]), with an equal lack of success as the method relies on a self-consistent calculation of phonon displacement that diverged very easily in our case, leading to highly inaccurate frequencies. As such, we are still investigating for other ab-initio methods in order to compute the phonon spectrum at finite temperature, notably near the transition point as this is an entropy mediated phenomenon as to the extent of our knowledge no one has ever carried such as study on the intramolecular phonons of the FePhen molecule, most of the literature available being on intermolecular interactions (which is understandable, as these are the main driving force behind the cooperativity parameter which plays an essential role in the shape of the spin-transition phenomenon as we have seen with the Slichter-Drickamer model, see for example ([257])).

The second part of this Thesis dealt with the simulation of X-Ray absorption within the spin crossover compounds, which is one the most used tool to characterize spin crossover compounds, along with other examples such as scanning tunnel microscopy and Mossbauer spectroscopy. We have therefore implemented the calculation of XAS and XMCD within VASP, using the dipolar approximation, in order to compute the $L_{2,3}$ edge absorption in the iron atom of the FePhen molecule. we obtained results in qualitative accordance with the already available experimental results, with however issues related to the intensities of the absorption peaks that are known to depend on the influence of the multiplet structure or electron-hole interaction which we have neglected thus far. However, VASP has implemented the static calculation of electron-hole interactions by allowing the creation of a static hole within the core. Using this, we show that after relaxation the valence shell electrons shield the created hole which therefore leads to a strong reduction of the magnetic moment of the Iron atom and therefore to a spurious modification of the absorption signal. We have also carried an analysis of the resulting signal in terms of the density of states, showing within our implementation of XAS the well-known formula relating absorption spectra and densities of states so that it is possible to know which states contribute to the XAS signal by analyzing the structure of the DOS, but also to directly compute the absorption spectrum from the densities of state of the valence electrons under some assumptions. We have also shown that the incidence angle of the polarized beam has a direct impact on the XMCD signal, and that this can be directly correlated to the local deformation of the octahedral complex as it lifts the degeneracy between the 3d states. Similarly, we have shown that the magnetisation direction also has an impact on the XMCD signal and therefore its relation to the magnetic anisotropy of the Iron atom. We have therfore computed the magnetization blocking temperature of the system, and shown that the sum rules are well respected for all directions of the magnetization as long as one adds the oft-neglected contribution of the magnetic dipole tensor, that we have also implemented within VASP. Once again, these last predictions are awaiting for future experimental confirmation. As such, a natural extension to this work would be going beyond the dipolar approximation, by adding quadrupolar corrections to the absorption calculation, whose relevance in some systems has already been demonstrated ([258]) and for which sum rules have also already been computed ([259]). Interestingly, it is possible to relate the magnetic dipole tensor to the quadrupole contribution ([260]) so that implementing it would give another way of computing the corrections to the sum rules. Beyond this, we have also started to implement the calculation of X-ray spectra within a so-called Ligand Field DFT (LFDFT) approach, as it provides a convenient way to take into account the multiplet structure within the XAS spectra calculation ([261]) that is a requirement for more accurate results as we have already emphasized. Besides, we were also looking forward to add electron-hole corrections based on the seminal work of De Dominicis and Nozières ([262]) on the treatment of the scattering of conduction electrons by the hole created during X-Ray absorption, so that we can fully take into account the two

major contributions (multiplet and eletron-hole) to the spectrum that we have neglected.

Finally, we implemented the calculation of STM images within and beyond the Tersoff-Hamann approximation, interfaced with VASP and directly based on the bSKAN code of Hofer *et al.* ([250, 249]). This allowed us to compute the Tersoff-Hamann images, with great accordance wth the already available theoretical and experimental literature, but also to go beyond the Tersoff-Hamann approximation and use the Chen approximation to show the influence of diffrent tip symmetries on the spectra. While pure tips of p and d character show great similarities at first glance to the Tersoff-Hamann formula, we can clearly see differences in the corrugation depending on the tip symmetry. Such diffrences may be observed in an eventual experimental STM investigation of a single FePhen molecule, as most available results were taken at a large distance from the surface in order to see clusters of molecules, conditions under which the Tersoff-Hamann limit is perfectly valid so that no supplementary insight could be obtained from other more advanced approximations. The simulation of realistic iron and tungsten tips within the total Chen derivative formula show as expected images in great accordance with a perfect d tip, although we also noted an interesting lack of difference between the ferromagnetic iron tip and the non-magnetic tungsten tip. This could be seen as surprising given that both the sample and the tip are magnetic, and as such one could have expected some spin-polarized effects to arise with the iron tip. The images within the Bardeen approximation are in great accordance with the Tersoff-Hamann result, as expected given the large separation between the tip and the surface, and we are still investigating the short range limit to see if we are able to reproduce the Chen corrections. A natural next step in the simulation of these STM images is to use a multiparticle approach such as the one based on the Landauer-Büttiker formula [263], which was already leveraged with success in order to compute STM images [264] with better accuracy than the full Bardeen formula [265]. Extension beyond the Landauer-Büttiker formula based on the Meir-Wingreen formula [266] within a non equilibrium Green Function framework (NEGF) [267] have also been studied, most notably within the context of inelastic tunneling spectroscopy [268] which could be of huge intrest in our case as this can be used in principle to detect and analyse vibrationnal modes excited by tunneling electrons and therefore provide another means to study the phonon spectrum of these molecules. Naturally, we are also investigating scanning tunnel spectroscopy (STS), expecially with the idea of trying to reproduce and study the well known Kondo effect observed in certain SCO compounds on metallic surfaces ([242]) that has been the basis of a widespread body of work linked to its potential functionalization for e.g. memristive components ([21]), although a one-particle approach such as the Bardeen formula might not be sufficient in this case, instead requiring a full NEGF based calculation.

Appendix

A   The point charge model

A point charge model is a simple model neglecting all hydridizations, that allows one to qualitatively understand the d orbital splitting caused by an arbitrary ligand field. In this model, all ligands are assumed to be point-like charges which create a Coulomb potential which interacts with the central metal orbitals. As we are interested in the octahedral $e_g - t_{2g}$ splitting, it is necessary to rotate the global frame of reference to the local frame of reference, i.e., to find the frame that is maximally oriented along the ligands as the octahedral e_g and t_{2g} are only well defined with respect to a local frame along the atomic bonds. Working in said local frame, it is possible to expand the ligand field potential as:

$$V(r) = \sum_{i,l,m} (-1)^m \frac{4\pi q_i}{2l+1} Y_l^{-m}(\mathbf{r}) Y_l^m(\mathbf{R_i}) \frac{r_<^l}{r_>^{l+1}}, \tag{40}$$

with q_i the charge of the ligand i and R_i the vector between i and the central metal, and the Y_l^m are the spherical harmonics. The $r_<$ and $r_>$ should be understood as a shorter notation for $min(|\mathbf{r}|, |\mathbf{R_i}|)$ and $max(|\mathbf{r}|, |\mathbf{R_i}|)$.

We can then compute the overlap matrix elements of the iron 3d orbitals:

$$M_{m,m''} = \langle \Phi_2^m | V | \Phi_2^{m''} \rangle = \int \sum_{i,l,m'} (-1)^{m+m'} \frac{4\pi q_i}{2l+1} \phi(r)^2 Y_2^{-m}(\mathbf{r}) Y_l^{-m'}(\mathbf{r}) Y_l^{m'}(\mathbf{R_i}) Y_2^{m''}(\mathbf{r}) \frac{r_<^l}{r_>^{l+1}} d\mathbf{r}, \tag{41}$$

where the Φ_l^m are the nlm orbitals wavefunctions, with here $n = 3$ and $l = d = 2$, the n index being implicit. After some calculations, this can be written as:

$$M_{m,m''} = \sum_{i,l,m'} (-1)^{m+m'} \frac{Z}{a_0} \frac{q_i}{216\, X_i} \sqrt{\frac{4\pi}{2l+1}} \begin{pmatrix} 2 & 2 & l \\ 0 & 0 & 0 \end{pmatrix} \begin{pmatrix} 2 & 2 & l \\ m'' & -m & -m' \end{pmatrix} \tag{42}$$
$$\times \left[\frac{1}{X_i^l} \gamma(l+7, X_i) + X_i^{l+1} \Gamma(6-l, X_i) \right],$$

where $Z = 6.25$ is the shielded atomic number of iron according to Slater's rules [269], a_0 the Bohr radius and $X_i = 2ZR_i/3a_0$.

We use the Wigner-3j symbols, defined from the Clebsch-Gordan coefficients as:

$$\begin{pmatrix} l_1 & l_2 & l_3 \\ m_1 & m_2 & m_3 \end{pmatrix} = \frac{(-1)^{l1-l2-m3}}{\sqrt{2l_3 + 1}} \langle l_1 \, m_1 \, l_2 \, m_2 | \, l_3 \, (-m_3) \rangle. \tag{43}$$

They have wholesome properties such as:

— $-l_i \leq m_i \leq l_i$

— $(-m_3) = m_1 + m_2$.

— $l_1 + l_2 + l_3$ must be an integer, an even integer if $m_1 = m_2 = m_3 = 0$.

— $|l_1 - l_2| \leq l_3 \leq l_1 + l_2$

This allows us to restrict the summation over $l = 0, 2, 4$ and $m' = m - m"$.

We used the lower incomplete gamma function $\gamma(s, x)$ and higher incomplete gamma function $\Gamma(s, x)$, defined as:

$$\gamma(s, x) = \int_0^x \rho^{s-1} exp(-\rho) d\rho \tag{44}$$

$$\Gamma(s, x) = \int_x^\infty \rho^{s-1} exp(-\rho) d\rho. \tag{45}$$

We can then diagonalize the M matrix and extract the eignevalues and their e_g and t_{2g} mixing parts. We have to be careful about the fact that the matrix M is in the spherical harmonics basis set, while the e_g and t_{2g} orbitals are in the cubic harmonics set. For convenience, we directly define the transformation matrix between the spherical harmonics and the cubic harmonics:

$$U = \begin{pmatrix} \frac{i}{\sqrt{2}} & 0 & 0 & 0 & \frac{-i}{\sqrt{2}} \\ 0 & \frac{1}{\sqrt{2}} & 0 & \frac{-1}{\sqrt{2}} & 0 \\ 0 & 0 & 1 & 0 & 0 \\ 0 & \frac{i}{\sqrt{2}} & 0 & \frac{i}{\sqrt{2}} & 0 \\ \frac{1}{\sqrt{2}} & 0 & 0 & 0 & \frac{1}{\sqrt{2}} \end{pmatrix}, \tag{46}$$

and we will directly work on the transformed matrix $M' = UMU^\dagger$, with the t_{2g} being the $m = -2, -1, 1$ states and e_g the $m = 0, 2$ states.

B   Note on the Magnetic dipole operator

It is well knwon that the contribution of T_z always vanishes for a perfect O_h symmetry complex of a $3d$ transition metal without spin-orbit coupling. In order to demonstrate this, we first note that in that case the magnetic dipole moment can be rewritten as:

$$\langle \hat{T}_z \rangle = -4\sqrt{\frac{\pi}{5}} \sum_i m_{s,i} \langle i|(\hat{Y}_2^0)|i \rangle \tag{47}$$

$$= -2\sqrt{\frac{\pi}{5}} \sum_{u,d} (\langle u|(\hat{Y}_2^0)|u \rangle - \langle d|(\hat{Y}_2^0)|d \rangle), \tag{48}$$

where the index i runs over all the electrons of the ground state, and u, d runs over the up and down populations respectively. For a d^6 Fe^{2+} complex, we now need to consider the ground state configuration in both spin states:

— In the LS state, the ground state corresponds to a closed t_{2g} subshell. In that case, the magnetic dipole operator is trivially vanishing as the two spin contributions that are summed over are the same up to the spin sign.

— In the HS state, the ground state can be constructed by half-filling all five d orbitals with the same spin direction, then filling with an equal probability one of the three t_{2g} orbitals with an electron of opposite spin. Sum rules over the Clebsch-Gordan coefficients can be used to show that:

$$\begin{cases} \sum_m C_{2,0,2,m}^{2,m} = 0 \\ 2C_{2,0,2,-1}^{2,-1} + 2C_{2,0,2,1}^{2,1} + C_{2,0,2,2}^{2,2} + C_{2,0,2,-2}^{2,-2} = 0. \end{cases} \tag{49}$$

Using the definition of the d orbitals and equation (3.25), it can easily be seen that the majority spin contribution to the magnetic dipole operator is proportional to the first line, whereas the minority spin is proportional to the second line. As such, the magnetic dipole tensor vanishes exactly in this case.

When the spin-orbit interaction is taken into account, the moment still vanishes in the LS state as the two spinor directions are effectively degenerate in that case and we can therefore use a very similar reasoning than in the non-relativistic case. The case of the HS state is much more complex, and it can be shown that the magnetic dipole tensor takes a non-vanishing value for certain ground state geometries, including the d^6 geometry of Fe^{2+} [240]. With this in mind, we computed the value of the magnetic dipole moment in our molecules with (SO) and without (NSO) the spin orbit:

Molecule	NSO	SO
LS (surface/gas)	0	0
HS (surface)	-0.091	-0.101
HS (gas phase)	-0.150	-0.161

TABLE 2 – Value of T_z in the molecular systems in the HS and LS state (in μ_B).

As expected, the magnetic dipole operator vanishes in the low spin state. For the high spin state, we immediately note that the moment is superior in the gas phase than on the surface, but most importantly that the operator does not vanish even without spin-orbit, and the spin orbit contribution is minimal. To rationalize this apparent contradiction, we need to recall that our previous reasoning was only valid for a perfect octahedral geometry, and that the deformation of a real complex is often non-negligible especially in the HS state. Distortion is known to play a noticeable effect on the features of x-ray absorption spectra (see for example Ref. [270]), and therefore it is of no surprise that it should influence the value of T_z (this was already noted, but not shown explicitly, in [219]). Informally, distortion breaks the ideal symmetry between the d-states that is observed in Eq. 47, and as consequence the sum rules of Eq. 49 are no longer applicable. Instead, each state is now a mixture weighted by the PAW projections such as in equation Eq. 3.26, and there is no *a priori* reason for said sum to vanish when both spin directions are not degenerate such as in the HS state, even in the absence of SOC. In order to give a better illustration of this phenomenon, we will quantify the "amount" of deformation of these systems away from their ideal geometry. We need first to optimally rotate and rescale our system before comparing it to a reference geometry. This is the essence of the so-called extended orthogonal Procrustes algorithm [271]. As a short summary, assume a set of points $\mathbf{u}$ and a reference set of points $\mathbf{v}$ (the molecular octahedral coordinates and an ideal octahedron coordinates respectively in our case). An obvious way of defining a "distance" to quantitatively compare these structure is to carry a root median square displacement calculation between these two structures, taking into account the fact that both systems need to be properly rescaled together to have an accurate comparison. Then, we can recast the associated least-square deviation problem as a search for the ideal rotation $\mathbf{R}$ and scale factor c between $\mathbf{u}$ and $\mathbf{v}$, so that we can write the cost function associated to this RMSD calculation as:

$$L(\theta, \Phi) = \frac{1}{2}||\mathbf{v} - c\mathbf{R}(\theta, \Phi)\mathbf{u}||^2,$$

that needs to be minimized over the set of angular variables (θ, Φ) and c. For the rotation part, the solution can be found ([271]) by computing the singular value decomposition of the covariance matrix $H = \mathbf{u}^{\mathbf{T}}\mathbf{v}$:

$$\mathbf{H} = \mathbf{U}\mathbf{\Sigma}\mathbf{V}^{\mathbf{T}} \rightarrow \mathbf{R} = \mathbf{V}\mathbf{\Sigma}'\mathbf{U}^{\mathbf{T}},$$

where $\mathbf{\Sigma}'$ is a $3x3$ diagonal matrix with diagonal elements $d_1 = 1, d_2 = 1$ and $d_3 = \text{sign}(\det(\mathbf{VU^T}))$, which is used to enforce the positive definiteness of the determinant of the rotation matrix, so that we always have a proper transformation. For the scale factor, using the definition of the matrix norm $||A|| = \text{Tr}(A^T A)$ in the previous formula for the RMSD cost function, one can show ([271]) that the minimization yields the following result:

$$c = \frac{\text{Tr}(\mathbf{u^T R^T v})}{\text{Tr}(\mathbf{u^T u})}. \tag{50}$$

Applying these to our case, we can obtain a quantitative estimate of the deviation of the molecular geometries from the ideal octahedral geometry. We also add a deviation to an ideal tetrahedral geometry by comparing it to an imperfect tetrahedron using the 4 shortest ligand bonds in our molecular octahedron (as the average bond length in a tetrahedral complex is shorter than for an octahedral complex):

	HS (gas phase)	HS (surface)	LS (gas phase)	LS(surface)
Octahedral Loss	0.016	0.011	0.002	0.002
Tetrahedral Loss	0.044	0.048	0.082	0.147
Ratio Oct/Tet	0.363	0.229	0.024	0.014

TABLE 3 – Value of the Loss function in the molecular systems (in Å^2) with respect to an ideal octahedral and tetrahedral geometry, and ratio between the two values.

We can see that the octahedral RMSD is an order of magnitude higher in the high spin state than the low spin state, and the same applies to the ratio between the octahedral and tetrahedral RMSD. As such, not only is the geometry more strongly deformed in the high spin state than in the low spin states, the non negligible ratio between the octahedral and tetrahedral RMSD in the HS state shows that the absolute deformation away from the ideal case is sizeable. Besides, the deformation in the HS state is clearly larger in the gas phase than when the molecule is adsorbed on the surface. It is therefore of no surprise that the magnetic dipole operator does not vanish in this case, even without spin-orbit corrections. However, this approach is quite rough as it "averages" over all the angular and length distortions and therefore it will not be able to discriminate between the finer details that characterize distortion, and as a consequence the exact dependence of the magnetic dipole moment with the value of the RMSD is highly non-trivial.

C Relation between XAS and local DOS

It is interesting to note that the XAS can be shown to be directly related to the iron $3d$ DOS, as noted for example in [272]. In our formulation, the relation takes a very simple form. First, we will need to use the position representation of the transition operator. Using the Schroedinger Equation, one can easily show that the Hamiltonian H and the position operator r_μ follow the commutation relation $[r_\mu, H] = i\hbar p_\mu/m_e$. This allows us to rewrite the cross section as:

$$\sigma^\mu(\omega) = 4\pi\alpha\hbar\omega \sum_{M,n,\mathbf{k},s} \left| \sum_{m'} C^{J,M}_{\ell',m',1/2,s}\langle n,\mathbf{k},s|r_\mu|\ell',m'\rangle \right|^2 \delta(\hbar\omega - \epsilon_{n\mathbf{k}s} + \epsilon_J).$$

Note that we used here the fine-structure degeneracy of the $\epsilon_{JM} = \epsilon_J$ over the set of M that was not relevant thus far for this study. We can then expand the squared norm as:

$$\sigma^\mu(\omega) = 4\pi\alpha\hbar\omega \sum_{\substack{M,m',m'' \\ n,\mathbf{k},s}} C^{J,M}_{\ell',m',1/2,s}C^{J,M}_{\ell',m'',1/2,s}\langle n,\mathbf{k},s|r_\mu|\ell',m'\rangle\langle \ell',m''|r_\mu|n,\mathbf{k},s\rangle \tag{51}$$

$$\delta(\hbar\omega - \epsilon_{n\mathbf{k}s} + \epsilon_J)$$

$$= 4\pi\alpha \sum_{\substack{M,m',m'' \\ n,\mathbf{k},s}} (\epsilon_{n\mathbf{k}s} - \epsilon_J)C^{J,M}_{\ell',m',1/2,s}C^{J,M}_{\ell',m'',1/2,s}\langle n,\mathbf{k},s|r_\mu|\ell',m'\rangle\langle \ell',m''|r_\mu|n,\mathbf{k},s\rangle$$

$$\delta(\hbar\omega - \epsilon_{n\mathbf{k}s} + \epsilon_J),$$

where we rewrote $\hbar\omega$ as $\epsilon_{n\mathbf{k}s} - \epsilon_J$ thanks to the delta function as we will need it for a following approximation. We will sum over the $\ell+1/2$ edge $\sigma^\mu_{\ell+1/2}(\omega)$ and $\ell-1/2$ edge $\sigma^\mu_{\ell-1/2}(\omega)$. To do so, we first need to shift them together as both spectra have different core energy references. We arbitrarily take the $\ell+1/2$ edge, and shift it by $\Delta\omega_J = (\epsilon_{\ell-1/2} - \epsilon_{\ell+1/2})/\hbar$. Doing so yields:

$$\sum_J \sigma^\mu_J(\omega) \approx 4\pi\alpha \sum_{\substack{J,M,m',m'' \\ n,\mathbf{k},s}} (\epsilon_{n\mathbf{k}s} - \epsilon_{\ell-1/2})C^{J,M}_{\ell',m',1/2,s}C^{J,M}_{\ell',m'',1/2,s} \tag{52}$$

$$\langle n,\mathbf{k},s|r_\mu|\ell',m'\rangle\langle \ell',m''r_\mu|n,\mathbf{k},s|\rangle\delta(\hbar\omega - \epsilon_{n\mathbf{k}s} + \epsilon_{\ell-1/2}),$$

where we neglected the variation of ϵ_J with respect to $\epsilon_{n\mathbf{k}s}$, because the core energies are located at several thousands of eV below the Fermi energy compared to our EXAFS range of a few hundreds of eV at the highest, and as such we will now write $\epsilon_{\ell-1/2} = \epsilon_C$. Now, we can

use the orthogonality property of the Clebsch-Gordan coefficients:

$$\sum_{J,M} C^{J,M}_{\ell',m',1/2,s} C^{J,M}_{\ell',m'',1/2,s} = \delta_{m',m''} \tag{53}$$

$$\sum_{m_1,m_2} C^{J,,M}_{\ell_1,m_1,\ell_2,m_2} C^{J',M'}_{\ell_1,m_1,\ell_2,m_2} = \delta_{J,J'}\delta_{M,M'},$$

and write:

$$\sum_{J} \sigma^{\mu}_{J}(\omega) = 4\pi\alpha \sum_{m',n,\mathbf{k},s} (\epsilon_{n\mathbf{k}s} - \epsilon_C)\langle n,\mathbf{k},s|r_\mu|\ell',m'\rangle\langle\ell',m'|r_\mu|n,\mathbf{k},s\rangle\delta(\hbar\omega - \epsilon_{n\mathbf{k}s} + \epsilon_C)$$

$$\tag{54}$$

$$= 4\pi\alpha\hbar\omega \sum_{m',n,\mathbf{k},s} \langle n,\mathbf{k},s|r_\mu|\ell',m'\rangle\langle\ell',m'|r_\mu|n,\mathbf{k},s\rangle\delta(\hbar\omega - \epsilon_{n\mathbf{k}s} + \epsilon_C).$$

Now, we can rewrite the Kohn-Sham eigenfunctions using the PAW method. For our purposes, we can remain at the partial wave contribution. We therefore have

$$\sum_{J} \sigma^{\mu}_{J}(\omega) = 4\pi\alpha\hbar\omega \sum_{\substack{m',n,\mathbf{k},s \\ p_1,\ell_1,p_2,\ell_2,m_1,m_2}} \langle p_1,\ell_1,m_1|r_\mu|\ell',m'\rangle\langle\ell',m'|r_\mu|p_2,\ell_2,m_2\rangle \tag{55}$$

$$\times P^{*n,\mathbf{k},s}_{p_1,\ell_1,m_1} P^{n,\mathbf{k},s}_{p_2,\ell_2,m_2}\delta(\hbar\omega - \epsilon_{n\mathbf{k}s} + \epsilon_C).$$

Writing $r_\mu = r\sqrt{\frac{4\pi}{3}}Y^\mu_1$, one can show that:

$$\langle p_1,\ell_1,m_1|r_\mu|\ell',m'\rangle = -\left(p_1,\ell_1|r|\ell'\right) C^{\ell',0}_{\ell_1,0,1,0}C^{\ell_1,m_1}_{1,\mu,\ell',m'}, \tag{56}$$

where the $(p_1,\ell_1|r|\ell')$ are the radial integrations introduced in Eq. 3.8. This leads to:

$$\sum_{J} \sigma^{\mu}_{J}(\omega) = 4\pi\alpha\hbar\omega \sum_{\substack{m',n,\mathbf{k},s \\ p_1,p_2,\ell_1,\ell_2,m_1,m_2}} (p_1,\ell_1|r|\ell')\,(\ell'|r|p_2,\ell_2)\, C^{\ell',0}_{\ell_1,0,1,0}C^{\ell',0}_{\ell_2,0,1,0}C^{\ell_1,m_1}_{1,\mu,\ell',m'}C^{\ell_2,m_2}_{1,\mu,\ell',m'}$$

$$\tag{57}$$

$$\times P^{*n,\mathbf{k},s}_{p_1,\ell_1,m_1} P^{n,\mathbf{k},s}_{p_2,\ell_2,m_2}\delta(\hbar\omega - \epsilon_{n\mathbf{k}s} + \epsilon_C).$$

We will now sum over all the polarization directions μ and use the orthogonality relations from equation (53):

$$
\begin{aligned}
\sigma(\omega) &= \sum_\mu \sum_J \sigma_J^\mu(\omega) \\
&= 4\pi\alpha\hbar\omega \sum_{\substack{\mu,m',n,\mathbf{k},s \\ p_1,\ell_1,p_2,\ell_2,m_1,m_2}} (p_1,\ell_1|r|\ell')\,(\ell'|r|p_2,\ell_2)\, C_{\ell_1,0,1,0}^{\ell',0} C_{\ell_2,0,1,0}^{\ell',0} C_{1,\mu,\ell',m'}^{\ell_1,m_1} C_{1,\mu,\ell',m'}^{\ell_2,m_2} \\
&\quad \times P^{*\,n,\mathbf{k},s}_{\ p_1,\ell_1,m_1} P^{n,\mathbf{k},s}_{p_2,\ell_2,m_2}\delta(\hbar\omega - \epsilon_{n\mathbf{k}s} + \epsilon_C) \\
&= 4\pi\alpha\hbar\omega \sum_{\substack{n,\mathbf{k},s \\ p_1,p_2,\ell_1,m_1}} (p_1,\ell_1|r|\ell')\,(\ell'|r|p_2,\ell_2)\,(C_{\ell',0,1,0}^{\ell_1,0})^2 \\
&\quad \times P^{*\,n,\mathbf{k},s}_{\ p_1,\ell_1,m_1} P^{n,\mathbf{k},s}_{p_2,\ell_1,m_1}\delta(\hbar\omega - \epsilon_{n\mathbf{k}s} + \epsilon_C).
\end{aligned}
\tag{58}
$$

Splitting the two allowed dipole transitions $\ell_1 = \ell'\pm 1$, and neglecting the overlap between different projectors, we can rewrite this as:

$$
\sigma(\omega) \approx 4\pi\alpha\hbar\omega \left[\left|(\ell'+1|r|\ell')C_{\ell'+1,0,1,0}^{\ell',0}\right|^2 \rho_{\ell'+1}(\omega + \epsilon_C/\hbar) + \left|(\ell'-1|r|\ell')C_{\ell',0,1,0}^{\ell'-1,0}\right|^2 \rho_{\ell'-1}(\omega + \epsilon_C/\hbar) \right]
\tag{59}
$$

$$
= 4\pi\alpha\hbar(\omega' - \epsilon_C/\hbar) \left[\frac{\ell'+1}{2\ell'+3} \left|(\ell'+1|r|l')\right|^2 \rho_{\ell'+1}(\omega') + \frac{\ell'}{2\ell'-1}\left|(\ell'-1|r|\ell')\right|^2 \rho_{\ell'-1}(\omega') \right]
$$

$$
= A_{\ell'}(\omega')\rho_{\ell'+1}(\omega') + B_{\ell'}(\omega')\rho_{\ell'-1}(\omega'),
$$

where we introduced the ℓ partial densities of states ρ_ℓ and the shifted frequencies $\omega' = \omega + \epsilon_C/\hbar$. Therefore, the normalized edge $\sigma(\omega)$ can be written as a weighted sum of the partial densities of states corresponding to the dipole allowed ℓ values.

Bibliographie

[1] L. Cambi et L. Szegö. "Über die magnetische Susceptibilität der komplexen Verbindungen". *Berichte der deutschen chemischen Gesellschaft (A and B Series)* 64.10 (1931), p. 2591-2598.

[2] L. Cambi et L. Szegö. "Über die magnetische Susceptibilität der komplexen Verbindungen (II. Mitteil.)." *Berichte der deutschen chemischen Gesellschaft (A and B Series)* 66.5 (1933), p. 656-661.

[3] Livio Cambi et Lamberto Malatesta. "Magnetismus und Polymorphie innerer Komplexsalze : Eisensalze der Dithiocarbamidsäuren". *Berichte der deutschen chemischen Gesellschaft (A and B Series)* 70.10 (1937), p. 2067-2078.

[4] Charles D. Coryell, Fred Stitt et Linus Pauling. "The Magnetic Properties and Structure of Ferrihemoglobin (Methemoglobin) and Some of its Compounds". *Journal of the American Chemical Society* 59.4 (1937), p. 633-642.

[5] Linus. Pauling. "THE NATURE OF THE CHEMICAL BOND. APPLICATION OF RESULTS OBTAINED FROM THE QUANTUM MECHANICS AND FROM A THEORY OF PARAMAGNETIC SUSCEPTIBILITY TO THE STRUCTURE OF MOLECULES". *Journal of the American Chemical Society* 53.4 (avr. 1931), p. 1367-1400.

[6] Leslie E. Orgel. "Some Applications of Crystal-field Theory to Problems in Transition-Metal Chemistry." *Quelques problèmes de chimie minérale : rapports et discussions : dixième Conseil de la chimie tenu à l'Université de Bruxelles du 22 au 26 mai 1956* (1956).

[7] Leslie E. Orgel. "Quelques problèmes de chimie minérale". *Journal of the American Chemical Society* 53.4 (avr. 1931), p. 1367-1400.

[8] Paul E. Figgins et Daryle H. Busch. "THE INFRARED SPECTRA OF THE OCTAHEDRAL COMPLEXES OF IRON(II), COBALT(II) AND NICKEL(II) WITH BIACETYL-BIS-METHYLIMINE AND PYRIDINAL METHYLIMINES". *The Journal of Physical Chemistry* 65.12 (1961), p. 2236-2240.

[9] W. A. Baker Jr. et H. M. Bobonich. "Magnetic Properties of Some High-Spin Complexes of Iron(II)". *Inorganic Chemistry* 3.8 (août 1964), p. 1184-1188.

[10] Edgar Koenig et K. Madeja. "5T2-1A1 Equilibriums in some iron(II)-bis(1,10-phenanthroline) complexes". *Inorganic Chemistry* 6.1 (jan. 1967), p. 48-55.

[11] A. H. Ewald et al. "Anomalous behaviour at the 6A1-2T2 crossover in iron (III) complexes". *Proceedings of the Royal Society of London. Series A. Mathematical and Physical Sciences* 280.1381 (1964), p. 235-257.

[12]   Enrique FRANK et Carlos R. ABELEDO. "Mössbauer Effect in Iron(III) Dithiocarbamates". *Inorganic Chemistry* 5.8 (août 1966), p. 1453-1455.

[13]   Muin S. HADDAD et al. "Spin-crossover ferric complexes : curiosities observed for unperturbed solids". *Inorganic Chemistry* 20.1 (jan. 1981), p. 123-131.

[14]   Jacqueline ZAREMBOWITCH et Olivier KAHN. "Magnetic properties of some spin-crossover, high-spin, and low-spin cobalt(II) complexes with Schiff bases derived from 3-formylsalicylic acid". *Inorganic Chemistry* 23.5 (fév. 1984), p. 589-593.

[15]   Antonio REAL et al. "Magnetic interaction and spin transition in iron(II) dinuclear compounds. Crystal structure of (.mu.-2,2'-bipyrimidine)bis[(2,2'-bipyrimidine)bis (thiocyanato)iron(II)]". *Inorganic Chemistry* 26.18 (sept. 1987), p. 2939-2943.

[16]   Ger Vos et al. "Crystal structure at 300 and 105 K, magnetic properties and Moessbauer spectra of bis(triaquatris(4-ethyltriazole-N1)iron(II)-N2,N2',N2")iron(II) hexakis(trifluoromethanesulfonate). A linear, trinuclear iron(II) compound, showing a unique high-spin-low-spin transition of the central iron atom". *Inorganic Chemistry* 23.18 (août 1984), p. 2905-2910.

[17]   Jaap G. HAASNOOT. "Mononuclear, oligonuclear and polynuclear metal coordination compounds with 1,2,4-triazole derivatives as ligands". English. *Coordination Chemistry Reviews* 200-202 (2000), p. 131 -185.

[18]   Sally BROOKER et al. "[Co(II)(2) L(NCS)(2) (SCN)(2)] : The First Cobalt Complex to Exhibit Both Exchange Coupling and Spin Crossover Effects". en. *Angew Chem Int Ed Engl* 38.3 (fév. 1999), p. 408-410.

[19]   Mario RUBEN et al. "Supramolecular spintronic devices : spin transitions and magneto-structural correlations in [Fe4IIL4]8+ [2x2]-grid-type complexes". en. *Chemistry* 9.18 (sept. 2003), p. 4422-4429.

[20]   Jean-François LÉTARD et al. "Towards Spin Crossover Applications". T. 235. Août 2006, p. 1-19.

[21]   Toshio MIYAMACHI et al. "Robust spin crossover and memristance across a single molecule". *Nature Communications* 3.1 (2012), p. 938.

[22]   W. Robert SCHEIDT et Christopher A. REED. "Spin-state/stereochemical relationships in iron porphyrins : implications for the hemoproteins". *Chemical Reviews* 81.6 (déc. 1981), p. 543-555.

[23]   M. F. PERUTZ et al. "Stereochemistry of cooperative mechanisms in hemoglobin". *Accounts of Chemical Research* 20.9 (sept. 1987), p. 309-321.

[24]   Philipp GÜTLICH et Harold A. GOODWIN. "Spin Crossover—An Overall Perspective". *Spin Crossover in Transition Metal Compounds I*. Sous la dir. de P. GÜTLICH et H. A. GOODWIN. Berlin, Heidelberg : Springer Berlin Heidelberg, 2004, p. 1-47.

[25]   Panagiotis ANGARIDIS et al. "Structural and Magnetic Evidence Concerning Spin Crossover in Formamidinate Compounds with Ru25+ Cores". *Journal of the American Chemical Society* 127.14 (avr. 2005), p. 5008-5009.

[26] Michio Sorai et Syûzô Seki. "Magnetic Heat Capacity Due to Cooperative Low-Spin 1A_1⇌High-Spin 5T2 Transition in Fe(phen)2(NCS)2 Crystal". *Journal of the Physical Society of Japan* 33.2 (1972), p. 575-575.

[27] M. Sorai et S. Seki. "Phonon coupled cooperative low-spin 1A1high-spin 5T2 transition in [Fe(phen)2(NCS)2] and [Fe(phen)2(NCSe)2] crystals". *Journal of Physics and Chemistry of Solids* 35.4 (1974), p. 555-570.

[28] Philipp Gütlich, Andreas Hauser et Hartmut Spiering. "Thermal and Optical Switching of Iron(II) Complexes". *Angewandte Chemie International Edition in English* 33.20 (1994), p. 2024-2054.

[29] Hans Toftlund. "Spin Equilibrium in Solutions". *Monatshefte für Chemie / Chemical Monthly* 132.11 (nov. 2001), p. 1269-1277.

[30] Geraldine Bradley et al. "5T2—1A1 Transitions in six-co-ordinate iron(II) complexes of 2,2-bi-2-thiazoline and 2,2-bi-4,5-dihydrothiazine ligands". *J. Chem. Soc., Dalton Trans.* (5 1978), p. 522-526.

[31] E. König et G. Ritter. "Hysteresis effects at a cooperative high-spin (5T2) low-spin (1A1) transition in dithiocyanatobis (4, 7-dimethyl-1, 10-phenanthroline) iron (II)". *Solid State Communications* 18.3 (1976), p. 279-282.

[32] Yuan-Yuan Peng et al. "Asymmetric seven-/eight-step spin-crossover in a three-dimensional Hofmann-type metal–organic framework". *Inorg. Chem. Front.* 7 (8 2020), p. 1685-1690.

[33] G. Ritter et al. "The high-spin(5T2) .dblharw. low-spin(1A1) transition in solid bis[2-(2-pyridylamino)-4-(2-pyridyl)thiazoleiron(II) dinitrate. Its dependence on time and on the previous history of the specimen". *Inorganic Chemistry* 17.2 (fév. 1978), p. 224-228.

[34] Marek Weselski et al. ""Normal" and "reverse" spin crossover induced by two different structural events in iron(ii) coordination polymer". *Chem. Commun.* 55 (49 2019), p. 7033-7036.

[35] S. Decurtins et al. "Light-induced excited spin state trapping in a transition-metal complex : The hexa-1-propyltetrazole-iron (II) tetrafluoroborate spin-crossover system". *Chemical Physics Letters* 105.1 (1984), p. 1-4.

[36] A. Hauser. "Reversibility of light-induced excited spin state trapping in the Fe(ptz)6(BF4)2, and the Zn1xFex(ptz)6(BF4)2 spin-crossover systems". *Chemical Physics Letters* 124.6 (1986), p. 543-548.

[37] Philipp Gütlich, Petra J. van Koningsbruggen Koningsbruggen et Franz Renz. "Recent Advances of Spin Crossover Research". *Optical Spectra and Chemical Bonding in Transition Metal Complexes : Special Volume dedicated to Professor Jørgensen.* Sous la dir. de T. Schönherr. Berlin, Heidelberg : Springer Berlin Heidelberg, 2004, p. 27-75.

[38] Jean-François Létard et al. "Structural, Magnetic, and Photomagnetic Studies of a Mononuclear Iron(II) Derivative Exhibiting an Exceptionally Abrupt Spin Transition. Light-Induced Thermal Hysteresis Phenomenon". *Inorganic Chemistry* 37.17 (août 1998), p. 4432-4441.

[39]   A. Desaix et al. "Light-induced bistability in spin transition solids leading to thermal and optical hysteresis". *The European Physical Journal B - Condensed Matter and Complex Systems* 6.2 (nov. 1998), p. 183-193.

[40]   F. Renz et al. "Light-perturbed hysteresis in an iron(II) spin-crossover compound observed by the Mössbauer effect". *Hyperfine Interactions* 126.1 (juill. 2000), p. 155-158.

[41]   Cecile Roux et al. "Toward Ligand-Driven Light-Induced Spin Changing. Influence of the Configuration of 4 Styrylpyridine (stpy) on the Magnetic Properties of FeII(stpy)4(NCS)2 Complexes. Crystal Structures of the Spin-Crossover Species Fe(trans-stpy)4(NCS)2 and of the High-Spin Species Fe(cis-stpy)4(NCS)2". *Inorganic Chemistry* 33.10 (mai 1994), p. 2273-2279.

[42]   V. Davesne et al. "First glimpse of the soft x-ray induced excited spin-state trapping effect dynamics on spin cross-over molecules". *The Journal of Chemical Physics* 139.7 (août 2013), p. 074708.

[43]   György Vankó et al. "Hard-X-ray-induced excited-spin-state trapping". en. *Angew Chem Int Ed Engl* 46.28 (2007), p. 5306-5309.

[44]   Philipp Gütlich, Vadim Ksenofontov et Ana B. Gaspar. "Pressure effect studies on spin crossover systems". *Coordination Chemistry Reviews* 249.17 (2005). 36th International Conference on Coordination Chemistry, Merida, Mexico, July 2004, p. 1811-1829.

[45]   Daniele Antonangeli et al. "Spin crossover in ferropericlase at high pressure : a seismologically transparent transition ?" en. *Science* 331.6013 (jan. 2011), p. 64-67.

[46]   Ryuichi Nomura et al. "Spin crossover and iron-rich silicate melt in the Earth's deep mantle". *Nature* 473.7346 (mai 2011), p. 199-202.

[47]   V. Ksenofontov et al. "Spin crossover behavior under pressure of Fe(PM-L)2(NCS)2 compounds with substituted 2-pyridylmethylene 4-anilino ligands". *Chemical Physics Letters* 294.6 (1998), p. 545-553.

[48]   Y. Qi et al. "The effect of a magnetic field on the high-spin low-spin transition in [Fe(phen)2(NCS)2]". *Chemical Physics Letters* 101.4 (1983), p. 503-505.

[49]   A. Bousseksou et al. "Dynamic triggering of a spin-transition by a pulsed magnetic field". *The European Physical Journal B - Condensed Matter and Complex Systems* 13.3 (fév. 2000), p. 451-456.

[50]   Nadjib Baadji et al. "Electrostatic spin crossover effect in polar magnetic molecules". en. *Nat Mater* 8.10 (août 2009), p. 813-817.

[51]   F. Renz et al. "Molecular Sensors for Moisture Detection by Mössbauer Spectroscopy". *Industrial Applications of the Mössbauer Effect.* Sous la dir. de Desmond C. Cook et Gilbert R. Hoy. Dordrecht : Springer Netherlands, 2002, p. 699-704.

[52]   A. Lindner et al. "Metallosupramolecular coordination polyelectrolytes investigated by Mössbauer spectroscopy". *Hyperfine Interactions* 166.1 (nov. 2005), p. 465-468.

[53] Biswanath MAITI et al. "A study of the low spin ⇌ high spin transitions in [Fe(phen)2(NCSe], [Fe(bipy)2(NCS)2], and [Fe(isoxazole)6](ClO4)2 complexes using 1H nuclear magnetic resonance". *Journal of Magnetic Resonance (1969)* 54.1 (1983), p. 99-110.

[54] Lalminthang KIPGEN et al. "Spin-Crossover Molecules on Surfaces : From Isolated Molecules to Ultrathin Films". *Advanced Materials* 33.24 (2021), p. 2008141.

[55] A. RUAUDEL-TEIXIER et al. "Spin transition in a magnetic Langmuir-Blodgett film". *Thin Solid Films* 160.1 (1988), p. 107-115.

[56] André BARRAUD. "Supermolecular engineering by the Langmuir-Blodgett method". *Thin Solid Films* 175 (1989). 22nd International Symposium on Trends and New Applications in Thin Films, p. 73-80.

[57] Mohammad S ALAM et al. "Spin-state patterns in surface-grafted beads of iron(II) complexes". en. *Angew Chem Int Ed Engl* 49.6 (fév. 2010), p. 1159-1163.

[58] S. SHI et al. "Study of molecular spin-crossover complex Fe(phen)2(NCS)2 thin films". *Applied Physics Letters* 95.4 (juill. 2009), p. 043303.

[59] Holger NAGGERT et al. "First observation of light-induced spin change in vacuum deposited thin films of iron spin crossover complexes". *Dalton Trans.* 40 (24 2011), p. 6364-6366.

[60] V. DAVESNE et al. "Hysteresis and change of transition temperature in thin films of Fe [Me2Pyrz]3BH
2, a new sublimable spin-crossover molecule". *The Journal of Chemical Physics* 142.19 (mai 2015), p. 194702.

[61] Torben JASPER-TOENNIES et al. "Robust and Selective Switching of an FeIII Spin-Crossover Compound on Cu2N/Cu(100) with Memristance Behavior". *Nano Letters* 17.11 (2017), p. 6613-6619.

[62] Talal MALLAH et Massimiliano CAVALLINI. "Surfaces, thin films and patterning of spin crossover compounds". en. *Comptes Rendus. Chimie* 21.12 (2018), p. 1270-1286.

[63] Thomas GROIZARD et al. "Enhanced Cooperativity in Supported Spin-Crossover Metal–Organic Frameworks". *The Journal of Physical Chemistry Letters* 8.14 (2017), p. 3415-3420.

[64] Kuppusamy Senthil KUMAR et al. "Engineering On-Surface Spin Crossover : Spin-State Switching in a Self-Assembled Film of Vacuum-Sublimable Functional Molecule". *Advanced Materials* 30.11 (2018), p. 1705416.

[65] Xuanyuan JIANG et al. "Tunable spin-state bistability in a spin crossover molecular complex". *Journal of Physics : Condensed Matter* 31.31 (2019), p. 315401.

[66] Stefano SANVITO. "The rise of spinterface science". *Nature Physics* 6.8 (2010), p. 562-564.

[67] Mirko CINCHETTI, V. Alek DEDIU et Luis E. HUESO. "Activating the molecular spinterface". *Nature Materials* 16.5 (2017), p. 507-515.

[68] Manuel GRUBER et Richard BERNDT. "Spin-Crossover Complexes in Direct Contact with Surfaces". *Magnetochemistry* 6.3 (2020).

[69] Bernard GALLOIS et al. "Structural changes associated with the spin transition in bis(isothiocyanato)bis(1,10-phenanthroline)iron : a single-crystal x-ray investigation". *Inorganic Chemistry* 29.6 (1990), p. 1152-1158.

[70] J. GAULTIER et al. "High pressure single crystal X-ray diffraction study of the spin crossover iron(II) complex Fe(Phen)2(NCS)2". *High Pressure Research* 7.1-6 (1991), p. 336-338.

[71] Thierry GRANIER et al. "High-pressure single-crystal x-ray diffraction study of two spin-crossover iron(II) complexes : Fe(Phen)2(NCS)2 and Fe(Btz)2(NCS)2". *Inorganic Chemistry* 32.23 (nov. 1993), p. 5305-5312.

[72] Tomohiko ISHII et al. "Universal spectrochemical series of six-coordinate octahedral metal complexes for modifying the ligand field splitting". *Dalton Trans.* (4 2009), p. 680-687.

[73] D. C. FISHER et H. G. DRICKAMER. "Effect of Pressure on the Spin State of Iron in Ferrous Phenanthroline Compounds". *The Journal of Chemical Physics* 54.11 (sept. 2003), p. 4825-4837.

[74] V. KSENOFONTOV et al. "Pressure Effect on Spin Crossover in [Fe(phen)2(NCS)2] and [CrI2(depe)2]". *The Journal of Physical Chemistry B* 108.23 (juin 2004), p. 7723-7727.

[75] Azzedine BOUSSEKSOU et al. "Triggering the spin-crossover of Fe(phen)$_2$(NCS)$_2$ by a pressure pulse. Pressure and magnetic field induce 'mirror effects'". en. *Comptes Rendus. Chimie* 6.3 (2003), p. 329-335.

[76] S. DECURTINS et al. "New examples of light-induced excited spin state trapping (LIESST) in iron(II) spin-crossover systems". *J. Chem. Soc., Chem. Commun.* (7 1985), p. 430-432.

[77] S. DECURTINS et al. "Light-induced excited-spin-state trapping in iron(II) spin-crossover systems. Optical spectroscopic and magnetic susceptibility study". *Inorganic Chemistry* 24.14 (juill. 1985), p. 2174-2178.

[78] R. HERBER et L. M. CASSON. "Light-induced excited-spin-state trapping : evidence from variable temperature Fourier transform measurements". *Inorganic Chemistry* 25.6 (mars 1986), p. 847-852.

[79] Jey-Jau LEE et al. "X-ray Absorption Spectroscopic Studies on Light-Induced Excited Spin State Trapping of an Fe(II) Complex". *Journal of the American Chemical Society* 122.24 (juin 2000), p. 5742-5747.

[80] K. KATO et al. "On-off optical switching of the magnetic and structural properties in a spin-crossover complex". *Applied Physics Letters* 90.20 (mai 2007), p. 201902.

[81] David COLLISON et al. "Soft X-ray induced excited spin state trapping and soft X-ray photochemistry at the iron L2,3 edge in [Fe(phen)2(NCS)2] and [Fe(phen)2(NCSe)2] (phen = 1,10-phenanthroline)‡". *J. Chem. Soc., Dalton Trans.* (22 1997), p. 4371-4376.

[82] V DAVESNE et al. "First glimpse of the soft x-ray induced excited spin-state trapping effect dynamics on spin cross-over molecules". en. *J Chem Phys* 139.7 (août 2013), p. 074708.

[83] György VANKÓ et al. "Probing the 3d spin momentum with X-ray emission spectroscopy : the case of molecular-spin transitions". en. *J Phys Chem B* 110.24 (juin 2006), p. 11647-11653.

[84] Hauke PAULSEN, Volker SCHÜNEMANN et Juliusz A. WOLNY. "Progress in Electronic Structure Calculations on Spin-Crossover Complexes". *European Journal of Inorganic Chemistry* 2013.5-6 (2013), p. 628-641.

[85] C. P. SLICHTER et H. G. DRICKAMER. "Pressure-Induced Electronic Changes in Compounds of Iron". *The Journal of Chemical Physics* 56.5 (sept. 2003), p. 2142-2160.

[86] E. A. GUGGENHEIM. "The Statistical Mechanics of Regular Solutions". *Proceedings of the Royal Society of London. Series A, Mathematical and Physical Sciences* 148.864 (1935), p. 304-312.

[87] William Lawrence BRAGG et Evan James WILLIAMS. "The effect of thermal agitation on atomic arrangement in alloys". *Proceedings of the Royal Society of London. Series A, Containing Papers of a Mathematical and Physical Character* 145.855 (1934), p. 699-730.

[88] E. KÖNIG et al. "The effect of pressure on the thermal hysteresis of the first-order spin transition in bis(1,10-phenanthroline-2-carbaldehyde phenylhydrazone) iron (II) complexes". *The Journal of Chemical Physics* 83.6 (sept. 1985), p. 3055-3061.

[89] Hélène BOLVIN et Olivier KAHN. "Ising model for low-spin high-spin transitions in molecular compounds ; within and beyond the mean-field approximation". *Chemical Physics* 192.3 (1995), p. 295-305.

[90] Cristian ENACHESCU et Andreas HAUSER. "Study of switching in spin transition compounds within the mechanoelastic model with realistic parameters". *Phys. Chem. Chem. Phys.* 18 (30 2016), p. 20591-20599.

[91] Keith F. PURCELL et Michael P. EDWARDS. "Cooperativity in thermally induced intersystem crossing in solids : Fe(phen)2(NCR)2, R = BH3, BPh3, S, Se". *Inorganic Chemistry* 23.17 (août 1984), p. 2620-2625.

[92] H. SPIERING. "Elastic Interaction in Spin-Crossover Compounds". *Spin Crossover in Transition Metal Compounds III*. Berlin, Heidelberg : Springer Berlin Heidelberg, 2004, p. 171-195.

[93] Takeshi KAMBARA. "Theory of high-spin ?low-spin transitions in transition metal compounds induced by the Jahn–Teller effect". *The Journal of Chemical Physics* 70.9 (juill. 2008), p. 4199-4206.

[94] Naoyuki SASAKI et Takeshi KAMBARA. "Theory of the two-step spin conversion induced by the cooperative molecular distortions in spin-crossover compounds". *Phys. Rev. B* 40 (4 août 1989), p. 2442-2449.

[95] H. CONSTANT-MACHADO et al. "Thermal hysteresis loops in spin-crossover compounds analyzed in terms of classical Preisach model". *IEEE Transactions on Magnetics* 34.4 (1998), p. 2213-2219.

[96] E. W. MÜLLER, H. SPIERING et P. GÜTLICH. "On the participation of domains in the high spin (5T2) low spin (1A1) transition in dithiocyanatobis (2,2-bi-2-thiazoline) iron (II)". *The Journal of Chemical Physics* 79.3 (août 1983), p. 1439-1443.

[97] Hong-Zhou Ye, Chong Sun et Hong Jiang. "Monte-Carlo simulations of spin-crossover phenomena based on a vibronic Ising-like model with realistic parameters". *Phys. Chem. Chem. Phys.* 17 (10 2015), p. 6801-6808.

[98] Jorge Linares et al. "Monte Carlo entropic sampling applied to spin crossover solids : the squareness of the thermal hysteresis loop". *Polyhedron* 22.14 (2003). Proceedings of the 8th International Conference on Molecule-Based Magnets (ICMM 2002), p. 2453-2456.

[99] Azusa Muraoka et al. "Two-dimensional Ising-like model with specific edge effects for spin-crossover nanoparticles : A Monte Carlo study". *Phys. Rev. B* 84 (5 août 2011), p. 054119.

[100] Linares, J. et al. "Monte Carlo for spin crossover compounds". *EPJ Web of Conferences* 14 (2011), p. 02004.

[101] J. Linares et al. "Monte Carlo simulations of spin-crossover transitions using the two level model. II : Binuclear case". *Journal of Magnetism and Magnetic Materials* 140-144 (1995). International Conference on Magnetism, p. 1503-1504.

[102] Suhwan Song et al. "Benchmarks and Reliable DFT Results for Spin Gaps of Small Ligand Fe(II) Complexes". *Journal of Chemical Theory and Computation* 14.5 (2018), p. 2304-2311.

[103] Marcel Swart et al. "Validation of ExchangeCorrelation Functionals for Spin States of Iron Complexes". *The Journal of Physical Chemistry A* 108.25 (juin 2004), p. 5479-5483.

[104] Marcel Swart. "Accurate Spin-State Energies for Iron Complexes". *Journal of Chemical Theory and Computation* 4.12 (déc. 2008), p. 2057-2066.

[105] Georg Ganzenmüller et al. "Comparison of density functionals for differences between the high- (T2g5) and low- (A1g1) spin states of iron(II) compounds. IV. Results for the ferrous complexes [Fe(L)('NHS4')]". *The Journal of Chemical Physics* 122.23 (juin 2005), p. 234321.

[106] Kristine Pierloot et Steven Vancoillie. "Relative energy of the high-(T2g5) and low-(A1g1) spin states of [Fe(H2O)6]2+, [Fe(NH3)6]2+, and [Fe(bpy)3]2+ : CASPT2 versus density functional theory". *The Journal of Chemical Physics* 125.12 (sept. 2006), p. 124303.

[107] Kristine Pierloot, Quan Manh Phung et Alex Domingo. "Spin State Energetics in First-Row Transition Metal Complexes : Contribution of (3s3p) Correlation and Its Description by Second-Order Perturbation Theory". *Journal of Chemical Theory and Computation* 13.2 (fév. 2017), p. 537-553.

[108] A. Droghetti, D. Alfè et S. Sanvito. "Assessment of density functional theory for iron(II) molecules across the spin-crossover transition". *The Journal of Chemical Physics* 137.12 (sept. 2012), p. 124303.

[109] Efthymios I. Ioannidis et Heather J. Kulik. "Towards quantifying the role of exact exchange in predictions of transition metal complex properties". *The Journal of Chemical Physics* 143.3 (juill. 2015), p. 034104.

[110]   Jordi Cirera et Francesco Paesani. "Theoretical Prediction of Spin-Crossover Temperatures in Ligand-Driven Light-Induced Spin Change Systems". *Inorganic Chemistry* 51.15 (août 2012), p. 8194-8201.

[111]   Jordi Cirera, Mireia Via-Nadal et Eliseo Ruiz. "Benchmarking Density Functional Methods for Calculation of State Energies of First Row Spin-Crossover Molecules". *Inorganic Chemistry* 57.22 (nov. 2018), p. 14097-14105.

[112]   Liam Wilbraham et al. "Multiconfiguration Pair-Density Functional Theory Predicts Spin-State Ordering in Iron Complexes with the Same Accuracy as Complete Active Space Second-Order Perturbation Theory at a Significantly Reduced Computational Cost". *The Journal of Physical Chemistry Letters* 8.9 (mai 2017), p. 2026-2030.

[113]   Sergi Vela et al. "Thermal spin crossover in Fe(ii) and Fe(iii). Accurate spin state energetics at the solid state". *Phys. Chem. Chem. Phys.* 22 (9 2020), p. 4938-4945.

[114]   Lorenzo A Mariano, Bess Vlaisavljevich et Roberta Poloni. "Improved Spin-State Energy Differences of Fe(II) Molecular and Crystalline Complexes via the Hubbard U-Corrected Density". en. *J Chem Theory Comput* 17.5 (avr. 2021), p. 2807-2816.

[115]   S. Lebègue, S. Pillet et J. G. Ángyán. "Modeling spin-crossover compounds by periodic DFT + U approach". *Phys. Rev. B* 78 (2 juill. 2008), p. 024433.

[116]   S. Gueddida et M. Alouani. "Spin crossover in a single $Fe(phen)_2(NCS)_2$ molecule adsorbed onto metallic substrates : An ab initio calculation". *Phys. Rev. B* 87 (14 avr. 2013), p. 144413.

[117]   S. Gueddida et M. Alouani. "Calculated impact of ferromagnetic substrate on the spin crossover in a $Fe(1,10-phenanthroline)_2(NCS)_2$ molecule". *Phys. Rev. B* 93 (18 mai 2016), p. 184433.

[118]   Tomáš Bučko et al. "Spin crossover transition of Fe(phen)2(NCS)2 : periodic dispersion-corrected density-functional study". *Phys. Chem. Chem. Phys.* 14 (16 2012), p. 5389-5396.

[119]   Saber Gueddida. "Theoretical study of the spin crossover in a single Fe(phen)2(NCS)2 molecule adsorbed onto metallic substrates". Thèse de doct. University of Strasbourg, sept. 2014.

[120]   Yachao Zhang. "Surface effects on temperature-driven spin crossover in Fe(phen)(2)(NCS)(2)". en. *J Chem Phys* 153.13 (oct. 2020), p. 134704.

[121]   Rocío Sánchez-de Armas, Iman Jaber El Lala et Carmen J Calzado. "How complex-surface interactions modulate the spin transition of Fe(II) SCO complexes supported on metallic surfaces ?" en. *Phys Chem Chem Phys* 25.32 (août 2023), p. 21673-21683.

[122]   M. Born et R. Oppenheimer. "Zur Quantentheorie der Molekeln". *Annalen der Physik* 389.20 (1927), p. 457-484.

[123]   R. P. Feynman. "Forces in Molecules". *Phys. Rev.* 56 (4 1939), p. 340-343.

[124]   P. Hohenberg et W. Kohn. "Inhomogeneous Electron Gas". *Phys. Rev.* 136 (3B 1964), B864-B871.

[125]   L. H. Thomas. "The calculation of atomic fields". *Mathematical Proceedings of the Cambridge Philosophical Society* 23.5 (1927), 542–548.

[126]   W. Kohn et L. J. Sham. "Self-Consistent Equations Including Exchange and Correlation Effects". *Phys. Rev.* 140 (4A 1965), A1133-A1138.

[127]   Aron J. Cohen et Paula Mori-Sánchez. "Landscape of an exact energy functional". *Phys. Rev. A* 93 (4 2016), p. 042511.

[128]   A. Holas et N. H. March. "Exact exchange-correlation potential and approximate exchange potential in terms of density matrices". *Phys. Rev. A* 51 (3 1995), p. 2040-2048.

[129]   P. A. M. Dirac. "Note on Exchange Phenomena in the Thomas Atom". *Mathematical Proceedings of the Cambridge Philosophical Society* 26.3 (1930), 376–385.

[130]   D. M. Ceperley et B. J. Alder. "Ground State of the Electron Gas by a Stochastic Method". *Phys. Rev. Lett.* 45 (7 1980), p. 566-569.

[131]   R.G. Parr et Y. Weitao. *Density-Functional Theory of Atoms and Molecules*. International Series of Monographs on Chemistry. Oxford University Press, 1994.

[132]   John P. Perdew et Karla Schmidt. "Jacob's ladder of density functional approximations for the exchange-correlation energy". *AIP Conference Proceedings* 577.1 (juill. 2001), p. 1-20.

[133]   Junji Seino et al. "Semi-local machine-learned kinetic energy density functional with third-order gradients of electron density". *The Journal of Chemical Physics* 148.24 (mars 2018), p. 241705.

[134]   Pavlo Golub et Sergei Manzhos. "Kinetic energy densities based on the fourth order gradient expansion : performance in different classes of materials and improvement via machine learning". *Phys. Chem. Chem. Phys.* 21 (1 2019), p. 378-395.

[135]   John P. Perdew. "Nonlocal Density Functionals for Exchange and Correlation : Theory and Applications". *Density Functional Theory of Molecules, Clusters, and Solids*. Sous la dir. de D. E. Ellis. Dordrecht : Springer Netherlands, 1996, p. 47-66.

[136]   John P. Perdew et Yue Wang. "Accurate and simple analytic representation of the electron-gas correlation energy". *Phys. Rev. B* 45 (23 1992), p. 13244-13249.

[137]   John P. Perdew, Kieron Burke et Matthias Ernzerhof. "Generalized Gradient Approximation Made Simple". 77.18 (1996), p. 3865-3868.

[138]   A. V. Postnikov, P. Entel et J. M. Soler. "Density functional simulation of small Fe nanopARTICLEs". *The European Physical Journal D - Atomic, Molecular, Optical and Plasma Physics* 25.3 (2003), p. 261-270.

[139]   V M García-Suárez et al. "Optimized basis sets for the collinear and non-collinear phases of iron". *Journal of Physics : Condensed Matter* 16.30 (2004), p. 5453-5459.

[140]   D. J. Singh et J. Ashkenazi. "Magnetism with generalized-gradient-approximation density functionals". *Phys. Rev. B* 46 (18 1992), p. 11570-11577.

[141]   Timothy J Giese et Darrin M York. "Density-functional expansion methods : evaluation of LDA, GGA, and meta-GGA functionals and different integral approximations". en. *J Chem Phys* 133.24 (déc. 2010), p. 244107.

[142] Vincent L. Lignères et Emily A. Carter. "An Introduction to Orbital-Free Density Functional Theory". *Handbook of Materials Modeling : Methods*. Sous la dir. de Sidney Yip. Dordrecht : Springer Netherlands, 2005, p. 137-148.

[143] Wenhui Mi et al. "Orbital-Free Density Functional Theory : An Attractive Electronic Structure Method for Large-Scale First-Principles Simulations". *Chemical Reviews* 123.21 (2023), p. 12039-12104.

[144] D. R. Hamann, M. Schlüter et C. Chiang. "Norm-Conserving Pseudopotentials". *Phys. Rev. Lett.* 43 (20 1979), p. 1494-1497.

[145] Pedro Borlido et al. "Validation of Pseudopotential Calculations for the Electronic Band Gap of Solids". *Journal of Chemical Theory and Computation* 16.6 (2020), p. 3620-3627.

[146] J. C. Slater. "An Augmented Plane Wave Method for the Periodic Potential Problem". *Phys. Rev.* 92 (3 1953), p. 603-608.

[147] P. E. Blöchl. "Projector augmented-wave method". *Phys. Rev. B* 50 (24 1994), p. 17953-17979.

[148] N F Mott et R Peierls. "Discussion of the paper by de Boer and Verwey". *Proceedings of the Physical Society* 49.4S (1937), p. 72.

[149] J. P. Perdew et Alex Zunger. "Self-interaction correction to density-functional approximations for many-electron systems". *Phys. Rev. B* 23 (10 1981), p. 5048-5079.

[150] J. Hubbard. "Electron Correlations in Narrow Energy Bands". *Proceedings of the Royal Society of London. Series A, Mathematical and Physical Sciences* 276.1365 (1963), p. 238-257.

[151] Vladimir I. Anisimov, Jan Zaanen et Ole K. Andersen. "Band theory and Mott insulators : Hubbard U instead of Stoner I". *Phys. Rev. B* 44 (3 1991), p. 943-954.

[152] Vladimir I. Anisimov, Jan Zaanen et Ole K. Andersen. "Band theory and Mott insulators : Hubbard U instead of Stoner I". 44.3 (1991), p. 943-954.

[153] V. I. Anisimov et al. "Density-functional theory and NiO photoemission spectra". *Phys. Rev. B* 48 (23 1993), p. 16929-16934.

[154] I. V. Solovyev, P. H. Dederichs et V. I. Anisimov. "Corrected atomic limit in the local-density approximation and the electronic structure of d impurities in Rb". *Phys. Rev. B* 50 (23 1994), p. 16861-16871.

[155] S. L. Dudarev et al. "Electron-energy-loss spectra and the structural stability of nickel oxide : An LSDA+U study". *Phys. Rev. B* 57 (3 1998), p. 1505-1509.

[156] A. I. Liechtenstein, V. I. Anisimov et J. Zaanen. "Density-functional theory and strong interactions : Orbital ordering in Mott-Hubbard insulators". *Phys. Rev. B* 52 (8 1995), R5467-R5470.

[157] Jiří Klimeš et Angelos Michaelides. "Perspective : Advances and challenges in treating van der Waals dispersion forces in density functional theory". *The Journal of Chemical Physics* 137.12 (sept. 2012), p. 120901.

[158] Stefan GRIMME. "Semiempirical GGA-type density functional constructed with a long-range dispersion correction". *Journal of Computational Chemistry* 27.15 (2006), p. 1787-1799.

[159] Stefan GRIMME. "Accurate description of van der Waals complexes by density functional theory including empirical corrections". *Journal of Computational Chemistry* 25.12 (2004), p. 1463-1473.

[160] Stefan GRIMME et al. "A consistent and accurate ab initio parametrization of density functional dispersion correction (DFT-D) for the 94 elements H-Pu". *The Journal of Chemical Physics* 132.15 (avr. 2010), p. 154104.

[161] Stefan GRIMME et al. "A consistent and accurate ab initio parametrization of density functional dispersion correction (DFT-D) for the 94 elements H-Pu". *The Journal of Chemical Physics* 132.15 (2010), p. 154104.

[162] P. E. BLÖCHL. "Projector augmented-wave method". *Phys. Rev. B* 50 (24 déc. 1994), p. 17953-17979.

[163] G. KRESSE et J. FURTHMÜLLER. "Efficient iterative schemes for ab initio total-energy calculations using a plane-wave basis set". *Phys. Rev. B* 54 (16 oct. 1996), p. 11169-11186.

[164] S. L. DUDAREV et al. "Electron-energy-loss spectra and the structural stability of nickel oxide : An LSDA+U study". *Phys. Rev. B* 57 (3 jan. 1998), p. 1505-1509.

[165] Lorenzo A. MARIANO, Bess VLAISAVLJEVICH et Roberta POLONI. "Biased Spin-State Energetics of Fe(II) Molecular Complexes within Density-Functional Theory and the Linear-Response Hubbard U Correction". *Journal of Chemical Theory and Computation* 16.11 (nov. 2020), p. 6755-6762.

[166] Damián A. SCHERLIS et al. "Simulation of Heme Using DFT + U : A Step toward Accurate Spin-State Energetics". *The Journal of Physical Chemistry B* 111.25 (juin 2007), p. 7384-7391.

[167] Angel ALBAVERA-MATA, S. B. TRICKEY et Richard G. HENNIG. "Mean Value Ensemble Hubbard-U Correction for Spin-Crossover Molecules". *The Journal of Physical Chemistry Letters* 13.51 (déc. 2022), p. 12049-12054.

[168] M. METHFESSEL et A. T. PAXTON. "High-precision sampling for Brillouin-zone integration in metals". *Phys. Rev. B* 40 (6 août 1989), p. 3616-3621.

[169] Rangsiman KETKAEW et al. "OctaDist : a tool for calculating distortion parameters in spin crossover and coordination complexes". *Dalton Transactions* 50.3 (2021), p. 1086-1096.

[170] Francesco BABUDRI et al. "Fluorinated organic materials for electronic and optoelectronic applications : the role of the fluorine atom". *Chem. Commun.* (10 2007), p. 1003-1022.

[171] H. BRINKMANN et al. "Fluorinated phthalocyanines as molecular semiconductor thin films". *physica status solidi (a)* 205.3 (2008), p. 409-420.

[172] Franck NGASSAM et al. "Fluorinated Phthalocyanine Molecules on Ferromagnetic Cobalt : A Highly Polarized Spinterface". *The Journal of Physical Chemistry C* 123.43 (oct. 2019), p. 26475-26480.

[173] R. Pasquier, K. Rassoul et M. Alouani. "Inverse spin crossover in fluorinated Fe(1,10-phenanthroline)2(NCS)2 adsorbed on Cu (001) surface". *Computational Condensed Matter* 32 (2022), e00735.

[174] Graeme Henkelman, Andri Arnaldsson et Hannes Jónsson. "A fast and robust algorithm for Bader decomposition of charge density". *Computational Materials Science* 36.3 (2006), p. 354-360.

[175] R. F. W. Bader. "Atoms in molecules". *Accounts of Chemical Research* 18.1 (jan. 1985), p. 9-15.

[176] C.J. Ballhausen. *Introduction to Ligand Field Theory*. New York, USA : McGraw-Hill Book Company, 1962.

[177] A. Dixit, D. Stoeffler et M. Alouani. "Effect of site disorder on the electronic, magnetic, and ferroelectric properties of gallium ferrite". *Phys. Rev. Mater.* 4 (7 juill. 2020), p. 074406.

[178] W. Kabsch. "A solution for the best rotation to relate two sets of vectors". *Acta Crystallographica Section A* 32.5 (sept. 1976), p. 922-923.

[179] Edmund Clifton Stoner. "Collective electron ferromagnetism". *Proceedings of the Royal Society of London. Series A. Mathematical and Physical Sciences* 165.922 (1938), p. 372-414.

[180] K. Tarafder et al. "Pressure and Temperature Control of Spin-Switchable Metal-Organic Coordination Polymers from Ab Initio Calculations". *Phys. Rev. Lett.* 109 (7 août 2012), p. 077203.

[181] Alessandro Laio et Michele Parrinello. "Escaping free-energy minima". *Proceedings of the National Academy of Sciences* 99.20 (2002), p. 12562-12566.

[182] *Classical and Quantum Dynamics in Condensed Phase Simulations*. Juin 1998.

[183] Tom K. Woo et al. "A Combined CarParrinello QM/MM Implementation for ab Initio Molecular Dynamics Simulations of Extended Systems : Application to Transition Metal Catalysis". *The Journal of Physical Chemistry B* 101.40 (oct. 1997), p. 7877-7880.

[184] C. Jarzynski. "Nonequilibrium Equality for Free Energy Differences". *Phys. Rev. Lett.* 78 (14 avr. 1997), p. 2690-2693.

[185] Vincent Davesne. "Organic spintronics : an investigation on spin-crossover complexes from isolated molecules to the device" (nov. 2013).

[186] Luqiong Zhang et al. "Anomalous Light-Induced Spin-State Switching for Iron(II) Spin-Crossover Molecules in Direct Contact with Metal Surfaces". en. *Angew Chem Int Ed Engl* 59.32 (juin 2020), p. 13341-13346.

[187] M. Parrinello et A. Rahman. "Polymorphic transitions in single crystals : A new molecular dynamics method". *Journal of Applied Physics* 52.12 (déc. 1981), p. 7182-7190.

[188] Renata M. Wentzcovitch. "Invariant molecular-dynamics approach to structural phase transitions". *Phys. Rev. B* 44 (5 1991), p. 2358-2361.

[189] Atsushi Togo et Isao Tanaka. "First principles phonon calculations in materials science". *Scripta Materialia* 108 (2015), p. 1-5.

[190] Stefano Baroni, Paolo Giannozzi et Eyvaz Isaev. "Density-Functional Perturbation Theory for Quasi-Harmonic Calculations". *Reviews in Mineralogy and Geochemistry* 71.1 (jan. 2010), p. 39-57.

[191] G. Leibfried et W. Ludwig. "Theory of Anharmonic Effects in Crystals". *Solid State Physics*. Sous la dir. de Frederick Seitz et David Turnbull. T. 12. Academic Press, 1961, p. 275-444.

[192] D.C. Wallace. *Thermodynamics of Crystals*. Dover books on physics. Dover Publications, 1998.

[193] Atsushi Togo, Fumiyasu Oba et Isao Tanaka. "First-principles calculations of the ferroelastic transition between rutile-type and $CaCl_2$-type SiO_2 at high pressures". *Phys. Rev. B* 78 (13 oct. 2008), p. 134106.

[194] K. Parlinski, Z. Q. Li et Y. Kawazoe. "First-Principles Determination of the Soft Mode in Cubic ZrO_2". *Phys. Rev. Lett.* 78 (21 mai 1997), p. 4063-4066.

[195] Xavier Gonze et Changyol Lee. "Dynamical matrices, Born effective charges, dielectric permittivity tensors, and interatomic force constants from density-functional perturbation theory". *Phys. Rev. B* 55 (16 avr. 1997), p. 10355-10368.

[196] Stefano Baroni et al. "Phonons and related crystal properties from density-functional perturbation theory". *Rev. Mod. Phys.* 73 (2 juill. 2001), p. 515-562.

[197] Tianli Feng et Xiulin Ruan. "Quantum mechanical prediction of four-phonon scattering rates and reduced thermal conductivity of solids". *Phys. Rev. B* 93 (4 jan. 2016), p. 045202.

[198] Terumasa Tadano et Shinji Tsuneyuki. "First-Principles Lattice Dynamics Method for Strongly Anharmonic Crystals". *Journal of the Physical Society of Japan* 87.4, 041015 (avr. 2018), p. 041015.

[199] R. M. Sternheimer. "Electronic Polarizabilities of Ions from the Hartree-Fock Wave Functions". *Phys. Rev.* 96 (4 nov. 1954), p. 951-968.

[200] Lorenzo Paulatto, Francesco Mauri et Michele Lazzeri. "Anharmonic properties from a generalized third-order ab initio approach : Theory and applications to graphite and graphene". *Phys. Rev. B* 87 (21 juin 2013), p. 214303.

[201] X. Gonze et J.-P. Vigneron. "Density-functional approach to nonlinear-response coefficients of solids". *Phys. Rev. B* 39 (18 juin 1989), p. 13120-13128.

[202] François Bottin, Jordan Bieder et Johann Bouchet. "a-TDEP : Temperature Dependent Effective Potential for Abinit – Lattice dynamic properties including anharmonicity". *Computer Physics Communications* 254 (2020), p. 107301.

[203] Brent Fultz. "Vibrational thermodynamics of materials". *Progress in Materials Science* 55.4 (2010), p. 247-352.

[204] Ling Ti Kong. "Phonon dispersion measured directly from molecular dynamics simulations". *Computer Physics Communications* 182.10 (2011), p. 2201-2207.

[205] Markus REIHER. "Theoretical Study of the Fe(phen)2(NCS)2 Spin-Crossover Complex with Reparametrized Density Functionals". *Inorganic Chemistry* 41.25 (déc. 2002), p. 6928-6935.

[206] Anton V. SINITSKIY, Andrei L. TCHOUGRÉEFF et Richard DRONSKOWSKI. "Phenomenological model of spin crossover in molecular crystals as derived from atom–atom potentials". *Phys. Chem. Chem. Phys.* 13 (29 2011), p. 13238-13246.

[207] Lars KREUTZBURG, Christian G. HÜBNER et Hauke PAULSEN. "Cooperativity of Spin Crossover Complexes : Combining Periodic Density Functional Calculations and Monte Carlo Simulation". *Materials* 10.2 (2017).

[208] V. KSENOFONTOV et al. "Pressure Effect on Spin Crossover in [Fe(phen)2(NCS)2] and [CrI2(depe)2]". *The Journal of Physical Chemistry B* 108.23 (juin 2004), p. 7723-7727.

[209] D. STEELE et D. H. WHIFFEN. "The vibrational frequencies of hexafluorobenzene". *Trans. Faraday Soc.* 55 (0 1959), p. 369-376.

[210] J.D. LAPOSA et Craig MONTGOMERY. "Infrared spectrum of hexafluorobenzene crystal at 77 K". *Spectrochimica Acta Part A : Molecular Spectroscopy* 38.11 (1982), p. 1109-1113.

[211] Hans C. ANDERSEN. "Molecular dynamics simulations at constant pressure and/or temperature". *The Journal of Chemical Physics* 72.4 (juill. 2008), p. 2384-2393.

[212] *Sigma-Aldrich IR tables*. `https : / / www . sigmaaldrich . com / FR / en / technical - documents / technical - article / analytical - chemistry / photometry - and - reflectometry / ir - spectrum - table`. Accessed : 09-01-2024.

[213] Daan FRENKEL et Berend SMIT. "Chapter 1 - Introduction". *Understanding Molecular Simulation (Second Edition)*. Sous la dir. de Daan FRENKEL et Berend SMIT. Second Edition. San Diego : Academic Press, 2002, p. 1-6.

[214] R. PASQUIER et M. ALOUANI. "Calculated iron $L_{2,3}$ x-ray absorption and x-ray magnetic circular dichroism of spin-crossover $Fe(phen)_2(NCS)_2$ molecules adsorbed on a Cu(001) surface". *Phys. Rev. B* 108 (9 2023), p. 094423.

[215] Deanne Jackson RUDD et al. "X-ray Absorption Spectroscopic Investigation of the Spin-Transition Character in a Series of Single-Site Perturbed Iron(II) Complexes". *Inorganic Chemistry* 44.5 (mars 2005), p. 1221-1229.

[216] V. BRIOIS et al. "Full Multiple Scattering and Crystal Field Multiplet Calculations Performed on the Spin Transition FeII(phen)2(NCS)2 Complex at the Iron K and L2,3 X-ray Absorption Edges". *Journal of the American Chemical Society* 117.3 (jan. 1995), p. 1019-1026.

[217] Rosalie K. HOCKING et al. "Fe L-Edge XAS Studies of K4[Fe(CN)6] and K3[Fe(CN)6] : A Direct Probe of Back-Bonding". *Journal of the American Chemical Society* 128.32 (août 2006), p. 10442-10451.

[218] Paul Adrien Maurice DIRAC et Niels Henrik David BOHR. "The quantum theory of the emission and absorption of radiation". *Proceedings of the Royal Society of London. Series A, Containing Papers of a Mathematical and Physical Character* 114.767 (1927), p. 243-265.

[219] Philippe Sainctavit, Marie-Anne Arrio et Christian Brouder. "Analytic calculation of the spin sum rule at the $L_{2,3}$ edges of Cu^{2+}". *Phys. Rev. B* 52 (17 nov. 1995), p. 12766-12769.

[220] Ferenc Karsai et al. "Effects of electron-phonon coupling on absorption spectrum : K edge of hexagonal boron nitride". *Phys. Rev. B* 98 (23 déc. 2018), p. 235205.

[221] Harry Ramanantoanina et Maja Gruden. "Theoretical insight into the magnetic circular dichroism of uranium N6,7-edge X-ray absorption". *International Journal of Quantum Chemistry* 120.3 (2020), e26081.

[222] Anant Dixit et M. Alouani. "Ab initio calculations of X-ray magnetic circular dichroism spectra within the projector augmented wave method : An implementation into the VASP code". *Computer Physics Communications* 207 (2016), p. 136-144.

[223] John C. Slater. "Statistical Exchange-Correlation in the Self-Consistent Field". *Advances in Quantum Chemistry*. Sous la dir. de Per-Olov Löwdin. T. 6. Academic Press, 1972, p. 1-92.

[224] J. C. Slater et K. H. Johnson. "Self-Consistent-Field $X\alpha$ Cluster Method for Polyatomic Molecules and Solids". *Phys. Rev. B* 5 (3 fév. 1972), p. 844-853.

[225] u, familyi=u., given=Oana, giveni=O., „ et Matteo Calandra. "Projector augmented wave calculation of x-ray absorption spectra at the $L_{2,3}$ edges". *Phys. Rev. B* 87 (20 mai 2013), p. 205105.

[226] Paul Adrien Maurice Dirac et Ralph Howard Fowler. "The quantum theory of the electron". *Proceedings of the Royal Society of London. Series A, Containing Papers of a Mathematical and Physical Character* 117.778 (1928), p. 610-624.

[227] Mathieu Taillefumier et al. "X-ray absorption near-edge structure calculations with the pseudopotentials : Application to the K edge in diamond and α-quartz". *Phys. Rev. B* 66 (19 nov. 2002), p. 195107.

[228] D D Koelling et B N Harmon. "A technique for relativistic spin-polarised calculations". *Journal of Physics C : Solid State Physics* 10.16 (août 1977), p. 3107.

[229] J J Sakurai et Jim Napolitano. *Modern quantum mechanics*. en. 3e éd. Cambridge, England : Cambridge University Press, sept. 2020.

[230] A. R. Edmonds. *Angular Momentum in Quantum Mechanics*. Princeton : Princeton University Press, 1957.

[231] Luis Grave de Peralta. "Exact quasi-relativistic wavefunctions of Hydrogen-like atoms". *Scientific Reports* 10.1 (sept. 2020), p. 14925.

[232] G van der Laan. "Applications of soft x-ray magnetic dichroism". *Journal of Physics : Conference Series* 430.1 (2013), p. 012127.

[233] M. Altarelli. "Sum rules for X-ray magnetic circular dichroism". *Il Nuovo Cimento D* 20.7 (juill. 1998), p. 1067-1073.

[234] B. T. Thole et al. "X-ray circular dichroism as a probe of orbital magnetization". *Phys. Rev. Lett.* 68 (12 mars 1992), p. 1943-1946.

[235] Paolo CARRA et al. "X-ray circular dichroism and local magnetic fields". *Phys. Rev. Lett.* 70 (5 fév. 1993), p. 694-697.

[236] Christophe Cartier dit MOULIN et al. "Spin transition evidenced by soft x-ray absorption spectroscopy". *The Journal of Physical Chemistry* 96.15 (juill. 1992), p. 6196-6198.

[237] J. VINSON et al. "Bethe-Salpeter equation calculations of core excitation spectra". *Phys. Rev. B* 83 (11 mars 2011), p. 115106.

[238] Robert LASKOWSKI et Peter BLAHA. "Understanding the $L_{2,3}$ x-ray absorption spectra of early $3d$ transition elements". *Phys. Rev. B* 82 (20 nov. 2010), p. 205104.

[239] J. SCHWITALLA et H. EBERT. "Electron Core-Hole Interaction in the X-Ray Absorption Spectroscopy of $3d$ Transition Metals". *Phys. Rev. Lett.* 80 (20 mai 1998), p. 4586-4589.

[240] J P CROCOMBETTE, B T THOLE et F JOLLET. "The importance of the magnetic dipole term in magneto-circular x-ray absorption dichroism for 3d transition metal compounds". *Journal of Physics : Condensed Matter* 8.22 (mai 1996), p. 4095.

[241] Ruqian WU et A. J. FREEMAN. "Limitation of the Magnetic-Circular-Dichroism Spin Sum Rule for Transition Metals and Importance of the Magnetic Dipole Term". *Phys. Rev. Lett.* 73 (14 oct. 1994), p. 1994-1997.

[242] Zhen XU et al. "Manipulation of Molecular Spin State on Surfaces Studied by Scanning Tunneling Microscopy". en. *Nanomaterials (Basel)* 10.12 (nov. 2020).

[243] J. BARDEEN. "Tunnelling from a Many-Particle Point of View". *Phys. Rev. Lett.* 6 (2 1961), p. 57-59.

[244] C. Julian CHEN. "Tunneling matrix elements in three-dimensional space : The derivative rule and the sum rule". *Phys. Rev. B* 42 (14 1990), p. 8841-8857.

[245] J. TERSOFF et D. R. HAMANN. "Theory and Application for the Scanning Tunneling Microscope". 50.25 (1983), p. 1998-2001.

[246] J. TERSOFF et D. R. HAMANN. "Theory of the scanning tunneling microscope". *Phys. Rev. B* 31 (2 1985), p. 805-813.

[247] Samir LOUNIS. "Theory of Scanning Tunneling Microscopy" (avr. 2014).

[248] M. JULLIERE. "Tunneling between ferromagnetic films". *Physics Letters A* 54.3 (1975), p. 225-226.

[249] W.A HOFER. "Challenges and errors : interpreting high resolution images in scanning tunneling microscopy". *Progress in Surface Science* 71.5 (2003). Proceedings of the IXth Symposium on Surface Physics, Trest Castle 2002, p. 147-183.

[250] W.A. HOFER. A Guide to simulation of STM images and spectra from first principles : bSKAN 3.6. Août 2005.

[251] Daniel G. a. SMITH et Johnnie GRAY. "opt_einsum - A Python package for optimizing contraction order for einsum-like expressions". *Journal of Open Source Software* 3.26 (2018), p. 753.

[252] Gábor MÁNDI et Krisztián PALOTÁS. "Chen's derivative rule revisited : Role of tip-orbital interference in STM". *Phys. Rev. B* 91 (16 avr. 2015), p. 165406.

[253] Gábor Mándi, Gilberto Teobaldi et Krisztián Palotás. "Contrast stability and 'stripe' formation in scanning tunnelling microscopy imaging of highly oriented pyrolytic graphite : the role of STM-tip orientations". *Journal of Physics : Condensed Matter* 26.48 (2014), p. 485007.

[254] Gábor Mándi, Gilberto Teobaldi et Krisztián Palotás. "What is the orientation of the tip in a scanning tunneling microscope ?" *Progress in Surface Science* 90.2 (2015), p. 223-238.

[255] W.A. Hofer et J. Redinger. "Scanning tunneling microscopy of binary alloys : first principles calculation of the current for PtX (100) surfaces." *Surface Science* 447.1 (2000), p. 51-61.

[256] P. Souvatzis et al. "Entropy Driven Stabilization of Energetically Unstable Crystal Structures Explained from First Principles Theory". *Phys. Rev. Lett.* 100 (9 2008), p. 095901.

[257] Jakob Herz et al. "Crystal effects in the vibrational spectra of one-dimensional molecular spin crossover crystals using molecular dynamics simulations". *Applied Physics A* 129.5 (2023), p. 345.

[258] Paolo Carra et al. "Magnetic x-ray dichroism in gadolinium metal". *Phys. Rev. Lett.* 66 (19 1991), p. 2495-2498.

[259] Paolo Carra et al. "Magnetic X-ray dichroism : General features of dipolar and quadrupolar spectra". *Physica B : Condensed Matter* 192.1 (1993), p. 182-190.

[260] J. Stöhr et H. König. "Determination of Spin- and Orbital-Moment Anisotropies in Transition Metals by Angle-Dependent X-Ray Magnetic Circular Dichroism". *Phys. Rev. Lett.* 75 (20 1995), p. 3748-3751.

[261] Harry Ramanantoanina. "LFDFT - A Practical Tool for Coordination Chemistry". *Computation* 10.5 (2022).

[262] P. NOZIÈRES et C. T. DE DOMINICIS. "Singularities in the X-Ray Absorption and Emission of Metals. III. One-Body Theory Exact Solution". *Phys. Rev.* 178 (3 1969), p. 1097-1107.

[263] R. Landauer. "Spatial variation of currents and fields due to localized scatterers in metallic conduction". *IBM Journal of Research and Development* 32.3 (1988), p. 306-316.

[264] J. Cerdá et al. "Efficient method for the simulation of STM images. I. Generalized Green-function formalism". *Phys. Rev. B* 56 (24 1997), p. 15885-15899.

[265] Nicolas Boulanger-Lewandowski et Alain Rochefort. "Intrusive STM imaging". *Phys. Rev. B* 83 (11 2011), p. 115430.

[266] Yigal Meir et Ned S. Wingreen. "Landauer formula for the current through an interacting electron region". *Phys. Rev. Lett.* 68 (16 1992), p. 2512-2515.

[267] Kerem Y. Camsari, Shuvro Chowdhury et Supriyo Datta. "The Nonequilibrium Green Function (NEGF) Method". *Springer Handbook of Semiconductor Devices*. Sous la dir. de Massimo Rudan, Rossella Brunetti et Susanna Reggiani. Cham : Springer International Publishing, 2023, p. 1583-1599.

[268] Emi Minamitani et al. "Inelastic electron tunneling spectroscopy by STM of phonons at solid surfaces and interfaces". *Progress in Surface Science* 93.4 (2018). Special Issue in Honor of Prof. Maki Kawai, p. 131-145.

[269] J. C. Slater. "Atomic Shielding Constants". *Physical Review* 36.1 (1930), p. 57-64.

[270] Valérie Jeanne-Rose et Bertrand Poumellec. "Coordination octahedron distortion effect on x-ray absorption fine structures of titanium in the rutile titanium dioxide". *Journal of Physics : Condensed Matter* 11.4 (fév. 1999), p. 1123.

[271] Peter H. Schönemann et Robert M. Carroll. "Fitting one matrix to another under choice of a central dilation and a rigid motion". *Psychometrika* 35.2 (juin 1970), p. 245-255.

[272] G A Rooke. "Soft X-Ray Band Spectra and Their Relationship to the Density of States". en. *J Res Natl Bur Stand A Phys Chem* 74A.2 (mars 1970), p. 273-279.

Rémi PASQUIER

Theory of the electronic structure of spin crossover molecules on metallic surfaces

Résumé

L'objectif de cette thèse est l'étude du comportement des molécules à transition de spin adsorbées sur des surfaces métalliques, en utilisant des méthodes ab-initio basées sur la théorie de la fonctionnelle de densité (DFT). En premier lieu, nous redécrivons les états de spin d'une molécule de FePhen et son interaction avec un substrat métallique de Cu(001) et nous la comparons à une molécule de FePhen dopée par fluorination. Nous montrons ainsi une inversion des états de spin après fluorination, que nous étudions en détail en utilisant l'analyse de Bader afin de déterminer les transferts de charge intramoléculaires, ainsi que la méthode « Nudged Elastic Band » (NEB) pour l'étude du chemin de transition entre les états de spin. Finalement, nous calculons le spectre des phonons dans ces systèmes dans l'approximation harmonqiue, et nous montrons les différences importantes entre les modes de la molécule non-dopée et dopée, ainsi que leur influence sur l'évolution avec la température de grandeurs thermodynamiques telles que l'énergie libre, et nous les utilisons avec la formule de Slichter-Drickamer afin de calculer l'évolution de la fraction en état HS avec la température. Nous introduirons également nos premiers résultats d'un calcul post-harmonique du spectre de phonons en dynamique moléculaire en utilisant la fonction d'autocorrélation des vitesses, afin d'étudier l'évolution des principaux modes du spectre eux-mêmes avec la température. En un second temps, nous développons et implémentons dans VASP le calcul des spectres d'absorption à rayons X (XAS et XMCD) afin d'obtenir de manière théorique les spectres au seuil L_{23} dans l'atome de fer de la molécule de FePhen, avec et sans la surface. En premier lieu, nous démontrons que la contribution des ondes planes à ce spectre est négligeable, ce qui facilite et accélère grandement le calcul, mais également que l'ajout d'un trou de cœur statique n'améliore pas dans ce cas les résultats obtenus. Ensuite, nous montrons l'impact relativement faible de ce substrat sur ces spectres. En outre, nous montrons que la déformation des complexes vis-à-vis d'une géométrie octahédrale parfaite induit des effets perceptible sur le spectre ainsi que sur l'anisotropie magnétique de la molécule. Finalement, nous implémentons dans VASP le calcul du tenseur dipolaire magnétique et nous mettons en évidence sa contribution importante, mais très souvent négligée, dans l'évaluation des règles d'intégration de ces spectres. Finalement, nous implémentons le calcul des images de microscopie à effet tunnel (STM) au-delà de l'approximation de Tersoff-Hamann (TH), en utilisant la règle différentielle de Chen, dans les cas idéaux et avec des pointes réalistes, et avec la formule de Bardeen complète. Nous comparons ces résultats avec les images déjà obtenues auparavant avec cette première approximation TH mais également aux quelques images expérimentales. Nous montrons ainsi qu'au-delà la claire et apparente similarité entre toutes les méthodes, les différentes approches présentent des détails fins clairement distinguables qui pourraient être observés expérimentalement avec des images de meilleure précision que les quelques résultats déjà disponibles.

<u>Mots clés :</u> Ab initio, DFT, VASP, transition de spin, dopage, phonons, modèle de Slichter-Drickamer, XAS, XMCD, anisotropie, STM.

Abstract

The aim of this thesis is to study the behaviour of spin-transition molecules adsorbed on metal surfaces, using ab-initio methods based on density functional theory (DFT). First, we re-describe the spin states of a FePhen molecule and its interaction with a Cu(001) metal substrate and compare it to a fluorine-doped FePhen molecule. We show an inversion of the spin states after fluorination, which we study in detail using Bader analysis to determine the intramolecular charge transfers, and the Nudged Elastic Band (NEB) method to study the transition path between the spin states. Finally, we calculate the phonon spectrum in these systems in the harmonic approximation, and we show the important differences between the modes of the undoped and doped molecule, as well as their influence on the evolution with temperature of thermodynamic quantities such as the free energy, and we use them with the Slichter-Drickamer formula to calculate the evolution of the fraction in the HS state with temperature. We will also introduce our first results for a post-harmonic calculation of the phonon spectrum in molecular dynamics using the velocity autocreelation function, in order to study the evolution of the main modes of the spectrum themselves with temperature. Secondly, we develop and implement in VASP the calculation of X-ray absorption spectra (XAS and XMCD) in order to obtain theoretically the L_{23} threshold spectra in the iron atom of the FePhen molecule, with and without the surface. Firstly, we show that the contribution of plane waves to this spectrum is negligible, which greatly facilitates and accelerates the calculation, but also that the addition of a static core hole does not improve the results obtained in this case. We then show the relatively small impact of this substrate on these spectra. In addition, we show that the deformation of the complexes with respect to a perfect octahedral geometry induces perceptible effects on the spectrum as well as on the magnetic anisotropy of the molecule. Finally, we implement the calculation of the magnetic dipole tensor in VASP and highlight its important, but very often neglected, contribution to the evaluation of the integration rules for these spectra. Finally, we implement the computation of scanning tunneling microscopy (STM) images beyond the Tersoff-Hamann (TH) approximation, using Chen's differential rule, in the ideal cases and with realistic tips, and with the full Bardeen formula. We compare these results with images obtained previously with this first TH approximation, as well as with the few experimentally available images. We thus show that beyond the clear and apparent similarity between all the methods, the different approaches present clearly distinguishable fine details that could be observed experimentally with images of better precision than the few results already available.

Key words: Ab initio, DFT, VASP, spin transition, doping, phonons, Slichter-Drickamer model, XAS, XMCD, anisotropy, STM.